Hydrogen production from water - methanol over visible light active modified titanium and indium oxides based photocatalysts

by

VINOTHKUMAR N.

Department of Chemical Engineering

Indian Institute of Technology Guwahati

Guwahati - 781039, India

August, 2014

Hydrogen production from water - methanol over visible light active modified titanium and indium oxides based photocatalysts

VINOTHKUMAR NATARAJAN

Hydrogen production from water - methanol over visible light active modified titanium and indium oxides based photocatalysts

Submitted in partial fulfillment of the requirements for the degree of

DOCTOR OF PHILOSOPHY

by

Vinothkumar N.

(Roll No.: 08610706)

Department of Chemical Engineering

Indian Institute of Technology Guwahati

Guwahati - 781039, India

August, 2014

Dedicated To

T. Natarajan and N. Mallika

&

T. Ramani and R. Vijaya

&

My lovable sister

You are the reason I am what I've become today

Department of Chemical Engineering
Indian Institute of Technology Guwahati
Guwahati - 781039, India

CERTIFICATE

It is certified that the work contained in the thesis entitled "**Hydrogen production from water-methanol over visible light active modified titanium and indium oxides based photocatalysts**", by Mr. Vinothkumar N, for the award of degree of Doctor of Philosophy, has been carried out under my supervision and that this work has not been submitted elsewhere for a degree.

Guwahati
August, 2014

_ _ _ _ _ _ _ _ _ _ _ _ _ _ _ _ _ _ _ _

Dr. Mahuya De
Associate Professor
Department of Chemical Engineering
Indian Institute of Technology Guwahati
Guwahati – 781 039

Acknowledgements

Words are inadequate to express my heartfelt gratitude to many people with whom I have spent many memorable occasions and who have been very supportive both in academic and personal.

I am absolutely indebted to my supervisor **Dr. Mahuya De** for her brilliant academic guidance, constant encouragement, patience, effort, enthusiasm and support at every stage of my research work. It is my privilege to express my gratitude to her for introducing me in to the field of catalysis. I would also like to express my sincere thanks to my supervisor for the tremendous effort that went to each of the drafts. I am really grateful to her for the meticulous discussions that helped me to write the papers and thesis.

I sincerely thank **Dr. Mohammad Qureshi** from the Department of Chemistry, for his insightful comments, continuous encouragement and valuable feedbacks during my study. I am really grateful to him for providing opportunities to learn various aspects in catalysis. I am also thankful to my doctoral committee members **Dr. Pallab Ghosh** and **Dr. V.V.Goud** for their constructive suggestions and orienting me into the line of logical thinking that have contributed enormously to enhance the quality of my research.

I would like to extend my heartfelt thanks to faculty members and staff members of Chemical Engineering and scientific officers of the **CIF** for their support during my stay in the department. I wish to convey my sincere gratitude to technical for their timely help in characterizing the samples. I am extremely grateful to **Dr. Ashok** and **Dr. Monash** for their help and co-operation in my research work. I am lucky to have true friends Dr. Saravanan, Dr. Kannan, Dr. Vasanth, Dr. Siva, Mr. Baskar, Dr. Vijayakumar, Dr. Muthukumaran and Dr. Rajesh for their unconditional support and timely assistance whenever needed. Special thanks to Dr. Ruhit, Dr. Ziya, Dipankar, Tridip, Momina and Anindya for their help and support.

Vinoth

Abstract

Photocatalysis is used in diverse areas such as air purification, degradation of dyes, self cleaning materials, solar cell, antibacterial printing applications etc. Photocatalysis is emerging as a potential method for hydrogen production from renewable sources. Hydrogen is considered as an energy carrier with high potential because of its high energy density and pollution free combustion products. At present, hydrogen is primarily produced from fossil fuels (95%) via steam reforming but the process is associated with formation of green house gas such as carbon dioxide. The faster depletion of the fossil fuels has necessitated exploring of alternative routes for production of hydrogen from the renewable energy sources. The alternative routes are also expected to reduce the emission of green house gases. The photocatalytic hydrogen production from water using solar energy is one of the alternative processes that have attracted attention as a pollution free method for generation of hydrogen. However, the major drawback of the water splitting process is low production of hydrogen. One possible way to enhance the hydrogen production is to develop catalysts with high activity. Another method that has been reported to increase the hydrogen production rate is modification of the feed by alcohol. Further, for better utilization of the solar radiation, it is essential to develop visible light active photocatalysts since 50 % of solar radiations are in visible region. Most of the photocatalysts investigated for hydrogen production, such as TiO_2, ZnO, $SrTiO_3$, ZnS, etc., are UV radiation active catalysts. The development of visible light active catalysts can be done either by using photocatalysts having band gap energies in visible region or modifying the UV light active catalysts by several techniques, such as doping, sensitization or coupling with other semiconductors, to modify the band gap energy towards visible light region.

Among UV light active catalysts, titanium dioxide is one of the most widely investigated photocatalyst due to its advantageous features such as chemical and thermal stability, long durability, nontoxicity, low cost, high oxidizing power and photo-corrosion resistance. The objective of the present study was to develop a visible active catalyst with high activity for hydrogen production from water-methanol mixture. For this purpose initially titanium dioxide was selected as the base photocatalyst for the reason stated above. To enhance the visible light activity of titanium dioxide, it was modified with various metals and nonmetals. The titanium

Footer Page TH-1334_08610706

dioxide was initially modified with varied amount of cerium oxide. The cerium modified titanium dioxide with highest activity was further doped with various non metals such as boron, carbon, nitrogen and sulphur. The titanium dioxide was also modified with different transition metals such as Cu, Fe and Ni and further comodified with nitrogen. The effect of variation of nitrogen amount was studied for copper modified titanium dioxide catalyst. In the second phase, the titanium dioxide was coupled with indium oxide which is another visible light active but expensive semiconducting material. The effect of variation of indium oxide in coupled oxide was investigated. The coupled oxide was further modified with transition metal such as copper oxide. Thereafter the indium oxide was also coupled directly with other transition metals (Cu, Ni, Zn) and hydrogen activity was investigated. The influence of operation parameters such as, light intensity, catalyst amount, alcohol type and reaction time was studied. In the final phase, the kinetic model was developed for the most active catalyst.

All the photocatalysts were prepared by co-precipitation method. The prepared photocatalysts were characterized by BET surface area and pore analysis, X-ray diffraction analysis (XRD), ultraviolet-visible diffuse reflectance spectroscopic analysis (UV-Vis), field emission scanning electron microscopic analysis (FESEM), photoluminescence spectroscopic analysis (PL) to investigate the physiochemical and optical properties. The energy dispersive X-ray spectroscopy (EDS) was used to study the chemical composition of the photocatalysts. The photocatalytic activity of all the catalysts was performed in batch reactor under visible light irradiation using water methanol mixture as feed. Predetermined amount of catalyst and light intensity was used. The evolved gas was collected using an inverted burette and analyzed using gas chromatographs equipped with thermal conductivity and flame ionization detectors. The liquid phase products were analyzed by HPLC.

For cerium doped titanium dioxide, the cerium amount was varied in the range of 0.5-9 at.%. Highest hydrogen evolution of 403 µmol/g/h was observed for titanium dioxide containing 2.5 at.% cerium. Incorporation of cerium 4f electronic states into TiO_2 band structure decreased the band gap energy and absorption of visible light was enhanced. Higher light absorption in visible region resulted increased the number of photogenerated electrons. The incorporated Ce 4f electronic states also served as an electron trap reducing the rate of electron-hole pair recombination. The increased

Footer Page TH-1334_08610706

efficiency in trapping of photogenerated electrons resulted in higher availability of these electrons for hydrogen production. The higher activity can also be attributed to higher surface area of the 2.5 at.% cerium containing sample. The higher surface area resulted in increased surface active sites and higher hydrogen evolution rate.

The effect of calcination temperature on photocatalytic activity was studied for 2.5 at.% cerium doped titanium dioxide. The hydrogen evolution was observed to initially increase with the calcination temperature from 350 to 650 °C and then decrease at higher calcination temperature of 750 °C. The initial increase in photoactivity with calcination temperature can be attributed to increased formation of crystalline anatase phase. The lower photoactivity at higher calcination temperature may be due to decrease in anatase amount with predominant presence of rutile phase.

The 2.5 at.% cerium modified titanium dioxide was codoped with 1 at.% of various nonmetals, such as boron, carbon, nitrogen and sulfur, to study the effect on the hydrogen production. The simultaneous incorporation of cerium and nonmetals to titanium dioxide resulted in narrower band gap and improved absorption of visible light. For the codoped catalysts the band gap energy was reduced by formation of additional impurity states within titanium dioxide matrix by the interaction of p-orbitals of the nonmetal dopants and 2p-orbitals of oxygen. The relative position of the new states with respect to valence band of titanium dioxide depended on the properties of dopants and its position within the matrix. Photoluminescence studies showed that the radiative recombination rates of photogenerated electron-hole pairs were effectively suppressed by addition of cerium and nonmetals and contributed to higher activity. The hydrogen evolution rate was maximum for cerium and nitrogen codoped titanium dioxide with 1033 µmol/g/h and the highest activity can be attributed to its higher surface area, higher absorption of visible light and higher separation efficiency of electron-hole pairs. The lowest activity (135 µmol/g/h) observed for sulfur codoped catalyst may be attributed to its very low surface area as well as to lower mobility of the holes due to presence of the isolated states of sulphur which limited the number of charge carriers reaching the catalyst surface for reaction. For comparison, the photocatalytic activity of nitrogen modified titanium dioxide was also measured and the hydrogen evolution rate was 517 µmol/g/h which was slightly higher compared to that of cerium modified titanium dioxide (403 µmol/g/h) but much lower compared to that of cerium and nitrogen codoped titanium dioxide

Footer Page TH-1334_08610706

catalyst (1033 µmol/g/h) suggesting that both the doping components were contributory to photocatalytic activity giving higher hydrogen production.

The activity of transition metal modified titanium dioxide was studied by doping the titanium oxide with 2.5 at.% of copper, iron or nickel. The UV-visible spectra showed distinct red shift of the absorption edges for transition metal doped TiO_2. The visible light absorption was also enhanced. The photocatalytic hydrogen evolution rate for copper, iron and nickel modified titanium dioxide was found to be 938, 269 and 250 µmol/g/h, respectively. The higher activity for copper modified titanium oxide can be attributed to higher surface area and significant absorption of visible light. The significant absorption for copper doped titanium dioxide in visible region can also be attributed to its d electron transitions. The titanium dioxide modified with the transition metals was codoped with 1 at.% nitrogen and the effect on hydrogen production was investigated. Addition of nitrogen in transition metal doped titanium dioxide increased hydrogen production for all codoped catalysts. The enhancement in hydrogen production can be attributed to increased absorption of visible light and trapping of photogenerated electrons. Among codoped the highest hydrogen evolution rate was observed for copper and nitrogen comodified titanium dioxide with hydrogen production rate of 1109 µmol/g/h. For iron-nitrogen and nickel-nitrogen comodified titanium dioxide catalysts hydrogen productions were 499 and 405 µmol/g/h, respectively. The higher hydrogen production for copper-nitrogen comodified titania may be attributed to combined effect of higher surface area, increased absorption of visible light and enhanced efficiency in trapping of photogenerated electrons. To study the effect of variation of loading of nitrogen on hydrogen production rate, nitrogen amount was varied from 0.5 to 1.5 at.% for copper-nitrogen comodified titanium oxide. The loading of 1 at.% nitrogen was found to be optimum.

In the second phase the titanium dioxide was coupled with another visible light active semiconductor material such as indium oxide and hydrogen production was significantly higher in comparison to pure indium oxide. The amount of indium oxides was varied in the range of 5-16 at.% to determine the optimum composition. With increase in indium oxide content, the surface area and visible light absorption for binary catalyst increased. Separation of photogenerated electron-holes was also enhanced in indium-titanium binary oxides. For pure indium oxide the hydrogen evolution was 1250 µmol/g/h which increased to 1546, 1735 and 1829 µmol/g/h for 5,

Footer Page TH-1334_08610706

10 and 16 at.% indium oxide in binary oxides. The incorporation of 2 at.% copper oxide in titanium-indium binary oxide further enhanced the activity with hydrogen production of 2149 µmol/g/h. The higher activity of ternary catalyst can be attributed to the synergistic effects of increased surface area, stronger absorption in the visible light region and enhanced separation of photogenerated charge carriers. The schematic diagram for hydrogen generation over ternary catalyst is shown in Fig.1.

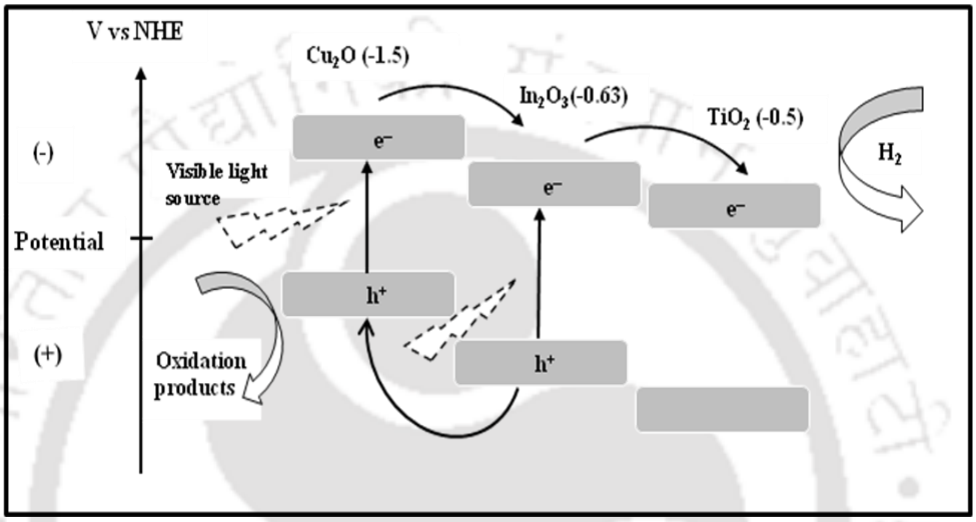

Fig.1. Schematic diagram of hydrogen generation for copper-indium-titanium ternary oxide

Indium oxide was also coupled with transition metals (Cu, Ni, Zn) to study the effect on hydrogen production. All the indium-transition metal coupled oxides showed improved activity for hydrogen production compared to pure indium oxide. The hydrogen evolution activity was observed to be highest for indium-copper coupled oxide and the lowest for indium-zinc coupled oxide. The indium-copper coupled oxide showed a very significant improvement with hydrogen production of 1792 µmol/g/h which can be attributed to significantly enhanced surface area, charge separation as well as visible light absorption compared to indium oxide. For indium-zinc coupled oxide, since light absorbance and charge separation were not significantly enhanced, the increased activity can be attributed only to higher surface area of the coupled oxide with respect to indium oxide. The morphology of indium-transition metal coupled oxides varied significantly with type of transition metals. The

Footer Page TH-1334_08610706

Fig.2 shows the hydrogen production over various modified titanium and indium oxide based photocatalysts.

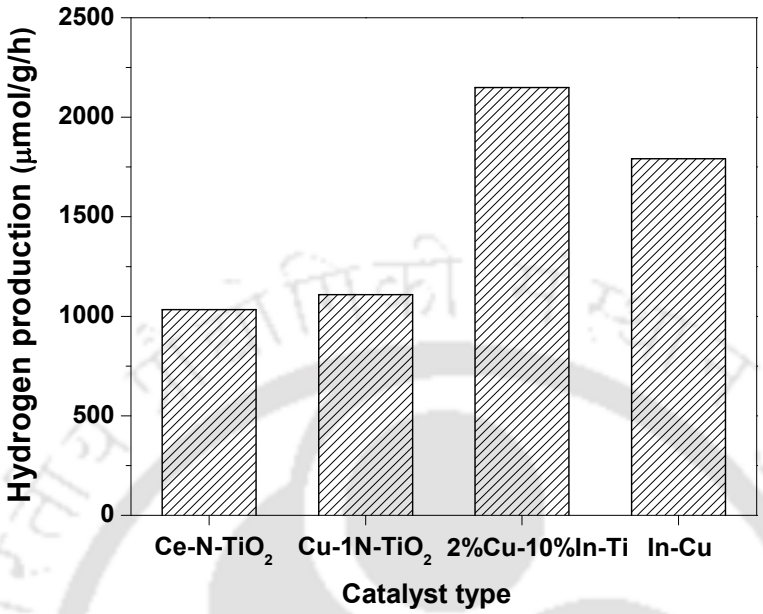

Fig.2. Hydrogen production over various modified titanium and indium oxides based photocatalysts

The overall possible mechanism steps for production of hydrogen from water-methanol mixture are summarized below.

$$\text{photocatalyst} \xrightarrow{h\nu} h^{+}_{vb} + e^{-}_{cb} \quad (1)$$

$$CH_3OH + 2h_{vb}^{+} \rightarrow 2H^{+} + HCHO \quad (2)$$

$$2H_2O + 2h^{+}_{vb} \rightarrow 2OH^{\bullet} + 2H^{+} \quad (3)$$

$$CH_3OH + 2OH^{\bullet} \rightarrow 2H_2O + HCHO \quad (4)$$

$$HCHO + H_2O \rightarrow HCO_2H + H_2 \quad (5)$$

$$HCO_2H + h^{+}_{vb} \rightarrow CO_2 + H^{+} \quad (6)$$

$$2H^{+} + 2e^{-}_{cb} \rightarrow H_2 \quad (7)$$

The product analysis showed that carbon dioxide was not formed for any catalyst or was below the detection level of the used gas chromatograph. For cerium and nitrogen codoped titanium dioxide catalyst both formaldehyde and formic acid were detected in liquid phase. On the other hand, for transition metal modified titanium dioxide as

Footer Page TH-1334_08610706

well as titanium-indium coupled oxide, only formaldehyde was detected in liquid phase after completion of reaction. Formation of equivalent amount of hydrogen and formaldehyde for titanium-indium coupled oxide implied occurrence of partial oxidation of methanol.

The influence of operational parameters such as, light intensity, catalyst amount, alcohol type and irradiation time was studied using the cerium and nitrogen codoped titanium dioxide photocatalyst. The hydrogen production rate was increased from 326 to 1024 μmol/g with increase in the light intensity from 5000 to 25600 lx. This enhancement in hydrogen production may be attributed to increased absorption of photons by photocatalyst at higher light intensity. This increased the number of available photogenerated charge carriers for redox reactions on the catalyst surface. The photocatalyst amount was varied in the range of 0.1 to 1 g and the highest hydrogen evolution was observed for 0.2 g of catalyst loading. With initial increase in catalyst amount, the absorption of photons increased thereby, increasing the hydrogen production. However, at high concentration of catalyst, the light reaching the catalyst surface was inhibited thereby, decreasing the light absorption and hydrogen production. The effect of using alcohol of higher carbon number than methanol was investigated by using ethanol and propanol under similar reaction conditions. It was observed that activity order was methanol > ethanol > propanol. The lower reactivity for the higher alcohol may be attributed to their higher bond energy. The durability test was performed for ten hours irradiation period with hydrogen evolution being recorded at every one hour. The hydrogen generation was significant for first 3 h of irradiation and thereafter, rate was slower. The total hydrogen evolution of 3687 μmol/g was obtained after 10 h of irradiation time. Based on the above results the optimum process conditions for photocatalytic hydrogen production were selected as 0.2 g photocatalyst, 25600 lx light intensity with methanol as alcohol source. These process conditions were used for all the photocatalytic studies if not mentioned otherwise.

Among all the visible light active catalysts developed for hydrogen production in this study, highest hydrogen production was observed for 2 at.% copper and 10 at.% indium oxide codoped titanium photocatalyst. This catalyst was further investigated for study of photocatalytic reaction kinetics. Kinetic data were collected by varying the mole fraction of methanol in the range of 0.05 to 0.25. The production of

Footer Page TH-1334_08610706

hydrogen and formaldehyde increased with increase in the mole fraction of methanol in the aqueous solution. This may be due to the increased adsorption of the methanol molecules on the active sites of the catalyst surface. The kinetic parameters were determined using Power Law and Langmuir-Hinshelwood (L-H) models. The L-H models were developed for the simultaneous occurrence of hydroxyl mediated and hole mediated oxidation path, and for the hole mediated path alone. For each model, the optimum values of kinetic parameters were determined by minimizing the residual sum of squares between the calculated and experimental rate of methanol oxidation. The kinetic parameters were estimated using non-linear regression analysis. The Langmuir-Hinshelwood model that considered simultaneous occurrence of hydroxyl mediated and hole mediated oxidation paths was observed to best describe the experimental data than the model considering only hole mediated path. The kinetic rate constants were determined to be 8.65×10^{-3} $(\mu mol/g)^{-1}h^{-1}$ for hydroxyl mediated oxidation and 9.12×10^{-3} $(\mu mol/g)^{-1}h^{-1}$ for hole mediated oxidation of methanol.

Thesis Organization

The thesis has been organized as follows:

Introduction, Literature review, Objective, Experimental details, Result and discussion, Conclusion and Recommendations.

Footer Page TH-1334_08610706

Publications from this work

1. **N.Vinothkumar** and Mahuya De, Enhanced photocatalytic hydrogen production from water–methanol mixture using cerium and nonmetals (B/C/N/S) co-doped titanium dioxide, **Materials for Renewable and sustainable Energy,** 3(2014), 1-25.

2. **N.Vinothkumar** and Mahuya De, Hydrogen production from water-methanol solution over visible light active Indium-Titanium oxide photocatalysts modified with copper oxide, **International Journal of Hydrogen Energy**, 39 (2014), 11494-11500

3. **N.Vinothkumar** and Mahuya De, Photocatalytic hydrogen production from aqueous methanol over visible light active Indium-transition metal coupled oxide photocatalysts, (submitted to The Journal of Physical Chemistry C)

4. **N.Vinothkumar** and Mahuya De , Enhanced hydrogen production from water-methanol over transition metal (Cu, Fe, Ni) and nitrogen co-doped titanium dioxide photocatalysts, (to be submitted)

5. **N.Vinothkumar** and Mahuya De, Kinetic and modeling studies for hydrogen production over Cu-In-TiO_2 from water-methanol mixture, (under preparation)

Conferences

6. **N.Vinothkumar** and Mahuya De, Photocatalytic hydrogen production over cerium and nitrogen modified titania under visible light irradiation, **12th Mediterranean Congress of Chemical Engineering,** 15-18 November, 2011, Barcelona, Spain

7. **N.Vinothkumar** and Mahuya De, Cu doped TiO_2 and ZnO photocatalysts for hydrogen production under visible light irradiation, **CHEMCON**, International conference on sustainable technologies for energy and environment in process industries**,** 27-30 December, 2012, Jalandhar, India

Footer Page TH-1334_08610706

Additional publications

1. Dipankar Barpuzary, Ziyauddin Khan, **N.Vinothkumar**, Mahuya De and Mohammad Qureshi, Hierarchically Grown Urchin-like CdS@ZnO and CdS@Al_2O_3 Heteroarrays for Efficient Visible Light Driven Photocatalytic Hydrogen Generation, **The Journal of Physical Chemistry C**, 116 (2012), 150-156

2. Ziyauddin Khan, Momina Khannam, **N.Vinothkumar**, Mahuya De and Mohammad Qureshi, Hierarchical 3D NiO-CdS Heteroarchitecture for Efficient Visible Light Photocatalytic Hydrogen Generation, **Journal of Materials Chemistry**, 22 (2012), 12090-12095

3. Anindya Sundar Patra, **Natarajan Vinothkumar**, Dipankar Barpuzary, Mahuya De and Mohammad Qureshi, Strontium doped lanthanum manganites for efficient and robust photocatalytic water oxidation coupled with graphene oxide, **Material Letters**, 131 (2014), 125-127

Footer Page TH-1334_08610706

Contents

		Page No.
Abstract		**i**
List of Figures		**xiv**
List of Tables		**xx**
Nomenclature		**xxii**
Chapter 1	**Introduction**	**1**
	1.1 Energy demand	3
	1.2 Hydrogen as energy carrier	4
	1.3 Hydrogen production methods	5
	1.4 Thesis objective	8
Chapter 2	**Literature review**	**9**
	2.1 Photocatalytic hydrogen production	11
	2.1.1 Charge carrier trapping	12
	2.1.2 Visible light activity	13
	2.1.3 Effect of alcohol	14
	2.2 Photocatalytic systems	15
	2.2.1 Titania based photocatalysts	15
	2.2.1.1 Modification with metals	16
	2.2.1.2 Modification with nonmetals	20
	2.2.1.3 Comodification with metal and nonmetals	21
	2.2.2 Indium oxide based photocatalysts	22
	2.2.3 Coupled semiconductor based photocatalysts	23
	2.3 Photocatalytic reaction kinetics	25
Chapter 3	**Experimental details**	**28**
	3.1 Materials used	30
	3.2 Preparation of TiO_2 based catalysts	30
	3.2.1 Preparation of TiO_2	30

Footer Page TH-1334_08610706

3.2.2 Preparation of cerium and nonmetal doped TiO_2 30
3.2.3 Preparation of transition metal and nitrogen doped TiO_2 32
3.3 Preparation of In_2O_3 based catalysts 33
3.3.1 Preparation of In_2O_3 33
3.3.2 Preparation of indium-titanium coupled oxide 34
3.3.3 Preparation of copper doped indium-titanium oxide 34
3.3.4 Preparation of indium-transition metal coupled oxide 35
3.4 Characterization of catalysts 36
3.4.1 BET surface area and pore size measurements 36
3.4.2 X-ray diffraction studies 36
3.4.3 Field emission scanning electron microscopic studies 36
3.4.4 Energy dispersive X-ray spectroscopic analysis 36
3.4.5 UV-Visible diffuse reflectance absorption studies 37
3.4.6 Photoluminescence spectroscopic analysis 37
3.5 Photocatalytic studies 37
3.5.1 Experimental setup and procedure 37
3.5.2 Product analysis 40
Chapter 4 Results and discussions 41
4.1 Preliminary studies 43
4.1.1 Effect of stirring 43
4.1.2 Variation of light intensity 44
4.2 Cerium doped titania 45
4.2.1 Effect of cerium loading 45
4.2.2 Effect of calcination temperature 53
4.2.3 Effect of cerium and nonmetal codoping 55
4.3 Transition metal doped titania 69
4.3.1 Effect of transition metal doping 69
4.3.2 Effect of transition metal and nonmetal codoping 77
4.3.3 Effect of variation of nitrogen doping 82
4.4 Indium-titanium coupled oxide 89
4.5 Indium-transition metal coupled oxide 102

Footer Page TH-1334_08610706

	4.6 Effect of operational parameters	115
	4.6.1 Effect of incident light intensity	115
	4.6.2 Effect of catalyst amount	116
	4.6.3 Effect of type of alcohols	117
	4.6.4 Effect of irradiation time	118
	4.7 Kinetic studies	119
	4.7.1 Kinetic models	121
	4.7.2 Kinetic analysis of rate equations	124
Chapter 5	**Conclusions and Recommendations**	**128**
	5.1 Conclusions	130
	5.2 Recommendations	132
References		**133**
Appendices		**161**
Appendix A	Preparation steps for various catalysts	163
Appendix B	Calibration plots	165
Appendix C	Calculation of lattice parameters, d-spacing and lattice distortion	167
Appendix D	Calculation of band gap energy	168
Appendix E	Calculation of apparent quantum efficiency	170
Appendix F	Derivation of rate expression	172

Footer Page TH-1334_08610706

S. No	List of Figures	Page No.
Figure 1.1	Global energy consumption	3
Figure 1.2	Global consumption of various fuels	4
Figure 1.3	Various hydrogen production technologies	5
Figure 3.1	Steps for preparation of cerium doped TiO_2	31
Figure 3.2	Steps for preparation of transition metal doped TiO_2	32
Figure 3.3	Steps for preparation of indium-titanium coupled oxide	34
Figure 3.4	Steps for preparation of indium-transition metal coupled oxide	35
Figure 3.5	Schematic representation of experimental setup	38
Figure 3.6	Emission spectrum of 500 W tungsten halogen lamp	39
Figure 4.1	Hydrogen production at different stirring conditions	43
Figure 4.2	Light intensity profile as function of time	44
Figure 4.3	N_2 adsorption-desorption isotherms of Ce_x-TiO_2 and TiO_2 (inset: pore size distribution)	45
Figure 4.4	XRD patterns of undoped TiO_2 and Ce_xTiO_2	48
Figure 4.5	(A) UV-Visible diffuse reflectance spectra (B) Kubelka-Munk plot for undoped TiO_2 and Ce_x-TiO_2	49

Footer Page TH-1334_08610706

Figure 4.6	Photoluminescence spectra for undoped TiO_2 and Ce_xTiO_2	50
Figure 4.7	Hydrogen production for undoped TiO_2 and Ce_xTiO_2	51
Figure 4.8	XRD patterns of $Ce_{2.5}TiO_2$ at different calcination temperatures	53
Figure 4.9	Hydrogen production for $Ce_{2.5}TiO_2$ at different calcination temperatures	54
Figure 4.10	N_2 adsorption-desorption isotherms for (a) Ce-TiO_2 (b) Ce-NM-TiO_2 (NM = B, C, N, S) (inset: pore size distribution)	56
Figure 4.11	XRD patterns of undoped TiO_2, Ce-TiO_2 and Ce-NM-TiO_2 (NM = B, C, N, S)	59
Figure 4.12	FESEM images of (a) Undoped TiO_2 (b) Ce-TiO_2 (c) Ce-N-TiO_2 (d) Ce- S-TiO_2 (e) Ce-B-TiO_2 and (f) Ce-C-TiO_2	60
Figure 4.13	(A) UV-Visible diffuse reflectance spectra and (B) Kubelka-Munk plot for TiO_2, Ce-TiO_2 and Ce-NM-TiO_2 (NM = B, C, N, S)	62
Figure 4.14	Photoluminescence spectra for undoped TiO_2, Ce-TiO_2 and Ce-NM-TiO_2 (NM = B, C, N, S)	63
Figure 4.15	Hydrogen production for undoped TiO_2, Ce-TiO_2 and Ce-NM-TiO_2 (NM = B, C, N, S)	65
Figure 4.16	Comparison of hydrogen production for Ce-TiO_2, N-TiO_2 and Ce-N-TiO_2 catalysts	66
Figure 4.17	Schematic representation of hydrogen production over cerium and nonmetal codoped TiO_2 photocatalysts	67

Footer Page TH-1334_08610706

Figure 4.18 N_2 adsorption-desorption isotherms of M-TiO_2 (M = Cu, Fe, Ni); (Inset: pore size distributions) 69

Figure 4.19 XRD patterns of M-TiO_2 (M = Cu, Fe and Ni) 71

Figure 4.20 FESEM images of (a) Cu-TiO_2 (b) Cu-1N-TiO_2 (c) Fe-TiO_2 (d) Fe-1N-TiO_2 (e) Ni-TiO_2 and (f) Ni-1N-TiO_2 72

Figure 4.21 (A) UV-Visible diffuse reflectance spectra and (B) Kubelka-Munk plot of undoped TiO_2 and M-TiO_2 (M = Cu, Fe and Ni) 73

Figure 4.22 Photoluminescence spectra of undoped TiO_2 and M-TiO_2 (M = Cu, Fe and Ni) 74

Figure 4.23 Hydrogen production for M-TiO_2 and M-1N-TiO_2 (M = Cu, Fe and Ni) 76

Figure 4.24 N_2 adsorption-desorption isotherms for M-1N-TiO_2 (M = Cu, Fe and Ni; (Inset: pore size distributions) 77

Figure 4.25 XRD patterns of M-1N-TiO_2 (M = Cu, Fe and Ni) 78

Figure 4.26 (A) UV-Visible diffuse reflectance spectra and (B) Kubelka-Munk plot of M-1N-TiO_2 (M = Cu, Fe and Ni) 79

Figure 4.27 Photoluminescence spectra of M-1N-TiO_2 (M = Cu, Fe and Ni) 80

Figure 4.28 N_2 adsorption-desorption isotherms for (a) Cu-0.5N-TiO_2 (b) Cu-1N-TiO_2 and (c) Cu-1.5N-TiO_2 (Inset: pore size distributions) 82

Figure 4.29 XRD patterns of Cu-xN-TiO_2 (x = 0.5, 1 and 1.5 at.%) 83

Footer Page TH-1334_08610706

Figure 4.30 FESEM images of (a) Cu-0.5N-TiO_2 (b) Cu-1N-TiO_2 and (c) Cu-1.5N-TiO_2 84

Figure 4.31 (A) UV-Visible diffuse reflectance spectra and (B) Kubelka-Munk plot for Cu and N codoped TiO_2 (a) Cu-0.5N-TiO_2 (b) Cu-1N-TiO_2 and (c) Cu-1.5N-TiO_2 85

Figure 4.32 Photoluminescence spectra of Cu and N codoped TiO_2 (a) Cu-0.5N-TiO_2 (b) Cu-1N-TiO_2 and (c) Cu-1.5N-TiO_2 86

Figure 4.33 Hydrogen evolution for Cu-xN-TiO_2 (x = 0.5, 1, 1.5 at.%) 87

Figure 4.34 N_2 adsorption-desorption isotherms of *x*% In-Ti (*x* = 5, 10 and 16%) and 2%Cu-10%In-Ti 90

Figure 4.35 XRD patterns of *x*% In-Ti (*x* = 5, 10 and 16%) and 2%Cu-10%In-Ti 91

Figure 4.36 FESEM images of (a) 5% In-Ti (b) 10% In-Ti (c) 16% In-Ti and (d) 2%Cu-10%In-Ti 92

Figure 4.37 (A) UV-Vis diffuse reflectance spectra and (B) Kubelka-Munk plot of *x*% In-Ti (*x* = 5, 10 and 16%) and 2%Cu-10%In-Ti 93

Figure 4.38 Photoluminescence spectra of *x*% In-Ti (*x* = 5, 10 and 16%) and 2%Cu-10%In-Ti 95

Figure 4.39 Hydrogen production for *x*% In-Ti (*x* = 5, 10 and 16%) and 2%Cu-10%In-Ti 96

Figure 4.40 Schematic diagram of hydrogen generation in Cu_2O-In_2O_3-TiO_2 system 97

Footer Page TH-1334_08610706

Figure 4.41 Comparison of UV-Vis diffuse reflectance spectra of 2%Cu-10%In-Ti and 2%Cu-16%In-Ti 98

Figure 4.42 Generation of hydrogen and formaldehyde over 2%Cu-10%In-Ti catalyst (Feed composition; methanol: 1 ml and water: 25 ml) 100

Figure 4.43 (A) N_2 adsorption-desorption isotherms and (B) pore size distribution of In-Zn, In-Cu, In-Ni and In 103

Figure 4.44 XRD patterns of In-TM (TM = Cu, Ni, Zn) 105

Figure 4.45 FESEM images of (a) In (b) In-Ni (c) In-Cu and (d) In-Zn 107

Figure 4.46 (A) UV-Visible diffuse reflectance spectra and (B) Kubelka-Munk plot of (a) In-Cu (b) In-Ni (c) In-Zn and (d) In 108

Figure 4.47 Photoluminescence spectra of (a) In-Cu (b) In-Ni (c) In-Zn and (d) In 109

Figure 4.48 Hydrogen production for In and In-TM (TM = Cu, Ni, Zn) based on per gm of indium 111

Figure 4.49 Hydrogen production for In and In-TM (TM = Cu, Ni, Zn) based on per gm of catalyst 113

Figure 4.50 Hydrogen production at different light intensities (Reaction conditions: photocatalyst amount, 0.2 g; methanol concentration 0.96 mol/litre; irradiation time, 1 h) 115

Figure 4.51 Production of hydrogen using different amount of photocatalyst (Reaction conditions; methanol concentration 0.96 mol/litre; irradiation time, 1 h; light intensity, 25600 lx) 116

Footer Page TH-1334_08610706

Figure 4.52 Hydrogen production in presence of different alcohols (photocatalyst amount, 0.2 g; alcohol concentration 0.96 mol/litre; irradiation time, 1 h; light intensity, 25600 lx) 117

Figure 4.53 Production of hydrogen as a function of irradiation time (photocatalyst amount, 0.2 g; methanol concentration 0.96 mol/litre; light intensity, 25600 lx) 118

Figure 4.54 Methanol concentrations as a function of irradiation time at different initial concentration (a) 0.05 molar fraction (2.3 mol/litre), (b) 0.10 molar fraction (4.1 mol/litre), (c) 0.15 molar fraction (5.4 mol/litre) and (d) 0.25 molar fraction (7.4 mol/litre) 119

Figure 4.55 Conversion of methanol at different initial concentration 120

Figure 4.56 Hydrogen and formaldehyde production at different methanol concentration (photocatalyst amount, 0.2 g; irradiation time, 1 h; light intensity, 25600 lx) 121

Figure 4.57 Comparison of experimental and calculated rates for different kinetic models (a) P-1 (power law) (b) LH-1 (combination of hydroxyl mediated and hole mediated paths) and (c) LH-2 (hole mediated path) 126

Footer Page TH-1334_08610706

S. No	List of Tables	Page No.
Table 1.1	Comparison of higher heating value (HHV) and energy content of hydrogen with that of other fuels	5
Table 4.1	Surface area, pore volume and lattice parameters for undoped TiO_2 and Ce_xTiO_2	46
Table 4.2	Energy Dispersive X-Ray Spectroscopic analysis for undoped TiO_2 and Ce_xTiO_2	46
Table 4.3	Comparison between the actual and intended composition for Ce_xTiO_2	47
Table 4.4	Hydrogen production and phase distribution of $Ce_{2.5}TiO_2$ catalyst calcined at different temperatures	54
Table 4.5	Surface area, pore volume and lattice parameters for undoped TiO_2, Ce-TiO_2, Ce-NM-TiO_2 (NM = B, C, N, S)	57
Table 4.6	Energy Dispersive X-Ray Spectroscopic analysis and composition for undoped TiO_2, Ce-TiO_2, Ce-NM-TiO_2 (NM = B, C, N, S)	57
Table 4.7	Surface area, pore volume and lattice parameters of M-TiO_2, M-1N-TiO_2, Cu-xN-TiO_2 (M = Cu, Fe, Ni; N = nitrogen; x = 0.5, 1, 1.5)	70
Table 4.8	Reduction potential values of the transition metals	75
Table 4.9	Surface area, pore volume and lattice parameters of x% In-Ti (x = 5, 10, 16%) and 2%Cu-10%In-Ti catalysts	89
Table 4.10	Comparison of BET surface area and pore volume of 2%Cu-10%In-Ti and 2%Cu-16%In-Ti	99
Table 4.11	Surface area, pore volume and lattice parameters for In and In-TM (TM = Cu, Ni, Zn)	104

Footer Page TH-1334_08610706

Table 4.12 EDS results of In and In-TM (TM = Cu, Ni, Zn) 104

Table 4.13 Reduction potential values of Cu, Ni, Zn and In 111

Table 4.14 Estimated kinetic parameter values for different models 125

भारतीय प्रौद्योगिकी संस्थान गुवाहाटी • Indian Institute of Technology Guwahati •

Footer Page TH-1334_08610706

Nomenclature

A	Proportional constant
c	Speed of light, 3×10^{10} cm s^{-1}
$C_{H_2O_{ads}}$	Concentration of adsorbed water, mmol/m^3
$C_{CH_3OH_{ads}}$	Concentration of adsorbed methanol, mmol/m^3
C_{h^+}	Concentration of holes, mmol/m^3
C_v	Total vacant sites, mmol/m^3
e^-_{cb}	Photogenerated electrons in conduction band
E_g	Band gap, eV
h	Planck's constant, 4.13×10^{-15} eV s
h^-_{vb}	Photogenerated holes in valence band
$k^{'}_{H_2O}$	Rate constant for water oxidation, $(\mu mol/g)^{-1}$ h^{-1}
$k^{OH}_{CH_3OH}$	Rate constant for methanol oxidation reaction according to hydroxyl radical mediated path, $(\mu mol/g)^{-1}$ h^{-1}
$k^{h^+}_{CH_3OH}$	Rate constant for methanol oxidation reaction according to hole mediated path, $(\mu mol/g)^{-1}$ h^{-1}

Footer Page TH-1334_08610706

$k_{des,HCHO}$	Desorption rate constant of formaldehyde, (μmol/g)$^{-1}$ h^{-1}
k_{des,H_2}	Desorption rate constant of hydrogen, (μmol/g)$^{-1}$ h^{-1}
k_{red}	Rate constant of reduction reactions, (μmol/g)$^{-1}$ h^{-1}
$k_{recombination}$	Rate constant of recombination reactions,
K_{H_2O}	Adsorption equilibrium constant of water, (μmol/g) $^{-1}$
K_{CH_3OH}	Adsorption equilibrium constant of methanol, (μmol/g)$^{-1}$
n	Order of reaction
n	Type of transition

Greek letters

α	Absorption coefficient, cm^{-1}
λ	Wavelength, nm
ν	Frequency, s^{-1}

Footer Page TH-1334_08610706

Chapter 1

Introduction

1.1 Energy demand

One of the main challenges in the 21st century is to meet the growing energy demands. The energy requirement is projected to reach the value of 17 billion tons oil equivalents by 2035 (Chu and Majumdar, 2012). The world energy consumption values are presented in Fig.1.1.

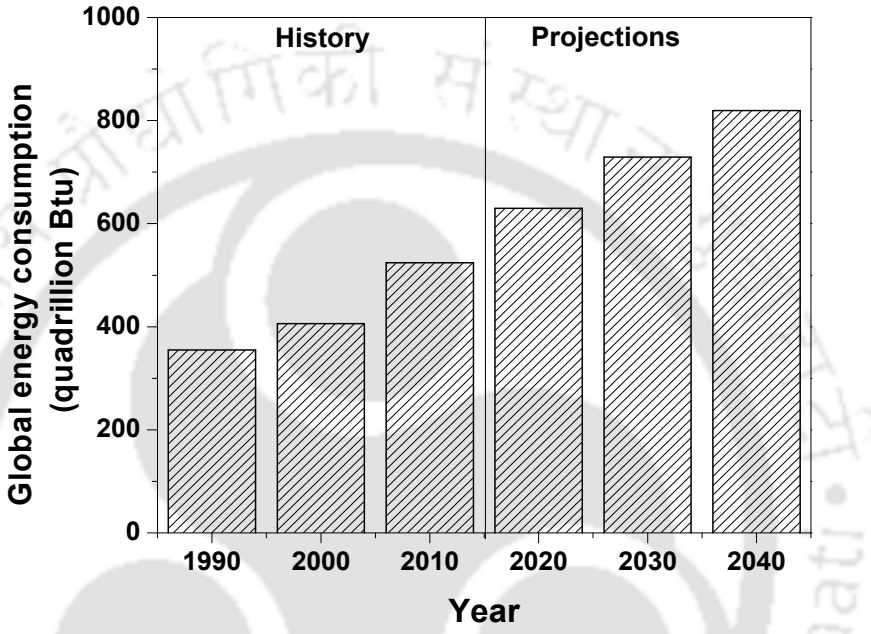

Fig.1.1. Global energy consumption (http://www.eia.gov/forecasts/ieo/)

Carbon based fossil fuels, such as petroleum, coal and natural gas, is the world's largest sources of energy and also expected to continue to supply most of the energy used in near future (Fig.1.2). The major disadvantage of carbon based fossil fuels is that their combustion generates not only the air pollutants, such as sulphur oxides, nitrogen oxides, heavy metals, but also CO_2, the major component of green house gases that contributes to global climate change (Scibioh and Viswanathan, 2004). The increase in green house gas emissions during the past centuries has increased the overall CO_2 level by 31% (Panwar et al., 2011). In addition very high rate of consumption and limited availability are resulting in very fast depletion of fossil fuels. This has initiated an intensive search for alternative energy sources to meet the increasing energy demand. In last few years, the global energy consumption from additional sources such as nuclear energy and renewable energy are increasing rapidly

Footer Page TH-1334_08610706

as can be observed from Fig.1.2. The major objective of alternative energy sources is to develop techniques to achieve clean and sustainable energy carriers that will solve the energy crisis as well as environmental issues.

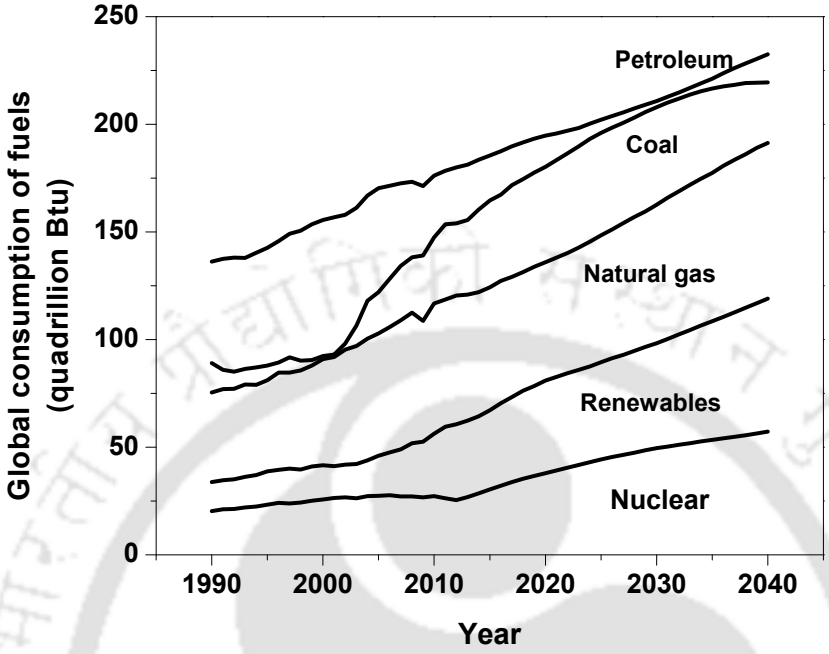

Fig.1.2. Global consumption of various fuels (http://www.eia.gov/forecasts/ieo/)

1.2 Hydrogen as energy carrier

Hydrogen is considered as a future energy carrier because of its higher energy content per unit mass and its clean combustion characteristics. The combustion of hydrogen results in no emission of greenhouse gases. In addition hydrogen has wide range of flammability, low ignition energy and high diffusivity in air. Higher heating values (HHV) and energy content of hydrogen compared to other fossil fuels are listed in Table 1.1. The energy output from combustion of hydrogen is higher than the other conventional fuels. Also hydrogen has high heating value, which represents the true energy content of the fuel. Hydrogen is also used in wide variety of applications such as synthesis of methanol, petroleum refinement, ammonia and fertilizer manufacture, etc., (Pagliaro and Konstandopoulos, 2012; Rajeshwar et al., 2009). Hydrogen is the most abundant element in the universe but it is always in combined state with other elements due to its high reactivity.

Footer Page TH-1334_08610706

Table 1.1. Comparison of higher heating value (HHV) and energy content of hydrogen with that of other fuels (Rajeshwar et al., 2009)

Fuel	HHV (MJ/kg)	Energy (kWh/kg)
Methane	55.5	12.8
Gasoline	47.5	12.4
Diesel	44.8	11.8
Methanol	20.0	5.0
Hydrogen	141.9	33.3

1.3 Hydrogen production methods

Hydrogen production methods can be classified into two main categories such as hydrocarbon reforming and non-reforming processes as shown in Fig.1.3. Currently, hydrogen is mainly (95 %) produced by steam reforming process from fuels such as, natural gas, methanol, lighter hydrocarbons and coal (Wang et al., 2004; Turner, 2004). The steam reforming of methane and naphtha are the primary methods. Steam methane reforming is an efficient technology because of high quality of its product compared to that of autothermal or partial oxidation. The disadvantage of steam reforming processes is the emission of carbon monoxide and carbon dioxide (Chen et al., 2004; Holladay et al., 2009).

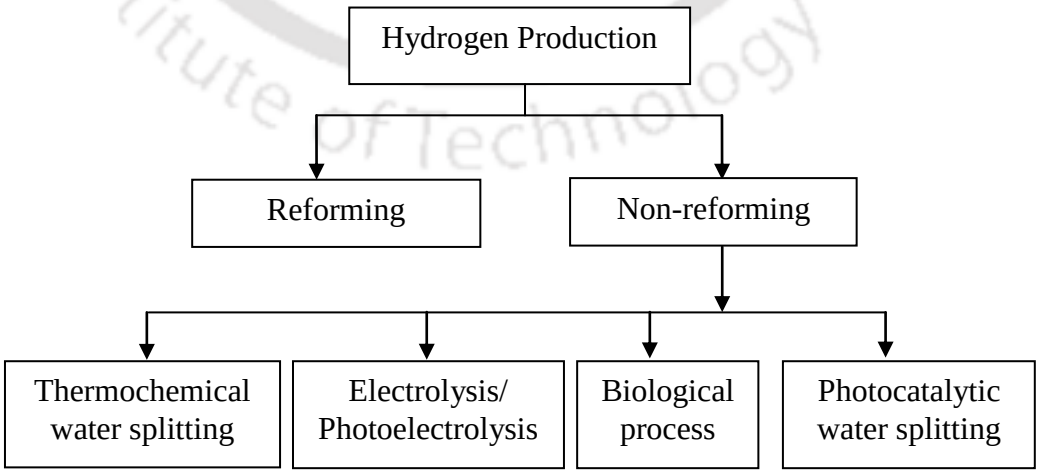

Fig.1.3. Various hydrogen production technologies

Footer Page TH-1334_08610706

Partial oxidation of hydrocarbons is less efficient than steam reforming process, because it requires very high process temperatures compared to steam reforming. The disadvantage is the production of higher levels of carbon monoxide with lower concentration of hydrogen. Autothermal reforming process does not require any external heat source and is relatively less expensive than steam methane reforming process. The main disadvantage of autothermal reforming process is the requirement of air or oxygen to control the oxygen-fuel and steam-carbon ratio for maintaining the reaction temperature and product gas composition (Lutz et al., 2004; Holmen, 2009; Ayabe et al., 2003; Semelsberger et al., 2004).

In order to decrease the dependence on fossil fuels, significant development in other hydrogen generation technologies from renewable resources such as biomass and water is needed. Electrolysis coupled with renewable energy is emerging as the low emission technology. The future energy sources include biohydrogen, thermochemical water splitting and photoelectrolysis (Holladay et al., 2009). The renewable hydrogen production technologies can be classified into four categories such as thermal processes, electrolysis processes, photobiological processes and photolytic processes.

In thermochemical water splitting, also called thermolysis, decomposition of water to hydrogen and oxygen will occur at 2500 °C. This technology needs high temperature, high pressure and corrosive resistant materials to generate hydrogen. Moreover, the sustainable heat sources and stable materials at this high temperature are not easily available. The high temperature of this process can create considerable explosion risk because of the presence of hydrogen and oxygen gas mixture in the thermolysis products (Funk, 2001; Andress et al., 2009; Holladay et al., 2009; Wang et al., 2012).

In photoelectrolysis method, generation of hydrogen and oxygen from water splitting occur at the theoretical applied potential of 1.23 V. But in practice, the water splitting reactions will occur at 1.7 V due to the over potentials of hydrogen and oxygen at the respective electrodes (Vogel, 1961). Other major obstacles are instability of the materials in aqueous solution, electrochemical reaction, semiconductor band edge differences and improper matching of semiconductor band gap with the solar spectra. This method is more expensive process because of the higher production cost due to the over potentials (Bak et al., 2002; Holladay et al., 2009; Viswanathan, 2003).

Footer Page TH-1334_08610706

Biological methods of hydrogen production can be classified as follows; (a) biophotolysis of water by green and blue-green algae (b) photo-fermentation (c) dark fermentation. Hybrid systems using photosynthetic and fermentative bacteria have also been under investigation (Kim and Kim, 2011; Dincer, 2012; Ngoh and Njomo, 2012). The conversion of electrons and protons into molecular hydrogen with the help of enzymes is the main step of all biological hydrogen production processes (Ball and Wietschel, 2009). The green algae, *Chlamydomonas reinhardtii* decomposes water into hydrogen with no greenhouse gas emissions. The produced hydrogen ions in the medium are converted into hydrogen gas through the reduction of protons by hydrogenase enzyme (Tiwari and Pandey, 2012). The major drawback of this process is the inhibition of hydrogenase enzyme by the generated oxygen. Several methods are investigated to overcome the drawbacks of oxygen inhibition effect such as separation of oxygen from hydrogen, oxygen scavenging, immobilization of chloroplasts and gas purging (Miura et al., 1997). However in the sulfur-deprived culture medium, sustainable hydrogen evolution was observed in *Chlamydomonas reinhardtii* (Melis et al., 2000). Fermentative bacteria, such as *Clostridium* and *Enterobacter* sp., have also been investigated for hydrogen production. However, the yield is too low to be economically viable when compared to other chemical or electro-chemical processes (Das and Veziroglu, 2001).

Among alternative energy sources solar energy is the most abundant and has the potential to meet the increasing world energy requirements. The solar energy striking the earth surface is about 3 x 10^{24} J/yr, which is approximately 10^4 times the energy consumed on the planet per year (Bartels et al., 2010; Kaneko and Okura, 2002). The solar energy has been used to produce hydrogen mainly by water splitting reactions (Fujishima et al., 2008). However, water splitting is difficult to achieve because of the large positive standard Gibb's free energy change (237 kJ/mol) (Chen et al., 2010). Various modification of methods and materials are under investigation to improve the photocatalytic conversion efficiency (Ni et al., 2007; Liao et al., 2012). However, only maximum efficiency of 18 % has been achieved so far in the laboratory scale (Peharz et al., 2007). In order to achieve high photoconversion efficiency, some of the important factors that are investigated include efficient separation of photogenerated charge carriers, suppression of backward reaction and utilization of a large fraction of the incident energy (Maeda and Domen, 2007; Guzman et al., 2013; Lin et al., 2009;

Footer Page TH-1334_08610706

Wang et al., 2012). However, till date no photocatalyst system has emerged that can give economically viable yield of hydrogen by water splitting reaction.

1.4 Thesis objective

The main aim of this research was to develop highly active photocatalysts for hydrogen production from water-methanol mixtures under visible light irradiation. The detail research objectives of this thesis include;

- Preparation of following photocatalysts and study the activity for hydrogen production under visible light :
  - Titanium oxide based photocatalytic system
    - Cerium and nonmetal (B, C, N, S) codoped TiO_2 catalysts
    - Transition (Cu, Fe and Ni) and nonmetal (N) doped TiO_2
  - Indium oxide based photocatalytic system
    - Indium-titanium coupled oxide
    - Copper doped indium-titanium coupled oxide
    - Transition metal doped indium oxide (Cu, Ni, Zn)
- Characterization of all the photocatalysts using surface area and pore analysis, X-ray diffraction analysis, ultraviolet-visible diffuse reflectance spectroscopic analysis, field emission scanning electron microscopic analysis, energy dispersive X-ray spectroscopic analysis and photoluminescence spectroscopic analysis to determine the physico-chemical and optical properties and correlate with hydrogen production activity
- Effect of preparation methods such as calcination temperature on hydrogen production
- Effect of various operational parameters such as light intensity, type and amount of alcohol, amount of catalyst and reaction time on hydrogen production
- Determination of kinetics for most active photocatalyst.

Footer Page TH-1334_08610706

Chapter 2

Literature Review

2.1 Photocatalytic hydrogen production

The initial step of photocatalytic reaction is the absorption of photons of energy corresponding to the band gap energy of the photoactive material. When light with energy equal to or greater than the band gap is incident on the photoactive material, the valence band electrons are excited to conduction band leaving positively charged holes in the former. These photogenerated conduction band electrons and valence band holes are transported from the bulk to surface and are expected to participate in reduction and oxidation reactions respectively. However these photogenerated electron and holes are unstable and tend to recombine. The charge carriers that are able to reach the surface of the photocatalyst without recombination can only take part in the redox reactions. The rate of charge carrier transfer depends on the position of lower conduction band edge and upper valence band edge and also on the redox potential of the adsorbates (Linsebigler et al., 1995).

For hydrogen production from water, the adsorbed water is oxidized by photogenerated holes to produce the stoichiometric 2:1 mixture of gaseous H_2 and O_2. The hydrogen ions are reduced to hydrogen gas by photogenerated electrons. These reactions can be presented as follows:

Oxidation: $$H_2O + 2h^+ \rightarrow 2H^+ + ½\, O_2 \qquad (2.1)$$

Reduction: $$2H^+ + 2e^- \rightarrow H_2 \qquad (2.2)$$

Overall reaction: $$H_2O \rightarrow H_2 + ½\, O_2 \qquad (2.3)$$

The water splitting reaction requires the Gibbs free energy change ($\Delta G°$) of 237 kJ/mol to split one molecule of water in to H_2 and O_2 (Chen et al., 2010). The width of the band gap and the redox potential of the conduction and valence bands are important to facilitate the water splitting reaction. For hydrogen production, the bottom level of the conduction band should be more negative than the reduction potential of H^+/H_2 (0 V vs. NHE), while the top level of the valence band should be more positive than the oxidation potential of O_2/H_2O (1.23 V) for O_2 formation. The complete decomposition of water is thus theoretically possible if a semiconductor has the minimum band gap energy of 1.23 eV (an absorption wavelength cut-off of 1008 nm). However, the potential of the semiconductor's band structure is just the

Footer Page TH-1334_08610706

thermodynamic requirement. Other photocatalytic properties such as charge separation as well as mobility and lifetime of photogenerated electron-hole pairs also have significant effect on the activity of the catalyst. These properties are strongly affected by electronic structure, bulk properties and surface properties of the material. The photocatalytic activity of semiconductor materials is affected by following three basic parameters (Zhou et al., 2012; Maeda and Domen, 2007; Kudo, 2006; Alonso et al., 2009; Carp et al., 2004):

(1) Light absorption capacity

(2) Rate of reduction and oxidation of substrate by e^-/h^+ respectively, and

(3) Rate (or probability) of e^-/h^+ recombination.

2.1.1 Charge carrier trapping

For efficient photocatalytic reactions, the stabilization of charge carriers is as important as their formation and transfer. The stabilization of the charge carriers can be achieved by trapping the photogenerated electrons and holes. Trapping increases the lifetime of the charge carriers enhancing photocatalytic activity. Trapping of photogenerated electrons, holes or both can be achieved by doping with foreign atoms (Choi et al., 1994). The electron trapping is reported to take place within 30 picoseconds (ps). The hole trapping on other hand is reported as a slower process taking an average time of 250 nanoseconds (Rothenberg et al., 1985). Skinner et al. (1995) reported 200 femtoseconds for the electron trapping and 30 picoseconds for electron-hole recombination.

Doping of photocatalysts with foreign atoms/ions results in formation of additional energy states within the band gap of parent materials that act as trapping centers. It is important to have enough number of trapping states on the surface to achieve efficient charge separation. Trapping of electron and hole takes place, if the energy level of the pair $M^{n+}/M^{(n-1)+}$ is located below/near the conduction band edge and the pair $M^{n+}/M^{(n+1)+}$ is located above/near to the valence band edge (Choi et al., 1994; Ni et al., 2007).

Electron trapping:

$$M^{n+} + e^-_{cb} \rightarrow M^{(n-1)+} \qquad (2.4)$$

Footer Page TH-1334_08610706

Hole trapping:

$$M^{n+} + h_{vb}^{+} \rightarrow M^{(n+1)+} \qquad (2.5)$$

At optimum dopant concentration, the dopants can trap only one type of charge carriers and allow the other to reach the catalyst surface to take part in the desired redox reaction (Hoffmann et al., 1995). On the other hand, doped metal ions above the optimum concentrations are reported to decrease the photocatalytic activity due to the higher recombination rate of charge carriers (Dvoranova et al., 2002). Metal ions doped near the surface of photocatalysts particles are reported to allow a better charge transfer, while in case of deep doping metal ions can act as recombination centers. Choi et al. (1994) reported that metals such as V^{4+}, Mn^{3+}, Co^{3+}, and Ru^{3+} can trap both electron and hole, whereas Cr^{3+} and Ni^{2+} can trap only hole. For example, by trapping of electron V^{5+} changes to V^{4+}, thus the former can trap an electron but later can trap both electrons and holes. In case of Fe, Fe^{3+} change in valence state to Fe^{2+} by trapping an electron and can transfer the trapped electrons to Ti^{4+}. This phenomenon of interfacial charge transfer can occur because the energy levels of Fe^{3+}/ Fe^{2+} lies close to Ti^{4+}/Ti^{3+} level. Litter (1999) reported that Cu and Fe have the ability to capture both electron and hole due to the position of the energy levels which lies close to conduction band and valence band edges of TiO_2. The oxygen vacancies are also suggested to be involved efficiently in the electron trapping process (Gan et al., 2013). Increased oxygen vacancies resulted in more efficient trapping of photogenerated electrons. But presence of excess oxygen vacancies can act as recombination centers for photogenerated electrons. Nakamura et al. (2004) discussed that the interstitial nitrogen impurities can act as strong hole trapping sites.

2.1.2 Visible light activity

In order to utilize the visible light irradiation, the band gap value should be less than 3.0 eV and the position of the band gap of the photocatalyst is also an important factor. There are only a limited number of known materials that could satisfy these requirements. For example, chalcogenides, such as CdS (2.4 eV) and CdSe (1.7 eV), have ideal band gap energies and band positions for the oxidation and reduction of water molecules under visible light. But they easily undergo photo-corrosion in water under irradiation, i.e. the material itself is oxidized by the hole produced in its valence band (Matsuoka et al., 2007; Kitano et al., 2007; Hashimoto et al., 2005). Several

Footer Page TH-1334_08610706

approaches have been adopted in order to develop visible light active photocatalysts. One of the most effective ways is to convert UV active photocatalyst to visible light active catalyst by doping with metal ions. The doping of metal ions introduces additional energy levels within the band gap of the photocatalyst to facilitated visible light absorption. This can be achieved by replacing cations in the lattice of wide band gap photocatalyst. Anion doping is another approach to improve visible light activity. Incorporation of non metal ions shifts the valence band edge upwards by mixing of p orbitals of the dopant ions and oxygen 2p orbitals (Kudo and Miseki, 2009; Asahi et al., 2001). Modification by codoping with metal and nonmetal ions in the wide band gap has also been studied to enhance the visible light activity. Dye sensitization and semiconductor coupling are other effective methods to absorb the visible light energy. Dyes such as rhodamine B, crystal violet and Eosin etc., are used for improving the photocatalytic activity because of their redox property and visible light sensitivity. Coupled semiconductors are used to improve the separation efficiency and stability of charge centers. A small band gap semiconductor (visible light active) is coupled with a large band gap semiconductor (UV active) to increase the activity in visible light (Maeda, 2011; Chen et al., 2010; Ni et al., 2007).

2.1.3 Effect of alcohol

Alcohols such as methanol, ethanol, propanol, etc., have been reported to greatly enhance the photogenerated electron-hole separation, which results in higher quantum efficiency. Alcohols consume the valence band holes and undergo oxidation reaction thereby acting as efficient hole scavenger. This reduces electron-hole recombination and facilitates the accumulation of electrons in the conduction band which participate in reduction of hydrogen ions. Yang et al. (2006) studied activity of Pt-TiO_2 in presence of different alcohols such as, methanol, ethanol, n-propanol, i-propanol and butanol. Based on the polarity of the solvents, the results exhibited a decrease in hydrogen generation rate from methanol to butanol. Bahruji et al. (2010) investigated hydrogen production from different alcohols over Pd-TiO_2 catalyst. The formation of products depended on the nature of the substrate. With methanol, H_2 and CO_2 were observed while for ethanol and 2-propanol, methane was also obtained as the coproduct. The 1-propanol formed ethane and butanol generated propane and ethane. Wang et al. (2013) studied effect of concentration of methanol and ethanol on the

Footer Page TH-1334_08610706

activity of the CoO_x/TiO_2 catalyst. The results showed that methanol had higher activity than ethanol.

2.2 Photocatalytic systems

Studies have been conducted to investigate the potential use of photocatalysts in various areas of interest (Lan et al., 2013; Fujishima et al., 2007; Nakata and Fujishima, 2012). The major area of investigation has been the photodegradation of pollutants along with the photocatalytic water splitting for hydrogen production (Ni et al., 2007). At present photocatalytic conversion of carbon dioxide is emerging as a new area of interest (Centi and Perathoner, 2009). Generally, semiconductors are used for photocatalytic hydrogen production due to their suitable band gap and the position of the band edges with respect to the potential required for water decomposition reaction. Metals cannot promote redox reactions due to overlap of the conduction and valence bands, while insulators have very large band gap (Nash, 2008). Hence, metals and insulators are not suitable for photocatalytic water splitting reactions. Metal oxides (SnO_2, $CaTiO_3$, $KTaO_3$, α-Fe_2O_3, ZnO, $SrTiO_3$, TiO_2) and chalcogenides (CdS, NiS, CdTe) are the most commonly investigated semiconductor photocatalysts (Osterloh, 2008; Maeda, 2011; Chen et al., 2010).

2.2.1 Titania based photocatalysts

Honda and Fujishima (1972) first reported water splitting using a titanium dioxide (TiO_2) electrode for water electrolysis giving hydrogen and oxygen. Photocatalysis by TiO_2 in UV region has received great attention. Among various semiconductors, titanium dioxide is considered as one of the most promising material due to its high oxidation efficiency, nontoxicity, high photostability and environment friendly nature (Ide et al., 2013, Kudo, 2007; Daghrir et al., 2013). TiO_2 exists in three crystallographic forms, anatase (3.2 eV), rutile (3.06 eV) and brookite (~3.2 eV) (Pelaez et al., 2012). Anatase TiO_2 is the most stable form and can be converted to rutile phase by heating above temperature of 700 °C. In photocatalytic applications, anatase is reported to be more efficient than rutile due to the lower rates of recombination and higher surface adsorptive capacity (Li et al., 2007; Hurum et al., 2003). TiO_2 as photocatalyst is used in many applications such as the degradation of pollutants from water and air (Beydoun et al., 1999; Stathatos et al., 1999; Comparelli

Footer Page TH-1334_08610706

et al., 2005), photocatalytic and photoelectrochemical hydrogen production (Abe, 2010), solar cells (Deb, 2005; Mor et al., 2006) and sensors (Seeley et al., 2009; Galstyan et al., 2013) etc. Many researchers have reported the photocatalytic activity of TiO_2 for hydrogen production from water under ultra violet (UV) irradiation (Tabata et al., 1995; Sato et al., 1980; Kutty et al., 1988; Sreethawong et al., 2006; Sakata et al., 1981; Wang et al., 2013). The main drawback of hydrogen production by photocatalytic water-splitting using TiO_2 is the fact that titania is active only under UV light radiation due to its larger band gap (Tan et al., 2013). The UV light only accounts for about 4 % of the total solar energy while the visible light contributes about 50 %. , This limits the solar-hydrogen efficiency of TiO_2. The efficiency is also reduced due to the quick recombination of conduction band electrons with valence band holes releasing energy in the form of heat or photons.

Therefore, the important aspect for the application of TiO_2 as photocatalyst is to enhance the photocatalytic efficiency in visible light region. In order to utilize the abundant source of light energy reaching the earth's surface and to stabilize the photogenerated charge carriers different strategies, such as metal ion doping, anion doping, noble metal loading, metal ion-implantation, dye sensitization, semiconductor coupling, addition of electron donors (hole scavengers), addition of carbonate salts etc., were investigated (Liao et al., 2012; Rehman et al., 2009; Zhu and Zach, 2009; Paleocrassas, 1974; Nowotny et al., 2005; Nowotny et al., 2007; Ni et al., 2007)

2.2.1.1 Modification with metals

Doping is a strategy to alter the optical properties of the material by replacing Ti or oxygen sites in the TiO_2 lattice with other element. The charge-transfer transition between the d electrons of the transition metals and the conduction or the valence band of TiO_2 shifts the absorption edge to the visible light region (Teh and Mohamed, 2011). The dopant induced new electronic states are formed within the electronic structure of TiO_2, below the conduction band edge or above the valence band edge. These states influence the recombination rate of charge carriers, since the metal ions can act as electrons or hole traps (Choi et al., 1994). Efforts have been made to modify TiO_2 by doping various metals in order to reduce the band gap and retard the recombination of photogenerated electron-hole pairs effectively. Combination of both the factors can enhance the photocatalytic activity of TiO_2 under visible light (Litter,

Footer Page TH-1334_08610706

1999; Kudo and Miseki, 2009; Tong et al., 2012; Maeda, 2011; Teoh et al., 2012; Chen et al., 2010). The new energy levels formed within the band gap of TiO_2 by the metal ion dopants can alter the recombination rate of charge carriers, since the metal ions can act as electrons or hole traps (Choi et al., 1994). The metal dopant ions can occupy the lattice sites either at substitutional or interstitial position depending on the ionic radii of metal dopants compared to that of the matrix cation. Based on the valence states of the cationic dopants compared with that of valence state of titanium in TiO_2, dopants could behave in two different ways either as electron donors (cationic dopants having higher valence states than that of host material cation) or electron acceptors (cationic dopants having lower valence states than that of host material cation) (Wieckowski et al., 2003).

Karakitsou and Verykios (1993) studied the effect of different transition metal dopants such as (W^{6+}, Nb^{5+}, Ta^{5+}, Ge^{4+}, In^{3+}, Zn^{2+}, Li^{+}) on TiO_2 for photodecomposition of water. Among the different transition metals, the dopant cations having higher valence than those of Ti^{4+} were reported to show higher hydrogen production and the dopants cations having lower valence showed decreased hydrogen activity. The cationic dopants having equal valence state did not influence the efficiency for hydrogen production. Reddy et al. (2014) investigated Fe (0.2-2.0 wt%) doped TiO_2 for hydrogen production under visible light illumination and found that the absorption edge was red-shifted as the dopant concentration increased from 0.2-2.0 wt%. The authors have shown that Fe^{3+} (0.5 wt%) ions doped on the surface of TiO_2 resulted in maximum hydrogen production rate of 270 μmol/h compared to 2.8 μmol/h for undoped TiO_2. They have suggested that metal ion dopants located deep within the band gap of TiO_2 behave as recombination center. Khan et al. (2008) also reported hydrogen production on Fe doped TiO_2 from aqueous methanol solution and pure water. The hydrogen evolution of 12.5 μmol/h and 1.8 μmol/h, was observed from methanol solution and pure water respectively for 1.0 wt% Fe/TiO_2. Copper doped titanium dioxide was reported to enhance hydrogen production significantly (Wu and Lee, 2004; Lee et al., 2013). The catalytic activity was attributed to the photogeneration of excited electrons in the conduction bands of both TiO_2 and CuO. CuO was suggested to act as an active site for redox reactions (Bandara et al., 2005). The presence of CuO acted as effective electron traps and reduced the recombination rate of electron-hole pair (Choi and Kang, 2007). The optimum amount of CuO and

Footer Page TH-1334_08610706

the crystalline structure were observed to be crucial for the catalytic activity of CuO-TiO_2. Sreethawong and Yoshikawa (2005) reported H_2 production activity (360 μmol/h) for Cu loaded TiO_2 from aqueous methanol solution. They have reported that the cocatalyst doped at a lower concentration with uniform dispersion can acts as separation center and sink for photogenerated electrons. Yoong et al. (2009) prepared Cu or Ni doped TiO_2 by precipitation method and wet impregnation method, the dopant loading amount was varied from 2-15 wt % and calcined at 300, 400 and 500 °C. The catalyst prepared with 10% (wt) of Cu at calcination temperature of 300 °C by precipitation method was reported to result in higher hydrogen evolution of 8.5 ml/h from aqueous methanol solution. Ni doped TiO_2 also showed photocatalytic activity, but the hydrogen production rate was observed to be lower compared to that of Cu doped TiO_2. Sasikala et al. (2009) prepared SnO_2 doped TiO_2 for hydrogen production under visible light irradiation. They suggested that the enhanced activity can be ascribed to highly dispersed phase of SnO_2 on TiO_2, which results in an efficient electron trapping and charge transfer.

Incorporation of noble metals such as, platinum, gold and ruthenium was also reported to extend the light absorption of TiO_2 band gap to the visible light region. Kitano et al. (2005) and Huang et al. (2011) reported Pt-TiO_2 for hydrogen production activity. Their results showed that the higher visible light absorption and inhibition of recombination of charge carriers by Pt were responsible for higher activity. Sayama and Arakawa (1997) studied the photocatalytic hydrogen evolution of Pt loaded TiO_2 photocatalysts under UV irradiation with the addition of carbonate salts such as Na_2CO_3, $NaHCO_3$, Li_2CO_3 and K_2CO_3. Pt-loaded TiO_2 photocatalyst during reaction was covered with several types of carbonate species and the average rate of hydrogen production was found as 568 μmol/h using Na_2CO_3 aqueous solution. These carbonate species was reported to effectively suppress the back reaction of water splitting to form water and prevent the photo absorption of oxygen on the TiO_2. Shi et al. (2007) reported hydrogen evolution of 3300 μmol after 5 h of irradiation period for Pt-TiO_2 from water-methanol solution under UV light irradiation. The authors proposed that excited electrons trapped in oxygen vacancies of anatase were transferred to Pt and retarded the recombination of charge carriers at oxygen vacancies in anatase. Similar transfer was not observed for rutile phase. Silva et al. (2011) investigated Au-TiO_2 catalyst for hydrogen production activity and suggested that the presence of Au

Footer Page TH-1334_08610706

increased the separation of photogenerated charge carriers and consequently improved the photocatalytic activity. The effect of Ru/TiO_2 for hydrogen production from methanol and water solution was reported by Sobczynski et al. (1989). Bowker et al. (2014) studied hydrogen generation on Au and Pd doped TiO_2 catalysts from aqueous solution of methanol. The higher hydrogen activity was observed for Pd than Au doped TiO_2 at low loadings. They also reported higher activity with increase in calcination temperature (200-400 °C) and loadings (0.001-0.5 wt%). But a sharp drop in the rate of hydrogen production was observed at loading higher than 0.1 wt% for both the catalysts. The authors reported higher activity for codoped $Au\text{-}Pd/TiO_2$ and was attributed to the improved rate of trapping of photogenerated electrons. Chiarello et al. (2008) investigated hydrogen production from photoreforming of methanol and reported 30 times higher hydrogen production for $Au\text{-}TiO_2$ prepared by flame pyrolysis (7890 μmol/g/h) compared to that of titania (439 μmol/g/h). Chiarello et al. (2009) also reported hydrogen production with improved activity for gold doped TiO_2. An apparent photon efficiency of 6.3 % was reported under halogenide mercury lamp in photoreforming process of methanol.

Dye sensitized metal doped titania was also studied for photocatalytic activity. Le et al. (2012) prepared rhodamine B sensitized Co doped TiO_2 by impregnation method. The maximum hydrogen evolution rate of 227.3 μmol/g/h was obtained from 70 ml of pure water solution. The rhodamine B dye, absorbed on the catalyst surface, transferred the electrons to cobalt metal under visible light irradiation. They reported that the efficient electron transfer from dye to cobalt metal through TiO_2 led to better hydrogen evolution efficiency than those of $Co\text{-}TiO_2$ (hydrogen evolution rate, 37.67 μmol/g/h). Ou et al. (2006) studied $MWNT\text{-}TiO_2\text{-}Ni$ (MWNT = mutiwalled carbon nanotubes) prepared by chemical vapor deposition for hydrogen evolution from aqueous methanol solution. The authors reported that MWNT could act as a sensitizer and transfer the photogenerated electrons of MWNT to TiO_2. The electrons were thereafter can be transported to the isolated Ni particles present on the surface of TiO_2 for the reduction of water molecules. They reported hydrogen evolution of 38.1 μmol/h for $MWNT\text{-}TiO_2\text{-}Ni$ under visible light radiation. Jin et al. (2007) studied hydrogen generation over eosin-sensitized CuO/TiO_2 photocatalyst under visible light irradiation. The authors reported 5.1% apparent quantum efficiency for eosin dye-sensitized 1.0 wt% CuO/TiO_2 from diethanolamine-water solution. They also

Footer Page TH-1334_08610706

investigated hydrogen production in the presence of different electron donors such as triethanol amine, diethanolamine, acetonitrile and triethylamine. Among the sacrificial electron donors, maximum hydrogen production of 127 μmol/10 h was reported for aqueous solution of diethanolamine and water.

2.2.1.2 Modification with nonmetals

Another approach to sensitize TiO_2 in visible light region is doping with nonmetal elements such as nitrogen (Pelaez et al., 2012; Nosaka et al., 2005; Irie et al., 2003; Sathish et al., 2007; Sathish et al., 2005; Wang et al., 2013) carbon (Lettmann et al., 2001; Valentin et al., 2005, Xu et al., 2006), sulphur (Umebayashi et al., 2002; Ohno 2004a; Yang et al., 2012; Yamamoto et al., 2004), fluorine (Wu et al., 2010; Li et al., 2005; Hattori et al., 1999) and boron (Finazzi et al., 2009; Chen et al., 2006). Asahi et al. (2001) reported that N-doped TiO_2 showed a significant shift of the absorption edge to lower energy in the visible light region. N_{2p} level mixed with O_{2p} was reported to result in narrow band gap and enhanced photoactivity for degradation of the acetaldehyde and methylene blue. Yuan et al. (2006) investigated N-TiO_2 for hydrogen production under UV and visible light irradiation in the presence of Na_2SO_3 as hole scavenger. The higher activity was attributed to the presence of more substitutional nitrogen. Joshi et al. (2012) reported hydrogen yield for N-TiO_2 from water-ethanol solution, while Sreethawong et al. (2008) reported from aqueous methanol solution. It was reported that the boron oxide played an important role in the suppression of recombination of evolved H_2 and O_2 (Moon et al., 1998; Moon et al., 2000). Boron incorporation in TiO_2 was suggested to promote the partial reduction of Ti^{4+} to Ti^{3+}, which can act as electron traps. Boron was also reported to create shallow traps for electrons and thereby prolong the life of photogenerated charge carriers. Li et al. (2008) observed a decrease in band gap and higher photocatalytic activity under visible radiation for B-N-TiO_2.

Khan et al. (2002) reported 8.35% photoconversion efficiency from a 150 W xenon lamp radiation for C-doped TiO_2. Sakthivel and Kisch (2003) prepared carbon modified TiO_2 by the hydrolysis of titanium tetrachloride with tetrabutylammonium hydroxide and reported superior activity for mineralization of 4-chlorophenol and azo dye remazol red. Recently, Liu and Syu (2013) prepared C/N doped TiO_2 using ionic liquids as templates for the formation of mesoporous TiO_2. For this catalyst 81.8

Footer Page TH-1334_08610706

μmol/g/h of hydrogen evolution rate was reported from aqueous methanol solution under visible light irradiation. Pal et al. (2012) studied visible light driven hydrogen production for nonmetal doped titanium oxide using electron donors. TEOA (tri-ethanolamine) showed hydrogen activity for C-TiO_2 (2947 μmol/g/h), N-TiO_2 (1008 μmol/g/h) and S-TiO_2 (1269 μmol/g/h). The direct electron transfer from electron donors to TiO_2 was suggested to reduce the recombination of charge carriers and increase photoactivity.

Umebayashi et al. (2003a and b) investigated the photocatalytic activity of sulphur incorporated TiO_2 for degradation of methylene blue TiS_2 as starting material. They suggested that the lattice oxygen sites were substituted by sulfur atoms and formed new sulphur doped impurity energy states above the valence band and narrowed the band gap. Periyat et al. (2008) reported that anionic sulphur doping may be difficult due to the larger ionic radius of S^{2-}(1.7Å) compared to that of O^{2-} (1.22 Å). The visible light activity of anionic S doped TiO_2 was attributed to the mixing of S_{3p} state with O_{2p} states. Yu et al. (2005) confirmed that substitution of Ti^{4+} by S^{6+} is chemically more favorable than replacing O^{2-} with S^{2-} ions. The cationic S doped TiO_2 was studied by Ohno et al. (2003; 2004b) for the degradation of methylene blue under visible light radiation. They proposed that S^{4+} atoms were incorporated as cations and replaced Ti ions. Niu et al. (2012) reported that photogenerated electrons can be trapped by the anchored sulphate group on the surface of TiO_2. Naik et al. (2010) observed excellent photocatalytic activity of N and S incorporated TiO_2 for photodegradation of phenol and methyl orange under direct solar light. The authors suggested that interaction of sulphate and nitrogen with titania enhanced the photocatalytic activity.

2.2.1.3 Comodification with metal and nonmetals

Recently it was observed that codoping of metal and nonmetal in TiO_2 was able to enhance both the visible light absorption efficiency and separation of photo-generated charge carrier compared to that of single dopant. Visible light active photocatalysts have been reported by codoping TiO_2 with metal and nonmetal such as V/N (Liu et al., 2011), Ni/N (Zhang and Liu, 2008), N/Sn (Wang et al., 2011), N/Fe (Yang et al., 2010), C/V (Liu et al., 2011), etc. Selcuk et al. (2012) reported Ni-N codoped TiO_2 catalysts for hydrogen production from 10% aqueous methanol solution under visible

Footer Page TH-1334_08610706

light irradiation. They have also investigated Fe-N-TiO_2, Cr-N-TiO_2, Pt-N-TiO_2, N-TiO_2 and TiO_2 for hydrogen production under the same conditions. Among these catalysts, Pt-N-TiO_2 and Ni-N-TiO_2 showed a hydrogen evolution rate of 11620 and 2946 μmol/6h, respectively. The activity was attributed to the improved dispersion of Ni particles over N-TiO_2. Ni nanoparticles were suggested to behave as an electron sink to separate the photoinduced electron-hole pairs effectively. Sasikala et al. (2010) investigated the photocatalytic activity of H_2 evolution of In and N codoped TiO_2 prepared by polyol method under visible light irradiation. The authors found that the codoped catalyst showed much higher hydrogen production rate than that of single doped TiO_2 catalyst due to the improved visible light absorption and charge carrier separation efficiency. Sreethawong et al. (2009) prepared Pt loaded N-doped TiO_2 with excellent photoactivity from aqueous methanol solution under visible light irradiation. It has been reported by the authors that the higher activity for hydrogen evolution can be attributed to the presence of Pt, which rapidly captured the electron and promoted the reduction reactions.

Li et al. (2012) prepared Ga and N codoped TiO_2 by sol-gel method having lower band gap and higher surface area than that of pure TiO_2. They suggested that Ga doping created trapping centers for electrons, while N dopant created oxygen vacancies or new intra band gap states within TiO_2 lattice. Ga^{3+} was also reported to increase the oxygen vacancies. Various cerium-nitrogen codoped catalysts were reported for photocatalytic degradation (Priyanka et al., 2014, Yu et al., 2010, Nasir et al., 2013). Sun et al. (2010) studied visible light photoactivity of Ce and N codoped TiO_2 from water-methanol mixture. The maximum hydrogen evolution of 120 μmol/h was obtained for Ce (0.6%)-N-TiO_2 catalyst. Codoped TiO_2 was reported to show better activity in the visible light region than single doped TiO_2.

2.2.2 Indium oxide based photocatalysts

In_2O_3 is an important semiconductor material used in sensors, solar cells and photocatalysis (Gurlo et al., 1998, Calnan and Tiwari, 2010, Yin and Cao, 2012). It is an n-type semiconductor with a direct bandgap of 3.6 eV and an indirect bandgap of 2.8 eV (Li et al., 2012). In_2O_3 based composite systems such as $Ba_2In_2O_5$-In_2O_3 and In_2O_3-Ta_2O_5 have been reported for water splitting applications (Wang et al., 2005, Xu et al., 2011). Wang et al. (2005) investigated Cr-doped $Ba_2In_2O_5$-In_2O_3 for

Footer Page TH-1334_08610706

photocatalytic H_2 production in the presence of methanol as a sacrificial reagent. They reported that the H_2 evolution was higher for Cr-doped $Ba_2In_2O_5$-In_2O_3 compared to that of Cr-doped $Ba_2In_2O_5$ and Cr-doped In_2O_3 catalysts. Xu et al. (2011) reported enhanced hydrogen evolution activity for In_2O_3-Ta_2O_5 coupled oxide compared to that of the In_2O_3 catalyst. The higher activity of the catalyst was attributed to the synergistic effect of mesoporous structure and higher surface area of the catalyst.

Chang et al. (2007) studied In_2O_3/$CaIn_2O_4$ for the photocatalytic degradation of methylene blue under visible light irradiation. They suggested that the coupled In_2O_3/$CaIn_2O_4$ showed improved activity than the single phased $CaIn_2O_4$ due to the difference in their band edges. In_2O_3 decorated TiO_2 was investigated for photocatalytic decolorisation of methyl orange by Zhong et al. (2014). The photocatalytic activity of the In_2O_3-TiO_2 was investigated for the degradation of rhodamine B. The results showed that the In_2O_3-TiO_2 has higher activity than TiO_2 and In_2O_3 due to the better separation efficiency of the charge carriers (Mu et al., 2011). Another study of In_2O_3-TiO_2 by Niyomkarn et al. (2014) for degradation of azo dye showed that incorporation of In_2O_3 increased the surface area and inhibited the anatase-rutile transformation. The authors suggested that the enhanced photocatalytic activity was attributed to the higher surface area and lower electron-hole pair recombination effect. Li et al. (2014) reported In_2O_3-TiO_2 with significant photocatalytic activity for the decomposition of methyl orange and rhodamine B under visible light irradiation. Liu et al. (2014) reported In_2O_3-ZnO composites for methylene blue degradation under visible light irradiation. The improved photocatalytic activity was attributed to the strong visible light absorption and higher separation efficiency of the photogenerated electron-hole pairs. Zeng et al. (2013) showed In_2O_3-Bi_2O_3 with enhanced photoactivity for the degradation of methyl orange. They suggested that the increased activity was mainly due to the higher surface area and recombination of photogenerated charge carriers. From the literature studies, it can be observed that only few studies were reported for hydrogen production.

2.2.3 Coupled semiconductor based photocatalysts

Coupling between different semiconductors with proper band energy levels is another interesting approach to improve the charge separation efficiency. Transfer of the

Footer Page TH-1334_08610706

charge carriers from small band gap semiconductors to the wide band gap semiconductors can occur with proper positioning of the conduction band and valence band. This ensures an efficient separation of photogenerated electron-hole pairs between the semiconductors. This transfer of charge carriers from small band gap to wide band gap semiconductors enhances the photoresponse of wide band gap material. The charge transfer process studied in CdS-TiO_2 coupled system suggests that the interparticle electron transfer occurs within 500 femtoseconds to 2 picoseconds (Evans et al., 1994). However, in many cases, due to the lesser electron transfer rate the migration of electrons from one semiconductor to the other makes the process inactive (Keller and Garin, 2003). This suggests that the effectiveness of the coupling of the semiconductor photocatalysts depends on the interfacial charge transfer between the two different semiconductors and its recombination rate.

For the photocatalytic enhancement of TiO_2 under visible light irradiation, CdS has been used as a sensitizer due to its lower band gap and more negative H^+/H_2 reduction potential. Recently, CdS-TiO_2 prepared with Pt or Au gold as cocatalyst showed efficient hydrogen production under visible light irradiation (Cui et al., 2013; Fang et al., 2013; Strataki et al., 2010; Ju et al., 2011). SiC-TiO_2 was reported for H_2 production from aqueous solution of ethanol under visible light illumination. The authors also studied the photocatalyst activity of SiC-TiO_2 using NiO_X and IrO_2 as cocatalysts to enhance the activity. The results showed that the rate of hydrogen evolution was higher for IrO_2/ SiC-NiO_x/TiO_2 compared to that of SiC-TiO_2, IrO_2/SiC-TiO_2, NiO_x/TiO_2 or SiC-NiO_x/TiO_2 catalysts. The increased activity was attributed to the addition of NiO and IrO_2 which acted as electron collector and trigger the oxidation reactions, respectively. The higher visible light absorption of SiC and the movement of electron-holes were reported to facilitate improved H_2 evolution (Li et al., 2013). Majrik et al., (2013) recently reported hydrogen production activity of SnO_x-TiO_2 using Pt as cocatalyst from aqueous solution of methanol under UV and visible light irradiation. The increased H_2 evolution was reported due to the surface Sn moieties which acted as electron trapping sites. Li et al. (2012) prepared Cu_2O-Cu-TiO_2 nanotube arrays by two-step anodization method at 500 °C. The authors attributed the higher photocatalytic reaction rate to the efficient charge transfer between Cu_2O and TiO_2 due to a lower resistance of copper contact layer. Cheng et al. (2013) used Cu_2O-CdS for visible light photocatalytic hydrogen production with a

Footer Page TH-1334_08610706

yield of 238 μmol/h. NiO_x on CdS was studied for hydrogen production and a maximum evolution rate of 590.8 μmol/h was obtained with a quantum efficiency of 8.6% at 400 nm in presence of methanol (Chen et al., 2014). CuO-Cr_2O_3 loaded carbon nanotubes sensitized with eosin Y showed visible light photoactivity for hydrogen production. The authors reported that the hydrogen evolution was increased due to the synergistic effect of eosin Y as sensitizer and triethanolamine as electron donor (Li et al., 2014). Lv et al. (2010) observed that the hydrogen evolution can be achieved using $NaNbO_3$-In_2O_3 as photocatalyst and methanol as sacrificial reagent. The NiO-$InVO_4$ has been studied by Lin et al. (2007) for water splitting reaction. The authors suggested that the addition of NiO improved the hydrogen evolution.

2.3 Photocatalytic reaction kinetics

Kinetic studies are important to understand the photocatalytic processes, design of photocatalytic reactors, optimization of photocatalysts as well as for efficient utilization of light. The photocatalytic reactions involves series of elementary steps such as transportation of reactant to the catalyst surface, adsorption, absorption of photon, electron-hole pair generation, charge trapping, charge carriers migration, recombination, surface reaction, diffusion and desorption of the products or intermediates. The photocatalytic reaction rate (r) is a function of initial reactant concentration (C_i), catalyst amount (C_c) and the photon absorption rate (P_a) (Lasa et al., 2005).

$$r = f(C_i, C_c, P_a) \qquad (2.6)$$

The reaction rate is controlled by the surface kinetics. Mass transfer limitation can be neglected in a well mixed photoreactor system (Matthews, 1988). The most common method applied to analyze the kinetic data is Langmuir-Hinshelwood (L-H) model, which can relate the surface reactions with surface coverage of the substrate (Mathews, 1988; Turchi and Ollis, 1989). The reaction rate (r) is proportional to the surface coverage of the substrate (θ_x).

$$r = -dc/dt = k_r\theta_x = k_r K_s C / 1 + K_s C \qquad (2.7)$$

The k_r is the reaction rate constant, K_s is the adsorption equilibrium constant of the reactant and C is the concentration of the substrate 'x'. The reaction rate is reported to

Footer Page TH-1334_08610706

be dependent on the light intensity showing a proportionality of $I^{0.5}$ and $I^{1.0}$ at high and low ligh intensities, respectively (Ohtani, 2014; Li et al., 2008; Malato et al., 2009). The terms k_r and K_s showed square-root dependency on light intensity.

Other kinetic models such as, Eley-Rideal, have also been applied to study the rate expressions in terms of product formation and reactant consumption (Brosillon et al., 2008). The most critical factor in the photocatalytic process is the quantum efficiency, which determines the practical importance of a photocatalytic technique. The efficiency involves the rate of photon absorbed by the photocatalyst (Sun and Bolton, 1996). Detailed kinetic studies are limited for photocatalytic reaction. Matthews (1988) investigated the kinetics of photooxidation of various organic solutes for TiO_2 under UV irradiation. Li et al. (2008) estimated the kinetic parameter for degradation of rhodamine B at different light intensities and TiO_2 content. The authors found that the reaction rate constant for rhodamine B increased with increase in the light intensity. They also suggested from their kinetic model that the reciprocal of the reaction rate constant and adsorption rate constant have dependency on the reciprocal of the square root of the light intensity. It was reported that reaction rate constant increased with increase in titania content and then decreased, whereas adsorption rate constant decreased with increase in the titania content. It was concluded that the rhodamine B degradation rate was determined by the titania amount and followed the first order kinetics. Lin et al. (2009) reported that the electron-hole pairs mainly resulted in chemical reactions and followed L-H kinetics for methylparaben degradation at low UV light flux. Different parameters such as pH, TiO_2 amount and oxygen concentration were investigated for photodegradation processes of methylparaben. The amount of hydroxyl radicals and surface charge of the catalyst were influenced by the pH, which led to change in the overall rate. Also the removal time was observed to decrease linearly with increase in oxygen concentration. The authors showed that at higher oxygen concentration, the reaction rate increased linearly with increase in light intensity. In case of higher TiO_2 loading, the authors stated that the decrease in reaction rate was due to the scattering of particles and decrease in light penetration. Turchi and Ollis (1990) proposed four modified mechanisms based on the hydroxyl radical reaction pathway. The hydroxyl group adsorbed on the catalyst surface and the holes generated in the valence band of semiconductor material were suggested to be involved in the photooxidation

Footer Page TH-1334_08610706

reactions. The organic compounds or intermediates on the catalyst surface can be attacked by hydroxyl radical, while the valence band hole can attack the water as well as adsorbed intermediates formed during the water splitting reaction. Hydroxyl radical attack is stated as the predominant mechanism in aqueous photocatalytic processes. K_s was reported to be independent of light intensity by Turchi and Ollis (1990). On the other hand Xu and Langford (2000) investigated the degradation rate of acetophenone at different light intensities and proposed that increase in incident intensity decreased the K_s. Chen and Ray (1998) studied the photodegradation kinetics of nitrophenol as a function of different parameters such as initial pollutant concentration, light intensity, partial pressure of oxygen, catalyst concentration, pH, chloride ion and temperature. The degradation rate was observed to be pseudo first-order as a function of concentration of nitrophenol. At both low and high pH, they observed a slower photodegradation rate. The presence of chloride ion had negative effect on the rate of degradation at low pH. The calculated equilibrium adsorption constants of oxygen and nitrophenol were 9.98 atm^{-1} and 0.075 ppm^{-1}. Nomikos et al. (2014) reported the kinetic study of methanol photoreforming on Pt/TiO_2 catalyst at different initial methanol concentration and light intensity. The hydrogen production rate was increased with increase in the concentration of methanol. They also observed increase in the reaction rate with increase in the light intensity (up to 2.3mW cm^{-2}) at lower methanol concentration. The authors reported that the hydrogen evolution was accompanied with CO_2 formation in the presence of methanol, while only hydrogen production was observed using pure water. Sahu et al. (2009) studied the kinetics of hydrogen production from photocatalytic splitting of water over Pt-CdS catalyst. The hydrogen production rate was reported to increase up to 2 h of irradiation period and thereafter decreased. The authors suggested that hydrogen production rate is directly proportional to the concentration of sulfide ions adsorbed on the surface.

Footer Page TH-1334_08610706

Chapter 3

Experimental Details

3.1 Materials used

Titanium tetra isopropoxide [$C_{12}H_{28}O_4Ti$, 97%] and zinc nitrate hexahydrate [Zn $(NO_3)_2$ $6H_2O$, 98%] was procured from Sigma-Aldrich. Indium nitrate [In $(NO_3)_3$, 99.99%] was obtained from Alfa Aesar. Copper nitrate trihydrate [Cu $(NO_3)_2.3H_2O$, ≥ 99%], cerium nitrate hexahydrate [Ce $(NO_3)_2$ $6H_2O$, 99%], iron nitrate nonahydrate [Fe $(NO_3)_3$ $9H_2O$, ≥ 98%], nickel nitrate hexahydrate [Ni $(NO_3)_2$ $6H_2O$, ≥ 97%], ethanol (CH_3CH_2OH, 99.9%), urea (CH_4N_2O), boric acid (H_3BO_3, ≥ 99.5%), thiourea (CH_4N_2S, > 99%), ammonia (NH_3, 25 wt%), formaldehyde (HCHO, 37-41 w/v%), D-glucose ($C_6H_{12}O_6.H_2O$, > 99%), isopropanol (C_3H_8O, ≥ 99%), sodium hydroxide pellets (NaOH, 98%), methanol (CH_3OH, 99.8%), acetonitrile (HPLC grade, CH_3CN, 99.8%) and methanol (HPLC grade, CH_3OH, 99.7%) were purchased from Merck. All these chemicals were used as received without any further purification.

3.2 Preparation of TiO_2 based catalysts

All the titanium oxide based photocatalysts were prepared by precipitation or coprecipitation method.

3.2.1 Preparation of TiO_2

Titanium tetra isopropoxide was used as precursor of titanium oxide. The titanium tetra isopropoxide solution was prepared by dissolving requisite amount in isopropanol under continuous stirring for 10 min. Then, aqueous ammonia (25 wt %) was added dropwise to the titanium tetra isopropoxide solution until complete precipitation occurred. The resultant mixture was stirred for 2 h at room temperature. Thereafter it was placed in a water bath for overnight at 90 °C. The precipitate was filtered and washed repeatedly. The precipitate was dried at 100 °C for 24 h and finally calcined at 450 °C for 3 h. The sample is denoted as TiO_2 in the text.

3.2.2 Preparation of cerium and nonmetal doped TiO_2

The cerium nitrate hexahydrate was used as the precursor for cerium. The requisite amount of nitrate salt was dissolved in deionized water to prepare the corresponding solution. The cerium nitrate solution and aqueous ammonia were simultaneously

Footer Page TH-1334_08610706

added dropwise to the solution of titanium tetra isopropoxide under continuous stirring. Addition of ammonia was continued until the precipitation was complete. Thereafter, similar steps were followed as used in case of preparation of titanium dioxide sample. Stirring of mixture for 2 h at room temperature was followed by keeping in a water bath for overnight at 90 °C. The obtained precipitate was filtered, dried and calcined at 450 °C for 3 h as described earlier. The preparation steps for Ce_xTiO_2 samples are shown in Fig.3.1. The cerium amount was varied in the range of 0.5 to 9 at.%. The samples were denoted as Ce_xTiO_2 where x= 0.5, 2.5 and 9.0 at.%.

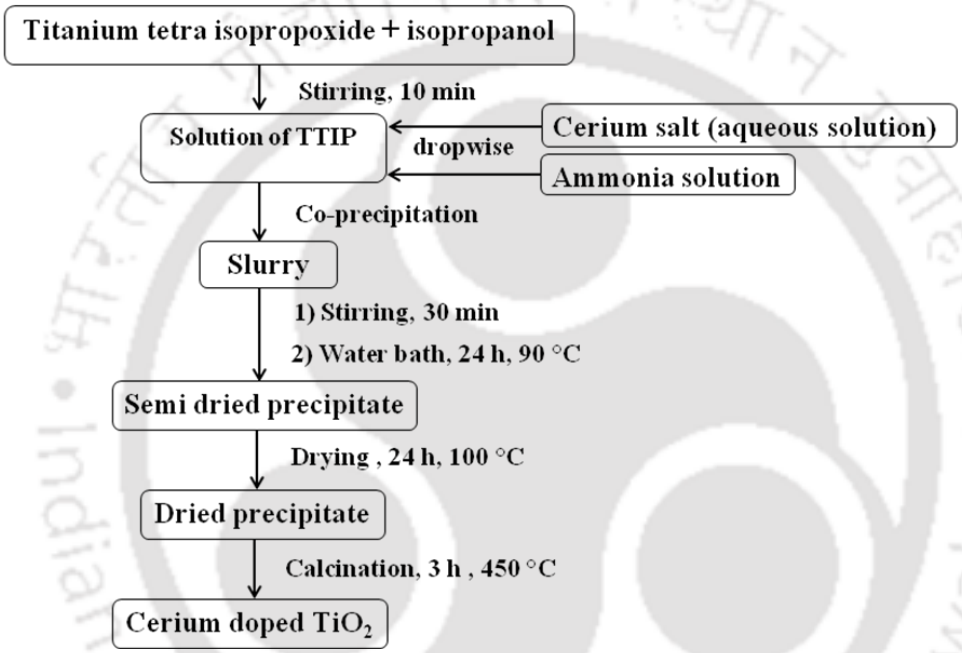

Fig.3.1. Steps for preparation of cerium doped TiO_2

To study the effect of calcination temperature the $Ce_{2.5}$-TiO_2 containing 2.5 at % cerium, was calcined at different calcination temperatures (350, 550, 650 and 750 °C). For preparation of cerium and nonmetals codoped samples boric acid, glucose, urea and thiourea were used as precursors for incorporation of B, C, N and S respectively. The aqueous solution containing requisite amount of cerium nitrate and nonmetal precursors were added dropwise along with ammonia solution to titanium tetra isopropoxide solution for co-precipitation. The subsequent steps were similar as described earlier. The preparation steps for Ce-NM-TiO_2 samples are shown in Appendix A (Fig.A.1). The loadings for Ce and nonmetals were 2.5 and 1 at.% of titanium respectively. The loadings of Ce (x) and nonmetals (y) are defined as

Footer Page TH-1334_08610706

$x = \frac{Ce(at.)}{Ti(at.)} \times 100 = 2.5$ at.% and $y = \frac{NM(at.)}{Ti(at.)} \times 100 = 1$ at.%. In text the codoped samples are referred as Ce-NM-TiO_2 where NM = B, C, N or S.

3.2.3 Preparation of transition metal and nitrogen doped TiO_2

For preparation of transition metal doped titanium dioxide catalysts iron nitrate nonahydrate, copper nitrate trihydrate and nickel nitrate hexahydrate were used as precursors for Fe, Cu and Ni respectively. In this case aqueous solution of respective metal nitrate was prepared. The metal nitrate solution and aqueous ammonia was added to titanium tetra isopropoxide solution for co-precipitation. The resultant mixture was stirred continuously for 30 min. Thereafter, the reaction mixture was transferred to a round bottom flask and refluxed for 6 h at 70 °C. The obtained wet precipitate was filtered, washed and dried at 120 °C for 24 h followed by calcination at 550 °C for 3 h. The preparation steps for transition metal doped TiO_2 samples are shown in Fig.3.2. The loading of transition metals was maintained at 2.5 at.%. Based on the transition metals used, the samples were designated as M-TiO_2 (M= Cu, Fe, Ni).

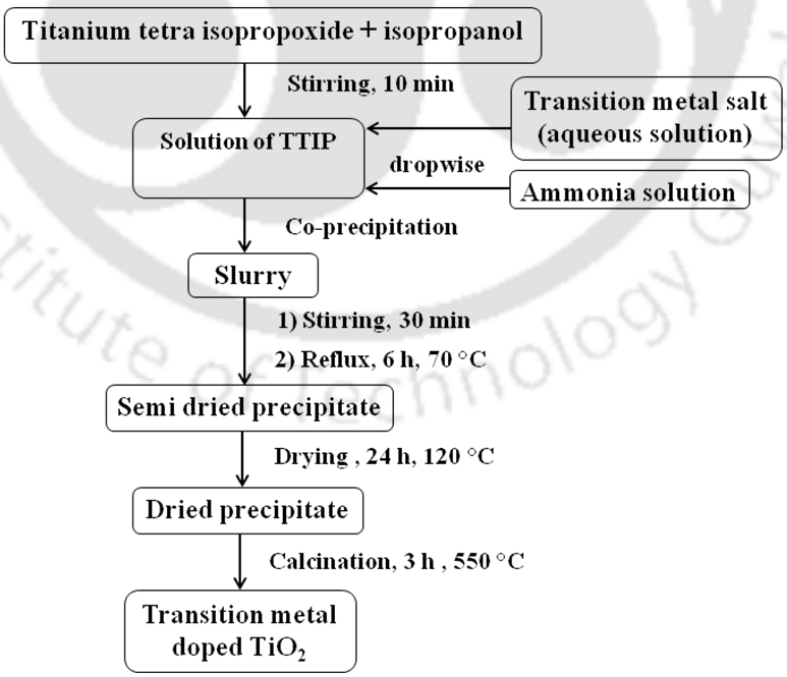

Fig.3.2. Steps for preparation of transition metal doped TiO_2

Footer Page TH-1334_08610706

For preparation of transition metal and nitrogen codoped catalysts requisite amount of urea was added as nitrogen precursor to the solution containing respective metal nitrate salt. This aqueous solution was used for coprecipitation from titanium tetra isopropoxide solution followed by aging, filtration, washing, drying and calcination of the precipitate as described for transition metal doped titanium dioxide catalysts. The loading of transition metals was 2.5 at.%, whereas nitrogen was 1 at.%. The preparation steps for transition metal and nitrogen codoped TiO_2 samples are shown in Appendix A (Fig.A.2).The transition metal and nitrogen codopedTiO_2 samples were designated as M-1N-TiO_2 (M= Cu, Fe, Ni). For comparison, N doped TiO_2 was prepared using similar procedure without the addition of any transition metal precursor in aqueous solution.

The photocatalysts containing copper and different amount of nitrogen were prepared keeping the copper amount at 2.5 at.%, where as nitrogen amount was varied from 0.5 to 1.5 at.%. The preparation procedure was same as preparation of copper and nitrogen codoped catalyst. The amount of urea was varied to vary the nitrogen content. These codoped samples were represented as Cu-xN-TiO_2 where x is 0.5, 1 or 1.5 at.% loading of nitrogen.

3.3 Preparation of In_2O_3 based catalysts

All the indium oxide based catalysts were prepared by precipitation or co-precipitation.

3.3.1 Preparation of In_2O_3

The required amount of indium nitrate was dissolved in deionized water under stirring condition for about 30 min. Then, sodium hydroxide solution (0.3 mol/l) was added to the nitrate solution until precipitation was complete. The obtained solution was transferred to a round bottom flask, attached to a condenser, and aged at 80 °C for 5 h. After washing and filtration, the precipitate was dried at 100 °C overnight and calcined at 550 °C for 4 h to obtain the indium oxide sample. It is denoted as ‘In’ in text.

Footer Page TH-1334_08610706

3.3.2 Preparation of indium-titanium coupled oxide

For preparation of indium-titanium coupled oxides, aqueous solution containing required amount of indium nitrate was added drop wise to the titanium tetra isopropoxide solution and stirred for 30 min. Thereafter, precipitation was carried out by addition of sodium hydroxide solution. The subsequent steps were similar as used for preparation of indium oxide. The preparation steps for indium-titanium coupled oxide samples are shown in Fig.3.3. The indium amount was varied as 5, 10 and 16 at.% and the corresponding samples are designated as 5% In-Ti, 10% In-Ti and 16% In-Ti respectively in text.

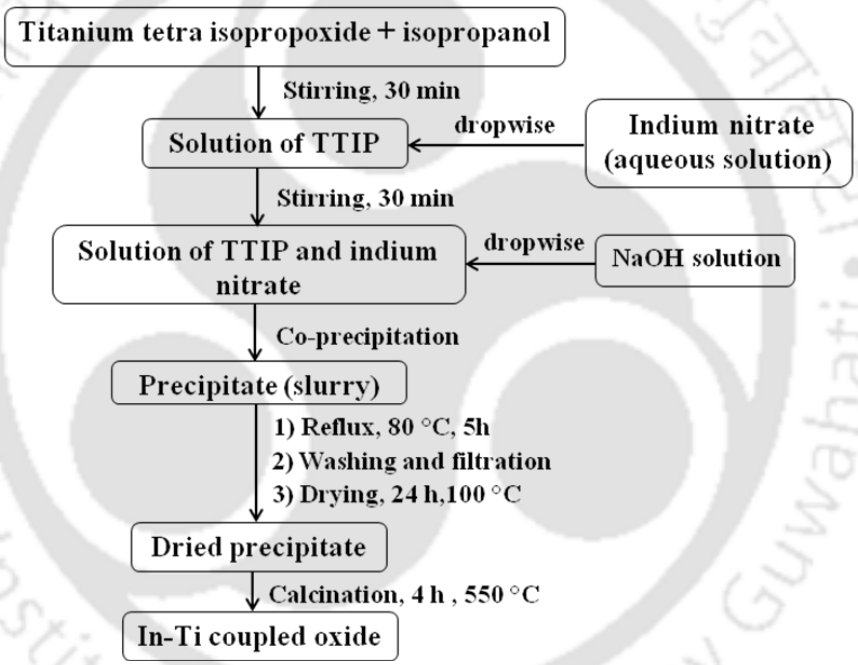

Fig.3.3. Steps for preparation of indium-titanium coupled oxide

3.3.3 Preparation of copper doped indium-titanium oxide

The ternary system containing copper-indium and titanium oxides was also prepared using co-precipitation technique. The indium nitrate solution was added drop wise to the titanium tetra isopropoxide solution and was stirred continuously for 30 min. Thereafter, aqueous solution containing required amount of copper nitrate and D-glucose (0.1 mol/l) was added slowly to the above solution of isopropoxide and

Footer Page TH-1334_08610706

indium nitrate. The precipitation was carried out by addition of sodium hydroxide solution and slurry was aged for 5 h at 80 °C. Subsequent steps such as filtration, washing, drying and calcination were similar as used for preparation of indium oxide. The preparation steps for copper doped indium-titanium coupled oxide samples are shown in Appendix A (Fig.A.3). The sample is designated as 2%Cu-10%In-Ti in text containing 2 at.% Cu and 10 at.% In.

3.3.4 Preparation of indium-transition metal coupled oxide

The indium and transition metal coupled oxides were prepared from the aqueous solutions of indium nitrate and metal nitrates. Required amount of transition metal precursor was first dissolved in deionized water and stirred for 30 min. Then, the metal nitrate solution was added to the aqueous solution of indium nitrate under stirring condition for well mixing. The co-precipitation was carried out using sodium hydroxide solution (0.3mol/l). The precipitate was treated similarly as done for indium oxide preparation. The preparation steps for indium-transition metal coupled oxide samples are shown in Fig.3.4. The samples were abbreviated as In-TM, where TM= Cu, Ni, Zn. In case of preparation of In-Cu, D-glucose (0.1 mol/l) was added to aqueous solution of copper nitrate.

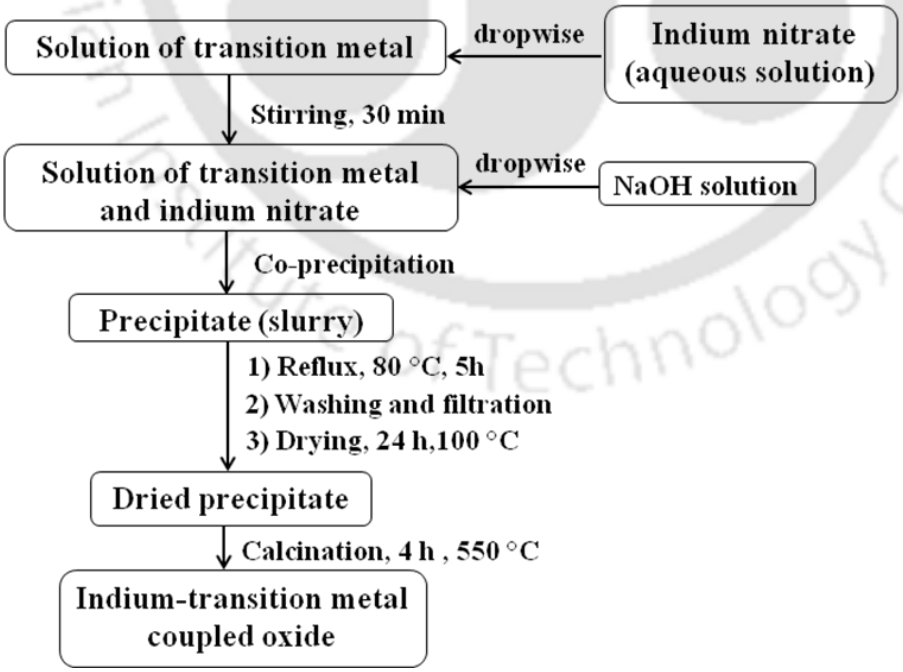

Fig.3.4. Steps for preparation of indium-transition metal coupled oxide

Footer Page TH-1334_08610706

3.4 Characterization of catalysts

3.4.1 BET surface area and pore size measurements

The surface area of the samples was determined from N_2 isotherms collected at 77 K using a Beckman-Coulter SA^{TM} 3100 analyzer. The sample tube was loaded with about 0.5-1.0 g of the photocatalyst. Prior to the experiment, the sample was degassed at 423 K for a period of 2 h. High purity nitrogen was used as adsorbate at liquid nitrogen temperature for adsorption experiments. The pore size distribution of the photocatalysts was determined from desorption branch of the isotherm using Barrett-Joyner-Halenda (BJH) method.

3.4.2 X-ray diffraction studies

The X-ray diffraction (XRD) patterns of the various samples were recorded on a Bruker D2 phaser X-ray diffractometer using Ni filtered Cu K_α as radiation source (λ=1.5406 Å) in the 2θ range from 20 to 80° at a scanning rate of 1°/min with a step size of 0.02°/s. A beam voltage and beam current of 40 kV and 40 mA were used respectively.

3.4.3 Field emission scanning electron microscopic studies

Field emission scanning electron microscopic analysis was done using instrument of Zeiss-Sigma. For analysis samples were prepared as follows. The samples were dispersed in a solvent and sonicated for about15 min. Then a drop of suspension of sample was deposited on an aluminum foil which was mounted on a sample holder for gold coating. Gold coated sample was used for analysis.

3.4.4 Energy dispersive X-ray spectroscopic analysis

The composition of the samples was determined by EDS analysis (Energy Dispersive X-Ray Spectroscopy) equipped with SEM instrument (LEO 1430 VP). The powder sample was deposited on a carbon tape, followed by gold coating and then was mounted on the sample holder. The analysis was performed at three different locations and the average result was used.

Footer Page TH-1334_08610706

3.4.5 UV-Visible diffuse reflectance absorption studies

The diffuse reflectance UV-Vis spectra of the photocatalysts were measured on a Perkin Elmer Lambda 750 instrument equipped with a 60 mm labsphere specular reflectance accessory at room temperature. The baseline correction was done using a calibrated sample of barium sulfate as reference. The scan parameter was set with slit size 2 nm and scan in the spectral range of 250-650 nm.

3.4.6 Photoluminescence spectroscopic analysis

The photoluminescence (PL) measurements were performed in a Thermo Spectronic (Aminco Bowman Series 2) instrument with a Xe lamp as the excitation source at room temperature. The sample powder was dispersed in ethanol followed by sonication for 15 min. The emission spectra were collected at an excitation wavelength of 325 nm. The same quantity of sample amount was used for recording PL spectra of all the samples. The entrance and exit slit widths were fixed as same for all the measurements.

3.5 Photocatalytic studies

3.5.1 Experimental setup and procedure

Photocatalytic activity studies were carried out in a three necked round bottom flask, used as the reactor, and placed in a water bath with water circulation arrangements as shown in Fig.3.5. The photocatalytic reaction was typically carried out by adding 0.2 g of catalyst to aqueous solution of methanol under stirred condition if not specified otherwise. Aqueous methanol solution typically consisted of 25 ml water and 1 ml methanol. Before irradiation, the reaction mixture was de-aerated with N_2 gas (50 ml/min) for 30 min to completely remove the dissolved oxygen. Then the reaction mixture was irradiated with a 500 W tungsten halogen lamp (Halonix, India) as source of visible light. The lamp was placed approximately 15 cm away from the reactor. The emission spectrum of the lamp was measured in front of the reactor using Ocean optics USB4000 spectrometer. The emission spectrum of the used lamp is shown in Fig.3.6. As can be observed from Fig 3.6, the percentage of UV light in emission spectrum is negligible. Hence no UV filter was used. The temperature of the reaction

Footer Page TH-1334_08610706

mixture was maintained at 34 °C using a water circulation bath, which also acted as an IR filter. The evolved gas was collected in an inverted burette by water displacement method. The products were analyzed using gas chromatograph equipped with thermal conductivity and flame ionization detector and high performance liquid chromatography (HPLC).

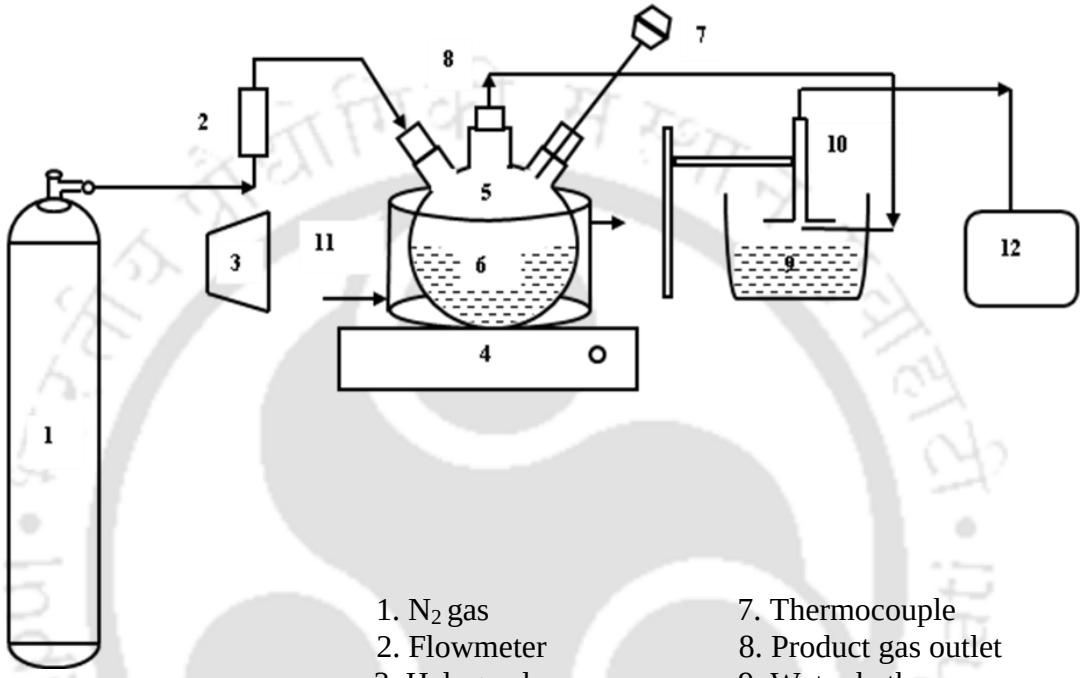

1. N_2 gas
2. Flowmeter
3. Halogen lamp
4. Magnetic stirrer
5. Reactor
6. Reactant mixture
7. Thermocouple
8. Product gas outlet
9. Water bath
10. Gas collector
11. Cooling water inlet
12. Gas Chromatograph

Fig.3.5. Schematic representation of experimental setup

Blank experiments were conducted, in absence of light with presence of catalyst and also in presence of light without any catalyst. In both cases no hydrogen evolution was observed. The hydrogen evolution was observed only when reaction was carried out in presence of both light and catalyst. In both cases same feed mixture was used.

Footer Page TH-1334_08610706

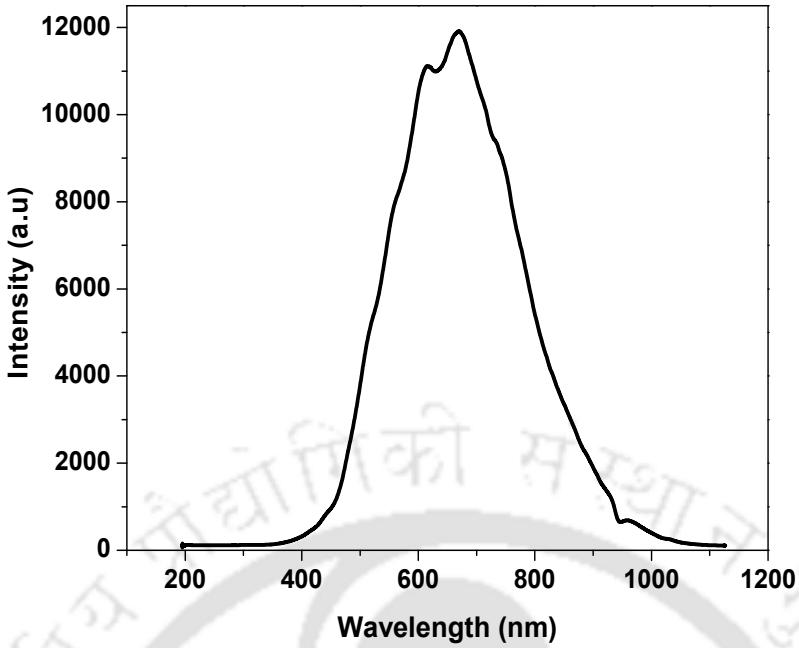

Fig.3.6. Emission spectrum of 500 W tungsten halogen lamp

The effect of operational parameters such as light intensity, catalyst amount, alcohol type and irradiation time was investigated. The hydrogen production activity of the catalyst was investigated at different light intensities in the range of 5000 to 25600 lux. In order to achieve different light intensities, a rheostat (1 kΩ) was used to vary the input current. The varying input current was monitored by ammeter (0-5 A). The light intensity of the lamp was measured using a lux meter (Lutron LX101) at a distance of 15 cm from the lamp at the position of reactor. The hydrogen production activity of the catalyst was investigated at different catalyst amount in the range of 0.1 to 1.0 g. The effect of type of alcohol on photocatalytic activity of catalyst was studied using methanol, ethanol and propanol. The photocatalytic efficiency of catalyst was evaluated for a period of 10 h of irradiation time to investigate the durability of the catalyst.

For kinetic analysis, the experiments were carried out using different concentration of methanol (2.3, 4.1, 5.1 and 7.4 mol/l). During the irradiation period, the gas phase sample was withdrawn at every 10 min for duration of 60 min at photoreactor outlet. The liquid phase products were analyzed, by taking an aliquot after every 10 min, for the detection of intermediates (formaldehyde and formic acid) and unconverted methanol. Before starting the photoreaction experiments, the lamp was switched on

Footer Page TH-1334_08610706

for about 20 min to achieve stable and constant light intensity during the irradiation period. The reaction mixture was kept under constant stirred condition to maintain uniform suspension and minimize any effect of external mass transfer resistance. Since the catalysts were in form of fine powder effect of internal mass transfer resistance can be neglected.

3.5.2 Product analysis

Gas chromatographic analysis

The gaseous products were analyzed using a gas chromatograph (Varian CP 3800 or Nucon 5765) equipped with carbosieve SII column and thermal conductivity detector. Nitrogen was used as the carrier gas with a flow rate of 20 ml/min. The oven temperature, detector temperature and injection temperature were 35 °C (isothermal), 200 °C and 75 °C, respectively. The unconverted methanol was analyzed using Nucon 5765 with capillary column (CP Sil 8 CB) and flame ionization detector. Temperature of injector, oven, and detector were 80, 200 and 150 °C, respectively.

High performance liquid chromatographic analysis

The liquid samples were analyzed for the detection of intermediates (formaldehyde and formic acid) by HPLC (Shimadzu, C18 column). The sample volume was fixed at 10 μl and the mobile phase was acetonitrile-water (60:40 v/v) with a flow rate of 1ml/min. Three injections were performed for each sample to confirm the reproducibility of retention time and the peak area values.

Calibration curves were initially determined for both gas chromatograph and high performance liquid chromatograph and used for quantitative determination of products. The calibration plots are given in Appendix B.

Footer Page TH-1334_08610706

Chapter 4

Results and Discussion

4.1 Preliminary studies

4.1.1 Effect of stirring

The effect of external mass transfer resistance on hydrogen production, if any, was determined by measuring the hydrogen evolution at different stirring conditions. Three different stirring conditions were selected with increasing stirring speed. In the used instrument, position 1, position 5 and position 10 were chosen and experiments were carried out. The stirring speeds of the three positions were in the order of position 1 < position 5 < position 10. The hydrogen production at three stirring positions is presented in Fig.4.1. It was observed that, the rate of hydrogen evolution as a function of irradiation time did not change in the range of stirring speed used. The result suggested that the external mass transfer resistance can be neglected in presence of stirring. For all studies the stirring position of 5 was used. The internal mass transfer resistance can also be neglected as the catalyst was used in form of fine powder.

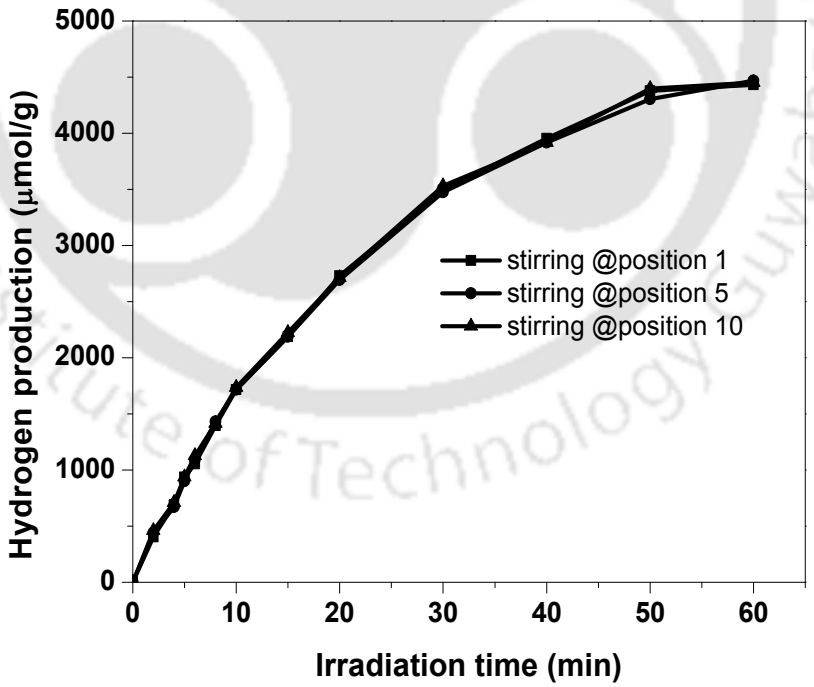

Fig.4.1. Hydrogen production at different stirring conditions

Footer Page TH-1334_08610706

4.1.2 Variation of light intensity

Fig.4.2 shows the profile of light intensities determined as a function of time. The light intensity of the lamp was measured using the Lutron LX-101 luxmeter. The light source (500 W tungsten halogen lamp) was positioned approximately at a distance of 15 cm away from the luxmeter and the measurements were taken as a function of time. From the results it can be observed that, for the first 10 min the light intensity gradually increased with increase in the irradiation time and thereafter, reached a maximum of 25600 lx and was stabilized. Hence, before starting the photocatalytic reactions, the lamp was switched on for about 20 min to achieve the stable light intensity. All the photocatalytic reactions were performed at condition of stable light intensity condition unless otherwise mentioned.

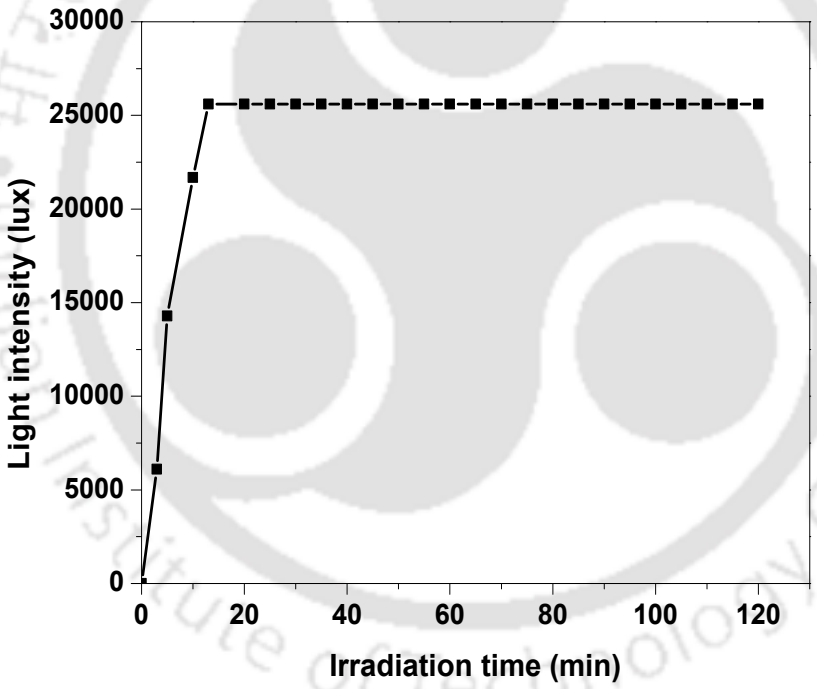

Fig.4.2. Light intensity profile as function of time

Footer Page TH-1334_08610706

4.2 Cerium doped titania

4.2.1 Effect of cerium loading

The cerium loading was varied in the range of 0.5 to 9 at.%.

Characterization of photocatalysts

The surface area and pore volumes of undoped TiO_2 and Ce_xTiO_2 (x = 0.5, 2.5 and 9 at.%) are shown in Table 4.1. Surface area and pore volume of titania decreased with addition of ceria. Structure modification and partial pore blockage in presence of cerium may be responsible for decrease in surface area and pore volume. Among Ce doped TiO_2 samples, surface area of $Ce_{2.5}TiO_2$ was highest. The isotherm of $Ce_{2.5}TiO_2$ and corresponding pore size distribution are shown in Fig.4.3. The $Ce_{2.5}TiO_2$ sample exhibited a type IV isotherm with a H1 type hysteresis loop associated with open-ended cylindrical pores (Rouquerol et al., 1999, Sing et al., 1985). The pore size distribution of $Ce_{2.5}TiO_2$ showed the presence of both mesopores and macropores with pore diameter in the range of 3-148 nm.

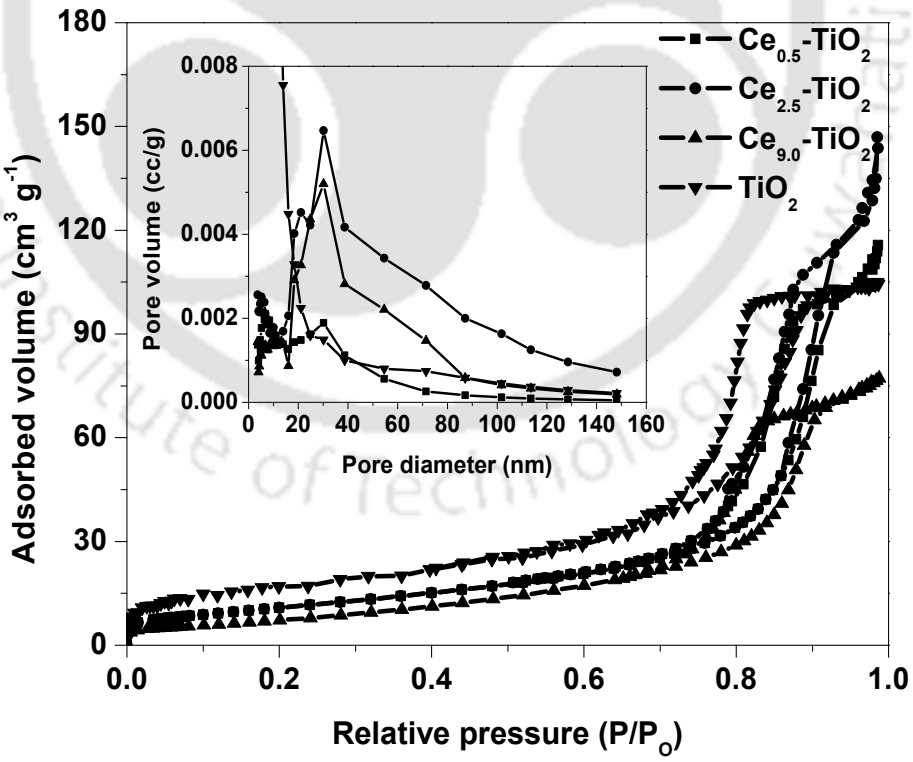

Fig.4.3. N_2 adsorption-desorption isotherms of Ce_x-TiO_2 and TiO_2 (inset: pore size distribution)

Footer Page TH-1334_08610706

The actual composition of the prepared photocatalysts was determined by EDS and results are shown in Table 4.2 and 4.3. The actual cerium content in samples were determined to be 0.23, 2.45 ad 8.28 at.% for $Ce_{0.5}$-TiO_2, $Ce_{2.5}$-TiO_2 and $Ce_{9.0}$-TiO_2, respectively. Thus, the actual composition was in agreement with the intended composition of the photocatalysts within experimental error.

Table 4.1. Surface area, pore volume and lattice parameters for undoped TiO_2 and Ce_xTiO_2

Samples	BET surface area (m^2/g)	Pore volume cc/g	Lattice parameters Anatase		Lattice distortion	d spacing (Å)
			a (Å) (101)	c (Å) (004)		
TiO_2	84	0.45	3.7435	9.4217	0.378	3.4790
$Ce_{0.5}$-TiO_2	26	0.08	3.7579	9.4712	0.346	3.4930
$Ce_{2.5}$-TiO_2	70	0.36	3.7451	9.4599	0.268	3.4822
$Ce_{9.0}$-TiO_2	41	0.19	3.7804	9.5421	0.632	3.5147

Table 4.2. Energy Dispersive X-Ray Spectroscopic analysis for undoped TiO_2 and Ce_xTiO_2

Sample name	Elements (at.%)		
	Ce	Ti	O
TiO_2	–	39.26	60.74
$Ce_{0.5}$ -TiO_2	0.12	52.08	47.80
$Ce_{2.5}$-TiO_2	1.05	42.83	56.12
$Ce_{9.0}$-TiO_2	1.95	23.53	74.52

Footer Page TH-1334_08610706

Table 4.3. Comparison between the actual and intended composition for Ce_xTiO_2

Sample name	Actual composition (at.%)	Intended composition (at.%)
	Cerium(x)[a]	Cerium(x)[a]
$Ce_{0.5}$ -TiO_2	0.23	0.5
$Ce_{2.5}$-TiO_2	2.45	2.5
$Ce_{9.0}$-TiO_2	8.28	9.0

(a) $x = \frac{Ce(at)}{Ti(at)} \times 100$

The X-ray diffraction patterns of Ce doped TiO_2 samples (Fig.4.4) shows that all the doped samples were dominated by anatase phase (2θ = 25.5°, 37°, 48°, 53.8°, 55.1°, 64°, JCPDS 21-1272). For $Ce_{2.5}TiO_2$ both anatase and rutile phase (2θ = 28°, 36.1°, 41.5°, JCPDS 21-1276) were observed. The intensity of the anatase peak (101) decreased with increase in cerium concentration suggesting decrease in crystallinity of the material. No characteristic peaks of CeO_2 phase were observed in the XRD profiles, which suggested that the ceria was in well dispersed state. In addition, no peaks due to any Ce-Ti mixed oxides were observed in any samples. On addition of cerium oxide to TiO_2, cerium ions can substitute Ti^{4+} sites (Saliby et al., 2011) or can occupy the interstitial sites (Yu et al., 2010, Reddy et al., 2003) with Ce-O-Ti linkages. But this is expected to be associated with distortion in titania lattice due to larger size of Ce^{4+} (IR = 0.101 nm) and Ce^{3+} (IR = 0.111 nm) compared to Ti^{4+} (IR=0.068 nm) ions. The distortion is expected to increase with cerium content and become significant at very high loading. This is confirmed by the lattice distortion values given in Table 4.1, which shows larger distortion for higher cerium loaded samples. The detail calculation of lattice parameters and lattice distortion is given in Appendix C.

Footer Page TH-1334_08610706

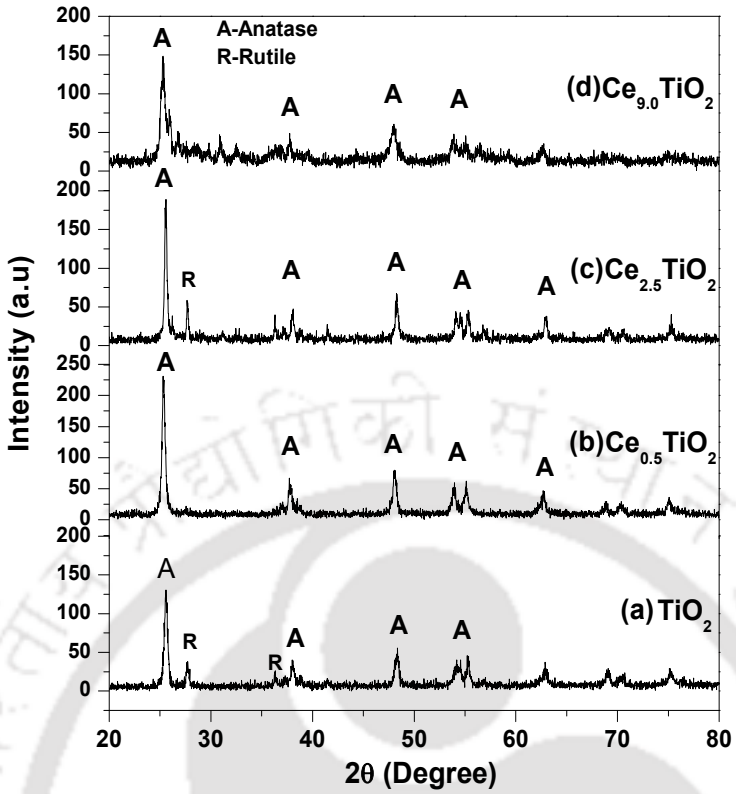

Fig.4.4. XRD patterns of undoped TiO_2 and Ce_xTiO_2

The UV-visible absorption spectra of TiO_2 and Ce_xTiO_2 are shown in Fig.4.5 (A). All the cerium doped TiO_2 samples showed intense absorption bands in the visible light region ranging from 400 to 500 nm. The Kubelka-Munk plots of Ce_x-TiO_2 samples are shown in Fig.4.5 (B). The band gap values calculated using the Kubelka-Munk method were 3.01 eV (TiO_2), 2.95 eV ($Ce_{0.5}$-TiO_2), 2.85 eV ($Ce_{2.5}$-TiO_2) and 2.15 eV ($Ce_{9.0}$-TiO_2). The detail of band gap energy calculation by Kubelka-Munk method is included as Appendix D. The decreased band gap energy values of cerium doped samples indicated formation of new energy levels within the TiO_2 band gap and resulted in red-shift of the absorption edge (Chen and Burda, 2004). This shift can be attributed to incorporation of Ce 4f levels into the TiO_2 crystal structure just below the conduction band of TiO_2 and thereby reducing the effective bandgap (Magesh et al., 2009). At higher loading significant visible light absorption was observed.

Footer Page TH-1334_08610706

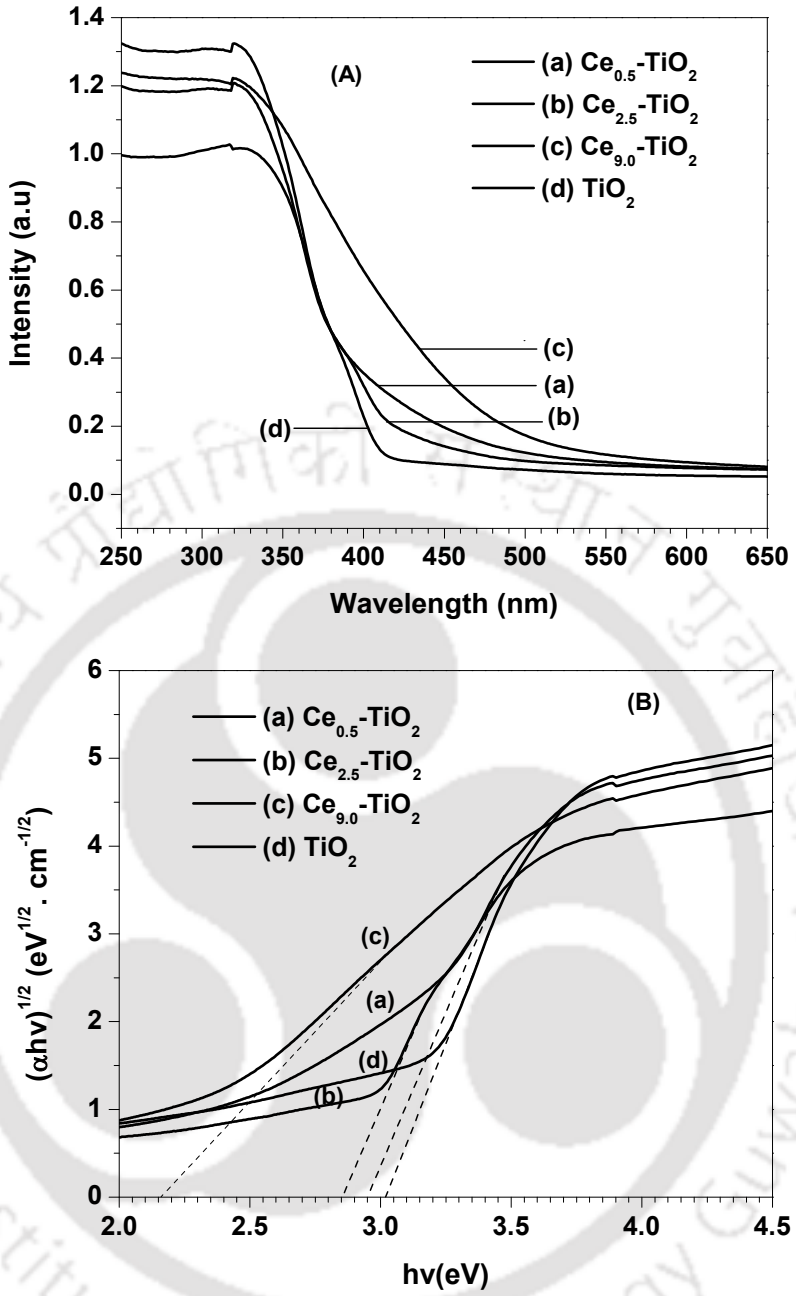

Fig.4.5. (A) UV-Visible diffuse reflectance spectra (B) Kubelka-Munk plot for undoped TiO_2 and Ce_x-TiO_2

The radiative recombination of electron-hole pairs in photocatalysts can be studied by the photoluminescence (PL) emission spectra. Fig.4.6 shows the room temperature photoluminescence spectra of the Ce_xTiO_2 catalysts in the range of 350-600 nm. For all the samples, six emission peaks appeared at 360, 396, 450, 468, 481 and 492 nm wavelengths and the corresponding transition energy were 3.44, 3.13, 2.76, 2.65, 2.8

Footer Page TH-1334_08610706

and 2.52 eV respectively. In literature the peak in the range of 360 -370 nm has been assigned to either anatase particle less than 10 nm (Li et al., 2004) or to self trapped excitons localized in TiO_6 octahedral (Hu et al., 2011). In this study the emission peak at 360 nm can be ascribed to the latter as particle were much larger than 10 nm. The emission signal at 396 nm (3.13 eV) corresponded to the band gap transition of the anatase (Li et al., 2004). This agrees well with the band gap energy of titania calculated from UV-Vis spectra. The excitonic emissions in titania result due to presence of defects and oxygen vacancies. The bands at 450 and 468 nm can be attributed to free excitons and emission peaks at longer wavelength of 481 and 492 nm can be attributed to the bound excitons (Yu et al., 2011, Zhang et al., 2002). The bound excitons results due to presence of oxygen vacancies (Yu et al., 2011, Wang et al., 2009, Selvam et al., 2012).

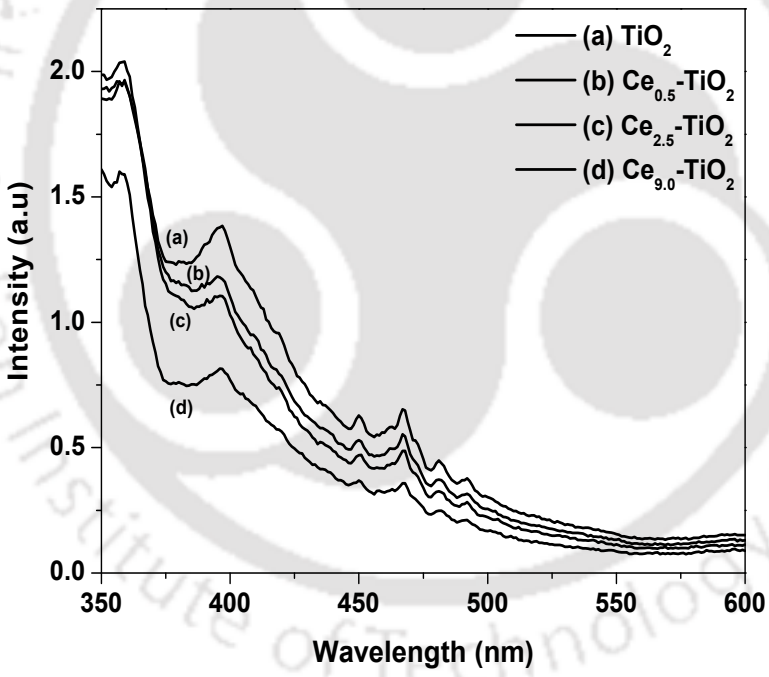

Fig.4.6. Photoluminescence spectra for undoped TiO_2 and Ce_xTiO_2

It can be observed from the Fig.4.6, that all the cerium doped TiO_2 showed lower PL intensity compared to TiO_2 implying increased separation efficiency of excitons in former. In cerium doped samples formation of Ce 4f electronic states into TiO_2 band structure, as discussed earlier, might serve as electron trap as represented by step 1

Footer Page TH-1334_08610706

and reduce the rate of electron-hole pair recombination. With increase in cerium loading the peak intensity decreased suggesting increased stability of electron and holes.

(1) $Ce^{4+} + e^{-} \rightarrow Ce^{3+}$

Photocatalytic activity studies

The photocatalytic activities of Ce_xTiO_2 (where x = 0.5, 2.5 and 9.0 at.%) and undoped TiO_2 samples for hydrogen production from water-methanol mixture shown in Fig.4.7. In visible light region, activity of undoped TiO_2 was very low but all the cerium doped TiO_2 showed significant photocatalytic activity and high hydrogen evolution. The H_2 evolution rate of the samples was in the order of $Ce_{2.5}TiO_2$ > $Ce_{0.5}TiO_2$ > $Ce_{9.0}TiO_2$ >> undoped TiO_2.

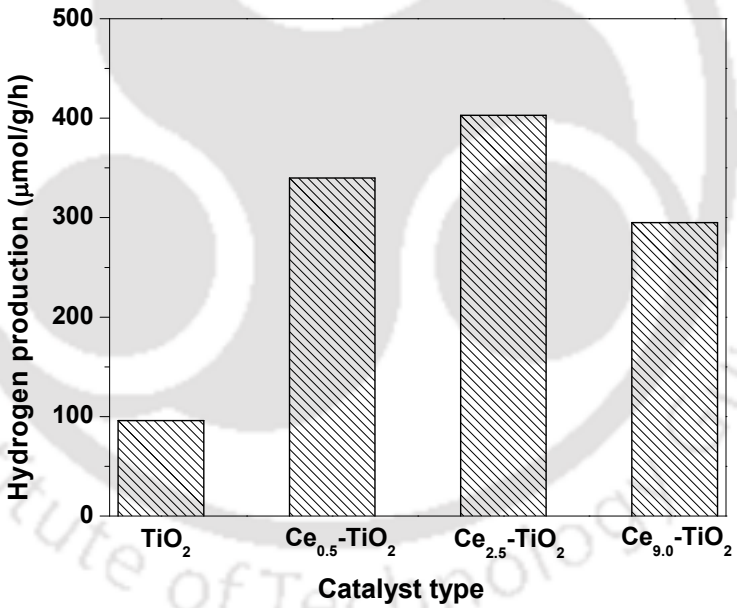

Fig.4.7. Hydrogen production for undoped TiO_2 and Ce_xTiO_2

The enhanced activity of cerium doped TiO_2 compared to undoped TiO_2 can be attributed to their ability of absorption of light in visible light region as shown in Fig.4.5 (A). Further, photoluminescence studies showed that addition of cerium into TiO_2 efficiently inhibited the recombination of photogenerated electron-hole pairs and this may have also contributed to higher activity of the cerium doped samples. The

Footer Page TH-1334_08610706

photocatalytic activity was increased with increase in the amount of cerium loading up to 2.5 at.% and decreased with the further increase of the cerium loading. The higher activity of $Ce_{2.5}TiO_2$ can be attributed to higher surface area. The higher surface area resulted in increased surface active sites and higher hydrogen evolution rate. The lower photocatalytic activity for catalyst with higher cerium loading of 9 at.% can be attributed mainly to lower surface area. The apparent quantum efficiency of the photocatalysts was calculated using the method followed by (Sasikala et al., 2008). The apparent quantum efficiency of TiO_2, $Ce_{0.5}$-TiO_2, $Ce_{2.5}$-TiO_2, and $Ce_{9.0}$-TiO_2 were 1.9, 6.8, 8.0 and 5.9 % respectively. The details of calculation are given in Appendix E.

Footer Page TH-1334_08610706

4.2.2 Effect of calcination temperature

To study the effect of calcination temperature $Ce_{2.5}TiO_2$ catalyst was calcined at four different calcination temperatures, 350, 550, 650 and 750 °C.

Characterization of photocatalysts

Fig.4.8. presents the XRD patterns of $Ce_{2.5}TiO_2$ calcined at different calcination temperatures. Pure anatase phase was observed for $Ce_{2.5}TiO_2$ calcined at 350, 550 and 650 °C, whereas both anatase and rutile phases were observed for sample calcined at 750 °C. The sharpness and intensity of peaks increased with increase in calcination temperature indicating enhancement of crystallinity.

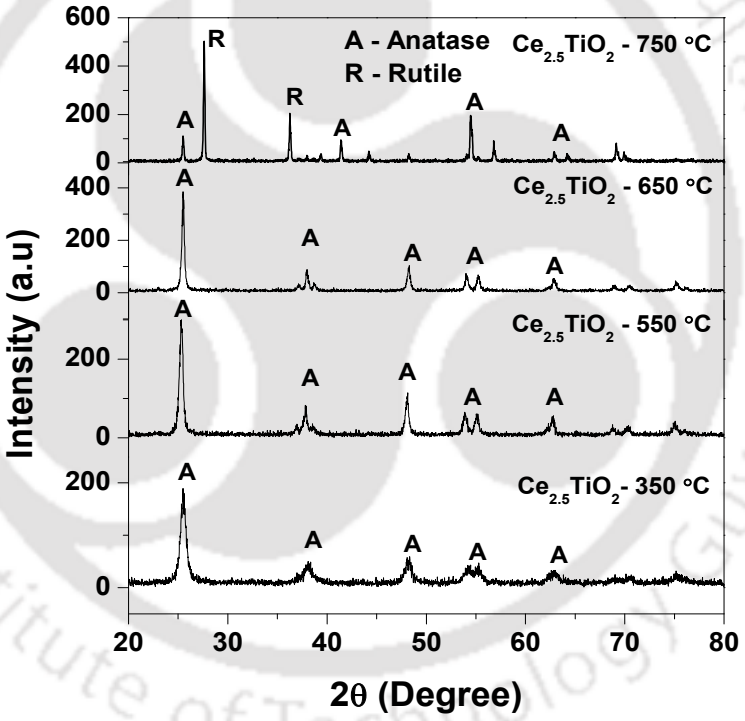

Fig.4.8. XRD patterns of $Ce_{2.5}TiO_2$ at different calcination temperatures

Fig.4.9. shows the hydrogen production for $Ce_{2.5}TiO_2$ photocatalysts prepared at different calcination temperatures. With increase in calcination temperature from 350 to 650 °C, the hydrogen production increased from 281 to 549 µmol/g/h. Further increase in the calcination temperature to 750 °C decreased the hydrogen production

Footer Page TH-1334_08610706

to 460 µmol/g/h. The increased hydrogen production can be attributed to higher crystallinity of the material. At 750 °C, the lower photoactivity may be due to the larger crystallite size and predominant rutile phase (85.2 %). The phase distribution of $Ce_{2.5}TiO_2$ calcined at different temperature is presented in Table 4.4.

Table 4.4. Hydrogen production and phase distribution of $Ce_{2.5}TiO_2$ catalyst calcined at different temperatures

Calcination temperature (°C)	H_2 evolution (µmol/g/h)	X_A (%)	X_R (%)
350	281	100	-
550	523	100	
650	549	100	
750	460	14.79	85.21

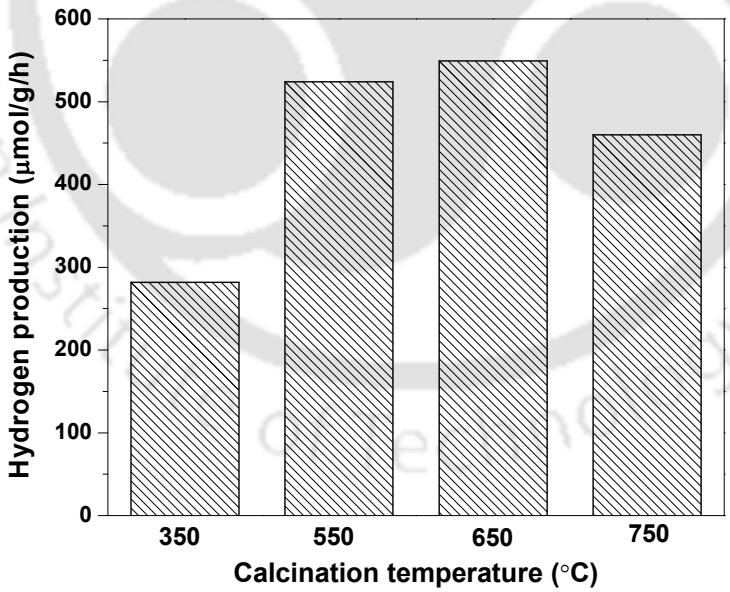

Fig.4.9. Hydrogen production for $Ce_{2.5}TiO_2$ at different calcination temperatures

Footer Page TH-1334_08610706

4.2.3 Effect of cerium and nonmetal codoping

Among different doped Ce_xTiO_2 catalysts (x = 0.5, 2.5 and 9.0 at.%), highest hydrogen production was obtained for $Ce_{2.5}$-TiO_2 sample. Therefore, the optimum loading amount of 2.5 at.% cerium was selected to investigate the effect of codoping of nonmetals on hydrogen production.

Characterization of photocatalysts

The surface area and pore volumes of undoped TiO_2, Ce-TiO_2, Ce-NM-TiO_2 (NM = B, C, N, S) samples are shown in Table 4.5. Surface area and pore volume of titania decreased with addition of ceria. Structure modification and partial pore blockage in presence of cerium may be responsible for decrease in surface area and pore volume in cerium doped samples. The isotherm of Ce-TiO_2 and corresponding pore size distribution are shown in Fig.4.10 (a). The Ce-TiO_2 sample exhibited a type IV isotherm with a H1 type hysteresis loop associated with open-ended cylindrical pores. The pore size distribution of Ce-TiO_2 showed the presence of both mesopores and macropores with pore diameter in the range of 3-148 nm. The codoped Ce-N-TiO_2, Ce-C-TiO_2 and Ce-B-TiO_2 exhibited Type II isotherm with H3 hysteresis loop corresponding to slit-shaped pores (Fig.4.10 (b)). For sulphur codoped sample H1 hysteresis loop was observed, which indicated presence of open cylindrical pores. Codoping of titania with nonmetals and cerium resulted in increase in surface area for Ce-B-TiO_2 and Ce-N-TiO_2 but surface area decreased for Ce-C-TiO_2 and Ce-S-TiO_2 as shown in Table 4.5. Fig.4.10 (b) shows that the pore size distribution varied significantly with nonmetals. For Ce-N-TiO_2 and Ce-B-TiO_2, narrow pore distribution was obtained, with 39 % and 47 % pores being below 10 nm respectively. The pore size distributions of Ce-C-TiO_2 and Ce-S-TiO_2 codoped samples were much broader. The presence of significant amount of pores in the range of 20-50 nm may have contributed to their lower surface area. The surface area and pore size distribution results showed that the presence of type of nonmetal had significant effect on formation of porous network. The significant stabilization effect was observed for Ce-N-TiO_2 resulting in highest surface area.

The actual composition of the prepared photocatalysts was determined by EDS and results are shown in Table 4.6. The actual cerium content in samples varied in the range of 2.39-2.49 at.% and nonmetal content varied in the range of 0.8 to 0.97 at.%.

Footer Page TH-1334_08610706

The intended composition of cerium and nonmetals were 2.5 and 1 at.%, respectively. Thus, the actual composition agreed well with the intended composition of the photocatalysts within experimental error.

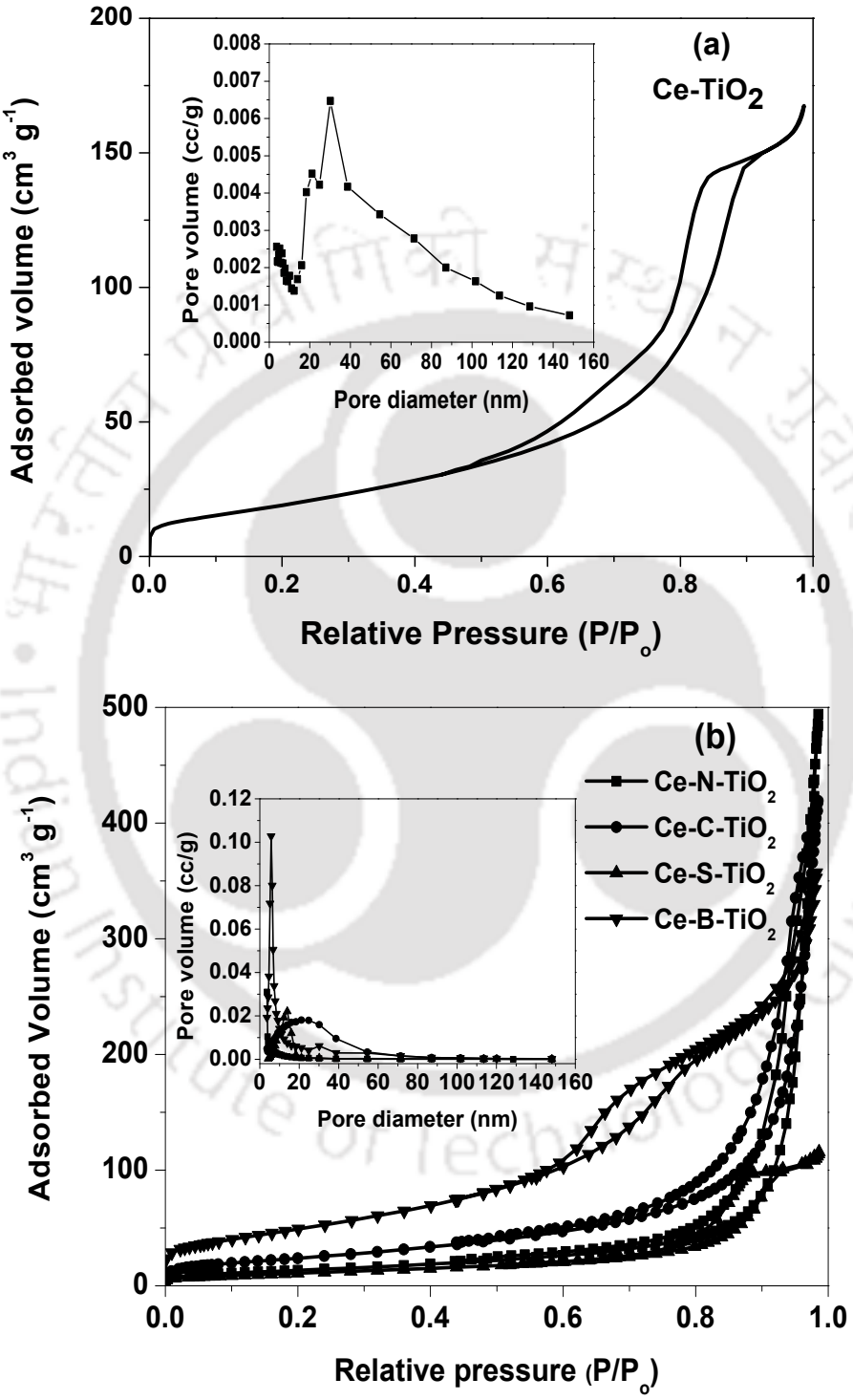

Fig.4.10. N_2 adsorption-desorption isotherms for (a) Ce-TiO_2 (b) Ce-NM-TiO_2 (NM = B, C, N, S) (inset: pore size distribution)

Footer Page TH-1334_08610706

Table 4.5. Surface area, pore volume and lattice parameters for undoped TiO_2, Ce-TiO_2, Ce-NM-TiO_2 (NM = B, C, N, S)

Samples	BET surface area (m^2/g)	Pore volume cc/g	Lattice parameters Anatase		Lattice distortion	d spacing (Å)
			a (Å) (101)	c (Å) (004)		
TiO_2	84	0.45	3.7435	9.4217	0.378	3.4790
Ce-TiO_2	70	0.36	3.7451	9.4599	0.268	3.4822
Ce-B-TiO_2	87	0.57	3.7907	9.5197	0.271	3.5128
Ce-C-TiO_2	53	0.67	3.7659	9.5080	0.387	3.5013
Ce-N-TiO_2	158	0.06	3.7936	9.7181	0.301	3.2240
Ce-S-TiO_2	39	0.18	3.7727	9.7014	1.391	3.5174

Table 4.6. Energy Dispersive X-Ray Spectroscopic analysis and composition for undoped TiO_2, Ce-TiO_2, Ce-NM-TiO_2 (NM = B, C, N, S)

Sample name	Elements (at.%)							Actual composition (at.%)	
	Ce	Ti	O	B	C	N	S	Cerium (x)[a]	Nonmetals (y)[b]
TiO_2	–	39.26	60.74	–	–	–	–	–	–
Ce-TiO_2	1.05	42.83	56.12	–	–	–	–	2.45	–
Ce-B-TiO_2	1.42	58.21	39.88	0.49	–	–	–	2.43	0.84
Ce-C-TiO_2	1.29	51.69	46.61	–	0.41	–	–	2.49	0.80
Ce-N-TiO_2	1.38	57.56	40.50	–	–	0.56	–	2.39	0.97
Ce-S-TiO_2	1.46	59.23	38.80	–	–	–	0.51	2.46	0.86

(a) $x = \frac{Ce(at)}{Ti(at)} \times 100$ **(b)** $y = \frac{NM(at)}{Ti(at)} \times 100$

Footer Page TH-1334_08610706

The X-ray diffraction patterns of Ce-TiO_2 and Ce-NM-TiO_2 are shown in Fig.4.11. All the samples, except Ce-N-TiO_2, were dominated by anatase phase (2θ = 25.5°, 37°, 48°, 53.8°, 55.1°, 64°, JCPDS 21-1272). For Ce-N-TiO_2 significant amount of rutile phase (2θ = 28°, 36.1°, 41.5°, JCPDS 21-1276) was observed. In general, the phase transformation of anatase to rutile occurs at temperature above 600 °C and anatase phase is expected to be dominant for samples calcined at lower temperature of 450 °C. Accordingly anatase phase was dominant in XRD profiles of all samples except Ce-N-TiO_2. For Ce-N-TiO_2 sample, the presence of significant amount of rutile phase suggests that nitrogen can catalyzes the anatase-rutile phase transformation significantly at lower temperature (Sidheswaran and Tavlarides, 2009). In addition Ce-S-TiO_2 codoped sample was more amorphous in nature as observed from broad XRD peaks of low intensity compared to that of other nonmetal doped samples. No characteristic peaks of CeO_2 phases were observed in the XRD profiles, which suggest that the ceria was well dispersed in TiO_2 matrix or were below detection limit. In addition, no peaks due to any Ce-Ti mixed oxides were observed in any of the samples.

As discussed earlier in section 4.1.2, in Ce-TiO_2 the cerium ions can substitute Ti^{4+} sites or can occupy the interstitial sites with Ce-O-Ti linkages. Due to larger size of cerium ions compared to that of titanium ions lattice distortion occurs. The lattice distortion values are shown in Table 4.5 and correspond to maximum strain observed in crystal lattice due to distortion by incorporation of dopant metals. Maximum value of lattice distortion was obtained, as expected for Ce-S-TiO_2 sample, since sulphur has largest ionic radii among the nonmetals used. The corresponding change in lattice parameters for tetragonal titania lattice is also included in Table 4.5. With addition of Ce in TiO_2, due to the lattice distortion the lattice parameters increased compared to that of undoped titania. Co-addition of nonmetals resulted in further increase in lattice parameter values.

Footer Page TH-1334_08610706

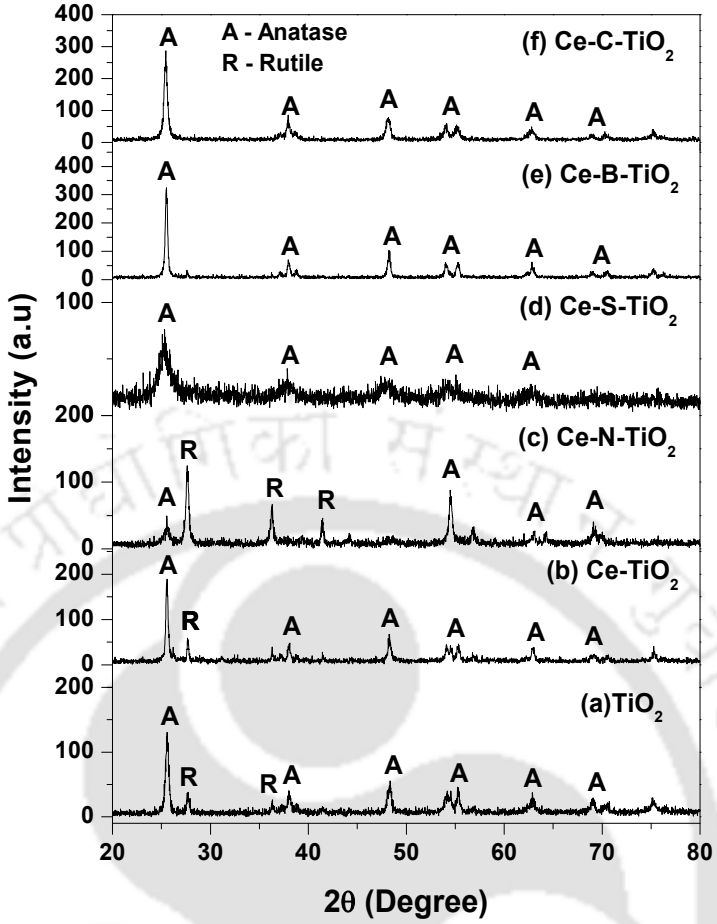

Fig.4.11. XRD patterns of undoped TiO_2, Ce-TiO_2 and Ce-NM-TiO_2 (NM = B, C, N, S)

The FESEM images of undoped TiO_2, Ce-TiO_2, Ce-NM-TiO_2 are shown in Fig.4.12. The images showed a definite change in morphology of the samples when cerium and nitrogen was added to titania suggesting that the dopants played a prominent role in development of material structure during co-precipitation. This resulted in different physical properties as observed in Table 4.5. Particles of irregular shape and size were observed for undoped titania where as ceria doped titania prepared by co-precipitation consisted of particles of regular size and shape. The particles were spherical in the range of 100-200 nm. The morphology again changed when titania was codoped with cerium and nonmetals. All the codoped Ce-NM-TiO_2 samples were agglomerated in nature.

Footer Page TH-1334_08610706

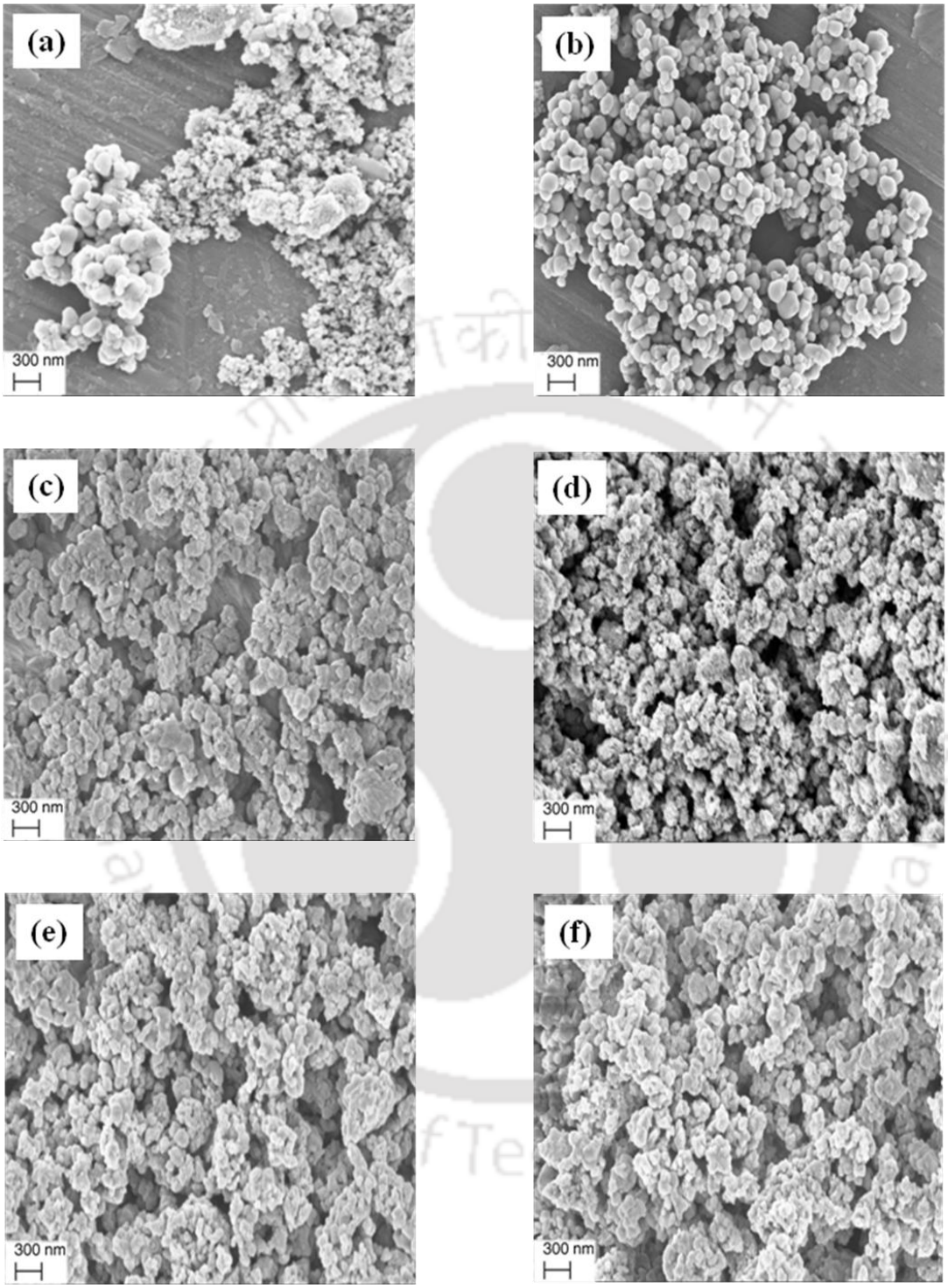

Fig.4.12. FESEM images of (a) Undoped TiO_2 (b) Ce-TiO_2 (c) Ce-N-TiO_2 (d) Ce-S-TiO_2 (e) Ce-B-TiO_2 and (f) Ce-C-TiO_2

Footer Page TH-1334_08610706

The UV-visible absorption spectra of TiO_2, Ce-TiO_2 and Ce-NM-TiO_2 are shown in Fig.4.13 (A). The Ce-TiO_2 sample showed intense absorption bands in the visible light region ranging from 400 to 500 nm. The Kubelka-Munk plots of Ce_x-TiO_2 samples are shown in Fig.4.13 (B). The band gap values calculated using the Kubelka-Munk method were 3.01 eV (TiO_2), 2.85 eV (Ce-TiO_2) 2.8 eV (Ce-B-TiO_2), 2.6 eV (Ce-C-TiO_2), 2.2 eV (Ce-N-TiO_2) and 2.1 eV (Ce-S-TiO_2). The decreased band gap energy values of cerium doped sample as discussed earlier indicated formation of new energy levels within the TiO_2 band gap and resulted in red-shift of the absorption edge. This shift was attributed to incorporation of Ce 4f levels into the TiO_2 crystal structure just below the conduction band of TiO_2 and thereby reducing the effective bandgap (Magesh et al., 2009). Addition of nonmetal to cerium doped TiO_2 samples resulted in further shift in the bandgap energy to longer wavelength. For the codoped catalysts the band gap energy was affected by formation of additional impurity states within titania matrix by the interaction of p-orbitals of the nonmetal dopants (B, C, N, S) and 2p-orbitals of oxygen (Zhao et al., 2004, Sathish et al., 2007, Yu and Yu, 2009, Tian et al., 2011). The relative position of the new states with respect to valence band of titania depends on the properties of dopants and its position within the matrix. Whether the nonmetal dopant would occupy anionic or cationic substitutional sites or interstitial site depends upon its size, chemical valence and electronegativity compared that of the host TiO_2. The probability that a dopant will substitute oxygen depends on its electronegativity (Lu et al., 2012). As difference in electronegativity values of dopant and oxygen becomes smaller, the probability that dopant will substitute oxygen becomes higher. Substitutional dopants form the new band states at higher energy level compared to interstitial dopant (Valentin and Pacchioni, 2013). For boron codoped catalyst, it is difficult to replace Ti^{4+} sites by B^{3+} due to the smaller ionic radius of B^{3+} (IR=0.023 nm) compared to Ti^{4+} (IR=0.068 nm). Therefore boron may replace either an oxygen atom or incorporate in the interstitial position in TiO_2 matrix. But due to the lower electronegativity of boron, its probability of occupying the interstitial sites is higher. Similarly carbon can also substitute oxygen or occupy an interstitial site. In nitrogen codoped sample the substitution of oxygen sites is most probable due to their closer electronegativity values (Kitano et al., 2007). Substitutions of S in both anionic and cationic sites of TiO_2 have been reported in the literature (Umebayashi et al., 2002, Yu et al., 2005).

Footer Page TH-1334_08610706

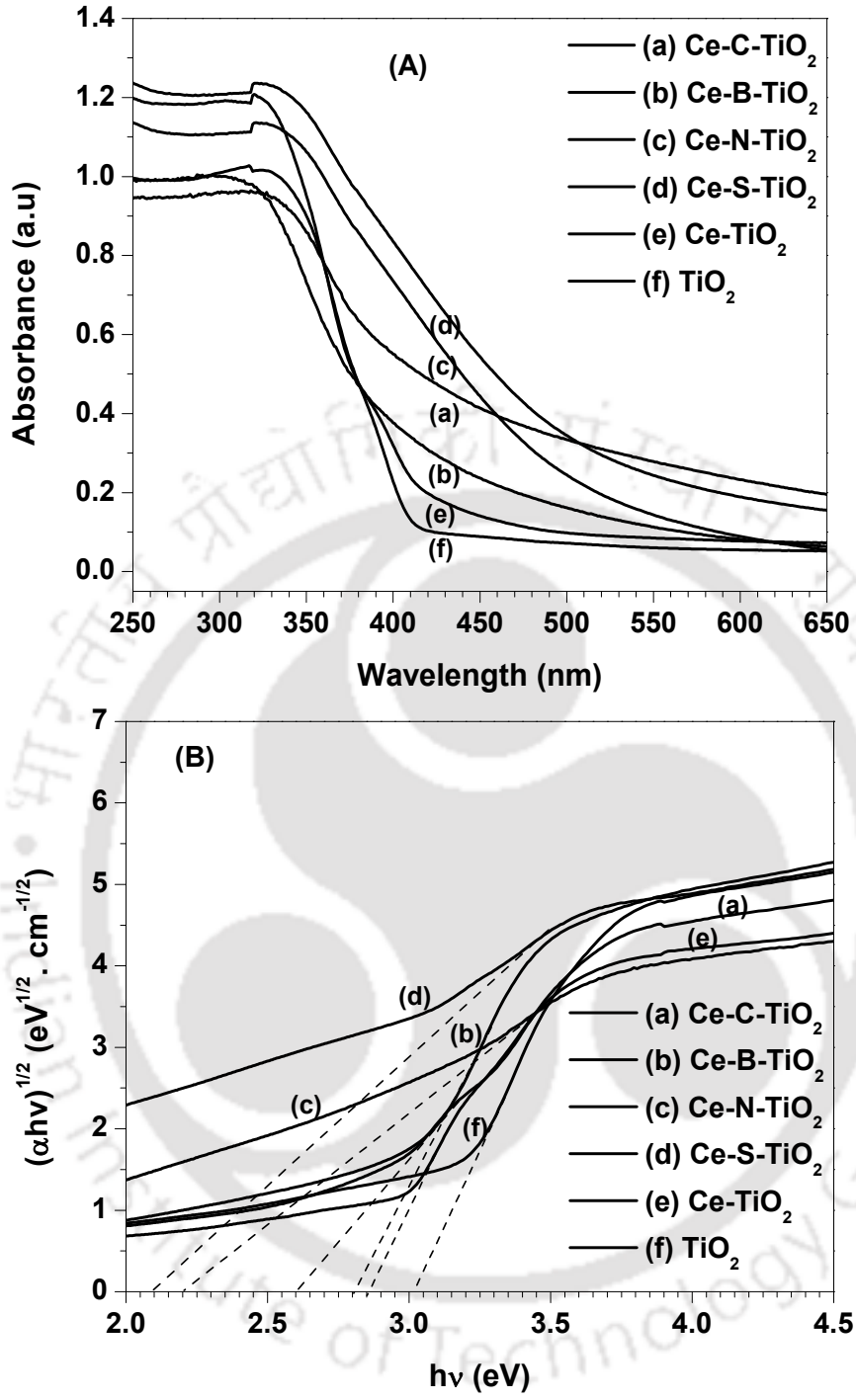

Fig.4.13. (A) UV-Visible diffuse reflectance spectra and (B) Kubelka-Munk plot for TiO_2, Ce-TiO_2 and Ce-NM-TiO_2 (NM = B, C, N, S)

However, anionic sulphur substitution by S^{2-} (IR=0.17 nm) might be difficult because of its larger ionic radius than O^{2-} (IR=0.122 nm). But the cationic substitution of Ti^{4+} (IR=0.068 nm) by S^{6+} (IR=0.029 nm) would be more favorable due to smaller size of

Footer Page TH-1334_08610706

latter. When TiO_2 is doped with sulphur, either the mixing of S 3p states with valence band O 2p states or the formation of isolated p-orbitals of S above the valence band contributed towards narrowing the band gap (Xiang et al., 2011).

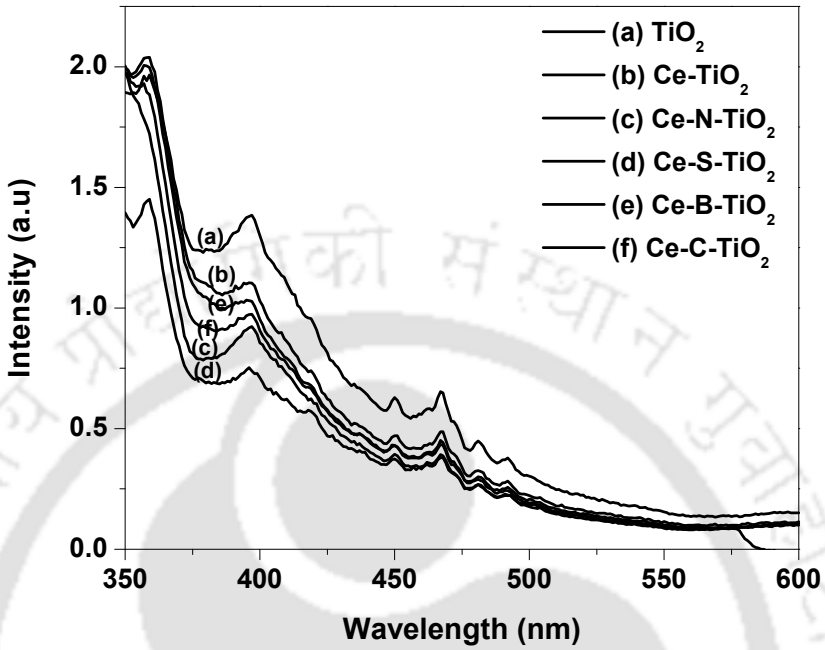

Fig.4.14. Photoluminescence spectra for undoped TiO_2, Ce-TiO_2 and Ce-NM-TiO_2 (NM = B, C, N, S)

Fig.4.14 shows the room temperature photoluminescence spectra of the TiO_2, Ce-TiO_2 and Ce-NM-TiO_2 samples in the range of 350-600 nm, respectively. As discussed in section 4.2.1, all the titania based catalysts showed six emission peaks at 360, 396, 450, 468, 481 and 492 nm corresponding to band gap transitions and excitonic emissions. The lower PL intensity of Ce-TiO_2 compared to that of TiO_2 as discussed earlier is due to the cerium induced energy level in TiO_2 band structure that serves as electron traps. As can be observed from Fig.4.14, the PL emission intensities of the cerium and nonmetal codoped samples further decreased in the order of TiO_2 > Ce-TiO_2 > Ce-B-TiO_2 > Ce-C-TiO_2 > Ce-N-TiO_2 > Ce-S-TiO_2. In the cerium and nonmetal codoped samples, the oxygen vacancies generated by substituting nonmetal dopants can act as additional effective traps for photo induced electrons thereby reducing the radiative recombination rate of charge carriers further. The photogenerated electrons are trapped by oxygen vacancies by non-radiative combinations (Wang et al., 2009). The decreasing emission intensity order can be

Footer Page TH-1334_08610706

attributed to increased oxygen vacancies resulted by increasing substitution effects from B to N as discussed in earlier section. In sulfur codoped samples the presence of isolated cationic S^{6+} dopant state may further act as surface trap states for photogenerated electrons thereby resulting in a significant decrease in the recombination rate and lowering the PL emission.

Photocatalytic activity studies

The photocatalytic hydrogen production from water-methanol mixture for TiO_2, Ce-TiO_2 and Ce-NM-TiO_2 (NM = B, C, N, S) catalysts are shown in Fig.4.15. The activity of undoped TiO_2 was very low but Ce-TiO_2 showed significant photocatalytic activity and high hydrogen evolution. The high activity of cerium doped TiO_2 can be attributed to their ability of absorption of light in visible light region as shown in Fig. 4.13 (A). This has also been discussed in section 4.2.1. Addition of nonmetals such as B, C and N to Ce-TiO_2 samples further enhanced hydrogen evolution activity. This may be attributed to higher surface area, enhanced visible light absorption as well as lower recombination rate of electron-hole pairs in codoped samples. The highest activity of Ce-N-TiO_2 among codoped samples may be attributed to its higher surface area, higher visible light absorption and lower recombination rate of electron-hole pairs compared to other nonmetals, B and C, doped samples. The activity of Ce-C-TiO_2 should be higher than Ce-B-TiO_2 due to higher absorption of visible light and lower recombination of photogenerated electron-hole pairs for former as shown by absorption spectra (Fig.4.13 (A)) and PL spectra (Fig.4.14) respectively. But slightly higher hydrogen evolution observed for Ce-B-TiO_2 compared to that of Ce-C-TiO_2 may be attributed to higher surface area of former providing more active sites. Much lower hydrogen production was observed for Ce-S-TiO_2 sample, although it has enhanced absorption in the visible light region and efficient charge separation. The lower activity of Ce-S-TiO_2 can be attributed to its very low surface area. Moreover the S may be in isolated state and that may lead to lower mobility of the holes and limits the number of charge carriers reaching the catalyst surface. This may have also resulted in lower photocatalytic activity in S doped samples.

Footer Page TH-1334_08610706

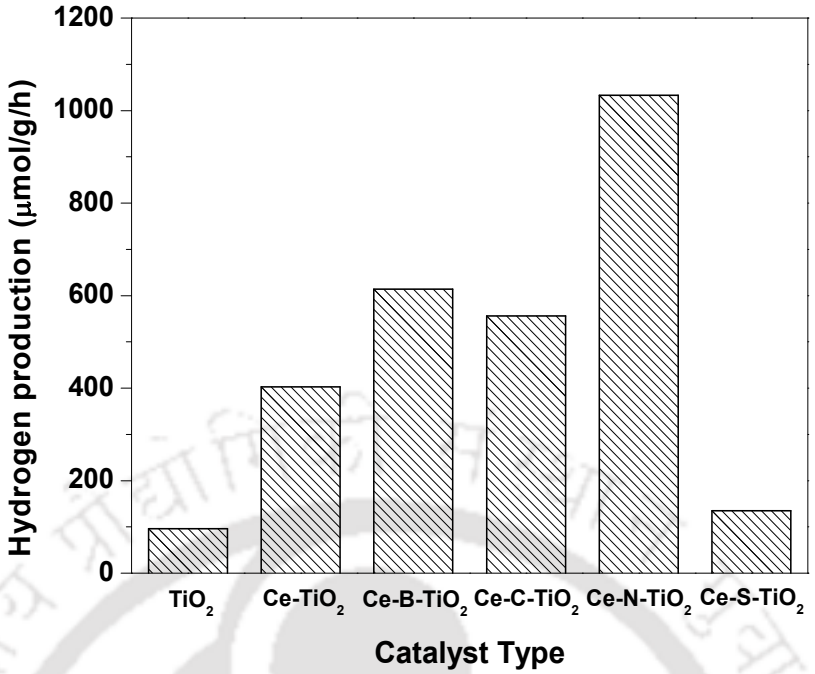

Fig.4.15. Hydrogen production for undoped TiO_2, Ce-TiO_2 and Ce-NM-TiO_2 (NM = B, C, N, S)

The apparent quantum efficiency of the photocatalysts was calculated using the method followed by (Sasikala et al., 2008). The apparent quantum efficiency of TiO_2, Ce-TiO_2, Ce-B-TiO_2, Ce-C-TiO_2, Ce-N-TiO_2 and Ce-S-TiO_2 were 1.9, 8.0, 12.2, 11.1, 20.6 and 2.7 % respectively. The calculated values agreed with the reported apparent quantum efficiency range of 2-22 % for different photocatalysts (Jin et al., 2007). For comparison the photocatalytic activity of N-TiO_2 was also measured. The apparent quantum efficiency of N-TiO_2 (10.3 %) was slightly higher than that Ce-TiO_2 (8.0 %) but the efficiency increased significantly for codoped Ce-N-TiO_2 to 20.6 % suggesting that both doping components were contributory to photocatalytic activity, as discussed earlier, giving higher hydrogen production. The results are shown in Fig.4.16.

Footer Page TH-1334_08610706

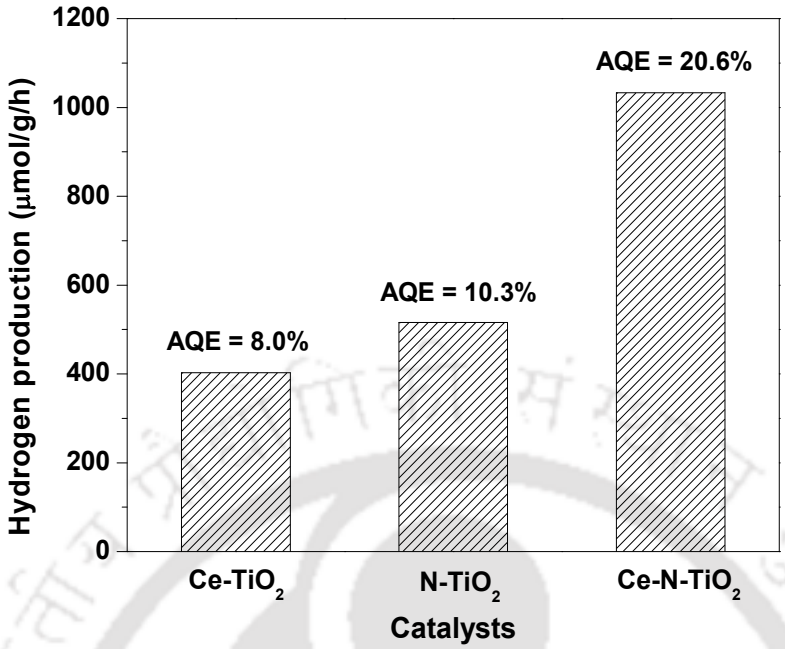

Fig.4.16. Comparison of hydrogen production for Ce-TiO_2, N-TiO_2 and Ce-N-TiO_2 catalysts

Based on the observed band gap energies of codoped samples the position of the impurity states and probable transitions of electrons are schematically shown in Fig.4.17. In Ce-TiO_2 the photogenerated electrons are excited from the valence band to extended conduction band where electrons are trapped effectively by Ce^{4+}/Ce^{3+} couple. This results in accumulation of electrons in extended conduction band which can serve as hydrogen formation site. On addition of nonmetals to cerium doped titania, the excitation of electrons can also takes place from nonmetal induced impurity levels resulting in absorption of visible light. In liquid phase, formaldehyde and trace of formic acid were detected. In gas phase, only hydrogen was detected. The product formation suggested that the extent of oxidation of formaldehyde was low.

Footer Page TH-1334_08610706

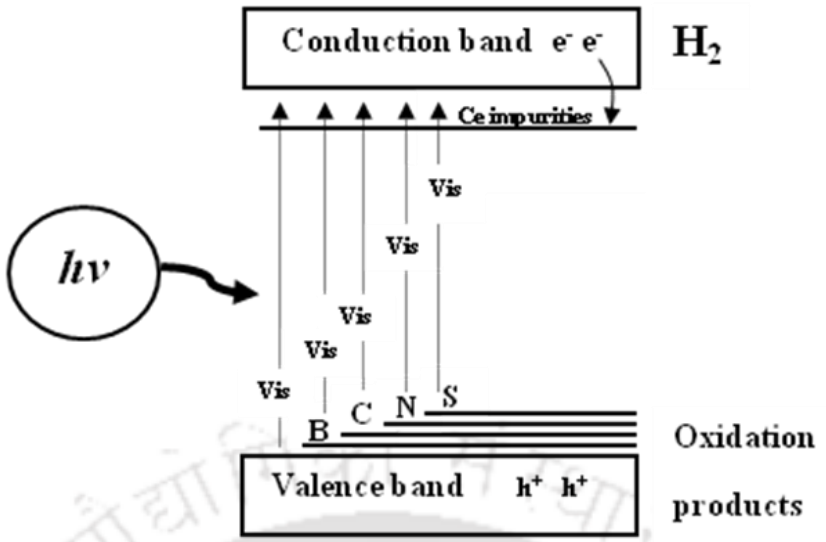

Fig.4.17. Schematic representation of hydrogen production over cerium and nonmetal codoped TiO_2 photocatalysts

No detection of CO_2 in gas phase suggested that the amount of CO_2 formed, if any, by oxidation of formic acid was negligible and below the detection level of instrument. The reduction and oxidation reactions occurring in conduction band and valance band respectively can be represented as follows (Wu and Lee, 2004; Choi and Kang, 2007).

$$(2)\ \text{Photocatalyst} + h\nu \rightarrow e^- + h^+$$

Reduction reaction

$$(3)\ 2e^-_{cb} + 2H^+ \rightarrow H_2$$

Oxidation reactions:

$$(4)\ CH_3OH + 2h^+_{vb} \rightarrow 2H^+ + HCHO$$

$$(5)\ HCHO + H_2O \rightarrow HCO_2H + H_2$$

The photocatalyst absorbs photon to generate electrons and holes. The methanol is oxidized by holes to generate hydrogen ions and formaldehyde. The hydrogen ions are reduced by photogenerated electrons. In addition to proposed hole mediated path as shown in the above reaction scheme, methanol can also enhances hydrogen generation by reacting with hydroxyl radicals generated from photocatalytic water

Footer Page TH-1334_08610706

splitting (Chiarello et al., 2011). For oxidation of formaldehyde to formic acid, the extra oxygen atom is provided by water through hydroxyl radical. Intermediate products were only detected in liquid phase and no intermediate products were detected in gaseous phase in present study.

Summary

Cerium doped samples synthesized by co-precipitation method were found to be potential photocatalysts for hydrogen generation under visible light radiation. Doping of titania with cerium induced distinct red shift of the absorption edge in visible light region. Among cerium doped titania, $Ce_{2.5}TiO_2$ gave highest hydrogen evolution rate of 403 µmol/g/h. The higher activity of $Ce_{2.5}TiO_2$ can be attributed to highest surface area and significant absorption of visible light.

Nonmetal modification of cerium doped titania catalyst further enhanced the visible light absorption and separation efficiency of photogenerated electron-hole pairs. The effective band gap energies of codoped samples depended on properties of nonmetals. The surface area and phase distribution was also modified in presence of nonmetal. Highest hydrogen evolution rate of 1033 µmol/g/h was observed for cerium-nitrogen codoped sample. The higher photoactivty of Ce-N-TiO_2 can be attributed to higher surface area, higher light absorption and efficient charge separation.

Footer Page TH-1334_08610706

4.3 Transition metal doped titania

The titania was doped with 2.5 at.% of different transition metals, such as copper, iron and nickel and effect on hydrogen generation was studied.

4.3.1 Effect of transition metal doping

Characterization of photocatalysts

The nitrogen adsorption-desorption isotherms and pore size distributions of M-TiO_2 (M = Cu, Fe, Ni) samples are shown in Fig.4.18. All the M-TiO_2 photocatalysts exhibited Type III isotherm with H3 hysteresis loop corresponding to slit shape pores. The hysteresis volume was highest for Cu-TiO_2 and lowest for Ni-TiO_2 sample. The pore size distribution (inset) showed a broad distribution in the range of 2-120 nm for all samples. The BET surface area and pore volume of the samples are shown in Table 4.7. The surface area of the M-TiO_2 samples varied in the range of 20-41 m^2/g, depending on the type of the dopant metals. The surface area was observed to be highest for Cu-TiO_2 with 41 m^2/g. The variation in the surface area of the catalysts, at similar metal loading, may be attributed to the difference in formation of porous network during co-precipitation in presence of different metals.

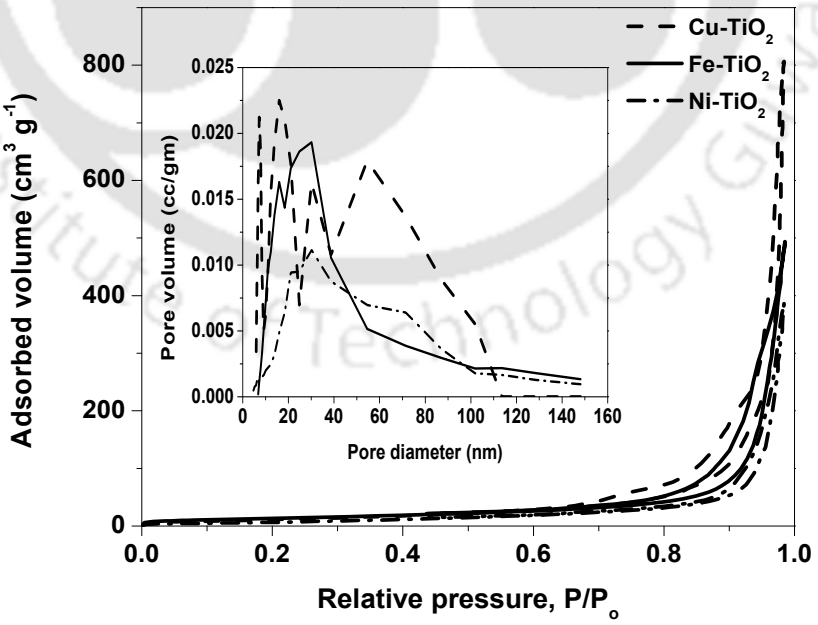

Fig.4.18. N_2 adsorption-desorption isotherms of M-TiO_2 (M = Cu, Fe, Ni); (Inset: pore size distributions)

Footer Page TH-1334_08610706

Fig.4.19 shows the XRD patterns of M-TiO_2 catalysts. Anatase phase was observed to be dominant in all samples with peaks at 2θ = 25.3°, 36.9°, 48.0°, 53.9°, 55.1° and 62.1° (JCPDS No: 21-1272-TiO_2-Anatase). No characteristic peaks corresponding to transition metal oxides were detected in any of the samples suggesting that the metal oxides were in a highly dispersed state. The lattice parameters and lattice distortion values of the samples are given in Table 4.7.

Table 4.7. Surface area, pore volume and lattice parameters of M-TiO_2, M-1N-TiO_2, Cu-xN-TiO_2 (M = Cu, Fe, Ni; N = nitrogen; x = 0.5, 1, 1.5 at.%)

Catalyst	BET surface area (m^2/g)	Pore volume (cc/g)	Lattice parameters Anatase		Lattice distortion
			a (Å) (101)	c (Å) (004)	
Cu-TiO_2	41	0.17	3.8390	9.5440	0.317
Fe-TiO_2	20	0.18	3.8027	9.5685	0.248
Ni-TiO_2	25	0.15	3.7885	9.5197	0.309
Cu-1N-TiO_2	49	0.23	3.8747	9.5416	0.486
Fe-1N-TiO_2	30	0.60	3.8036	9.5807	0.415
Ni-1N-TiO_2	46	0.53	3.8375	9.5685	0.497
Cu-0.5N-TiO_2	54	0.70	3.8580	9.5220	0.432
Cu-1.5N-TiO_2	26	0.14	3.8876	9.6178	0.743
TiO_2-Anatase	84	0.97	3.7852	9.5139	-

The lattice distortion values correspond to the maximum strain observed in the crystal lattice due to incorporation of dopant metals. The origin of lattice distortion for doped TiO_2 can be attributed to the difference between the ionic radii of dopant ions and Ti^{4+} ion. The effective ionic radii of used transition metals ions are; Cu^{2+}: 0.073 nm, Fe^{3+}: 0.064 nm, Ni^{2+}: 0.072 nm and Ti^{4+}: 0.068 nm (Hsiang and Liu, 2009; Ganesh et al., 2012). The higher lattice distortion as observed for Cu-TiO_2 and Ni-TiO_2 may be attributed to the higher ionic radius of copper and nickel ions as compared to that of

Footer Page TH-1334_08610706

titanium ions. The Cu^{2+} and Ni^{2+} ions are more likely to reside in the interstitial sites of the TiO_2 lattice due their larger ionic radii compared to that of Ti^{4+}. The value of lattice parameters of the M-TiO_2 catalysts were higher compared to that of TiO_2 due to the distortion of the lattice.

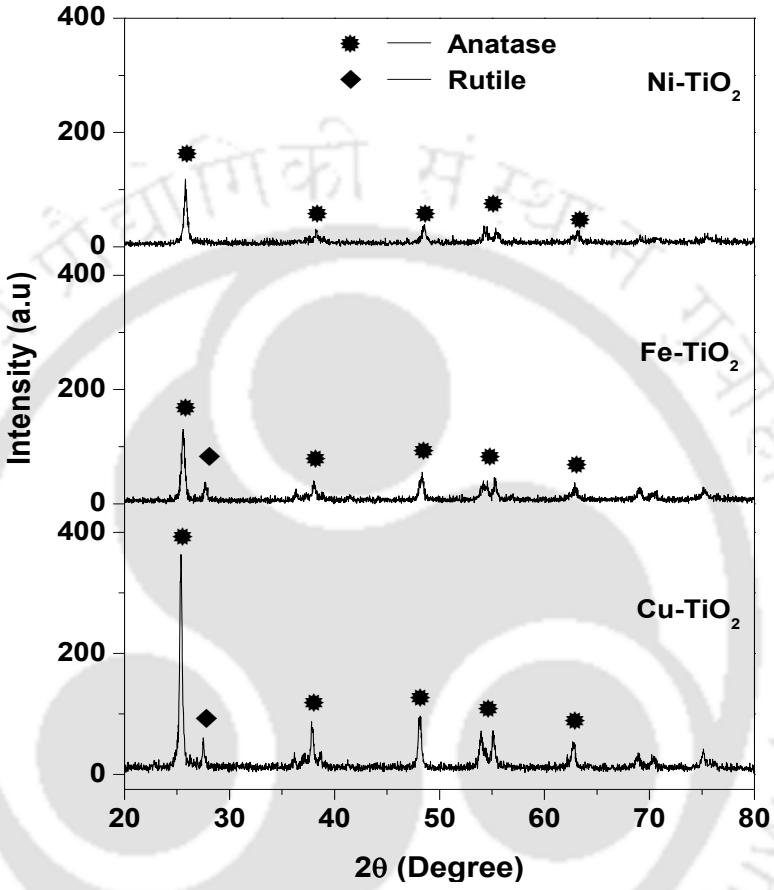

Fig.4.19. XRD patterns of M-TiO_2 (M = Cu, Fe and Ni)

The FESEM images of M-TiO_2 samples are shown in Fig.4.20 (a, c and e). All the catalysts were in agglomerated state. For Cu doped titania, the particles were less agglomerated and had spherical shape. For the Fe doped TiO_2, the agglomeration seemed to be highest.

Footer Page TH-1334_08610706

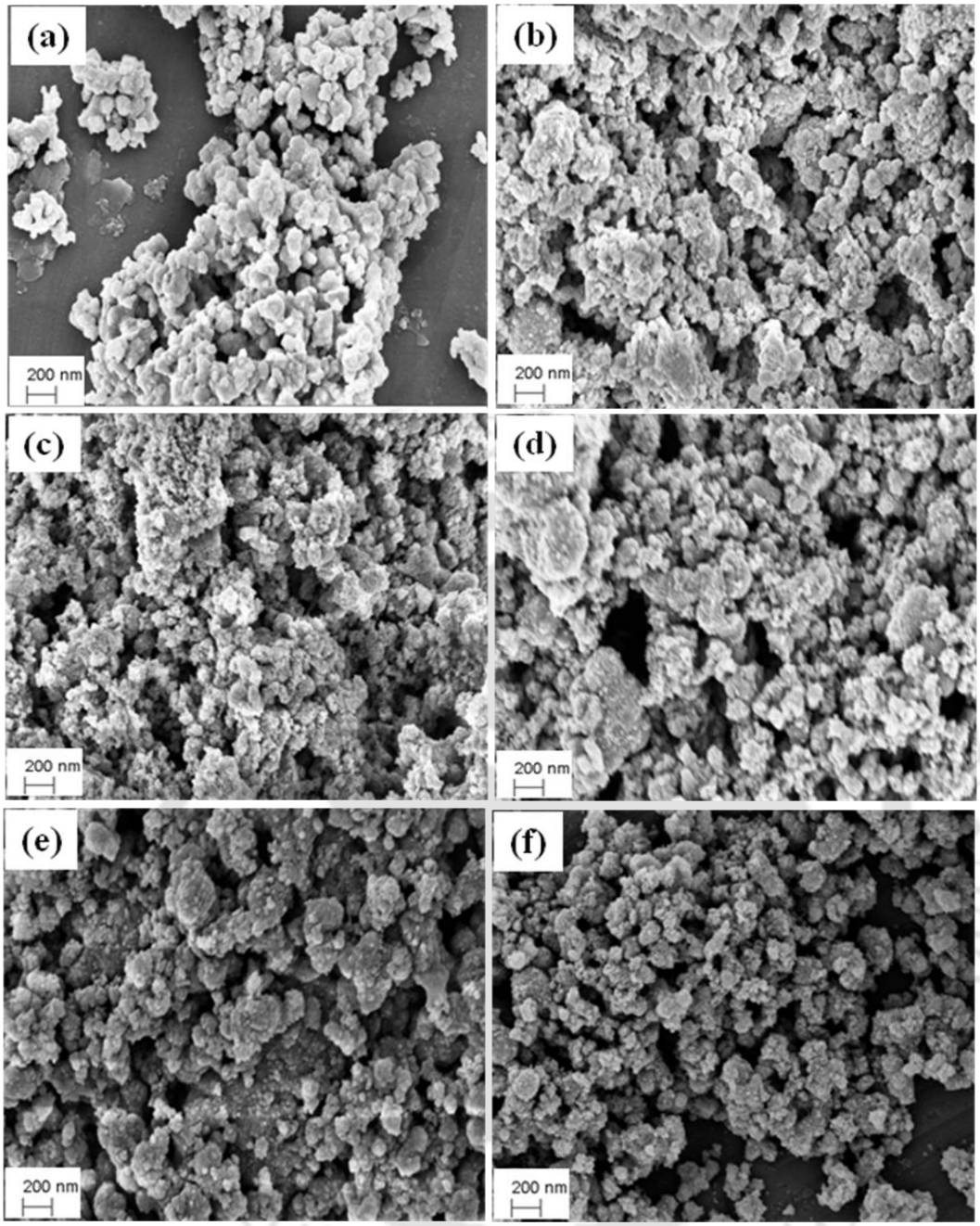

Fig.4.20. FESEM images of (a) Cu-TiO_2 (b) Cu-1N-TiO_2 (c) Fe-TiO_2 (d) Fe-1N-TiO_2 (e) Ni-TiO_2 and (f) Ni-1N-TiO_2

The optical absorption properties of M-TiO_2 and TiO_2 samples are shown in Fig. 4.21 (A). The M-TiO_2 samples exhibited significant absorption in visible light region compared to TiO_2 sample. The band gap energy of the oxides was estimated by the Kubelka-Munk method by extrapolating the straight line portion of $(\alpha h\nu)^{1/2}$ vs $h\nu$ plot to the energy axis. The Kubelka-Munk plots of M-TiO_2 samples are shown in Fig.4.21

Footer Page TH-1334_08610706

(B). The band gap values obtained for the oxides were 3.0 eV (TiO_2), 2.3 eV (Cu-TiO_2), 2.5 eV (Fe-TiO_2) and 2.55 eV (Ni-TiO_2). The shift toward visible light absorption for doped titania has been attributed to the formation of intra band states by dopant transition metals within the titania bandgap.

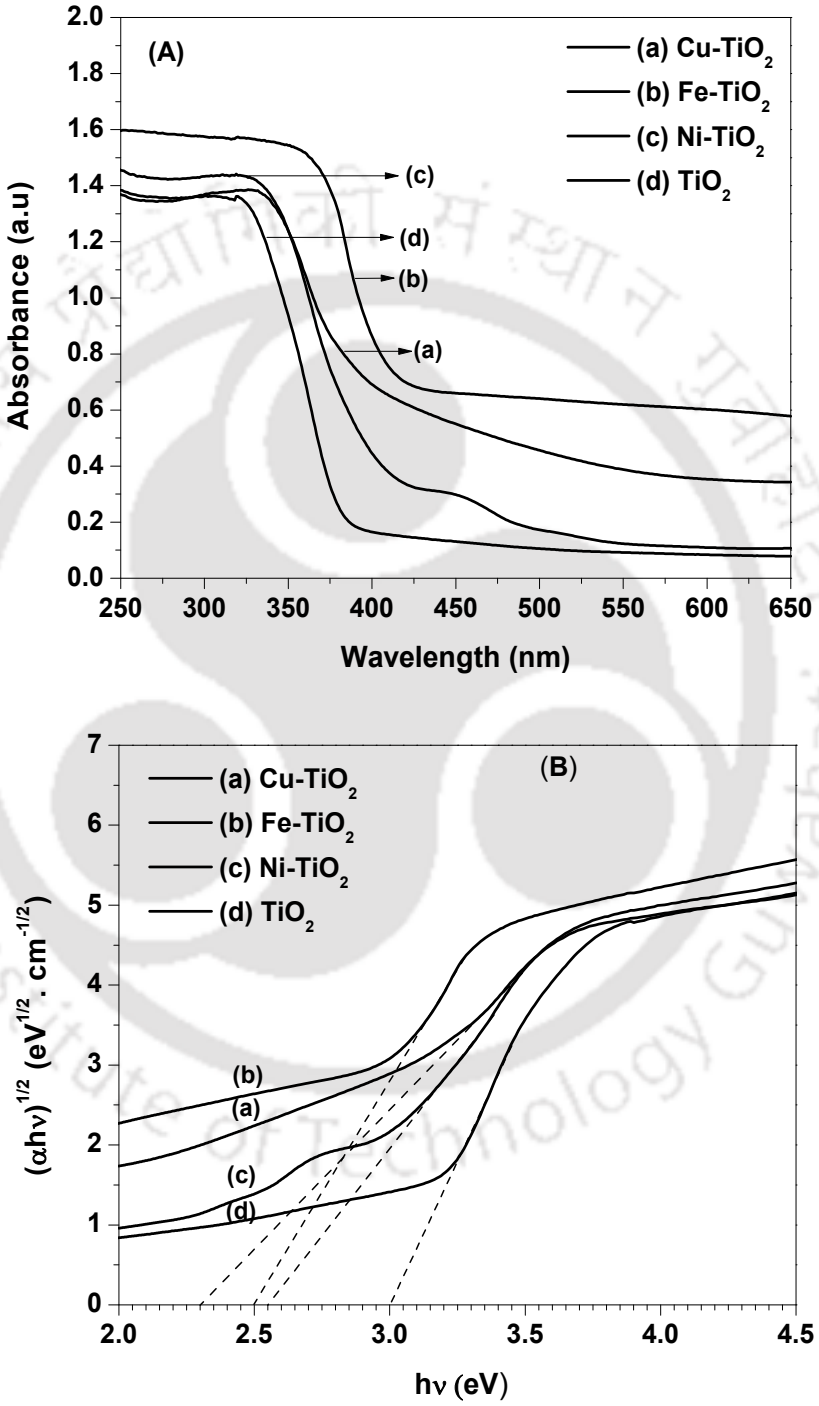

Fig.4.21. (A) UV-Visible diffuse reflectance spectra and (B) Kubelka-Munk plot of undoped TiO_2 and M-TiO_2 (M = Cu, Fe and Ni)

Footer Page TH-1334_08610706

Fig.4.22 shows the PL spectra of M-TiO_2 and TiO_2 samples. For all samples signals were obtained in the range of 350 to 600 nm. Six distinct peaks at about 360, 395, 450, 470, 481 and 492 nm wavelengths were observed for TiO_2. The corresponding transition energy values are 3.44, 3.13, 2.76, 2.65, 2.8 and 2.52 eV, respectively. As discussed in section 4.2.1, these peaks corresponded to band gap transition of anatase (395 nm) and emissions of free and bound excitons.

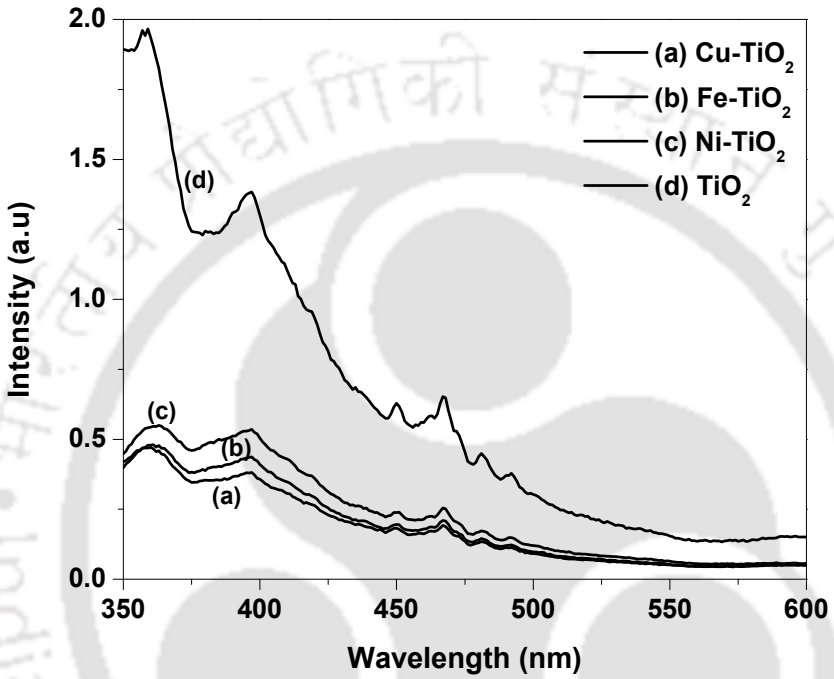

Fig.4.22. Photoluminescence spectra of undoped TiO_2 and M-TiO_2 (M = Cu, Fe and Ni)

Addition of transition metals to titania drastically reduced the intensity of the peaks suggesting reduction in the rate of radiative recombination of photogenerated electrons with valence band holes. This can be explained as follows. The transition metals can exist in multiple valance states such as $Cu^{+2}/Cu^{+1}/Cu^0$, $Fe^{+3}/Fe^{+2}/Fe^0$ and Ni^{+2}/Ni^0. These transition metals when incorporated into the TiO_2 crystal lattice can act as trap for photogenerated electrons resulting in non-radiative combinations as shown below.

$$M^{n+} + e^- \rightarrow M^{(n-1)+}$$

Footer Page TH-1334_08610706

Where 'n' represent the valence state of metal 'M' and 'e' is the photogenerated electron. This trapping mechanism reduces the rate of radiative recombination of photogenerated electrons with holes in valence band of titania decreasing the peak intensity. The stability of the photogenerated electrons is expected to increase the photoactivity of doped titania.

For M-TiO_2 catalysts, the peak intensity was minimum for Cu-TiO_2 and maximum for Ni-TiO_2. This suggests that non-radiative trapping of photogenerated electrons was maximum for Cu doped titania and minimum in presence of nickel. The relative trapping efficiency of transition metals is expected to depend on ease of accepting electrons, on other words on reduction potential. Hence the transition metal with more positive reduction potential with respect to that of titanium will have higher ability of trapping electrons. The reduction potentials of the transition metals are summarized in Table 4.8 (Nakamura et al., 2007; Litter, 1999; Slamet, 2005; Rajeshwar et al., 2002).

Table 4.8. Reduction potential values of the transition metals

Reduction reactions	Reduction potential (V)
Ti^{4+}/Ti^{3+}	-0.670
Fe^{2+}/Fe^{0}	-0.440
Ni^{2+}/Ni^{0}	-0.257
Cu^{2+}/Cu^{+}	0.159
Cu^{2+}/Cu^{0}	0.340
Cu^{+}/Cu^{0}	0.520
Fe^{3+}/Fe^{2+}	0.771

All the transition metals have positive reduction potential values with respect to that of titanium and hence all are expected to show some trapping efficiency. The copper with positive reduction potentials for all electronic transitions is expected to show the highest non-radiative electron trapping efficiency and hence the lowest peak intensity was observed for Cu-TiO_2 sample. Similarly nickel with lowest reduction potential is expected to be least efficient for electron trapping.

Footer Page TH-1334_08610706

Photocatalytic activity studies

The photocatalytic hydrogen production over transition metal doped TiO_2 is shown in Fig.4.23. Under the experimental conditions, the hydrogen production over unmodified titania, having surface area of 84 m^2/g and mainly anatase phase, was 96 µmol/g/h from water-methanol solution. In comparison, all the transition metal doped titania samples showed higher activity. The photocatalytic hydrogen production was highest for Cu-TiO_2 (938 µmol/g/h). For Fe-TiO_2 and Ni-TiO_2, the hydrogen production was 269 and 250 µmol/g/h, respectively. For Cu-TiO_2, the highest efficiency for trapping the photogenerated electrons contributed to higher availability of electrons for reduction of hydrogen at conduction band and resulted in higher activity. The higher activity for Cu-TiO_2 can be also attributed to higher surface area and significant absorption of visible light.

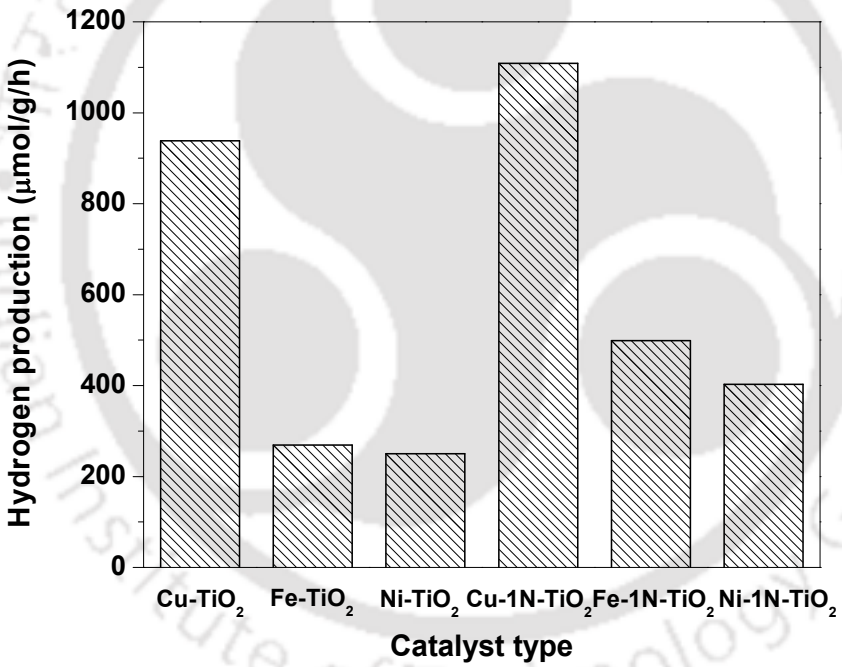

Fig.4.23. Hydrogen production for M-TiO_2 and M-1N-TiO_2 (M = Cu, Fe and Ni)

For Ni-TiO_2, lowest activity can be attributed its highest rate of recombination photogenerated electrons as observed in PL spectra as well as to lowest absorption of visible light. The apparent quantum efficiency of Cu-TiO_2, Fe-TiO_2 and Ni-TiO_2 were determined to be 18.7, 5.3 and 5.0 % respectively.

Footer Page TH-1334_08610706

4.3.2 Effect of transition metal and nonmetal codoping

Effect of codoping of TiO_2 with transition metals and nonmetal on hydrogen production activity was studied using nitrogen as the nonmetal. The loading of transition metal was maintained at 2.5 at.% and that of nitrogen at 1 at.%.

Characterization of photocatalysts

The nitrogen adsorption-desorption isotherms and pore size distributions of M-1N-TiO_2 (M = Cu, Fe, Ni) catalysts are shown in Fig.4.24. For codoped M-1N-TiO_2 samples, the isotherms were of type III and shape of hysteresis loop depended on type of transition metal dopant. For Cu-1N-TiO_2 photocatalyst, H3 loop was observed but for Ni-1N-TiO_2 and Fe-1N-TiO_2 samples, H2 loop corresponding to ink bottles pores was observed. The pore size distributions of the catalysts are shown in the inset of Fig.4.24. All the codoped photocatalysts, except Ni-1N-TiO_2, showed a broad pore size distribution in the range of 2-120 nm. For Ni-1N-TiO_2 a narrower pore size distribution in the mesoporous region of 2-20 nm was observed.

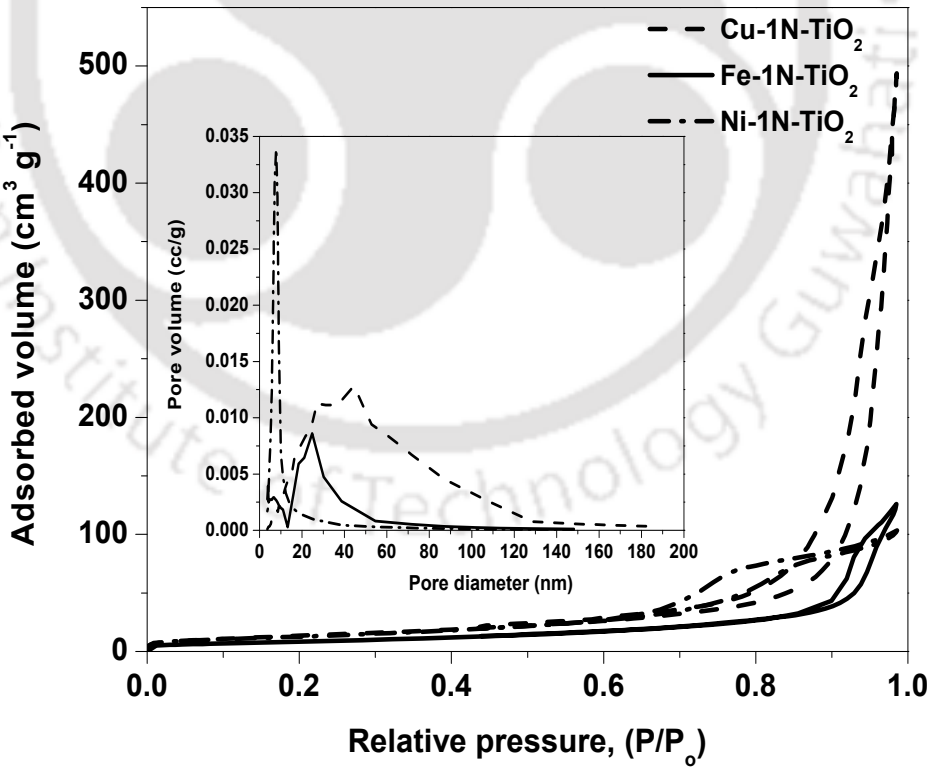

Fig.4.24. N_2 adsorption-desorption isotherms for M-1N-TiO_2 (M = Cu, Fe and Ni; Inset: pore size distributions)

Footer Page TH-1334_08610706

The X-ray diffraction patterns of metal and nitrogen codoped TiO_2 catalysts are shown in Fig.4.25. All the codoped catalysts exhibited only anatase phase. The lattice parameters and lattice distortion values of the samples are given in Table 4.7. The lattice distortion values increased slightly with the addition of nitrogen in codoped samples compared to that of respective M-TiO_2 sample. The result suggested incorporation of nitrogen in the titania lattice. Nitrogen is reported to substitute oxygen in titania matrix and the ionic radius difference between nitrogen (0.146 nm) and oxygen (0.138 nm) anions may have resulted in lattice distortion. The lattice parameters increased as observed in Table 4.7.

The surface area and pore volume of all the M-1N-TiO_2 samples were observed to be higher compared to the respective M-TiO_2 samples (Table 4.7). The observed increase in the surface area and pore volume of all codoped samples suggest increased network formation with incorporation of nitrogen. Addition of nitrogen to transition metal doped titania seemed to further increase the agglomeration nature of the catalysts as shown in Fig.4.20 (b, d, f).

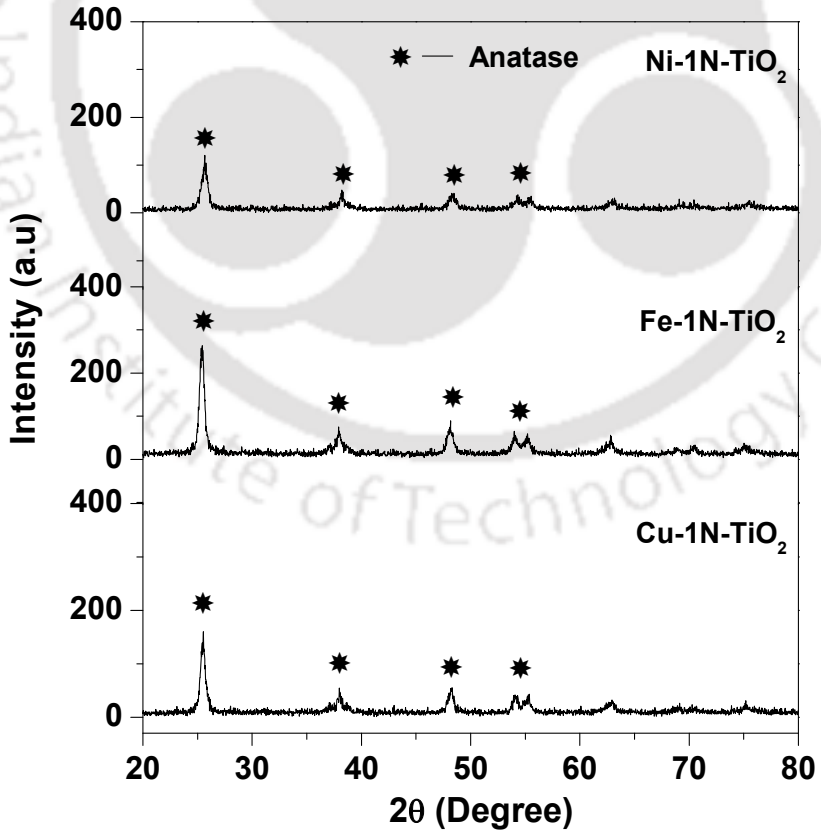

Fig.4.25. XRD patterns of M-1N-TiO_2 (M = Cu, Fe and Ni)

Footer Page TH-1334_08610706

The UV-Vis diffuse reflectance spectra and the Kubelka-Munk plot of codoped M-1N-TiO_2 samples are shown in Fig.4.26 (A) and (B). The band gap energy values obtained from the Kubelka-Munk method were 2.15, 2.5 and 2.6 eV for Cu-1N-TiO_2, Fe-1N-TiO_2 and Ni-1N-TiO_2, respectively.

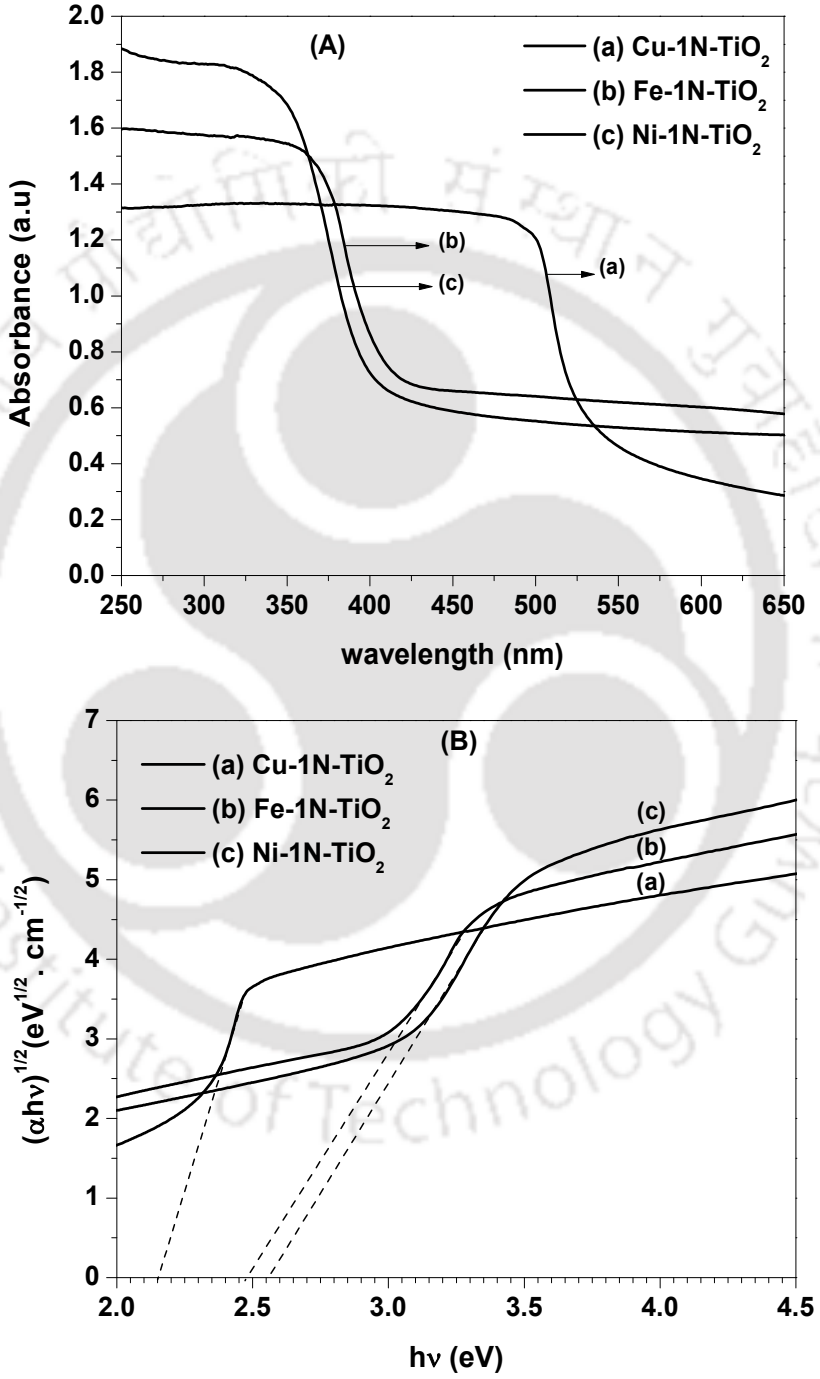

Fig.4.26. (A) UV-Visible diffuse reflectance spectra and (B) Kubelka-Munk plot of M-1N-TiO_2 (M = Cu, Fe and Ni)

Footer Page TH-1334_08610706

The incorporation of nitrogen reduced the band gap energy further in comparison with the respective M-TiO_2 samples. On codoping with nitrogen, the N 2p state is incorporated above the O 2p state. This increases the width of valance band, further lowering of the band gap energy of codoped samples. The most significant shift was observed Cu-1N-TiO_2 photocatalyst.

Fig.4.27 shows the PL spectra of M-1N-TiO_2 samples. The intensity of all the PL peaks of M-1N-TiO_2 samples was observed to be lower compared to that of respective M-TiO_2 samples (Fig.4.22). The decrease in peak intensity after incorporation of nitrogen in transition metal doped titania may be attributed to the oxygen vacancies generated by substitution of nitrogen. These oxygen vacancies have energies below conduction band and can trap the photogenerated electrons by non-radiative combinations (Wang et al., 2009). This further reduces the recombination rate of photogenerated electron with valance band holes. The effect was most intense for Ni-1N-TiO_2 samples for which peak intensity was lowest. Fe-1N-TiO_2 showed highest peak intensity.

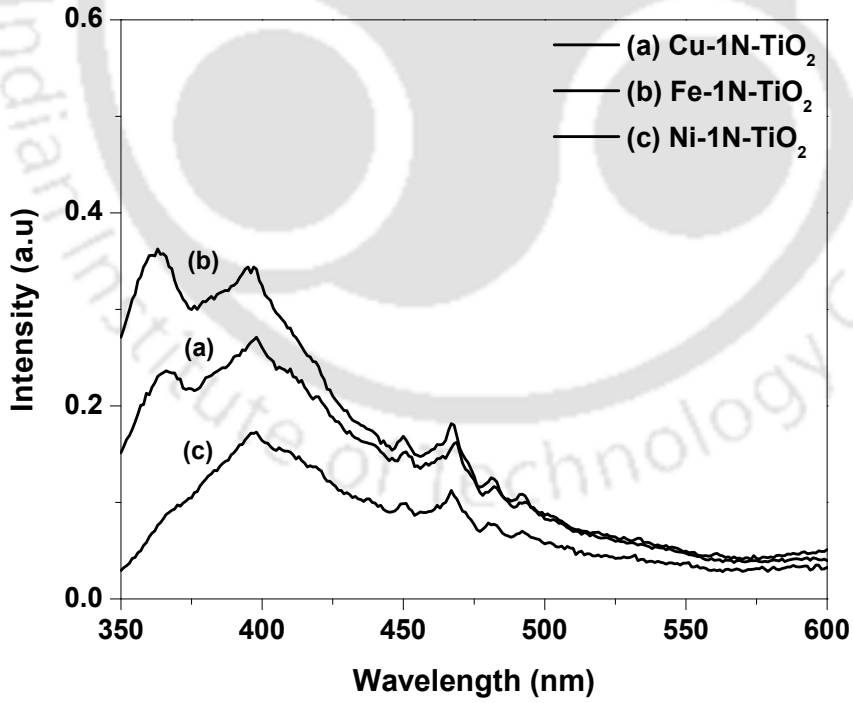

Fig.4.27. Photoluminescence spectra of M-1N-TiO_2 (M = Cu, Fe and Ni)

Footer Page TH-1334_08610706

Photocatalytic activity studies

The photocatalytic hydrogen production over codoped TiO_2 samples is shown in Fig.4.23. Addition of nitrogen in transition metal doped titania increased hydrogen production for all codoped samples with respect to M-TiO_2 samples. The highest hydrogen production was observed for Cu-1N-TiO_2 (1109 µmol/g/h) followed by that of Fe-1N-TiO_2 (499 µmol/g/h) and Ni-1N-TiO_2 (405 µmol/g/h). The enhancement in hydrogen production can be attributed to increased absorption of visible light and increased trapping of photogenerated electrons. Higher absorption of visible light gives increased number of photogenerated electrons. The increased efficiency in trapping of photogenerated electrons resulted in higher availability of these electrons for proton reduction reactions. The highest hydrogen production for Cu-1N-TiO_2 may be attributed to combined effect of higher surface area, increased absorption of visible light and enhanced efficiency in trapping of photogenerated electrons. The apparent quantum efficiency of Cu-1N-TiO_2, Fe-1N-TiO_2 and Ni-1N-TiO_2 were 22.1, 9.9 and 8.1 % respectively.

Footer Page TH-1334_08610706

4.3.3 Effect of variation of nitrogen doping

The effect of amount of nitrogen was studied for copper and nitrogen codoped samples. The amount of nitrogen was varied in the range of 0.5 to 1.5 at.%.

Characterization of photocatalysts

The N_2 adsorption-desorption isotherms of copper and nitrogen codoped samples at various nitrogen loadings are shown in Fig.4.28. The corresponding pore size distributions are shown in inset.

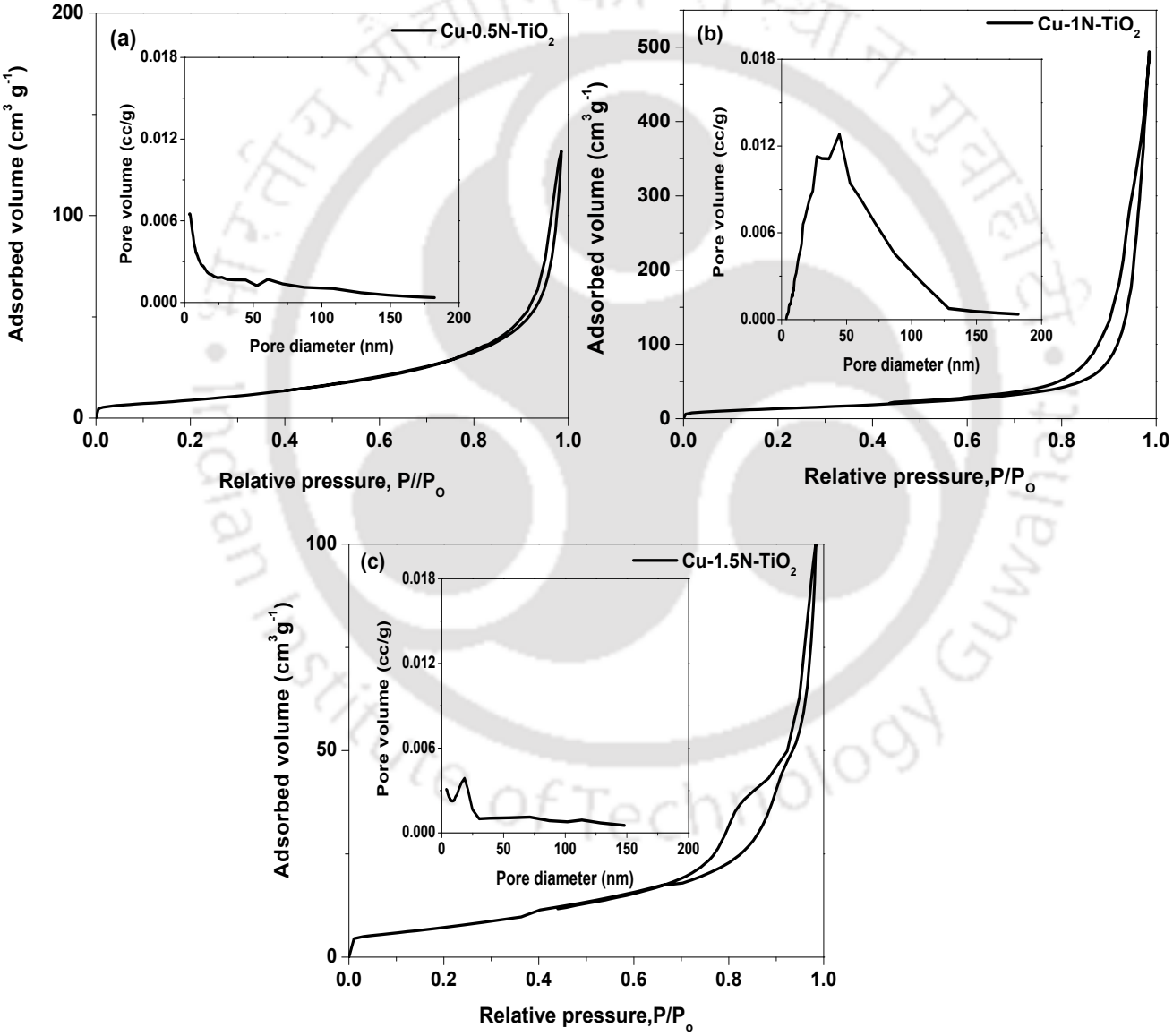

Fig.4.28. N_2 adsorption-desorption isotherms for (a) Cu-0.5N-TiO_2 (b) Cu-1N-TiO_2 and (c) Cu-1.5N-TiO_2 (Inset: pore size distributions)

Footer Page TH-1334_08610706

All the samples showed type III isotherms with H3 hysteresis loop. It can be observed that initially, with addition of nitrogen both surface area and pore volume of Cu-0.5N-TiO_2 increased compared to Cu-TiO_2 catalyst. However, with further increase in nitrogen loading both the surface area and pore volume decreased (Table 4.7) which can be attributed to partial pore blockage.

The XRD patterns of Cu-xN-TiO_2 samples were dominated by anatase phase as shown in Fig.4.29. With increasing nitrogen amount, lattice distortion value increased from 0.432 to 0.743 with corresponding change in lattice parameters as shown in Table 4.7. The higher amount of loading may have placed the nitrogen in interstitial as well as substitutional position causing the higher strain in lattice as observed.

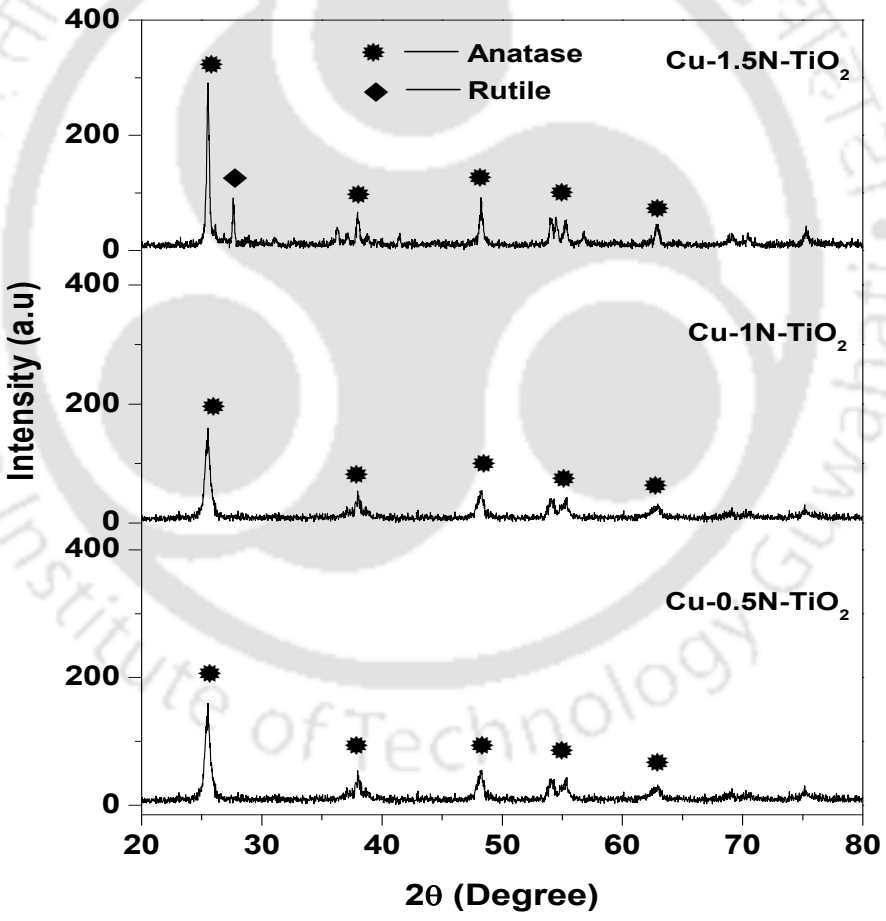

Fig.4.29. XRD patterns of Cu-xN-TiO_2 (x = 0.5, 1 and 1.5 at.%)

Footer Page TH-1334_08610706

The FESEM images of the copper and nitrogen codoped samples, at various nitrogen loadings, are shown in Fig.4.30 (a-c). At lower nitrogen doping, for Cu-0.5N-TiO_2 sample, the particles were less agglomerated and had spherical shape similar to Cu-TiO_2. However, with increase in content of nitrogen the extent of agglomeration increased. At highest doping, for Cu-1.5N-TiO_2 sample, the agglomeration was maximum with presence of larger pores.

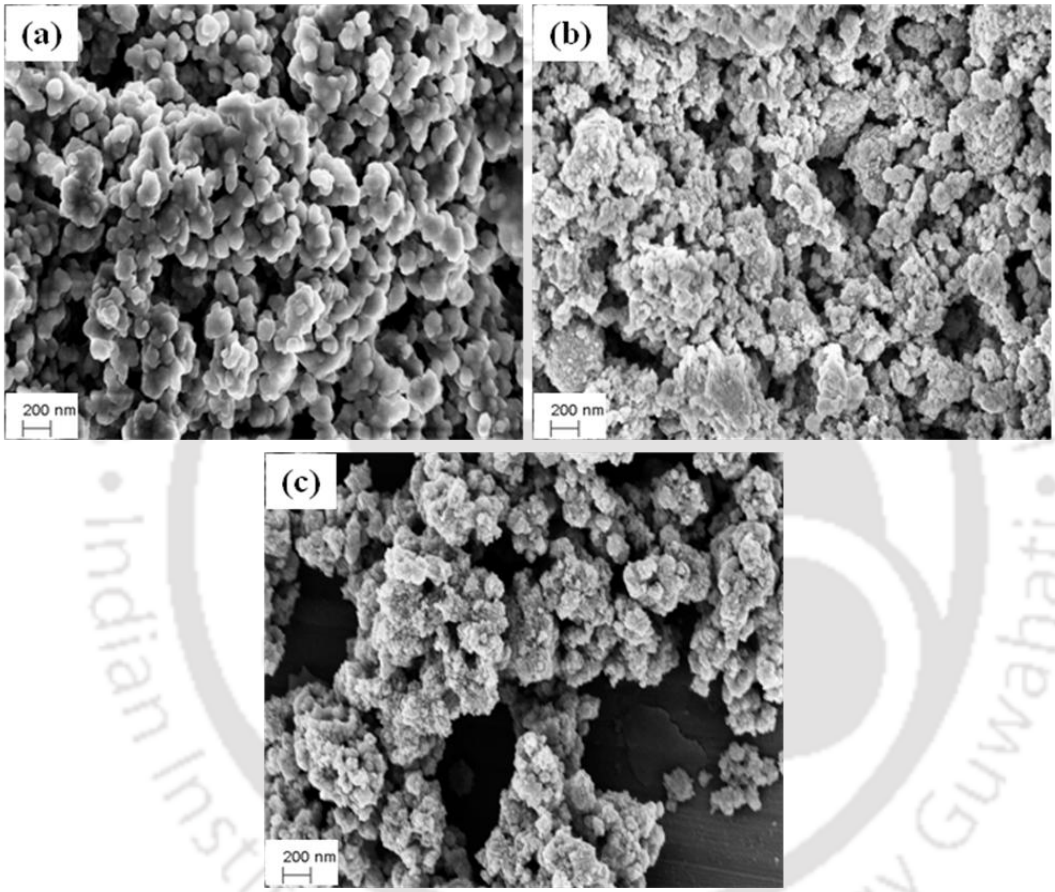

Fig.4.30. FESEM images of (a) Cu-0.5N-TiO_2 (b) Cu-1N-TiO_2 and (c) Cu-1.5N-TiO_2

Fig.4.31 (A) and (B), respectively, show the UV-Vis diffuse reflectance spectra and the Kubelka-Munk plot of codoped samples with different nitrogen amount. The band gap values calculated using the Kubelka-Munk method were 2.1 eV for Cu-0.5N-TiO_2, 2.15 eV for Cu-1N-TiO_2 and 2.83 eV for Cu-1.5N-TiO_2.

Footer Page TH-1334_08610706

All the Cu and N codoped samples showed a significant absorption in the visible light region. The maximum band gap reduction was observed for Cu-1N-TiO_2 sample. As the amount of nitrogen loading increased to 1.5 at.% in Cu-1.5N-TiO_2, a blue shift of the absorption edge was observed which may be attributed to the Burstein-Moss effect (Nair et al., 2011). With increase in doping concentration, the conduction band is expected to become filled due to the higher electron concentration. This results in an increase in the interband transition energy and also blocks the low energy transitions.

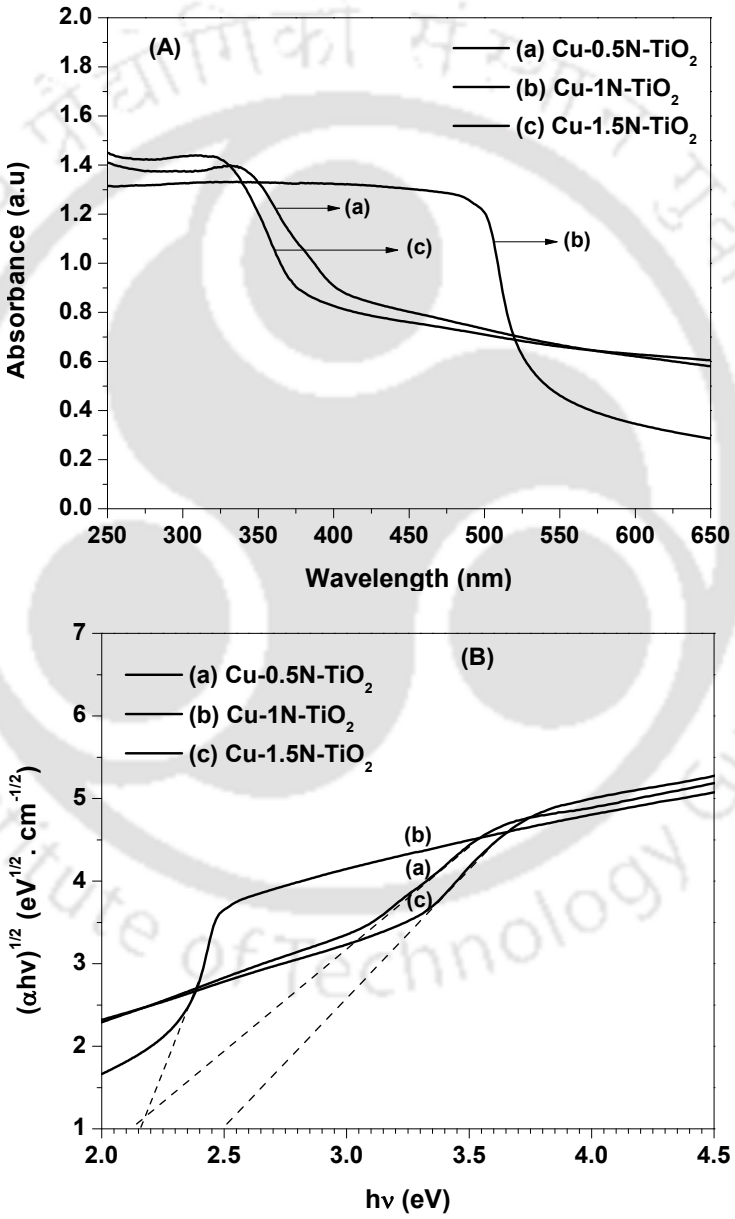

Fig.4.31. (A) UV-Visible diffuse reflectance spectra and (B) Kubelka-Munk plot for Cu and N codoped TiO_2 (a) Cu-0.5N-TiO_2 (b) Cu-1N-TiO_2 and (c) Cu-1.5N-TiO_2

Footer Page TH-1334_08610706

The photoluminescence spectra of Cu-xN-TiO_2 catalysts are shown in Fig.4.32. The PL emission intensity was lowest for Cu-1N-TiO_2. With increase in nitrogen content, increases in oxygen vacancies may have contributed to decrease in peak intensity through trapping of photogenerated electron by non-radiative recombination processes as discussed earlier. However again increase in peak intensity for Cu-1.5N-TiO_2 sample suggest that at higher nitrogen content, some of the nitrogen acted as radiative recombination centers for electron hole pair (Jagadale et al., 2008).

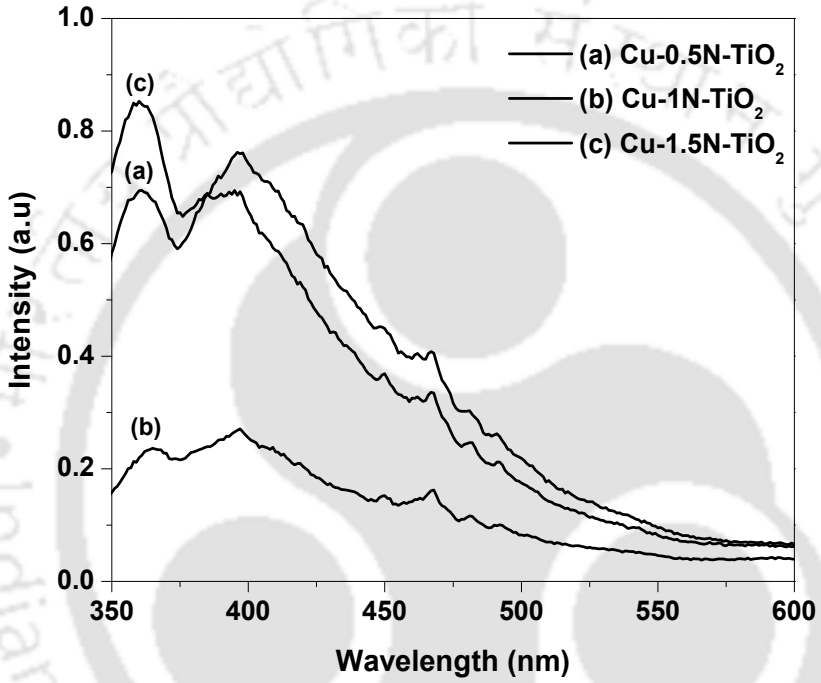

Fig.4.32. Photoluminescence spectra of Cu and N codoped TiO_2 (a) Cu-0.5N-TiO_2 (b) Cu-1N-TiO_2 and (c) Cu-1.5N-TiO_2

Photocatalytic activity studies

The hydrogen production values for various copper and nitrogen codoped titania photocatalysts were 1109 µmol/g/h (Cu-1N-TiO_2) > 900 µmol/g/h (Cu-1.5N-TiO_2) > 824 µmol/g/h (Cu-0.5N-TiO_2). The photocatalytic activity results are shown in Fig.4.33. Highest hydrogen production observed for Cu-1N-TiO_2 can be attributed to higher absorption of visible light and higher trapping of photogenerated electrons compared to other nitrogen doped samples. The apparent quantum efficiency of Cu-0.5N-TiO_2, Cu-1.0N-TiO_2 and Cu-1.5N-TiO_2 were 16.4, 22.1 and 18.0 % respectively.

Footer Page TH-1334_08610706

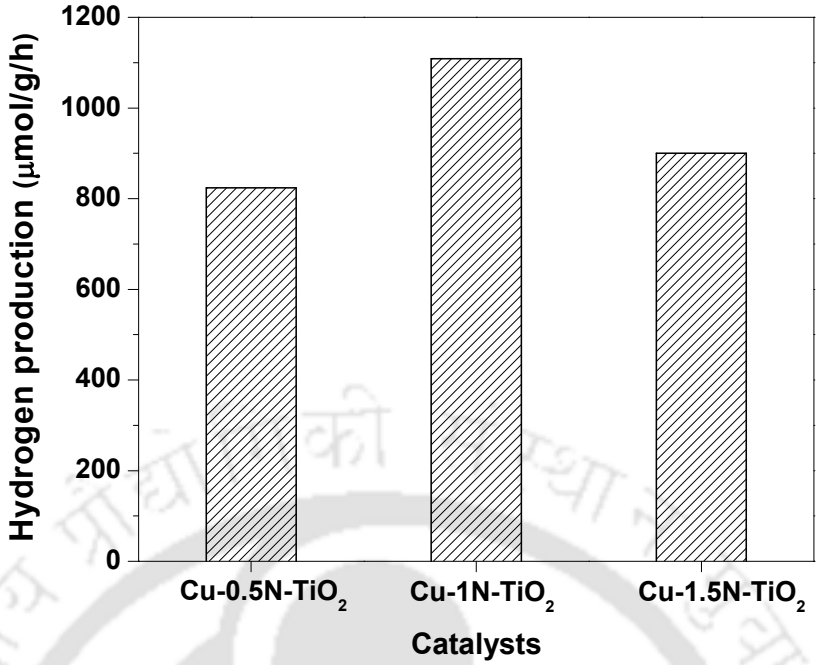

Fig.4.33. Hydrogen evolution for Cu-xN-TiO_2 (x = 0.5, 1, 1.5 at.%)

The analysis of the products showed that the gas phase contained only hydrogen and methanol vapor, while, in liquid phase only formaldehyde product was detected along with unreacted methanol. No other hydrocarbons or CO_2 were detected in gas phase and neither formic acid was detected in liquid phase. Hence it is assumed that the oxidation of methanol resulted in formaldehyde and further oxidation products, such as formic acid and CO_2, were not produced or was under detection level of the instruments. Hence the main reactions responsible for hydrogen production from water- methanol solution are proposed below in steps 1, 2, 3 and 4.

1. Photocatalyst + $h\nu \rightarrow e^- + h^+$

Reduction reaction (conduction band):

2. $2H^+ + 2e^-_{cb} \rightarrow H_2$

Oxidation reactions (valence band):

3. $H_2O + h^+_{vb} \rightarrow OH^\bullet + H^+$

4. $CH_3OH + 2h^+_{vb} (or\ 2OH^\bullet) \rightarrow 2H^+ \ (\text{or } 2H_2O) + HCHO$

Footer Page TH-1334_08610706

The e^{-}_{cb} and h^{+}_{vb} represent the electron in conduction band and hole in valence band respectively. The methanol can be oxidized either directly by holes or hydroxyl radicals generated from water splitting as shown by step 5. Using pure water as feed no hydrogen generation was observed while, using pure methanol hydrogen generation was low (173 µmol/g/h for Cu-1N-TiO_2). The hydrogen generation was drastically improved when water- methanol solution was used. This suggests that for the used catalysts, hydrogen generation was not possible by only water splitting. However, the hydroxyl radicals generated by water splitting may have significant contribution in oxidizing methanol for water-methanol system and enhance the hydrogen production. The negligible production of higher oxidation products such as formic acid and carbon dioxide may be attributed to catalyst and process conditions used. Thus the developed catalysts were able to generated hydrogen without co-products in gas phase, which is of great advantage.

Summary

The activity of transition metals (Cu, Fe or Ni) and nitrogen codoped TiO_2 photocatalysts was investigated for hydrogen production from water-methanol solution under visible light irradiation. The UV-visible spectra showed distinct red shift of the absorption edges for transition metal doped TiO_2. The visible light absorption was also enhanced for transition metal doped titania. Codoping with nitrogen further increased the absorption of visible light as well as more prominent shift of the absorption edge towards longer wavelength. The red shift can be attributed to the formation of electronic energy levels within the TiO_2 matrix by the dopants. The visible light absorption was highest for Cu-1N-TiO_2. The radiative recombination of photogenerated electron-hole pairs were effectively suppressed by codoping. The copper doped titania was most active among transition metal doped titania catalysts with hydrogen production of 938 µmol/g/h. The hydrogen evolution for copper doped titania increased on codoping with nitrogen and highest hydrogen generation of 1109 µmol/g/h was obtained. The observed high activity of copper and nitrogen codoped titania photocatalyst can be attributed to higher visible light absorption and higher electron trapping ability of multivalent copper.

Footer Page TH-1334_08610706

4.4 Indium-titanium coupled oxide

The indium-titanium coupled oxide was prepared by varying the indium amount in the range of 5-16 at.%. The coupled oxide was further doped with 2 at.% of copper.

Characterization of photocatalysts

Fig.4.34 shows the nitrogen adsorption-desorption isotherms of the indium-titanium oxides with different indium content and 2 %Cu-10%In-Ti sample. The isotherms of all the indium-titanium oxides were of type IV with H1 hysteresis loop corresponding to cylindrical pores (Sing et al., 1985). The isotherm pattern changed for 2 %Cu-10 %In-Ti. The isotherm was of type II and the hysteresis loop was of type H4 which corresponded to slit shaped pores. The surface area and pore volumes of the prepared samples are given in Table.4.9. With increase in indium content, the surface area increased and the highest value was observed for 16%In-Ti sample. The surface area was further enhanced with modification with copper oxide. The pore size distributions of samples are shown in the inset of Fig.4.34. The indium-titanium oxides exhibited a narrow pore size distribution in the range of 2-6 nm, whereas 2%Cu-10%In-Ti sample showed comparatively broader distribution in the range of 2-16 nm. The pore volume increased with increase in indium content in indium-titanium oxides. The pore volume was highest for 2%Cu-10%In-Ti. The amount of indium measured by energy dispersive spectroscopy (EDS) was 4.3, 9.5 and 16.7 at % Indium for 5%In-Ti, 10% In-Ti and 16% In-Ti, respectively. For copper doped indium-titanium ternary oxide, the contents of In and Cu were 8.6 and 1.9 at. %, respectively.

Table 4.9. Surface area, pore volume and lattice parameters of x% In-Ti (x = 5, 10, 16%) and 2%Cu-10%In-Ti catalysts

Catalyst	BET surface area (m^2/g)	Pore volume (cc/g)	Lattice parameters		Lattice distortion
			a(Å) (101)	c(Å) (004)	
5% In-Ti	159	0.3780	3.7703	9.4881	0.161
10% In-Ti	295	0.5760	3.7857	9.5123	0.235
16% In-Ti	328	0.6058	3.8186	9.5366	0.271
2%Cu-10% In-Ti	361	1.0613	3.9397	9.6401	0.283

Footer Page TH-1334_08610706

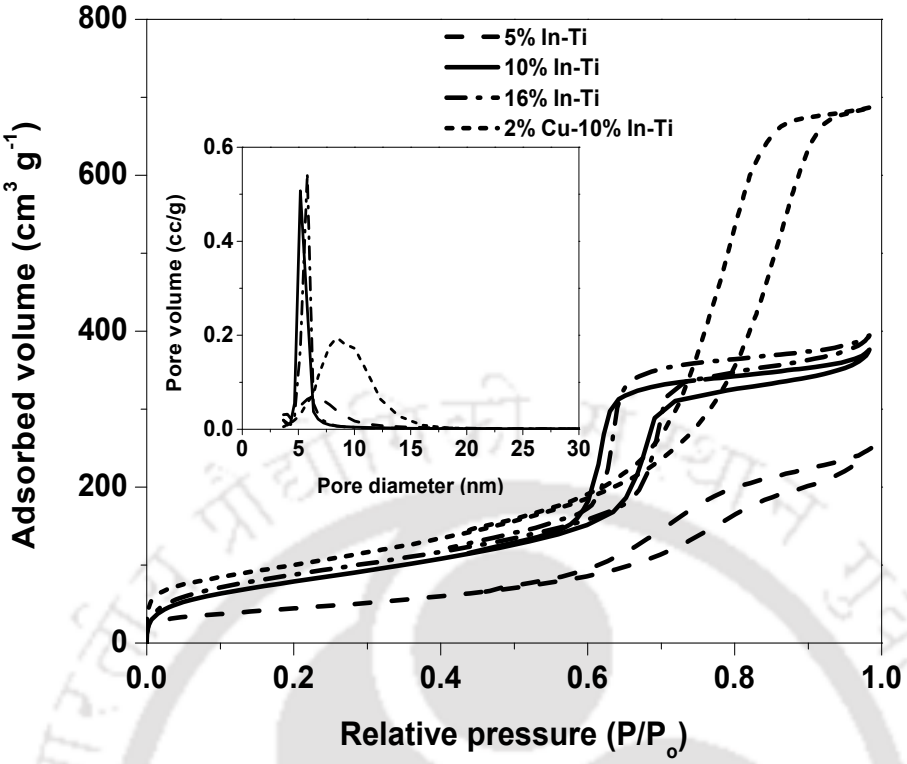

Fig.4.34. N_2 adsorption-desorption isotherms of *x*% In-Ti (*x* = 5, 10 and 16%) and 2%Cu-10%In-Ti

Fig.4.35. shows the XRD patterns of indium-titanium oxide samples with different indium content and 2 %Cu-10%In-Ti sample. The XRD patterns of indium -titanium oxides exhibited peaks that can be assigned to the cubic In_2O_3 and anatase TiO_2 structure. The diffraction peaks observed at 25.5° (101) and 30.6° (222) were the major peaks that can be attributed toTiO_2 and In_2O_3 respectively (JCPDS No: 76-0152 and JCPDS No:21-1272). The intensity of the In_2O_3 peak increased with increase in content of indium in binary oxides. In the ternary 2%Cu-10%In-Ti oxide, in addition to peaks of indium and titanium oxides, an additional broad peak was observed with highest intensity at 36.2^o. The peak observed at 36.2° can be attributed to the 111 plane of cubic phase of Cu_2O (JCPDS No: 05-0667). The CuO shows peaks at 2θ = 32.2, 35.5, 38.4, 50.1, 53.3 and 67.7 (JCPDS No: 80-1917). Though no prominent peak due to CuO was observed in the XRD profile of the ternary oxide however, the shoulder at 35.2 may be attributed to CuO. The intensity of peak due to CuO was much lower than that of Cu_2O. Hence, it may be assumed that the copper in the ternary oxide was mostly in Cu_2O state with minor amount of CuO. The preferential

Footer Page TH-1334_08610706

formation of Cu_2O can be attributed to reduction of Cu^{2+} ions to Cu^{+} ions by D-glucose during co-precipitation (Luo et al., 2005).

The lattice distortion values of the samples were calculated and given in Table 4.9. As expected, the lattice parameters increased with the increase in the amount of indium loading. The maximum strain was observed for 16 % In-Ti among the indium loaded samples. With the addition of Cu in to the In-Ti crystal lattice further increased the lattice distortion as well as the lattice parameters along the a and c axes. The origin of lattice distortion can be attributed to the ionic radius difference between the dopant metal ions and host Ti ions. The dopants In^{3+} and Cu^{+} are more likely to reside in the interstitial sites of TiO_2due to their higher ionic radii (In^{3+} 0.092 nm; Cu^{+} 0.077 nm) than Ti^{4+} (0.068 nm), accordingly higher lattice distortion was obtained.

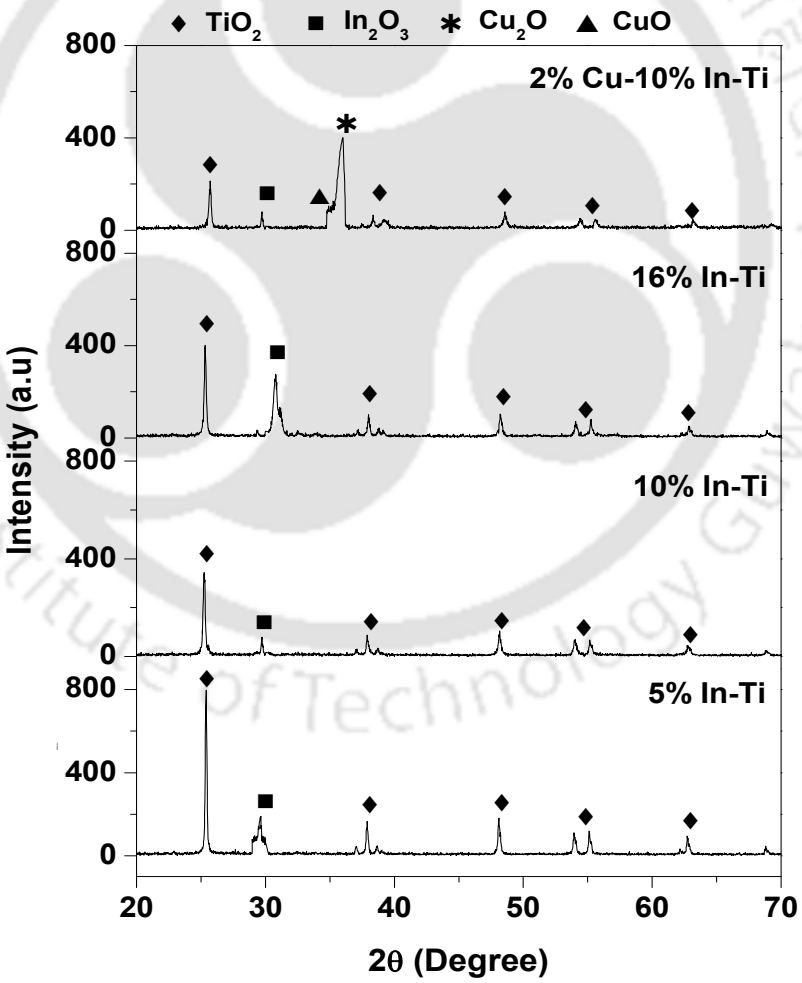

Fig.4.35. XRD patterns of *x*% In-Ti (*x* = 5, 10 and 16%) and 2%Cu-10%In-Ti

Footer Page TH-1334_08610706

Fig.4.36 (a-d) shows the FESEM images of different indium-titanium oxides and 2 %Cu-10%In-Ti oxide. The 5%In-Ti sample was more agglomerated in nature. As the indium oxide content increased in the binary oxides, the particles attained more distinct spherical shape. With increasing indium oxide content more structured spherical morphology may have resulted in increased surface area. The size of the spherical particles was in the range of 20-50 nm for 10% In-Ti and 20% In-Ti oxides. The 2%Cu-10%In-Ti sample also exhibited well structured spherical particles in the same range.

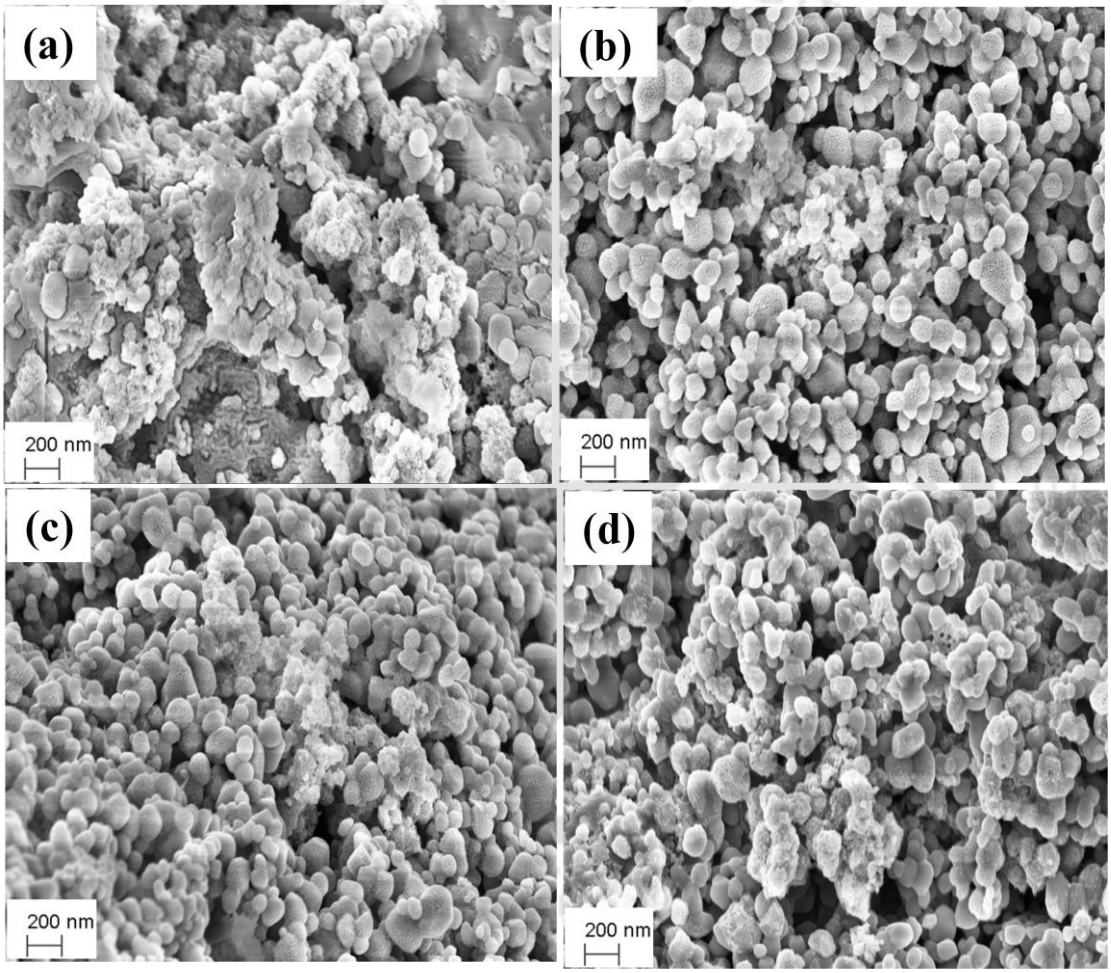

Fig.4.36. FESEM images of (a) 5% In-Ti (b) 10% In-Ti (c) 16% In-Ti and (d) 2%Cu-10%In-Ti

Footer Page TH-1334_08610706

Fig.4.37 (A) shows the UV-Vis diffuse reflectance spectra of the binary and ternary oxide samples. The Kubelka-Munk method was employed to calculate the band gap of the oxide samples (Lim et al., 2011). The plots of $(\alpha h\nu)^{1/2}$ vs. hν for indium-titanium oxides and 2% Cu-10% In-Ti are presented in Fig.4.37 (B).

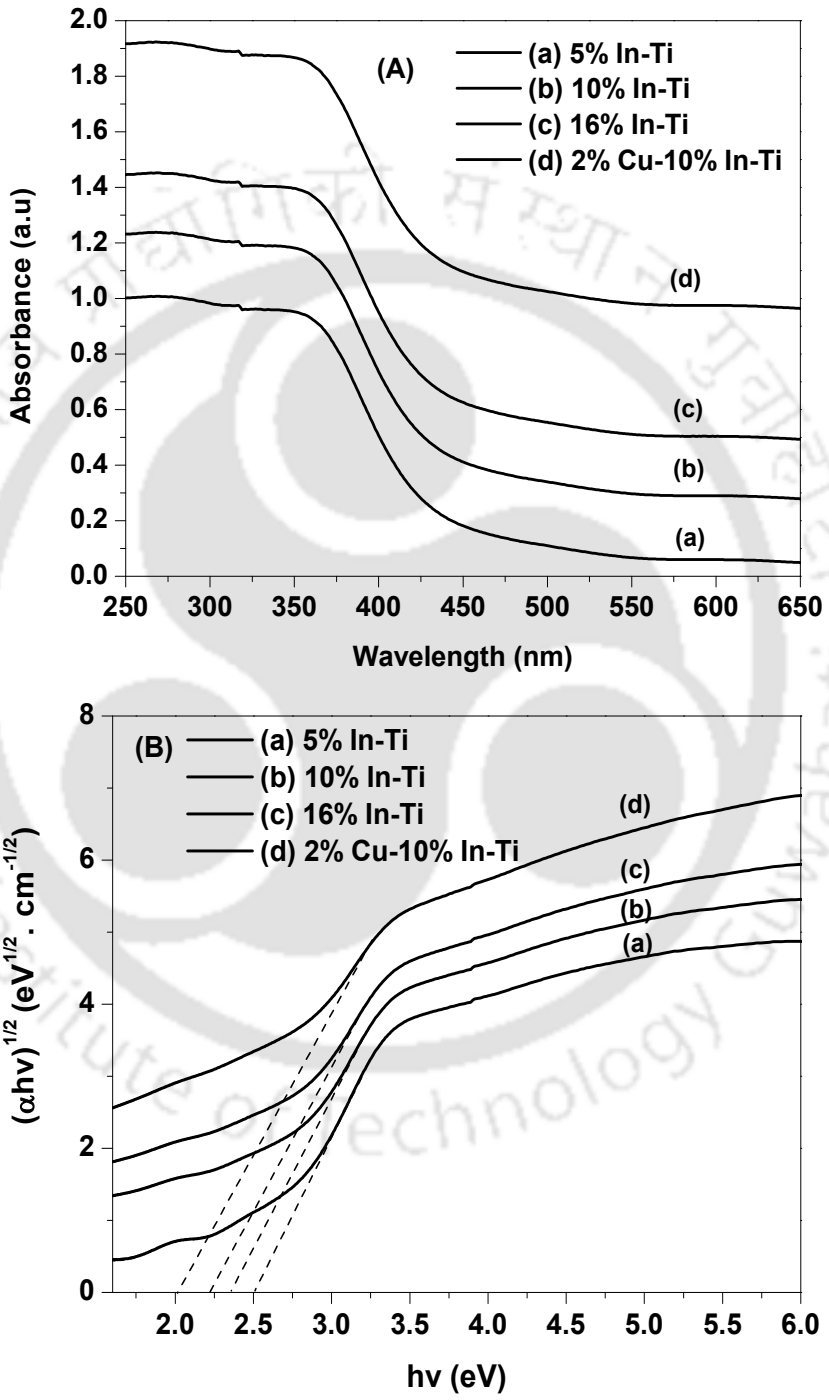

Fig.4.37. (A) UV-Vis diffuse reflectance spectra and (B) Kubelka-Munk plot of *x*% In-Ti (*x* = 5, 10 and 16%) and 2%Cu-10%In-Ti

Footer Page TH-1334_08610706

The band gap energy of the oxides was estimated by extrapolating the straight line portion of $(\alpha h\nu)^{1/2}$ vs $h\nu$ plot to the energy axis. The band gap values obtained for the oxides were 2.5 eV (5%In-Ti), 2.35 eV (10%In-Ti), 2.2 eV (16%In-Ti) and 2.01 eV (2%Cu-10%In-Ti). All the indium-titanium oxides exhibited absorption in the visible region. As the amount of lower band gap indium oxide increased, there was considerable increase in the visible light absorbance and red shift for the binary oxides. The 16% In-Ti sample showed highest absorption and the largest red shift. On addition of copper oxide, the ternary oxide showed further red shift in absorbance as well as increased absorption in the visible light region. This may be attributed to the copper ions, which can act as a chromophore and absorb light in the visible range.

The photoluminescence spectra of the indium-titanium oxides and 2%Cu-10%In-Ti are shown in Fig.4.38. All the samples exhibited a broad and strong photoluminescence peaks at 385, 440 and 460 nm, corresponding to the transition energy values 3.22, 2.81and 2.69 respectively. The peaks observed at 385 nm can be attributed to the emission of band gap transition of TiO_2 (Meng et al., 2012). The indium oxide is associated with oxygen vacancies due to its structural defects (Beena et al., 2011). Hence on coupling of indium oxide with titanium oxide these additional oxygen vacancies can act as traps for photogenerated electrons. The PL peaks at 440 and 460 nm can mainly be attributed to excitonic emissions due to presence of oxygen vacancies (Papageorgiou et al., 2011; Zhang, 2013). As observed from PL spectra, with increase in indium oxide content, the emission intensities of the binary oxides decreased suggesting that in the couple oxides the photogenerated electron-hole pairs were effectively separated and stabilized. The addition of copper oxide resulted in further decrease in the peak intensity of 2%Cu-10%In-Ti compared to that of 10%In-Ti sample.

Footer Page TH-1334_08610706

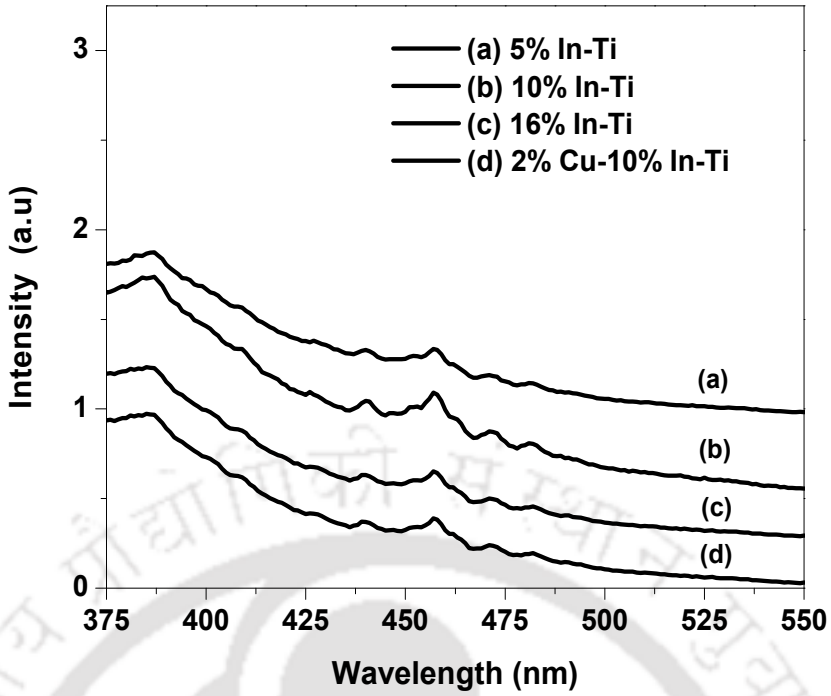

Fig.4.38. Photoluminescence spectra of *x*% In-Ti (*x* = 5, 10 and 16%) and 2%Cu-10%In-Ti

Photocatalytic activities

The photocatalytic activities of indium-titanium oxides and 2%Cu-10%In-Ti are shown in Fig.4.39. The hydrogen was produced from aqueous methanol solution under visible light irradiation for all the photocatalysts. For pure titanium oxide (surface area 84 m^2/g) the hydrogen generation was negligible under reaction conditions. For pure indium oxide (surface area 119 m^2/g) the hydrogen generation was observed to be 1250 µmol/g/h. The coupling of indium oxide and titanium oxide improved the hydrogen generation significantly in spite of using much lower amount of indium oxide. This is advantageous as precursor for indium oxide is expensive. For 5% In-Ti photocatalyst a hydrogen production of 1546 µmol/g/h was obtained. With increase in indium content for binary catalysts, the hydrogen evolution increased gradually and reached a maximum value of 1829 µmol/g/h for 16% In-Ti photocatalyst.

Footer Page TH-1334_08610706

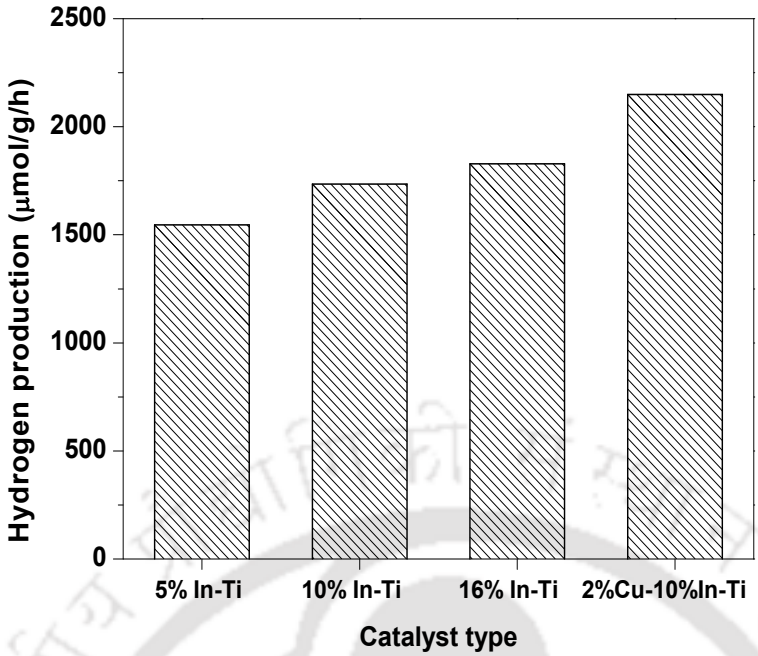

Fig.4.39. Hydrogen production for *x*% In-Ti (*x* = 5, 10 and 16%) and 2%Cu-10%In-Ti

The improved efficiency of the indium-titanium coupled oxides can be attributed to several factors. The coupling of two oxides enhanced the surface area and with increase in indium oxide content the surface area was increased further (Table 4.9). The increase in surface area generally increases the availability of the interaction sites on a catalyst. Increase in indium oxide content also increased the absorption of visible light (Fig.4.37 (A)). Both the factors can enhance the generation of photoelectron-hole pairs in the coupled oxide. The stability of the photogenerated electrons and holes in the indium-titanium coupled oxides was increased due to suitable band potentials providing efficient charge separation. As shown in Fig.4.40, visible light can be absorbed by low band gap indium oxide generating the photoexcited electrons in the conduction band of In_2O_3 that can be transferred to the TiO_2 at the heterojunction since the conduction band potential of In_2O_3 (-0.63 V vs NHE at pH=7) is more negative than that of TiO_2 (-0.5 V vs NHE at pH=7) (Mu et al., 2012; Hirakawa and Kamat, 2005). However, the titanium oxide cannot absorb any visible light due to its wide band gap. Thus the coupling of indium and titanium oxides enhanced the mobility of photogenerated electrons thereby, decreasing their recombination tendency and increasing participation in reactions.

Footer Page TH-1334_08610706

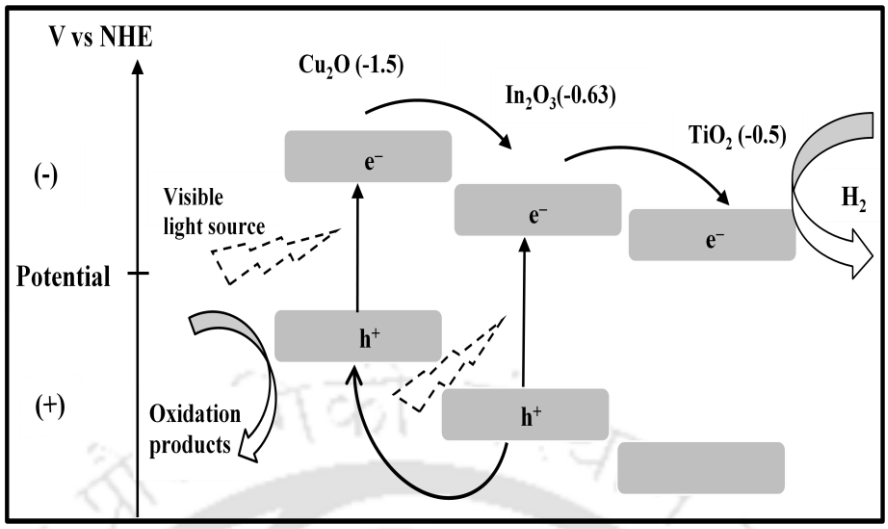

Fig.4.40. Schematic diagram of hydrogen generation in Cu_2O-In_2O_3-TiO_2 system

The hydrogen production was enhanced with increase in indium content in binary oxides, however the extent of increase was gradually reduced. The enhancement of hydrogen production was 189 µmol/g/h when In was increased from 5 at.% (1546 µmol/g/h) to 10 at.% (1735 µmol/g/h) which dropped to 94 µmol/g/h for increase from 10 at.% to 16 at.% (1829 µmol/g/h). Since indium nitrate is expensive and enhancement effect was reduced at higher indium loadings 10%In-Ti was chosen for preparation of ternary oxide. Incorporation of 2 at.% copper into 10 % In-Ti oxide showed higher photocatalytic activity compared to 10% In-Ti oxide. The hydrogen production for 10% In-Ti oxide was 1735 (µmol/g/h) which increased to 2149 µmol/g/h for 2%Cu-10%In-Ti oxide photocatalyst. Addition of copper oxide to binary oxide improved the surface area (Table 4.9) and visible light absorption (Fig. 4.37 (A)). The narrow band gap Cu_2O (2.17 eV) and CuO (1.7 eV) (Yu et al., 2012; Zhao et al., 2012) can generate additional electrons and holes under visible light irradiation. These photogenerated electrons in the conduction band of copper oxide can be stabilized by the mobility of the electrons from conduction band of copper oxide to indium oxide improving the charge separation. The mobility of electrons from Cu_2O/CuO band to the In_2O_3 band is facilitated by more negative conduction band potential of Cu_2O (-1.5 V vs NHE at pH=7) and CuO (-0.78 V vs NHE at pH=7) (Huang et al., 2009; Quin et al., 2011) compared to that of In_2O_3. The mobility of

Footer Page TH-1334_08610706

photogenerated electrons from Cu_2O to In_2O_3 to TiO_2 is shown in Fig.4.40. The reduction reaction occurs at the conduction band while oxidation reactions occur at the valence band. For comparison a ternary oxide was also prepared by incorporating 2 at.% copper in 16%In-Ti and evaluated for hydrogen production under similar reaction condition. The hydrogen evolution for 2%Cu-16%In-Ti was lower at 1848 µmol/g/h compared to 2149 µmol/g/h for 2%Cu-10%In-Ti. The lower activity of the 2%Cu-16%In-Ti can be attributed to its lower surface area and visible light absorption compared to that of 2%Cu-10%In-Ti. The comparisons of surface area and visible light absorption of two ternary oxides are shown in Table 4.10 and Fig. 4.41 respectively. The apparent quantum efficiency of the photocatalysts was calculated using the method followed by Sasikala et al. (2008). The calculated efficiencies of the 5%In-Ti, 10%In-Ti, 16%In-Ti and 2%Cu-10%In-Ti photocatalysts were 30.9, 34.7, 36.5 and 42.9 % , respectively.

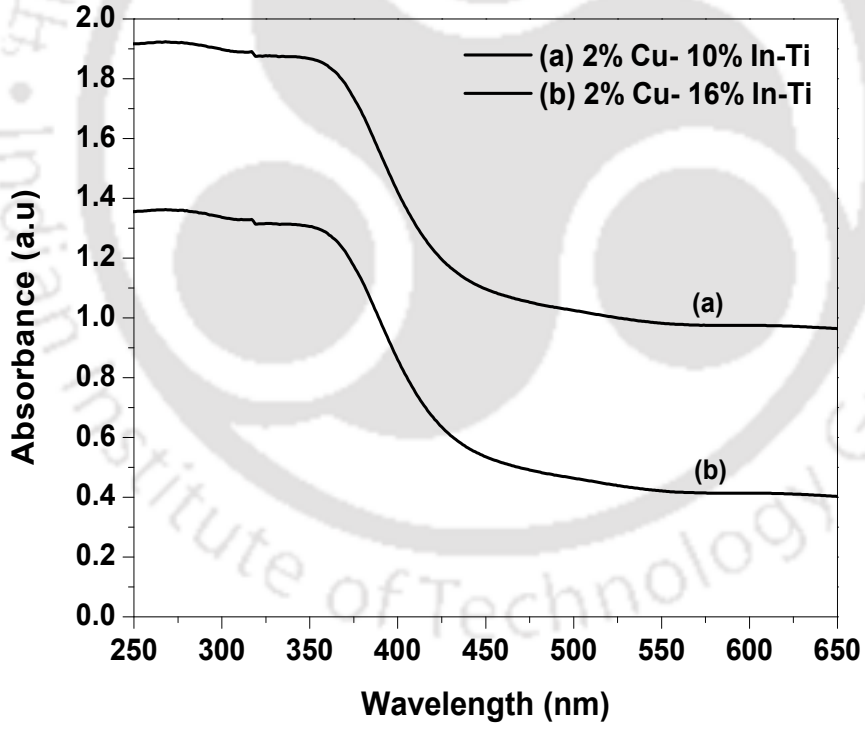

Fig.4.41. Comparison of UV-Vis diffuse reflectance spectra of 2%Cu-10%In-Ti and 2%Cu-16%In-Ti

Footer Page TH-1334_08610706

Table 4.10. Comparison of BET surface area and pore volume of 2%Cu-10%In-Ti and 2%Cu-16%In-Ti

Catalyst	BET surface area (m^2/g)	Pore volume (cc/g)
2%Cu-10% In-Ti	361	1.0613
2%Cu-16% In-Ti	319	0.5910

During product analysis it was observed that in gaseous state only hydrogen along with unconverted methanol was present. No other component was detected. In liquid phase only formaldehyde and unconverted methanol was detected. The results suggested that the methanol was partially oxidized in the reaction conditions to formaldehyde and hydrogen. However, the formaldehyde was not further oxidized to formic acid or carbon dioxide. Based on this analysis following reaction scheme has been proposed.

(A) Generation of electron (e^-) and holes (h^+)

$$(1)\ \text{photocatalyst} \xrightarrow{h\nu} h^+_{vb} + e^-_{cb}$$

(B) Reduction reactions at conduction band:

$$(2)\ 4H^+ + 2e^-_{cb} \rightarrow 2H_2$$

(C) Oxidation reactions at valence bands:

Path 1:

$$(3)\ CH_3OH + 2h^+_{vb} \rightarrow 2H^+ + HCHO$$

Path 2:

$$(4)\ 2H_2O + 2h^+_{vb} \rightarrow 2OH^\bullet + 2H^+$$

$$(5)\ CH_3OH + 2OH^\bullet \rightarrow 2H_2O + HCHO$$

Footer Page TH-1334_08610706

As shown in the reaction scheme, methanol can be oxidized by valence band holes (Path 1; step 3) producing formaldehyde and hydrogen ions. The hydrogen ions are reduced to hydrogen by conduction band electrons as shown in step 2. However, the methanol can also be oxidized by hydroxyl ions (Path 2; step 5) generated by oxidation of water (step 4). Though, the probability of occurrence of path 2 compared to path 1 is lower as methanol is easier to oxidize than water (Sabio et al., 2012). Irrespective of the oxidation path of methanol, it should result in formation of equimolar hydrogen and formaldehyde. The formation of almost equimolar amount of hydrogen (2149 µmol/g/h) and formaldehyde (2108 µmol/g/h) during experiment confirmed the occurrence of partial oxidation of methanol to formaldehyde and hydrogen. The results of equimolar amount of hydrogen and formaldehyde were shown in Fig.4.42.

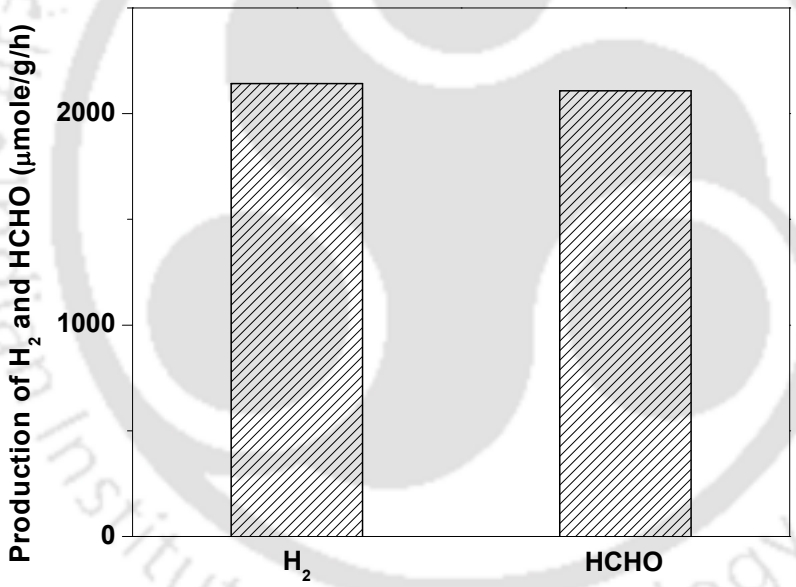

Fig.4.42. Generation of hydrogen and formaldehyde over 2%Cu-10%In-Ti catalyst (Feed composition; methanol: 1 ml and water: 25 ml)

Footer Page TH-1334_08610706

Summary

Titanium oxides coupled with different amount of indium oxides were studied for production of hydrogen under visible light irradiation from water methanol solution. With increases in indium oxide content, the surface area and visible light absorption of the binary catalyst increased. Separation of photogenerated electron-holes was also enhanced in indium-titanium binary oxides. For binary catalyst the activity was highest for 16.7 at.% indium content with hydrogen production of 1829 µmol/g/h whereas for ternary catalyst containing 1.9 at.% copper the hydrogen production increased to 2149 µmol/g/h. The higher hydrogen production for ternary catalyst can be attributed to the synergistic effects of higher surface area, stronger absorption in the visible light region and enhanced separation of photogenerated charge carriers. The hydrogen generation was attributed to partial oxidation of methanol to formaldehyde thereby producing pure hydrogen.

Footer Page TH-1334_08610706

4.5 Indium-transition metal coupled oxide

The indium oxide was coupled with various transition metals such as copper, nickel and zinc and was investigated for hydrogen production from water-methanol mixture under visible light irradiation.

Characterization of photocatalysts

The nitrogen adsorption-desorption isotherms of indium oxide and indium-transition metal coupled oxides are shown in Fig.4.43 (A) and the corresponding pore size distributions are shown in Fig.4.43 (B). The nature of isotherm and hysteresis loop was different for different couple oxides indicating development of different porous structure during co-preparation. The isotherm of indium oxide was of type II with H2 hysteresis loop corresponding to interconnected pores. The pores were in range of 6-22 nm as can be observed from Fig.4.43 (B). The In-Cu coupled oxide exhibited type IV isotherm and H2 hysteresis loop. The pore size distribution was narrower compared to pure indium oxide in the mesopore range of 5-10 nm. For In-Ni coupled oxide, the isotherm was more of type II with H3 hysteresis loop characteristics of wide slit shaped pores. A sharp increase in nitrogen adsorption was observed at higher pressure which suggested occurrence of significant condensation of nitrogen. A broad pore size distribution in the range of 6-58 nm was obtained (Fig.4.43 (B)). The nitrogen adsorption was comparatively lower for In-Zn coupled oxide. The isotherm was of type II with H4 hysteresis associated with slit shape pores in lower size range**.** The values of surface area and pore volume of all the samples are shown in Table 4.11. As can be observed from Table 4.11, the surface area was enhanced when indium oxide was coupled with transition metals. The surface area was highest for In-Cu coupled oxide closely followed by In-Ni. The enhancement in surface area of In-Zn was comparatively less. However, the highest pore volume was observed for In-Ni (0.977cc/g) followed by In-Cu (0.497 cc/g). The In-Zn sample exhibited the lowest pore volume of 0.190 cc/g. The higher pore volume of In-Ni agrees with the broader pore size distribution.

Footer Page TH-1334_08610706

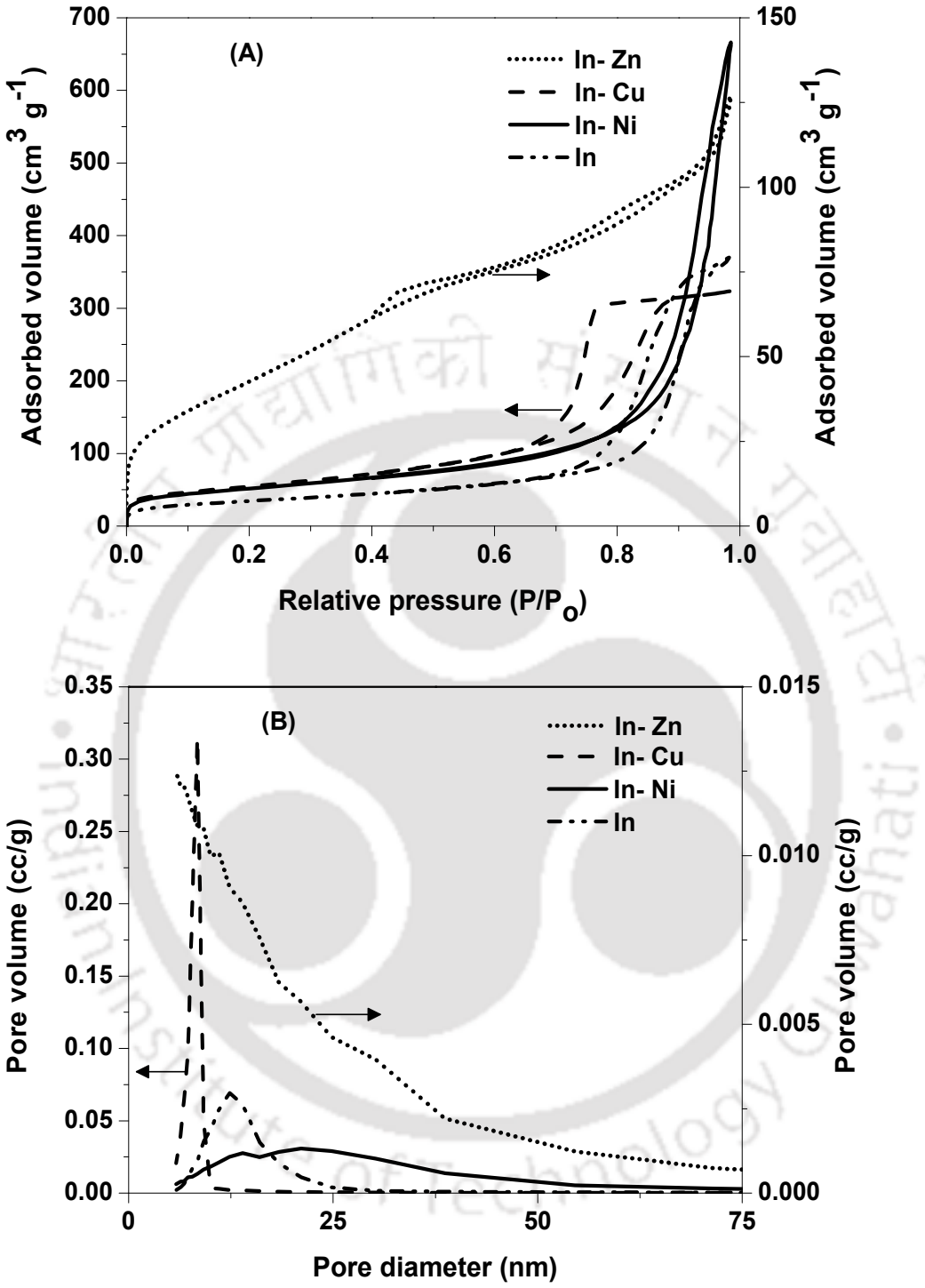

Fig.4.43. (A) N_2 adsorption-desorption isotherms and (B) pore size distribution of In-Zn, In-Cu, In-Ni and In

Footer Page TH-1334_08610706

Table 4.11. Surface area, pore volume and lattice parameters for In and In-TM (TM = Cu, Ni, Zn)

Catalyst	BET surface area (m^2/g)	Pore volume (cc/g)	In_2O_3 cell (rhombohedral structure) parameters		Lattice distortion
			a = b (Å)	c (Å)	
In	119	0.568	5.3107	14.3126	0.057
In-Cu	190	0.497	5.4031	14.4115	0.068
In-Ni	185	0.977	5.3812	14.3804	0.067
In-Zn	135	0.190	5.3604	14.3613	0.064

The composition of the coupled systems measured by EDS analysis is shown in Table 4.12. The results showed variation in indium amount in the coupled oxides which can be attributed to different batches of preparation as well as different precipitation characteristics of the components. The hydrogen production was normalized based on indium amount to minimize the effect of variation of indium content in the coupled oxides.

Table 4.12. EDS results of In and In-TM (TM = Cu, Ni, Zn)

Sample name	Elements (at.%)	
	In	Transition metals
In	41.69	-
In-Cu	3.96	49.16
In-Ni	5.51	13.61
In-Zn	11.0	33.63

The XRD patterns of the indium-transition metal coupled oxides are shown in Fig.4.44. In all coupled oxides the most prominent peaks were observed at 30.9° and 32.6 which can be attributed to rhombohedral In_2O_3 (JCPDS card No: 22-0336). The

Footer Page TH-1334_08610706

other peaks corresponding to this structure were obtained at 22.3°, 38.4°, 40.1°, 45.6° and 52.4°. In all the indium-transition coupled oxides the peaks assigned to rhombohedral In_2O_3 can be observed. The peak intensities of two prominent peaks of rhombohedral In_2O_3 phase did not change significantly when coupled with transition metal oxides, suggesting that the crystalline structure of indium oxide was mostly retained in coupled oxides. For In-Cu, the major peaks observed at 2θ =36.3° and 42.2° can be attributed to Cu_2O (JCPDS card No: 74-1230). Though, no prominent peaks due to CuO were observed, however the shoulders observed at 35.4 and 39.1° may be attributed to CuO (JCPDS No: 80-1917). The preferable formation of Cu_2O can be attributed to addition of D-glucose during preparation of In-Cu which acted as reducing agent (Yan et al., 2010). For In-Ni sample, the peaks at 39.2° and 63.9° corresponded to the cubic structure of NiO (JCPDS card No: 47-1049). The peaks observed at 34.2° and 36.0° for In-Zn couple oxide can be attributed to the wurtzite hexagonal phase of ZnO (JCPDS card No: 36-1451).

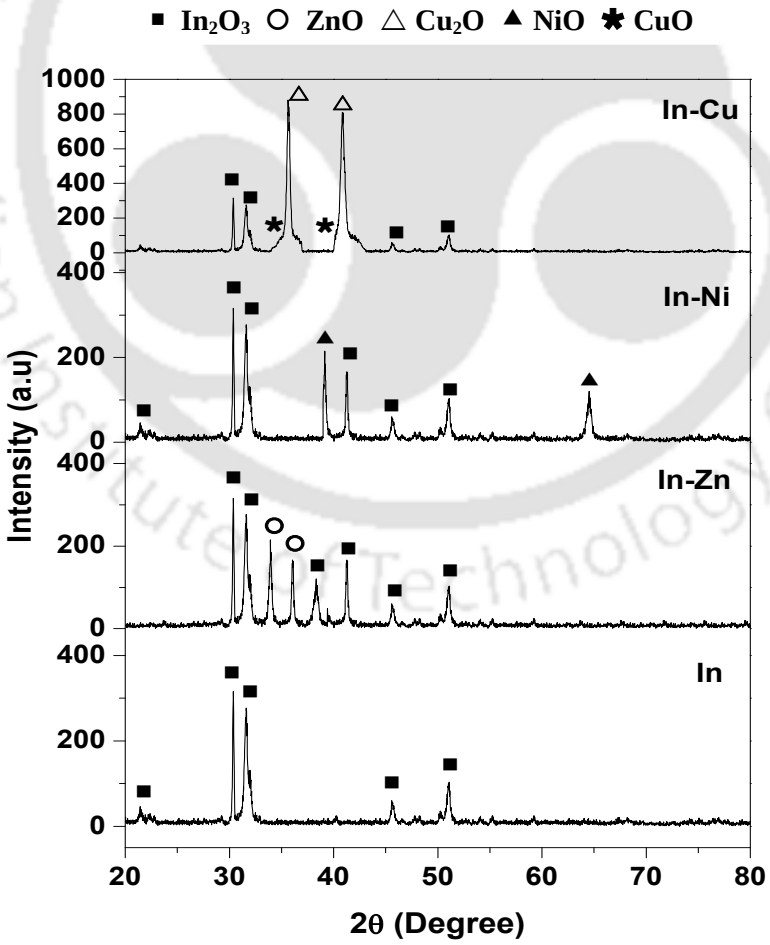

Fig.4.44. XRD patterns of In-TM (TM = Cu, Ni, Zn)

Footer Page TH-1334_08610706

For all the coupled oxides distinct peaks due to transition metal oxides as well as indium oxide entities were observed. No peaks were observed for any mixed phase in any sample. The observations suggested that the respective structure of the constituting oxides were more or less retained in coupled oxides resulting in heterogeneous system. The lattice parameters and distortion values for indium oxide are shown in Table 4.11. For coupled oxides the change in lattice parameter and distortion values for indium oxides was very small compared to that for pure indium oxide confirming the existence of heterogeneous crystalline system.

Fig.4.45 (a-d) shows the FESEM images of indium oxide and indium-transition metal coupled oxides. The large agglomerates were observed for indium oxide. Coupling of indium oxide with transition metal oxides resulted in development of different morphologies as can be observed from the Fig.4.45 (b-d). For In-Ni, flowery structures consisting of rod like petals were observed. For In-Cu uniform and rectangular particles were observed. In case of In-Zn, agglomerates were observed similar to indium oxide however the size was comparatively smaller for coupled oxide. The larger surface area and pore volume of In-Cu and In-Ni compared to that of indium oxide can be attributed to formation of highly crystalline structure of the formers. The unique morphology of widely separated rod shaped structure of In-Ni is also expected to result in wide slit pores and very high pore volume as observed. The low surface area for In-Zn compared to that of In-Cu and In-Ni may be attributed to its less crystalline nature. However, its higher surface area and pore volume with respect to indium oxide may have resulted from the smaller size of the agglomerates. The narrower pore size distribution of In-Cu compared to indium oxide and other coupled oxides may be attributed to its more uniform structure. The very broad pore size distribution for In-Ni with the presence of very large pores can be explained by its widely separated rod like structure. For In-Zn the very low pore volume may be due to the agglomerated structure with presence of significant amount of mesopores in lower range.

Footer Page TH-1334_08610706

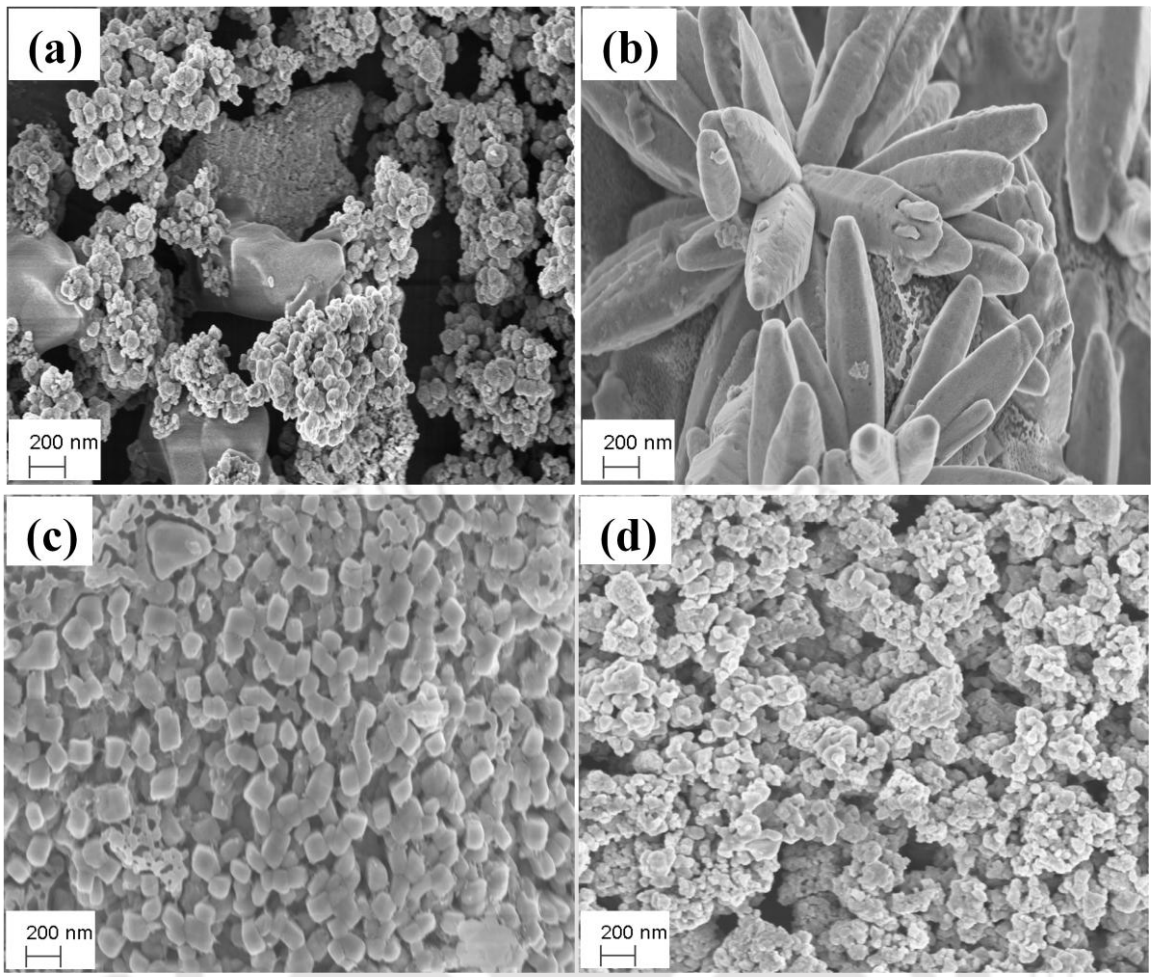

Fig.4.45. FESEM images of (a) In (b) In-Ni (c) In-Cu and (d) In-Zn

Fig.4.46 (A) shows the UV-Vis diffuse reflectance spectra of the indium oxide and indium-transition metal coupled oxides. The plot of $(\alpha h\nu)^{1/2}$ as a function of photon energy is shown in Fig.4.46 (B). As shown in the figure (Fig.4.46 (B)), a straight line was extrapolated to the x- axis, and at $\alpha = 0$, $E_{bg} = h\nu$. The estimated band gap energies of the samples were 2.05, 2.1, 2.6 and 2.2 eV for In-Cu, In-Ni, In-Zn and In respectively**.** The most significant red shift of the absorption edge and absorption in visible region were observed for In-Cu coupled oxide. For In-Ni only a small red shift of the absorption edge towards the visible region was observed, whereas in case of In-Zn the absorption edge showed a blue shift to 416 nm compared to that of indium oxide (480 nm). The significant increase in visible light absorption for In-Cu can be attributed d electron transition of copper ions. Nickel ions mostly absorbs in near UV region while zinc ions with filled d orbitals are unable to significantly contribute to

Footer Page TH-1334_08610706

light absorption. Accordingly for both In-Ni and In-Zn, the transition metals were unable to contribute significantly to visible light absorption.

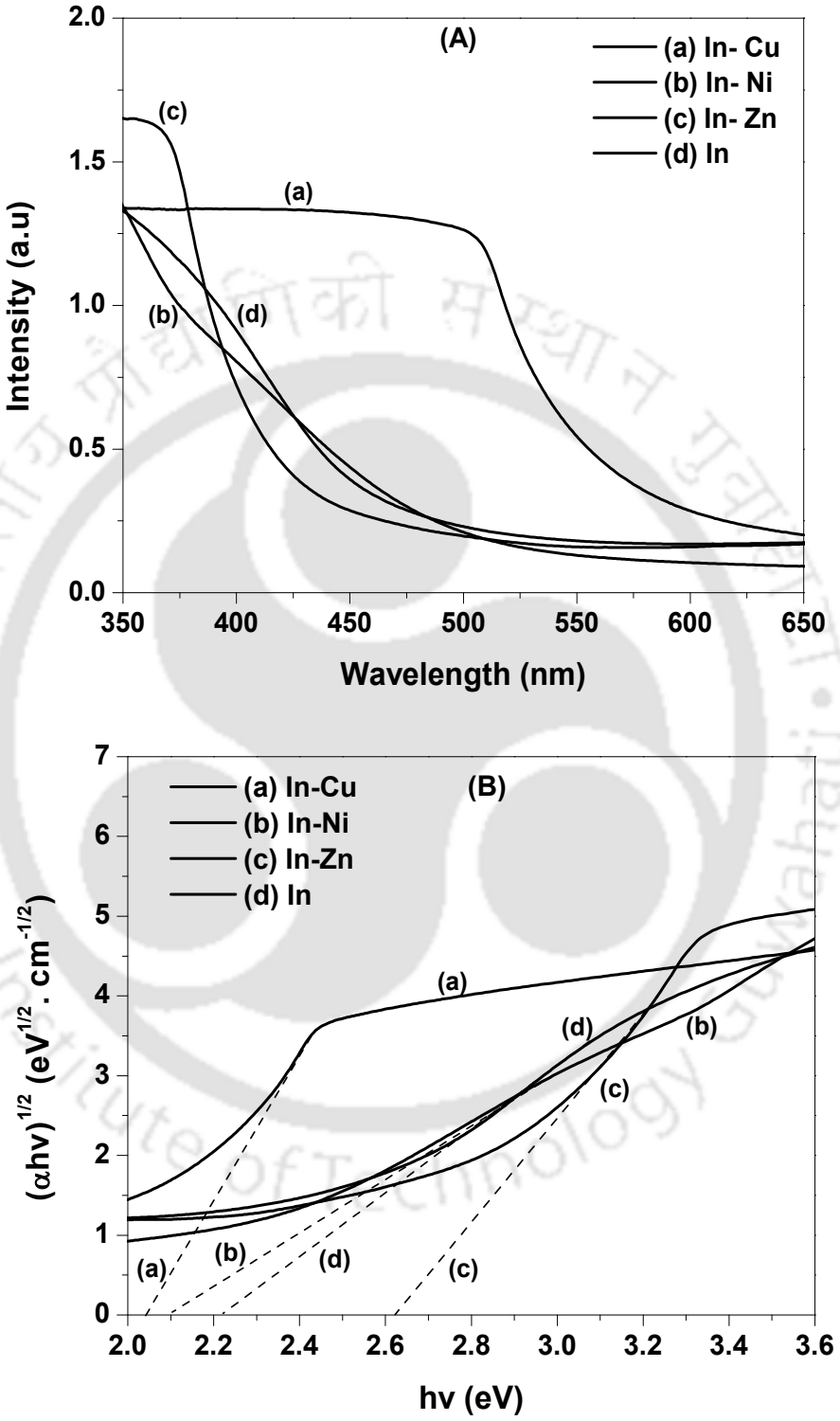

Fig.4.46. (A) UV-Visible diffuse reflectance spectra and (B) Kubelka-Munk plot of (a) In-Cu (b) In-Ni (c) In-Zn and (d) In

Footer Page TH-1334_08610706

Fig.4.47 shows the photoluminescence spectra of indium oxide and In-Cu, In-Ni, In-Zn coupled oxides. For indium oxide the main emission peaks were located at 400, 450, 468 and 480 nm corresponding to the transition energies of 3.1, 2.75, 2.64, 2.58 eV respectively. The observed PL peaks can be ascribed to the emissions originated from the oxygen vacancies in the indium oxide (Wu et al., 2009; Cao et al., 2003). The transition at near-UV region of 400 nm can be attributed to radiative recombination of a photogenerated hole with an electron occupying the single ionized oxygen vacancies (Gan et al., 2013; Jeong and Lee, 2011). The peaks in visible regions can be attributed to radiative emission due to deep level trapping by oxygen vacancies (Beena et al., 2011, Peng et al., 2002). The intensity of the peaks decreased when indium oxide was coupled with transition metals. The decrease in PL intensity was most significant when In was coupled with Cu and Ni and suggested enhanced charge separation. For In-Zn, only slight decrease in peak intensity was observed compared to that of indium oxide indicating poor separation of the charge carriers.

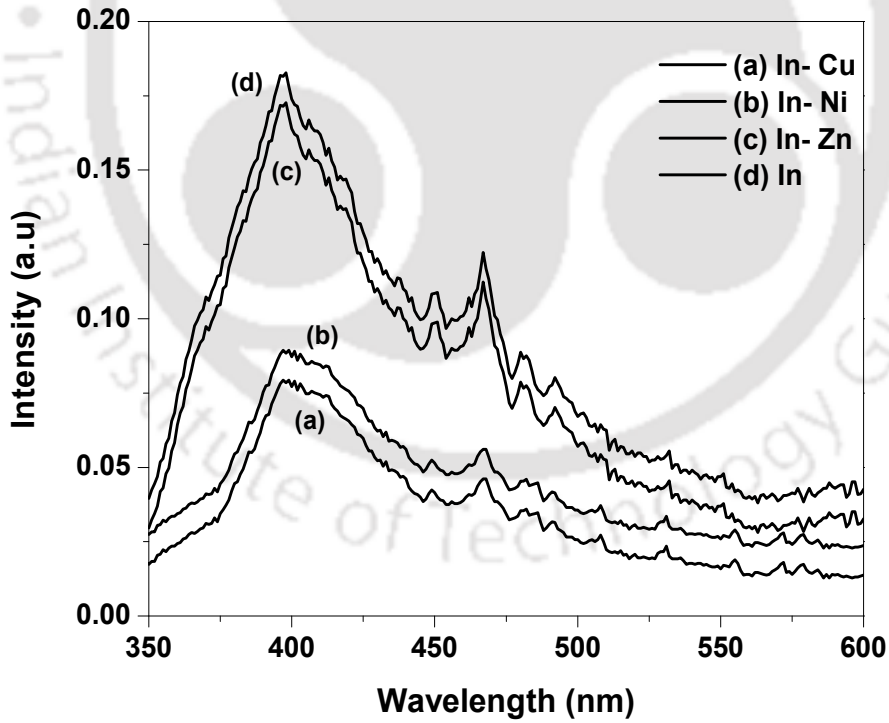

Fig.4.47. Photoluminescence spectra of (a) In-Cu (b) In-Ni (c) In-Zn and (d) In

Footer Page TH-1334_08610706

The change in peak intensity for coupled oxides can be explained based on the electron trapping ability of the transition metals. The transition metals can exist in multiple valance states such as, $Cu^{+2}/Cu^{+1}/Cu^{0}$, Ni^{+2}/Ni^{0} and $Zn^{+2/}Zn^{0}$. These transition metals when coupled with indium oxide can act as trap for photogenerated electrons/holes resulting in non-radiative combinations. Consequently rate of radiative trapping of photogenerated electrons by oxygen vacancies was reduced decreasing the peak intensity. The relative trapping efficiency of transition metals is expected to depend on respective reduction potential. Hence the transition metal with more positive reduction potential with respect to indium will have higher ability of trapping electrons. The reduction potentials of the transition metals are summarized in Table 4.13 (Bard et al., 1985; Litter, 1999; Slamet et al., 2005; Rajeshwar et al., 2002). Since, Cu and Ni have positive reduction potentials with respect to indium, hence they are expected to trap electrons more efficiently. The copper with most positive reduction potential is expected to show highest non-radiative charge trapping efficiency and accordingly the lowest peak intensity was observed for In-Cu. This stabilization of photogenerated electrons is expected to increase the photoactivity of coupled oxide. The zinc with negative reduction potential with respect to indium is not expected to contribute in electron trapping. However, the slight reduction in intensity for In-Zn compared to indium oxide can be attributed to stabilization of the photogenerated electrons to lower conduction band of ZnO. The conduction band of ZnO is more positive than that of In_2O_3 (ZnO -0.5 and In_2O_3 -0.63V vs NHE at pH=7) and can act as a sink for photogenerated electrons (Fu et al., 2008; Mu et al., 2012). However, the charge stabilization for In-Cu or In-Ni cannot be facilitated from the mobility of electrons at the heterojunction from In_2O_3 band to Cu_2O/CuO/NiO band due to more negative conduction band potentials of Cu_2O (-1.5 V vs NHE at pH=7), CuO (-0.78 V vs NHE at pH=7) and NiO (-3.06 V vs NHE at pH=7) (Huang et al., 2009; Qin et al., 2011; He et al., 1999) compared to that of In_2O_3 (-0.63 V vs NHE at pH=7).

Footer Page TH-1334_08610706

Table 4.13. Reduction potential values of Cu, Ni, Zn and In

Reduction reactions	Reduction potential (V)
Cu^{+}/Cu^{0}	0.520
Cu^{2+}/Cu^{+}	0.159
Cu^{2+}/Cu^{0}	0.340
Ni^{2+}/Ni^{0}	-0.257
In^{3+}/In^{+}	-0.444
Zn^{2+}/Zn^{0}	-0.761

Photocatalytic activities

Photocatalytic hydrogen production from aqueous solution of methanol was carried out over indium oxide and indium-transition metal coupled oxides under visible light irradiation. The hydrogen evolution values are shown in Fig.4.48. Since the actual amount of indium varied in the catalysts. For comparison the hydrogen production has been normalized with respect to indium content. The hydrogen production values normalized per gram of photocatalyst are presented in Fig.4.49.

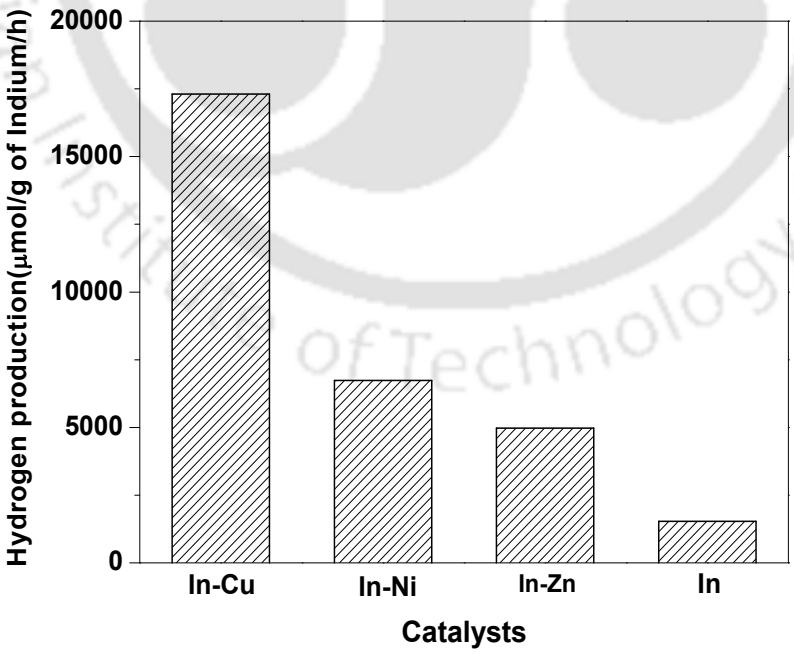

Fig.4.48. Hydrogen production for In and In-TM (TM = Cu, Ni, Zn) based on per gm of indium

Footer Page TH-1334_08610706

The hydrogen evolution rate of indium oxide was 1528 μmol/g of indium/h. All the coupled oxides showed enhanced hydrogen production but the extent of increase depended on the transition metals. The performance of the photocatalysts can be explained based on the physicochemical and optical properties determined by the various characterization techniques. For In-Cu, the hydrogen evolution rate was enhanced most and 17314 μmol/g of indium/h hydrogen was produced. For the In-Cu coupled oxide the surface area, charge separation as well as visible light absorption was most significantly enhanced compared to indium oxide. The increased surface area provided more reaction sites that were favorable to achieve higher photoactivity. Higher visible light absorption enhanced the generation of electron-hole pairs, while increased stabilization of the charge carriers improved the availability of electrons for reduction. Consequently activity for In-Cu increased significantly as observed. The hydrogen production for In-Ni of 6731 μmol/g of indium/h was lower with respect to In-Cu but slightly higher compared to that of In-Zn. The higher activity of In -Ni can be attributed to increased surface area and charge separation. But absorbance of visible light for In-Ni was not significantly improved with respect to indium oxide. That may be the reason for moderate increase in photocatalytic activity for In-Ni in comparison to indium oxide. The enhancement was lowest for In-Zn coupled oxide with hydrogen production of 4972 μmol/g of indium/h. The light absorbance of In-Zn actually showed a blue shift and charge separation was also not significantly enhanced. Hence the increased activity can be attributed to higher surface area of the coupled oxide with respect to indium oxide. Higher surface area may have increased the dispersion of indium oxide increasing the active sites. The hydrogen production in terms of per gm of catalyst (shown in Fig.4.49) also followed the same trend as Fig.4.48. The quantum efficiency of the photocatalysts was calculated for the indium and coupled oxides using the method followed by Sasikala et al. (2008). The values are found to be 35.8, 32.4, 28.6 and 25.2 % for In-Cu, In-Ni, In-Zn and In samples, respectively.

Footer Page TH-1334_08610706

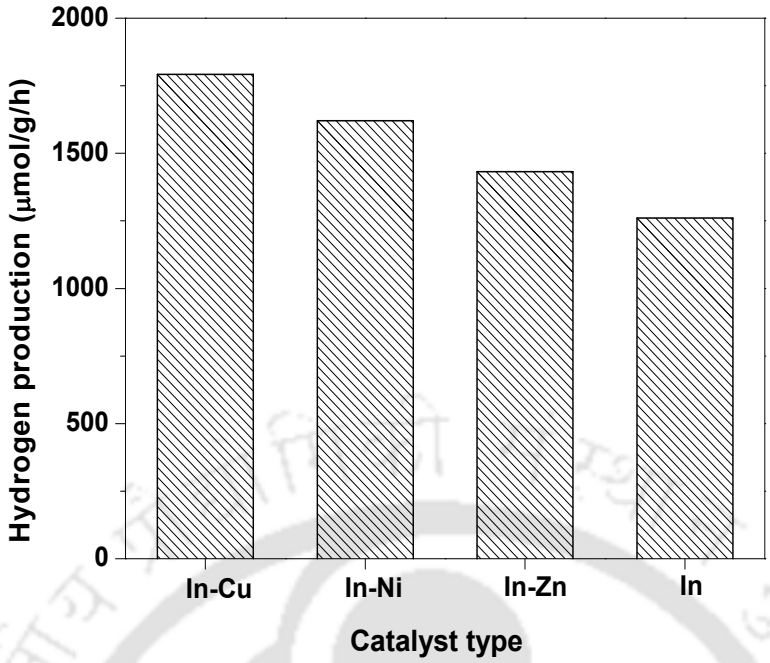

Fig.4.49. Hydrogen production for In and In-TM (TM = Cu, Ni, Zn) based on per gm of catalyst

The product analysis showed formation of only formaldehyde in the liquid phase and hydrogen in gaseous phase. The possible reactions are summarized below.

1. photocatalyst $\xrightarrow{h\nu} h^{+}_{vb} + e^{-}_{cb}$

2. $2H^{+} + 2e^{-}_{cb} \rightarrow H_2$

3. $CH_3OH + 2h^{+}_{vb} \rightarrow 2H^{+} + HCHO$

4. $2H_2O + 2h^{+}_{vb} \rightarrow 2OH^{\bullet} + 2H^{+}$

5. $CH_3OH + 2OH^{\bullet} \rightarrow 2H_2O + HCHO$

The other oxidation products either were not detected. The results suggested that hydrogen was mainly produced by the partial oxidation of methanol to hydrogen and formaldehyde by step 3, 4 and 5. Further, since methanol is easier to oxidize than water (Sabio et al., 2012) the probability of formation of hydrogen and formaldehyde by step 3 is more probable than step 4 and 5.

Footer Page TH-1334_08610706

Summary

Visible light active indium oxide was coupled with various transition metals to study the effect on hydrogen production from aqueous solution of methanol. The indium oxide was coupled with copper, nickel and zinc oxides. The surface area of all the coupled oxides was enhanced compared to that of indium oxide, however optical activity of coupled oxide differed with the nature of transition metals. The enhancement in visible light absorption was most substantial for coupled oxide containing copper, while charge separation was significantly improved both for indium-copper and indium-nickel coupled oxides. Accordingly highest hydrogen production was observed for the indium-copper coupled oxide 17314 μmol/g of indium/h compared to that of indium oxide (1528 μmol/g of indium/h). The second highest hydrogen production was for indium-nickel coupled oxide with 6731 μmol/g of indium/h. The least improvement in hydrogen production was observed for indium-zinc coupled oxide and was attributed to marginal improvement in surface area and charge separation. For all the coupled oxides partial oxidation of methanol to hydrogen and formaldehyde was observed to major contributing reaction.

Footer Page TH-1334_08610706

4.6 Effect of operational parameters

The effects of various operating variables such as light intensity, amount of catalyst, different types of alcohols (methanol, ethanol, 1-propanol) and irradiation time were investigated. The cerium and nitrogen codoped titania was used as the catalyst.

4.6.1 Effect of incident light intensity

The intensity of incident light plays an important role in the photocatalytic reaction. The present study examined the effect of different light intensities on the photocatalytic decomposition of water-methanol mixture. The light intensities were varied in the range of 5000-25600 lx. Fig.4.50 shows the hydrogen production at different light intensities for given amount of catalyst and methanol concentration of 0.02 molar fraction (0.96 mol/litre). The hydrogen production increased with increase in the light intensity. When the light intensity increased from 5000 to 25600 lx the hydrogen production increased from 326 to 1024 μmol/g/h. With increase in light intensity absorption of light increased and led to generation of higher number of photogenerated charge carriers available for redox reactions on the catalyst surface. Consequently, hydrogen production increased.

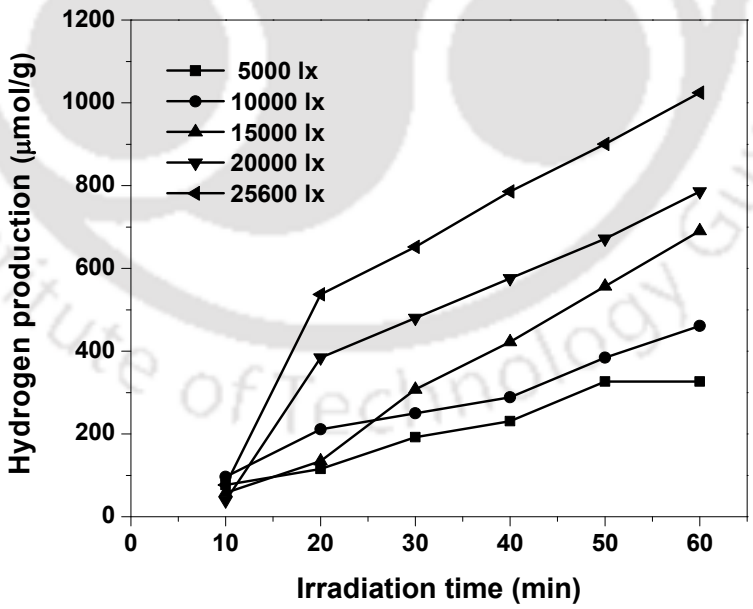

Fig.4.50. Hydrogen production at different light intensities (Reaction conditions: photocatalyst amount, 0.2 g; methanol concentration 0.96 mol/litre; irradiation time, 1 h)

Footer Page TH-1334_08610706

4.6.2 Effect of catalyst amount

The amount of catalyst is also likely to affect the photocatalytic hydrogen evolution. The hydrogen evolution using initial methanol concentration of 0.96 mol/litre is shown in Fig.4.51. The variation in the hydrogen production with the catalyst amount was determined in the range of 0.1 to 1 g. The results showed that the total hydrogen evolution was highest at the loading of 0.2 g and thereafter, decreased with increase in the catalyst loading up to 1g. The hydrogen production is expected to depend on number of surface active sites as well as light transmission in suspension (Sreethawong et al., 2007). Initially with increase in amount of catalyst the number of active sites increased resulting in higher hydrogen production. At higher catalyst loading, a considerable part of the light may be scattered and consequently amount of light reaching the catalyst surface was reduced. Further, at high catalyst loading the number of particles actually exposed to the light may also drop (Yang et al., 2009). All these phenomena may have contributed to decrease in light absorption on the photocatalyst surface and thereby in hydrogen production at higher loadings.

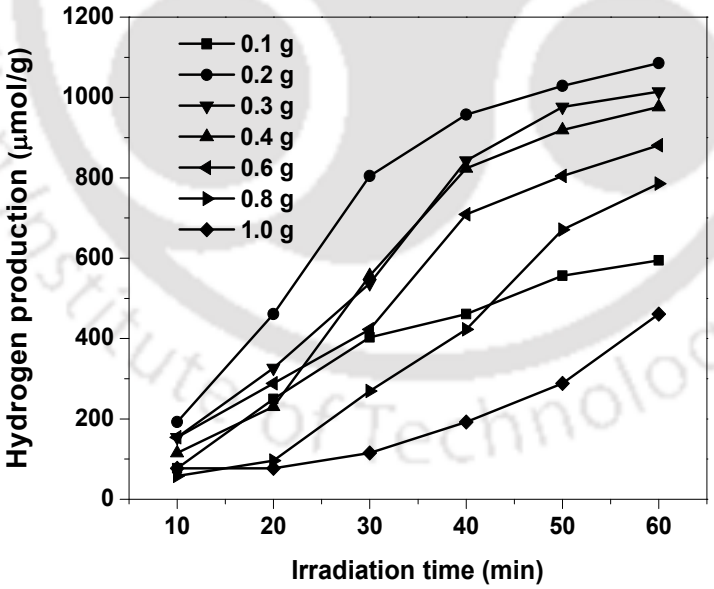

Fig.4.51. Production of hydrogen using different amount of photocatalyst (Reaction conditions; methanol concentration 0.96 mol/litre; irradiation time, 1 h; light intensity, 25600 lx)

Footer Page TH-1334_08610706

4.6.3 Effect of type of alcohols

The effect of types of alcohols on hydrogen production activity was studied using methanol, ethanol and 1-propanol. The hydrogen evolution is shown in Fig.4.52. The photocatalytic reactions were performed under identical reaction conditions with the same concentration of alcohol in aqueous solution. The hydrogen production increased in the order: methanol > ethanol > propanol. The maximum photocatalytic activity was observed for methanol, which may be attributed to the higher number of α-H (Bahruji et al., 2010). In higher alcohols the formation of hydrogen and formaldehyde also involves carbon-carbon bond breaking. The degree of carbon-carbon bond breaking decreases with increase in carbon number resulting in decrease in formation of the products (Lin et al., 2009).

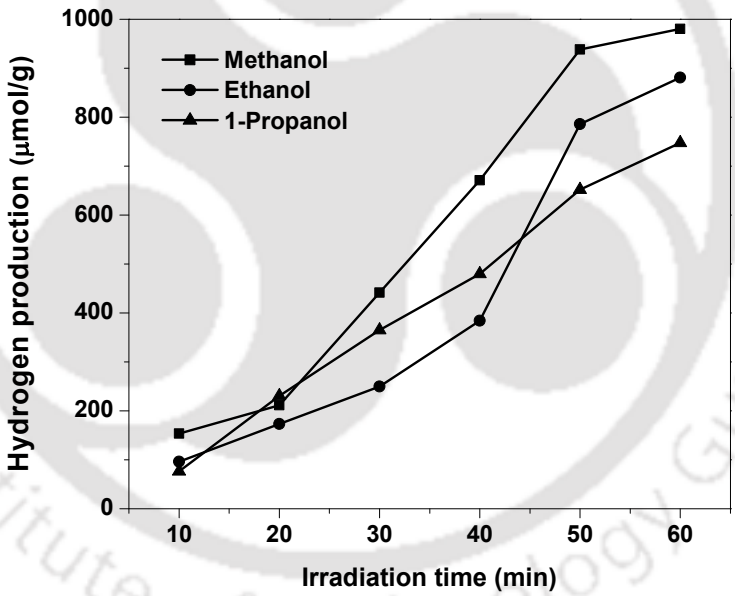

Fig.4.52. Hydrogen production in presence of different alcohols (photocatalyst amount, 0.2 g; alcohol concentration 0.96 mol/litre; irradiation time, 1 h; light intensity, 25600 lx)

Footer Page TH-1334_08610706

4.6.4 Effect of irradiation time

The effect of irradiation time on the photocatalytic hydrogen evolution from methanol/water mixtures is shown in Fig.4.53. The hydrogen production increased significantly up to 3 h of irradiation time. Thereafter, the hydrogen generation decreased. After 10 h of irradiation period amount of hydrogen produced was 3687 μmol/g. Initially higher activity can be ascribed to the higher absorption of photons on the catalyst surface due to the prolonged irradiation. The hydrogen production decreased at a long irradiation time may be due to the decrease in number of active sites available for the absorption of lights.

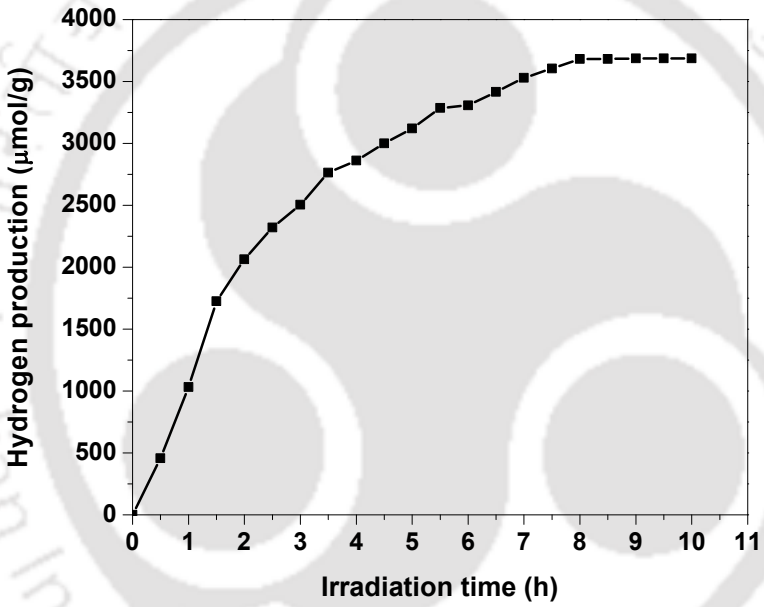

Fig.4.53. Production of hydrogen as a function of irradiation time (photocatalyst amount, 0.2 g; methanol concentration 0.96 mol/litre; light intensity, 25600 lx)

Summary

The effects of various operational parameters were investigated for hydrogen production. Among different type of alcohols, methanol showed a maximum hydrogen production. The best results for photocatalytic hydrogen production were obtained when 0.2 g photocatalyst was used. The use of higher light intensity resulted in higher hydrogen production.

Footer Page TH-1334_08610706

4.7 Kinetic studies

In this study, the 2 at.% copper and 10 at.% indium oxide codoped titanium dioxide photocatalyst showed highest activity for hydrogen production under visible light from water-methanol mixture. Kinetics for photocatalytic methanol oxidation for this catalyst was investigated. The hydrogen production at different concentration of methanol was determined in the range of 2.3 to 7.4 mol/litre. The photocatalytic reactions were performed at constant light intensity of 25600 lx using 0.2 g of catalyst. The reaction mixture was exposed to light only after constant intensity was reached which took approximately 20 min. The stirring was maintained to ensure homogeneous suspension of the catalyst in solution as well as to minimize the effect of any external mass transfer resistance. The profiles of methanol concentration as a function of irradiation time at different initial methanol amount are reported in Fig.4.54. The reaction was carried out for one hour. With increase in irradiation time methanol concentration decreased. The corresponding conversion is given in Fig.4.55. The conversion ranged from 85-95 %. The data were used for determination of kinetic parameters using various models.

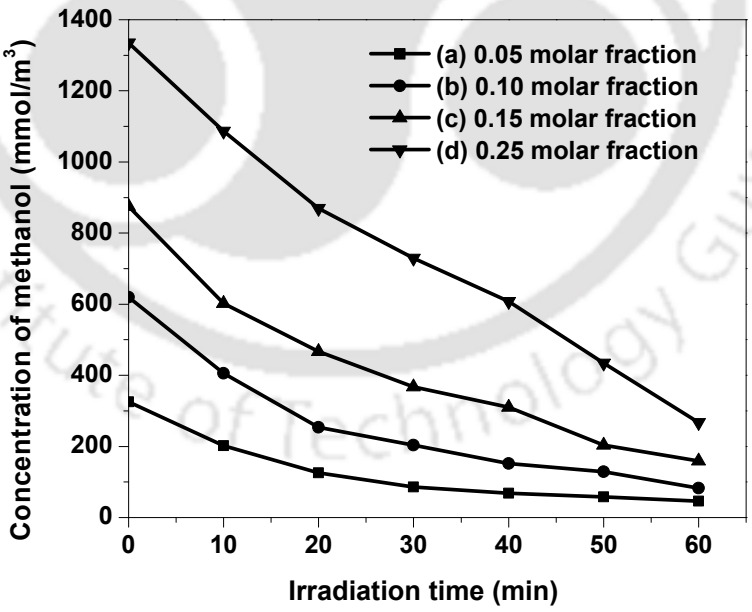

Fig.4.54. Methanol concentrations as a function of irradiation time at different initial concentration (a) 0.05 molar fraction (2.3 mol/litre), (b) 0.10 molar fraction (4.1 mol/litre), (c) 0.15 molar fraction (5.4 mol/litre) and (d) 0.25 molar fraction (7.4 mol/litre)

Footer Page TH-1334_08610706

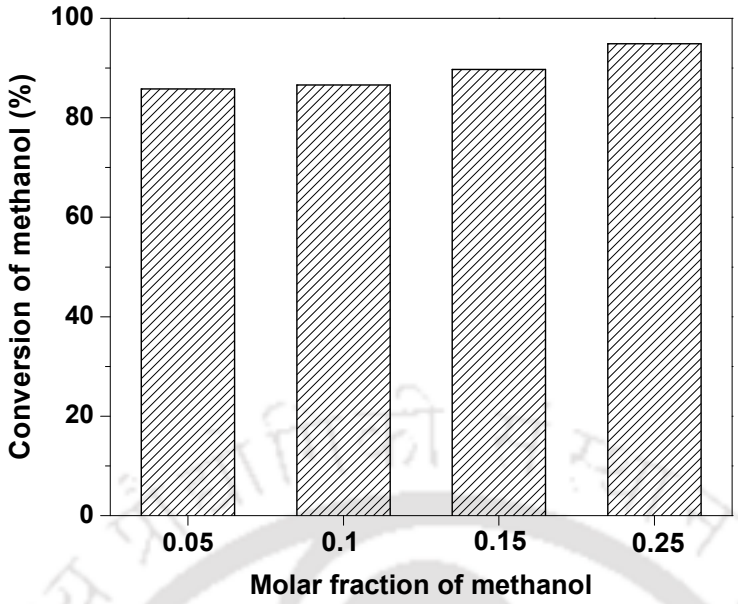

Fig.4.55. Conversion of methanol at different initial concentration

In gas phase only hydrogen along with unconverted methanol was present. No other component was detected. In liquid phase, only formaldehyde and unconverted methanol was detected. The amounts of hydrogen, formaldehyde and unconverted methanol were determined using the calibration plots given in Appendix B. The hydrogen and formaldehyde evolution at different initial molar fractions of methanol ranging from 0.05 to 0.25 are presented in Fig.4.56. With increase in the molar fraction of methanol, a gradual increase in the hydrogen and formaldehyde production was observed. This may be due to the increased adsorption of the methanol molecules on the active sites of the catalyst surface. It can also be observed that for all methanol concentrations, almost equivalent amounts of hydrogen and formaldehyde were produced. These results agreed with the observations reported in section 4.4. Therefore, for copper doped indium-titanium oxide catalyst, methanol was only partially oxidized in the reaction conditions to formaldehyde and hydrogen. The formaldehyde was not further oxidized to formic acid or carbon dioxide.

Footer Page TH-1334_08610706

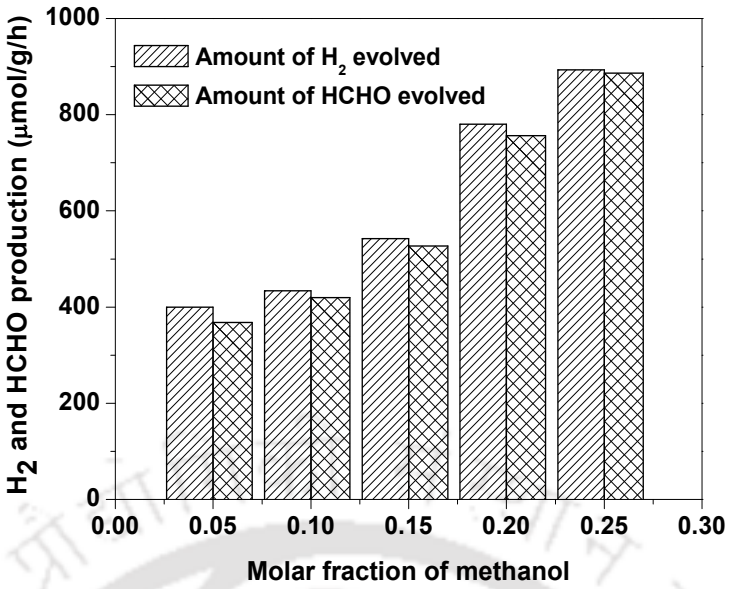

Fig.4.56. Hydrogen and formaldehyde production at different methanol concentration (photocatalyst amount, 0.2 g; irradiation time, 1 h; light intensity, 25600 lx)

4.7.1 Kinetic models

A power law model and two Langmuir-Hinshelwood (L-H) based mechanistic models were developed. The L-H models were developed for the simultaneous occurrence of hydroxyl mediated and hole mediated oxidation path, and for the hole mediated path alone. For each model, the optimum values of kinetic parameters were estimated by minimizing the residual sum of squares between the calculated and experimental rate of methanol oxidation. Non-linear regression analysis was used to estimate the optimum kinetic parameters.

Model 1: Power law model (P-1)

The power law model was used to describe the direct relationship of reaction rate with the concentration of methanol. The amount of water and incident light intensity was considered as excess and constant. The rate expression is then given as;

$$-r_A = k\ C_A^{\ n}$$

Footer Page TH-1334_08610706

Where,

$-r_A$: rate of reaction

k : rate constant

C_A : concentration of methanol

n **:** order of reaction

The proposed model has only two parameters. One rate constant and one order of reaction with respect to methanol concentration.

Model 2: Langmuir-Hinshelwood model based on hydroxyl radical and hole mediated oxidation path (LH-1)

The Langmuir-Hinshelwood model accounts for the adsorption-desorption of the reacting species and are expected to reflect the actual mechanism. The steps of methanol oxidation reactions based on the Langmuir-Hinshelwood model are given below (Chiarello et al., 2011; Nomikos et al., 2014).

[1] $\text{photocatalyst} + \text{h}\nu \rightarrow e_{cb}^{-} + h_{vb}^{-}$

[2] $H_2O_{(l)} + C_v \rightleftharpoons H2O_{ads}$

[3] $CH_3OH_{(l)} + C_v \rightleftharpoons CH_3OH_{ads}$

[4] $H_2O_{ads} + h_{vb}^{+} \xrightarrow{k'_{H_2O}} {}^{\bullet}OH_{ads} + H_{ads}^{+}$

[5] $CH_3OH_{ads} + h_{vb}^{+}(\text{or } {}^{\bullet}OH_{ads}) \xrightarrow{k_{CH_3OH}} HCHO_{ads} + H_{ads}^{+}(\text{or } H_2O)$

[6] $HCHO_{ads} \xrightarrow{k_{des,HCHO}} HCHO_{(l)}$

[7] $2H^{+} + 2e_{cb}^{-} \xrightarrow{k_{red}} H_{2ads}$

[8] $H_{2ads} \xrightarrow{k_{des,H_2}} H_2 \text{ (g)}$

[9] $e_{cb}^{-} + h_{vb}^{+} \xrightarrow{k_{recombination}} Q$

The electron and holes are generated on catalyst surface by absorption of light. During the photocatalytic reaction, the water present in excess, and methanol are adsorbed on the catalyst surface as in steps 2 and 3, respectively. The adsorbed water and methanol can react with photogenerated holes producing hydroxyl radical (step 4) and

Footer Page TH-1334_08610706

formaldehyde (step 5) respectively. Since oxidation potential of methanol is higher as discussed earlier consumption of holes by methanol is expected to occur faster. The methanol can also react with hydroxyl radical generated by water splitting and result in formation of formaldehyde (step 5). Thus methanol can undergo oxidation reactions in two ways; either directly by the photogenerated holes or by the indirectly by hydroxyl radicals. The H^+ ions produced in these steps are reduced by the photoelectrons to produce hydrogen as in step 7. The rate of methanol oxidation was derived as;

$$r = \left(\frac{k_{H_2O} K_{H_2O} + k_{CH_3OH} K_{CH_3OH} C_{CH_3OH}}{1 + K_{CH_3OH} C_{CH_3OH_{(l)}} + K_{H_2O} C_{H_2O_{(l)}}} \right)$$

Where k_{H_2O} and k_{CH_3OH} are rate constants for water and methanol oxidation respectively. K_{H_2O} and K_{CH_3OH} are the respective adsorption equilibrium constants of water and methanol. The derivation of rate equation is given in Appendix F.

Model 3: Langmuir-Hinshelwood model based on hole mediated oxidation path (LH-2)

For second Langmuir-Hinshelwood mechanism based model, it was assumed that the methanol oxidation occurred only by photogenerated holes on the surface. The corresponding rate expression for methanol oxidation was derived as;

$$r = \left(\frac{k_{CH_3OH} K_{CH_3OH} C_{CH_3OH}}{1 + K_{CH_3OH} C_{CH_3OH_{(l)}} + K_{H_2O} C_{H_2O_{(l)}}} \right)$$

This model has only one rate constant k_{CH_3OH} and two adsorption equilibrium constants K_{H_2O} and K_{CH_3OH}. Here the terms are defined as in model L-H 1.

Footer Page TH-1334_08610706

4.7.2 Kinetic analysis of rate equations

The data collected by varying the concentration of methanol in solution were used for kinetic analysis. The kinetic parameters were estimated using the developed models and tested for best fitting.

Parameter estimation

The kinetic parameters were estimated by the non linear regression analysis using the solver function in the Excel. For each model, the optimum values of parameters were determined by minimizing the residual sum of squares between the calculated and experimental rate of methanol oxidation. The value of squared sum of the difference between experimental data and model fit is given as (Brown, 2001).

$$ss = \sum_{n=1}^{N} (y_{n,exp} - y_{n,mod})^2 / (N-P-1)$$

Where, 'SS' is the sum square of all the data points, 'N' is the number of experimental data values, 'P' is the number of parameters to be estimated, $y_{n,exp}$ and $y_{n,mod}$ are the experimental and model rate values, respectively. This takes into account the difference in the number of parameters used in the different models as well as the number of experiments performed. The kinetic parameters were determined with confidence interval of 95%. The fitting of the models was tested by R^2 value. Higher the value of R^2 better the fit of the data for the rate model used.

Discussion

The estimated kinetic parameters for the developed models are shown in Table 4.14. From the power law model, rate of oxidation was found to be of 1.4 order with respect to methanol in the studied range of concentration. The Langmuir-Hinshelwood mechanism based model LH-1, considering methanol oxidation both by hydroxyl ions and photogenerated holes, was observed to best describe the experimental data corresponding to highest R^2 value. This suggested that the water splitting does have contribution in generation of hydroxyl radicals which in turn participate in methanol oxidation producing hydrogen and formaldehyde. The formaldehyde is immediately desorbed from catalyst surface under the reaction conditions used, thereby inhibiting further oxidations to formic acid and carbon dioxide. The rate constant for methanol

Footer Page TH-1334_08610706

oxidation was slightly higher compared to that of water oxidation as it is expected from higher tendency of oxidation for methanol. However, in presence of excess water the adsorption equilibrium constant for water is expected to be much higher compared to that methanol also as observed from both the models. In spite of lower number of adsorbed methanol molecules on catalyst surface compared to that of water, the higher oxidation rate of methanol can be attributed to its higher oxidation potential. The experimental rate and model rate values are compared for various models in Fig.4.57.

Table 4.14. Estimated kinetic parameter values for different models

Parameters	**n**	**k**	$\mathbf{k_{H_2O}}$	$\mathbf{k_{CH_3OH}}$	$\mathbf{K_{H_2O}}$	$\mathbf{K_{CH_3OH}}$	$\mathbf{R^2}$
		$(\mu mol/g)^{1-n}\ h^{-1}$	$(\mu mol/g)^{-1}\ h^{-1}$	$(\mu mol/g)^{-1}\ h^{-1}$	$(\mu mol/g)^{-1}$	$(\mu mol/g)^{-1}$	$1-\frac{\sum(y_{exp}-y_{pred})^2}{\sum(y_{exp}-y_{average})^2}$
P-1	1.4	$0.12x10^{-3}$	-	-	-	-	0.98
LH-1	-	-	$8.65x10^{-3}$	$9.12x10^{-3}$	21.3	5.2	0.99
LH-2	-	-	-	$5.42x10^{-3}$	17.3	3.3	0.94

Footer Page TH-1334_08610706

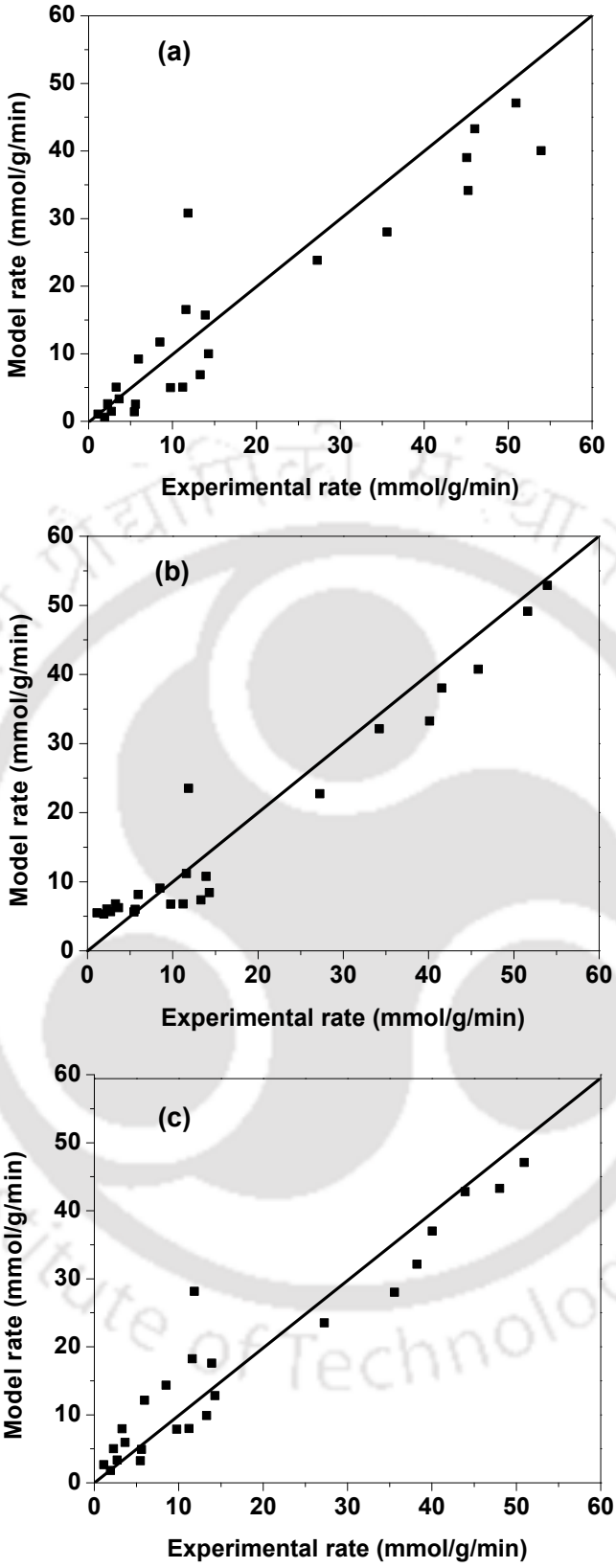

Fig.4.57. Comparison of experimental and calculated rates for different kinetic models (a) P-1 (power law) (b) LH-1 (combination of hydroxyl mediated and hole mediated path) and (c) LH-2 (hole mediated path)

Footer Page TH-1334_08610706

Summary

The hydrogen production increased with increase in methanol concentration in the studied range of 2.3 to 7.4 mol/litre. The products consisted of equivalent amount of hydrogen and formaldehyde. No other products were detected suggesting that for copper doped indium-titanium oxide oxidation of methanol resulted in formaldehyde which was intermediately desorbed from the catalyst surface preventing further oxidation. Three kinetic models, one power law and two Langmuir-Hinshelwood (L-H) based mechanistic models were developed. The L-H models were developed for the simultaneous occurrence of hydroxyl and hole mediated oxidation paths, and for the hole mediated path alone. For each model, the optimum values of kinetic parameters were estimated by minimizing the residual sum of squares between the calculated and experimental rate of methanol oxidation. Non-linear regression analysis was used to estimate the optimum kinetic parameters. From power law model, rate of methanol oxidation was observed to be of 1.4 order with respect to methanol in the studied range of concentration. The Langmuir-Hinshelwood mechanism based model considering oxidation of methanol both by photogenerated holes and hydroxyl radicals best described the experimental data.

Footer Page TH-1334_08610706

Chapter 5

Conclusions and Recommendations

5.1 Conclusions

All the developed photocatalysts showed significant hydrogen production under visible light irradiation from water-methanol solution. The main conclusions from the present work can be summarized as follows;

- Cerium modification of titanium dioxide showed shift of absorption edge towards visible light region and was attributed to the incorporation of Ce 4f energy levels. The cerium ions also acted as electron traps and enhanced separation efficiency of the charge carriers. Higher activity of cerium modified titanium dioxide thus can be attributed to the increased availability of photogenerated electrons. Enhanced surface area also facilitated higher activity. The highest hydrogen production of 403 µmol/g/h was observed for catalyst containing 2.5 at.% of cerium in the range studied. Oxidation of methanol resulted in formaldehyde and formic acid in liquid phase.
- Co-modification of titanium dioxide with cerium and nonmetals such as boron, carbon, nitrogen and sulphur further reduced the band gap energies compared to that of cerium modified titanium oxide. The interaction of nonmetals with oxygen 2p-orbitals facilitated the band gap reduction. The radiative recombination of photogenerated charge carriers were suppressed efficiently by oxygen vacancies created by substituent nonmetals. The extent of reduction in band gap and electron trapping depended on properties of nonmetals. The surface area and phase distribution was also modified in presence of nonmetal. Highest hydrogen evolution rate of 1033 µmol/g/h was observed for cerium-nitrogen codoped sample.
- Transition metal (Cu, Fe, Ni) modified titanium dioxide showed improved activity under visible light irradiation. A distinct red shift of the absorption edge was observed. Doping with copper exhibited a significant visible light absorption due to d electron transitions. The copper doped titania was most active among transition metal doped titania catalysts with hydrogen production of 938 µmol/g/h.
- Incorporation of nitrogen to transition metal (Cu, Fe, Ni) doped titanium dioxide increased visible light absorption and trapping of photogenerated charge carriers compared to transition metal doped oxide. The highest hydrogen evolution was

Footer Page TH-1334_08610706

observed for copper and nitrogen codoped titania with hydrogen generation of 1109 µmol/g/h.

- Amount of nitrogen also affected photocatalytic activity. Increased nitrogen content up to a certain amount improved the trapping efficiency of the photogenerated electrons due to the increased oxygen vacancies.
- Titanium dioxide coupled with different amount of indium oxide showed significant enhancement in hydrogen production. With increase in indium oxide content, the surface area and visible light absorption of the binary catalyst increased. Separation of photogenerated electron-holes was also enhanced in indium-titanium binary oxides. The separation efficiency may be attributed to the charge transfer at heterojunction as well as to electron trapping by the oxygen vacancies associated with indium oxide. For binary catalyst the activity was highest for 16.7 at.% indium content with hydrogen production of 1829 µmol/g/h in the range studied. The hydrogen generation was attributed to partial oxidation of methanol to formaldehyde thereby producing pure hydrogen.
- Incorporation of copper into titanium-indium coupled oxide reduced the band gap compared to binary catalyst. Addition of copper enhanced the surface area, visible light absorption and separation efficiency of the photogenerated charge carriers. The additional electrons were generated by absorption of visible light by narrow band gap copper oxide and stabilized by charge transfer at heterojunction to the suitably situated conduction band of indium oxides. The copper modified titanium-indium oxide showed the highest activity among all the studied photocatalysts with hydrogen production value of 2149 µmol/g/h.
- Coupling of indium oxide with copper, nickel and zinc oxides enhanced surface area and visible light absorption compared to indium oxide catalyst. Enhanced charge separation was observed for indium oxide coupled with copper and nickel. Positive reduction potential of copper and nickel with respect to indium facilitated trapping. The more positive conduction band of zinc with respect to indium facilitated its function as electron sink. Indium-copper coupled oxide showed higher hydrogen production compared to other catalysts (In-Ni, In-Zn and In).
- The operational parameters such as of light intensity, amount of catalyst, type of alcohols and irradiation time were observed to affect the hydrogen production

Footer Page TH-1334_08610706

activity. The activity was higher for methanol compared to alcohols with higher carbon number. The hydrogen production increased with light intensity in the studied range. With irradiation time hydrogen production increased significantly up to 3 h and thereafter, decreased. Optimum amount of catalyst resulted in highest hydrogen production.

❖ The Langmuir-Hinshelwood model that considered simultaneous occurrence of hydroxyl mediated and hole mediated oxidation paths for methanol was observed to best describe the experimental data compared to the model that considered only the hole mediated oxidation path. The kinetic rate constants were determined to be 8.65×10^{-3} $(\mu mol/g)^{-1}h^{-1}$ for hydroxyl mediated path and 9.12×10^{-3} $(\mu mol/g)^{-1}h^{-1}$ for hole mediated path. From power law model, rate of methanol oxidation was observed to be of 1.4 order with respect to methanol in the studied range of concentration.

5.2 Recommendations

❖ The photocatalytic hydrogen production should be carried out at continuous mode. The catalysts can be tested in vapor phase photocatalytic reaction.

❖ The effects of various preparation methods of catalyst and pH on hydrogen production can be studied.

❖ Hydrogen production activity as a function of different wavelength in incident light can be investigated.

❖ Kinetic analysis for other developed catalysts in this study needs to be done. Other mechanistic models, such as Eley-Rideal, can be tested. Effect of temperature on reaction kinetics need to be studied.

❖ Insitu studies are required for better understanding of the mechanism of photocatalysis.

Footer Page TH-1334_08610706

References

Abe, R., (2010). Recent progress on photocatalytic and photoelectrochemical water splitting under visible light irradiation, *Journal of Photochemistry and Photobiology C: Photochemistry Reviews*, 11, 179-209.

Alonso, M.D.H., Fresno, F., Silvia, S.and Coronado, J. M., (2009). Development of alternative photocatalysts to TiO_2: Challenges and opportunities, *Energy and Environmental Science*, 2, 1231-1257.

Andress, R.J., Huang, X., Bequette, B.W. and Martin, L.L., (2009). A systematic methodology for the evaluation of alternative thermochemical cycles for hydrogen production, *International Journal of Hydrogen Energy*, 34, 4146-4154.

Asahi, R., Morikawa, T., Ohwaki, T., Aoki, K. and Taga, Y., (2001). Visible-light photocatalysis in nitrogen-doped titanium oxides. *Science*, 293, 269-71.

Ayabe, S., Omoto, H., Utaka, T., Kikuchi, R., Sasaki, K., Teraoka, Y. and Eguchi, K., (2003). Catalytic autothermal reforming of methane and propane over supported metal catalysts, *Applied Catalysis A: General*, 241, 261-269.

Bahruji, H., Bowker, M., Davies, P.R., Al-Mazroai, L.S., Dickinson, A., Greaves, J., James, D., Millard, L. and Pedrono, F., (2010). Sustainable H_2 gas production by photocatalysis, *Journal of Photochemistry and Photobiology A: Chemistry*, 216, 115-118.

Bak, T., Nowotny, J., Rekas, M. and Sorrell, C.C., (2002). Photo-electrochemical hydrogen generation from water using solar energy, Materials-related aspects, *International Journal of Hydrogen Energy*, 27, 991-1022.

Ball, M. and Wietschel, M., (2009). The Hydrogen economy: Opportunities and challenges. Cambridge University Press, UK, 1-642.

Bandara, J., Udawatta, C.P.K. and Rajapakse, C.S.K., (2005). Highly stable CuO incorporated TiO_2 catalyst for photocatalytic hydrogen production from H_2O, *Photochemical & Photobiological Sciences*, 4, 857-861.

Bard, A. J., Parsons, R. and Jordan, J., (1985), Standard potentials in aqueous solution, CRC press, New York.

Footer Page TH-1334_08610706

Bartels, J.R., Pate, M.B. and Olson, N.K., (2010). An economic survey of hydrogen production from conventional and alternative energy sources, *International Journal of Hydrogen Energy*, 35, 8371-8384.

Beena, D., Lethy, K.J., Vinodkumar, R., Detty A.P., Mahadevanpillai, V.P. and Ganesan, V., (2011). Photoluminescence in laser ablated nanostructured indium oxide thin films, *Journal of Optoelectronics and Advanced Materials*, 1, 1-11.

Beydoun, D., Amal, R., Low, G. and McEvoy, S., (1999). Role of nanoparticles in photocatalysis, *Journal of Nanoparticle Research*, 1, 439-458.

Bowker, M., Morton, C., Kennedy, J., Bahruji, H., Greves, J., Jones, W., Davies, P.R., Brookes, C., Wells, P.P. and Dimitratos, N., (2014). Hydrogen production by photoreforming of biofuels using Au, Pd and Au-Pd/TiO_2 photocatalysts, *Journal of Catalysis*, 310, 10-15.

Brosillon, S., Lhomme, L., Vallet, C., Bouzaza, A. and Wolbert, D., (2008). Gas phase photocatalysis and liquid phase photocatalysis: Interdependence and influence of substrate concentration and photon flow on degradation reaction kinetics, *Applied Catalysis B: Environmental*, 78, 232-241.

Brown, A.M., (2001). A step-by-step guide to non-linear regression analysis of experimental data using a Microsoft Excel spreadsheet, *Computer Methods and Programs in Biomedicine*, 65, 191-200.

Calnan, S. and Tiwari, A.N., (2010). High mobility transparent conducting oxides for thin film solar cells, *Thin Solid Films*, 518, 1839-1849.

Cao, H., Qiu, X., Liang, Y., Zhu, Q. and Zhao, M., (2003). Room-temperature ultraviolet-emitting In_2O_3 nanowires, *Applied Physics Letters*, 83, 761-763.

Carp, O., Huisman, C. L. and Reller, A., (2004). Photoinduced reactivity of titanium dioxide. *Progress in Solid State Chemistry*, 32, 33-177.

Centi,G. and Perathoner, S., (2009). Opportunities and prospects in the chemical recycling of carbon dioxide to fuels, *Catalysis Today*,148, 191-205.

Chang, W.K., Rao, K.K., Kuo, H.C., Cai, J.F.and Wong, M.S., (2007). A novel core-shell like composite In_2O_3@$CaIn_2O_4$ for efficient degradation of methylene blue by visible light, *Applied Catalysis A*, 321, 1-6.

Chen, D. and Ray, A.K., (1998), Photodegradation kinetics of 4-nitrophenol in TiO_2 suspension. Water Research, 32, 3223-3234.

Chen, D., Yang, D., Wang, Q. and Jiang, Z., (2006). Effects of boron doping on photocatalytic activity and microstructure of titanium dioxide nanoparticles, *Industrial & Engineering Chemistry Research*, 45, 4110-4116

Chen, X. and C. Burda, C., (2004). Photoelectron spectroscopic investigation of nitrogen-doped titania nanoparticles, *Journal of Physical Chemistry B*, 108, 15446-15449.

Chen, X., Chen, W., Gao, H., Yang, Y. and Shangguan, W., (2014). In situ photodeposition of NiO_X on CdS for hydrogen production under visible light: Enhanced activity by controlling solution environment, *Applied Catalysis B: Environmental*, 152-153, 68-72.

Chen, X., Shen, S., Guo, L. and Mao, S.S., (2010). Semiconductor-based Photocatalytic Hydrogen Generation, *Chemical Reviews*, 110, 6503-6570.

Chen, Z., Yan, Y. and Elnashaie, S.S.E.H., (2004). Catalyst deactivation and engineering control for steam reforming of higher hydrocarbons in a novel membrane reformer, *Chemical Engineering Science*, 59, 1965-1978.

Cheng, W.Y., Yu, T.H., Chao, K.J. and Lu, S.Y., (2013). Cu_2O-decorated CdS nanostructures for high efficiency visible light driven hydrogen production, *International Journal of Hydrogen Energy*, 38, 9665-9672.

Chiarello, G.C., Ferri, D. and Selli, E., (2011). Effect of the CH_3OH/H_2O ratio on the mechanism of the gas-phase photocatalytic reforming of methanol on noble metal-modified TiO_2, *Journal of Catalysis*, 280, 168-177.

Chiarello, G.L., Forni, L. and Selli, E., (2009). Photocatalytic hydrogen production by liquid- and gas-phase reforming of CH_3OH over flame-made TiO_2 and Au/TiO_2, *Catalysis Today*, 144, 69-74.

Chiarello, G.L., Selli, E. and Forni, L., (2008). Photocatalytic hydrogen production over flame spray pyrolysis-synthesized TiO_2 and Au/TiO_2, *Applied Catalysis B: Environmental*, 84, 332-339.

Footer Page TH-1334_08610706

Choi, H.J. and Kang, M., (2007). Hydrogen production from methanol/water decomposition in a liquid photosystem using the anatase structure of Cu loadedTiO_2, *International Journal of Hydrogen Energy*, 32, 3841-3848.

Choi, W., Termin, A.and Hoffmann, M.R., (1994). The role of metal ion dopants in quantum-sized TiO_2: Correlation between photoreactivity and charge carrier recombination dynamics, *Journal of Physical Chemistry*, 98, 13669-13679.

Chu, S. and Majumdar, A., (2012). Opportunities and challenges for a sustainable energy future, *Nature*, 488, 294-303.

Comparelli, R., Fanizza, E., Curri, M.L., Cozzoli, P.D., Mascolo, G., Passino, R. and Agostiano, A., (2005). Photocatalytic degradation of azo dyes by organic-capped anatase TiO_2 nanocrystals immobilized onto substrates, *Applied Catalysis B: Environmental*, 55, 81-91.

Cui, X., Jiang, G., Zhu, M., Zhao, Z., Du, L., Weng, Y., Xu, C., Zhang, D., Zhang, Q., Wei, Y., Duan, A., Liu, J. and Gao, J., (2013). TiO_2/CdS composite hollow spheres with controlled synthesis of platinum on the internal wall for the efficient hydrogen evolution, *International Journal of Hydrogen Energy*, 38, 9065-9073.

Daghrir, R., Drogui, P. and Robert, D., (2013). Modified TiO_2 for environmental photocatalytic applications: A Review, *Industrial & Engineering Chemistry Research*, 52, 3581-3599.

Das, D. and Veziroglu, T.N., (2001). Hydrogen production by biological processes: a survey of literature, *International Journal of Hydrogen Energy*, 26, 13-28.

Deb, S.K., (2005). Dye-sensitized TiO_2 thin-film solar cell research at the National Renewable Energy Laboratory (NREL), *Solar Energy Materials & Solar Cells*, 88, 1-10.

Dincer, I., (2012). Green methods for hydrogen production, *International journal of Hydrogen Energy*, 37 1954-1971.

Dvoranová, D., Brezová, V., Mazúr, M. and Malati,M.A., (2002). Investigations of metal-doped titanium dioxide photocatalysts, *Applied Catalysis B: Environmental*, 37, 91-105.

Evans, J.E., Springer, K. W. and Zhang, J.Z., (1994). Femtosecond studies of interparticle electron transfer in a coupled CdS-TiO_2 colloidal system, *The Journal of Chemical Physics*,101, 6222-6225.

Fang, J., Xu, L., Zhang, Z., Yuan, Y., Cao, S., Wang, Z., Yin, L., Liao, Y.and Xue, C., (2013) Au@TiO_2-CdS ternary nanostructures for efficient visible-light-driven hydrogen generation, ACS *Applied Materials & Interfaces*, 5, 8088-8092.

Finazzi, E., Valentin, C.D., Pacchioni, G., (2009). Boron-doped anatase TiO_2: Pure and hybrid DFT calculations, *Journal of Physical Chemistry C*, 113, 220-228.

Fleming, I., (2009). Molecular orbitals and organic chemical reactions, John Wiley & Sons, United Kingdom, 1-378.

Fu, H., Xu, T., Zhu, S. and Zhu, Y., (2008). Photocorrosion inhibition and enhancement of photocatalytic activity for ZnO via hybridization with C_{60}, *Environmental Science & Technology*, 42, 8064-8069.

Fujishima, A., Zhang, X. and Tryk, D.A., (2007). Heterogeneous photocatalysis: From water photolysis to applications in environmental cleanup, *International Journal of Hydrogen Energy*, 32, 2664-2672.

Fujishima, A., Zhang, X. and Tryk, D.A., (2008). TiO_2 photocatalysis and surface phenomena, *Surface Science Reports*, 63, 515-582.

Funk, J.E., (2001). Thermochemical hydrogen production: past and present, *International Journal of Hydrogen Energy*, 26, 185-190.

Galstyan, V., Comini, E., Faglia, G. and Sberveglieri, G., (2013). TiO_2 nanotubes: recent advances in synthesis and gas sensing properties, *Sensors*, 13, 14813-14838.

Gan, J., Lu, X., Wu, J., Xie, S., Zhai, T., Yu, M., Zhang, Z., Mao, Y., Wang, S.C.L., Shen, Y. and Tong, Y., (2013). Oxygen vacancies promoting photoelectrochemical performance of In_2O_3 nanocubes, *Scientific Reports*, DOI:10.1038/srep01021.

Ganesh, I., Gupta, A.K., Kumar, P.P., Sekhar, P.S.C., Radha, K., Padmanabham, G. and Sundararajan, G., (2012). Preparation and characterization of Ni-doped TiO_2 materials for photocurrent and photocatalytic applications, *The Scientific World Journal*, Article ID 127326 (2012), 16pages.

Footer Page TH-1334_08610706

Gurlo, A., Barsan, N., Ivanovskaya, M., Weimar, U., Gopel, W., (1998). In_2O_3 and MoO_3-In_2O_3 thin film semiconductor sensors: interaction with NO_2 and O_3, *Sensors and Actuators B,* 47, 92-99.

Guzman, F., Chuang, S.S.C. and Yang, C., (2013). Role of methanol sacrificing reagent in the photocatalytic evolution of hydrogen, *Industrial & Engineering Chemistry Research,* 52, 61-65.

Hashimoto, K., Irie, H. and Fujishima, A., (2005). TiO_2 photocatalysis: A historical overview and future aspects. *Japanese Journal of Applied Physics,* 44, 8269-8285.

Hattori, A., Shimoda, K., Tada, H. and S Ito, S., (1999). Photoreactivity of sol-gel TiO_2 Films formed on soda-lime glass substrates: Effect of SiO_2 underlayer containing fluorine, *Langmuir,* 15, 5422-5425.

He, J., Lindstrom, H., Hagfeldt, A. and Lindquist, S.E., (1999). Dye-sensitized nanostructured p-type nickel oxide film as a photocathode for a solar cell, *Journal of Physical Chemistry B,* 103, 8940-8943.

Hirakawa, T. and Kamat, P.V., (2005). Charge separation and catalytic activity of Ag@TiO_2 core-shell composite clusters under UV-irradiation, *Journal of the American Chemical Society,* 127, 3928-3934.

Hoffmann, M.R., Martin, S.T., Choi,W. and Bahnemann,D.W., (1995). Environmental applications of semiconductor photocatalysis, *Chemical Reviews,* 95, 69-96.

Holladay, J.D., Hu, J., King, D.L. and Wang, Y., (2009). Review: An overview of hydrogen production technologies. *Catalysis Today,* 139, 244-260.

Holmen, A., (2009). Direct conversion of methane to fuels and chemicals, *Catalysis Today,* 142, 2-8.

Honda, K. and Fujishima, A., (1972). Electrochemical photocatalysis of water at a semiconductor electrode, *Nature,* 238, 37-38.

Hsiang, H.I. and Liu, Y.L., (2009). Electrical properties of copper and titanium-codoped zinc ferrites, *Journal of Alloys and compounds*, 472, 516-520.

http://www.eia.gov/forecasts/ieo/

Footer Page TH-1334_08610706

Hu, C., Zhang, R., Xiang, J., Liu, T., Li, W., Li, M., Duo, S. and Wei, F., (2011). Synthesis of carbon nanotube/anatase titania composites by a combination of sol-gel and self-assembly at low temperature, *Journal of Solid State Chemistry,* 184, 1286-1292.

Huang, B.S. and Wey, M.Y., (2011) Properties and H_2 production ability of Pt photodeposited on the anatase phase transition of nitrogen-doped titanium dioxide, *International Journal of Hydrogen Energy,* 36, 9479-9486.

Huang, L., Peng, F., Wang, H., Yu, H. and Li, Z., (2009). Preparation and characterization of Cu_2O/TiO_2 nano-nano heterostructures photocatalysts, *Catalysis Communications,* 10, 1839-1843.

Hurum, D.C., Agrios, A.G., Gray, K.A., Rajh, T. and Thurnauer, M.C., (2003). Explaining the enhanced photocatalytic activity of Degussa P25 mixed-phase TiO_2 using EPR, *Journal of Physical Chemistry B,* 107, 4545-4549.

Ide, Y., Kawamoto, N., Bando, Y., Hattori, H., Sadakane, M. and Sano, T., (2013). Ternary modified TiO_2 as a simple and efficient photocatalyst for green organic synthesis, *Chemical Communications*, 49, 3652-3654.

Irie, H., Watanabe, Y. and Hashimoto, K., (2003). Nitrogen-concentration dependence on photocatalytic activity of $TiO_{2-x}N_x$ powders, *Journal of Physical Chemistry B,* 107, 5483-5486.

Jagadale, T.C., Takale, S. P., Sonawane, R.S., Joshi, H.M., Patil, S.I., Kale, B. B. and Ogal, S.B., (2008). N-doped TiO_2 nanoparticle based visible light photocatalyst by modified peroxide sol-gel method, *Journal of Physical Chemistry C,* 112, 14595-14602.

Jeong, J.S. and Lee, J.Y., (2011). Formation mechanism and photoluminescence of necklace-like In_2O_3 nanowires, *Materials Letters,* 65, 1693-1695.

Jin, Z., Zhang, X., Li, Y., Li, S. and Lu, G., (2007) 5.1% Apparent quantum efficiency for stable hydrogen generation over eosin-sensitized CuO/TiO_2 photocatalyst under visible light irradiation, *Catalysis Communication,* 8, 1267-1273

Joshi, M.M., Mangrulkar, P.A., Tijare, S.N., Padole, P.S., Parwate, D.V., Labhsetwar, N.K. and Rayalu, S.S., (2012).Visible light induced photoreduction of water by N-

Footer Page TH-1334_08610706

doped mesoporous titania, *International Journal of Hydrogen Energy*, 37, 10457-10461.

Ju, S., Yali, M. and Gang, X., (2011). CdS/TiO_2 nanotubes hybrid as visible light driven photocatalyst for water splitting, *Rare metals*, 30, 280-283.

Kaneko, M. and Okura, I., (2002). Photocatalysis: Science and Technology, Springer, 356 pages.

Karakitsou, K.E. and Verykios, X.E., (1993). Effects of altervalent cation doping of TiO_2 on its performance as a photocatalyst for water cleavage, *Journal of Physical Chemistry*, 97, 1184-1189.

Keller V. and Garin, F., (2003). Photocatalytic behavior of a new composite ternary system:WO_3/SiC-TiO_2. Effect of the coupling of semiconductors and oxides in photocatalytic oxidation of methylethylketone in the gas phase, *Catalysis Communications*, 4, 377-383.

Khan, M.A., Woo, S.I. and Yang, O.B., (2008). Hydrothermally stabilized Fe(III) doped titania active under visible light for water splitting reaction, *International Journal of Hydrogen Energy*, 33, 5345-5351.

Khan, S.U.M., Al-Shahry Jr. M. and Ingle, W.B., (2002). Efficient photochemical water splitting by a chemically modified n-TiO_2, *Science*, 297, 2243-2245.

Kim, D.H. and Kim, M.S., (2011). Hydrogenases for biological hydrogen production, *Bioresource Technology*, 102, 8423-8431.

Kitano, M., Matsuoka, M., Ueshima, M. and Anpo, M., (2007). Recent developments in titanium oxide-based photocatalysts, *Applied Catalysis A: General*, 325, 1-14.

Kitano, M., Takeuchi, M., Matsuoka, M., Thomas, J.M. and Anpo, M.,(2005). Preparation of visible light-responsive TiO_2 thin film photocatalysts by an RF magnetron sputtering deposition method and their photocatalytic reactivity, *Chemistry Letters*, 34, 616-617.

Kudo, A. and Miseki, Y., (2009). Heterogeneous photocatalyst materials for water splitting, *Chemical Society Reviews*, 38, 253-278.

Kudo, A., (2006). Development of photocatalyst materials for water splitting, *International Journal of Hydrogen Energy*, 31, 197-202.

Kudo, A., (2007). Photocatalysis and solar hydrogen production, *Pure and Applied Chemistry*, 79, 1917-1927.

Kutty, T.R.N., Vivekanandan, R. and Murugaraj, P., (1988). Precipitation of rutile and anatase (Tio_{12}) fine powders and their conversion to $MTiO_3$ (M = Ba, Sr, Ca) by the hydrothermal method, *Materials Chemistry and Physics*, 19, 533-546.

Lan, Y., Lu, Y. and Ren, Z., (2013). Mini review on photocatalysis of titanium dioxide nanoparticles and their solar applications, *Nano Energy*, 2, 1031-1045.

Lasa, H.D., Serrano, B. and Salaices, M., (2005). Photocatalytic reaction engineering, Springer, USA, 1-199.

Le, T.T., Akhtar, M.S., Park, D.M., Lee, J.C. and Yang, O.B., (2012). Water splitting on Rhodamine-B dye sensitized Co-doped TiO_2 catalyst under visible light, *Applied Catalysis B: Environmental*, 111- 112, 397- 401.

Lee, S.S., Bai, H., Liu, Z. and Sun, D.D., (2013). Optimization and an insightful properties-Activity study of electrospun TiO_2/CuO composite nanofibers for efficient photocatalytic H_2 generation, *Applied Catalysis B: Environmental*, 140-141, 68-81.

Lettmann, C., Hildenbrand, K., Kisch, H., Macyk, W., and Maier, W.F., (2001). Visible light photodegradation of 4-chlorophenol with a coke-containing titanium dioxide photocatalyst, *Applied Catalysis B: Environmental*, 32, 215-227.

Li, C., Ming, T., Wang, J., Wang, J., Yu, J.C. and Yu, S., (2014). Ultrasonic aerosol spray-assisted preparation of TiO_2/In_2O_3 composite for visible-light-driven photocatalysis, *Journal of Catalysis*, 310, 84-90.

Li, D., Ohashi, N., Hishita, S., Kolodiazhnyi, T. and Haneda, H., (2005). Origin of visible-light-driven photocatalysis: A comparative study on N/F-doped and N-F-codoped TiO_2 powders by means of experimental characterizations and theoretical calculations, *Journal of Solid State Chemistry*, 178, 3293-3302.

Li, J.G., Ishigaki, T. and Sun, X., (2007). Anatase, brookite, and rutile nanocrystals via redox reactions under mild hydrothermal conditions: phase-selective synthesis and physicochemical properties, *Journal of Physical Chemistry C*, 111, 4969-4976.

Footer Page TH-1334_08610706

Li, X., Liu, Q., Jiang, X.Y. and Huang, J., (2012). Enhanced photocatalytic activity of Ga-N Co-doped anatase TiO_2 for water decomposition to hydrogen, *International Journal of Electrochemical Science*, 7, 11519-11527.

Li, X., Zhang, J., Kang, S., Li, G. and Mu, J., (2014). Visible light photocatalytic activity of CuO/Cr_2O_3 co-loaded multiwalled carbon nanotubes sensitized with eosin Y for hydrogen evolution from water, *Ceramic International*, 40, 10171-10176.

Li, Y., Lee, N.H., Hwang, D.S., Song, J.S., Lee, E.G. and Kim, S.J., (2004). Synthesis and characterization of nano titania powder with high photoactivity for gas-phase photo-oxidation of benzene from $TiOCl_2$ aqueous solution at low temperatures, *Langmuir*, 20, 10838-10844.

Li, Y., Ma, G., Peng, S., Lu, G., Li, S., (2008). Boron and nitrogen co-doped titania with enhanced visible-light photocatalytic activity for hydrogen evolution, *Applied Surface Science*, 254, 6831-6836.

Li, Y., Sun, S., Ma, M., Ouyang, Y. and Yan, W., (2008). Kinetic study and model of the photocatalytic degradation of rhodamine B (RhB) by a TiO_2-coated activated carbon catalyst: Effects of initial RhB content, light intensity and TiO_2 content in the catalyst, *Chemical Engineering Journal*, 142, 147-155.

Li, Y., Yu, Z Meng, J. and Li, Y., (2013). Enhancing the activity of a SiC-TiO_2 composite catalyst for photo-stimulated catalytic water splitting, *International Journal of Hydrogen Energy*, 38, 3898-3904.

Li, Z., Liu, J., Wang, D., Gao, Y. and Shen, J., (2012). $Cu_2O/Cu/TiO_2$ nanotube Ohmic heterojunction arrays with enhanced photocatalytic hydrogen production activity, *International Journal of Hydrogen Energy*, 37, 6431-6437.

Li, Z., Zhang, P., Shao, T. and Li, X., (2012). In_2O_3 nanoporous nanosphere: A highly efficient photocatalyst for decomposition of perfluorooctanoic acid, *Applied Catalysis B: Environmental*, 125, 350-357.

Liao, C.H., Huang, C.W. and Wu, J.C. S., (2012). Hydrogen production from semiconductor-based photocatalysis via water splitting, *Catalysts*, 2, 490-516.

Lim, C.S., Chen, M.L. and Oh, W.C., (2011). Synthesis of CdSe-TiO_2 photocatalyst and their enhanced photocatalytic activities under UV and visible light, *Bulletin of the Korean Chemical Society*, 32, 1657-1661.

Footer Page TH-1334_08610706

Lin, H.Y., Chen, Y.F. and Chen, Y.W., (2007). Water splitting reaction on $NiO/InVO_4$ under visible light irradiation, *International Journal of Hydrogen Energy*, 32, 86-92.

Lin, W.C., Yang, W.D., Huang, I.L., Wu, T.S. and Chung, Z.J., (2009). Hydrogen Production from methanol/water photocatalytic decomposition using $Pt/TiO_{2-x}N_x$ catalyst. *Energy & Fuels*, 23, 2192-2196

Lin, W.C., Yang, W.D., Huang, I.L., Wu, T.S. and Chung, Z.J., (2009). Hydrogen production from methanol/water photocatalytic decomposition using $Pt/TiO_{2-x}N_x$ catalyst, *Energy & Fuels*, 23, 2192-2196.

Lin, Y., Ferronato, C., Deng, N., Wu, F. and Chovelon, J.M., (2009). Photocatalytic degradation of methylparaben by TiO_2: Multivariable experimental design and mechanism, *Applied Catalysis B: Environmental*, 88, 32-41.

Linsebigler, A.L., Lu, G. and Yates, J.T., (1995). Photocatalysis on TiO_2 surfaces: Principles, mechanisms, and selected results, *Chemical reviews*, 95, 735-738.

Litter, M. I., (1999). Heterogeneous photocatalysis: Transition metal ions in photocatalytic systems, *Applied Catalysis B: Environmental*, 23, 89-114.

Liu, H., He, X., Hu, Y., Liu, X., Jia, H. and Xu, B., (2014). One-step hydrothermal synthesis of In_2O_3-ZnO heterostructural composites and their enhanced visible-light photocatalytic activity, *Materials Letters*, 131, 104-107.

Liu, H., Wu, Y. and Zhang, J., (2011). A new approach toward carbon-modified vanadium-doped titanium dioxide photocatalysts, ACS *Applied Materials & Interfaces*, 3, 1757-1764.

Liu, J., Han, R., Zhao, Y., Wang, H., Lu, W., Yu, T. and Zhang, Y., (2011). Enhanced photoactivity of V-N Codoped TiO_2 derived from a two-step hydrothermal procedure for the degradation of PCP-Na under visible light irradiation, *Journal of Physical Chemistry C*, 115, 4507-4515.

Liu, S.H., and Syu, H.R., (2013). High visible-light photocatalytic hydrogen evolution of C, N-codoped mesoporous TiO_2 nanoparticles prepared via an ionic-liquid-template approach, *International Journal of Hydrogen Energy*, 38, 13856-13865.

Footer Page TH-1334_08610706

Llordés, A., Palau, A., Gázquez, J., Coll, M., Vlad, R., Pomar, A., Arbiol, J., Guzmán, R., Ye, S., Rouco, V., Sandiumenge, F., Ricart, S., Puig, T., Varela, M., Chateigner, D., Vanacken, J., Gutiérrez, J., Moshchalkov, V., Deutscher, G., Magen, C. and X. Obradors, X., (2012). Nanoscale strain-induced pair suppression as a vortex-pinning mechanism in high-temperature superconductors, *Nature Materials*, 11, 329-336.

Lu, J., Jin, H., Dai, Y., Yang, K. and Huang, B., (2012). Effect of electronegativity and charge balance on the visible-light-responsive photocatalytic activity of nonmetal doped anatase TiO_2, *International Journal of Photoenergy*, Article ID 928503, 8 pages.

Luo, F., Wu, D., Gao, L., Lian, S., Wang, E., Kang, Z., Lan, Y. and Xu, L., (2005). Shape-controlled synthesis of Cu_2O nanocrystals assisted by Triton X-100, *Journal of Crystal Growth*, 285, 534-540.

Lutz, A.E., Bradshaw, R.W., Bromberg, L. and Rabinovich, A., (2004). Thermodynamic analysis of hydrogen production by partial oxidation reforming, *International Journal of Hydrogen Energy*, 29, 809-816.

Lv, J., Kako, T., Li, Z., Zou, Z. and Ye, J., (2010). Synthesis and photocatalytic activities of $NaNbO_3$ rods modified by In_2O_3 nanoparticles, *Journal of Physical Chemistry C*, 114, 6157-6162.

Maeda, K. and Domen, K., (2007). New non-oxide photocatalysts designed for overall water splitting under visible light, *Journal of Physical Chemistry C*, 111, 7851-7861.

Maeda, K., (2011). Photocatalytic water splitting using semiconductor particles: History and recent developments, *Journal of Photochemistry and Photobiology C: Photochemistry Reviews*, 12, 237-268.

Magesh, G., Viswanathan, B., Viswanath, R.P. and Varadarajan, T.K., (2009). Photocatalytic behavior of CeO_2-TiO_2 system for the degradation of methylene blue, *Indian Journal of Chemistry*, 48A, 480-488.

Majrik, K., Tálas, E., Pászti, Z., Sajó, I., Mihály, J., Korecz, L., Drotár, E. and Tompos, A., (2013). Enhanced activity of sol-gel prepared SnO_x-TiO_2 in photocatalytic methanol reforming, *Applied Catalysis A: General*, 466, 169-178.

Footer Page TH-1334_08610706

Malato, S., Ibanez, P.F., Maldonado, M.I., Blanco, J. and Gernjak, W.,(2009). Decontamination and disinfection of water by solar photocatalysis: Recent overview and trends, *Catalysis Today*, 147, 1-59.

Matsuoka, M., Kitano, M., Takeuchi, M., Tsujimaru, K., Anpo, M. and Thomas, J. M., (2007). Photocatalysis for new energy production: Recent advances in photocatalytic water splitting reactions for hydrogen production, *Catalysis Today*, 122, 51-61.

Matthews, R. W., (1988). Kinetics of photocatalytic oxidation of organic solutes over titanium dioxide, *Journal of Catalysis*, 111, 264-272.

Melis, A., Zhang, L.P., Forestier, M., Ghirardi, M.L. and Seibert, M., (2000). Sustained photobiological hydrogen gas production upon reversible inactivation of oxygen evolution in the green alga *Chlamydomonas reinhardtii*, *Plant Physiology*, 122, 127-135.

Meng, X., Qi, L., Xiao, Z., Gong, S., Wei, Q., Liu, Y, Yang, M. and Wang, F., (2012). Facile synthesis of direct sunlight-driven anatase TiO_2 nanoparticles by in situ modification with trifluoroacetic acid, *Journal of Nanoparticle Research*, 14, 1176-1182.

Miura, Y., Akano, T., Fukatsu, K., Miyasaka, H., Mizoguchi, T., Yagi, K., Maeda, I., Ikuta, Y. and Matsumoto, H., (1997). Stably sustained hydrogen production by biophotolysis in natural day/night cycle, *Energy Conversion and Management*, 38, S533-S537.

Moon, S.C., Mametsuka, H., Suzuki, E. and Nakahara, Y., (1998). Characterization of titanium-boron binary oxides and their photocatalytic activity for stoichiometric decomposition of water, *Catalysis Today*, 45, 79-84.

Moon, S.C., Mametsuka, H., Tabata, S. and Suzuki, E., (2000). Photocatalytic production of hydrogen from water using TiO_2 and B/TiO_2, *Catalysis Today*, 58, 125-132.

Mor, G.K., Varghese, O.K., Paulose, M., Shankar, K. and Grimes, C.A., (2006). A review on highly ordered, vertically oriented TiO_2 nanotube arrays: Fabrication, material properties, and solar energy applications, *Solar Energy Materials & Solar Cells*, 90, 2011-2075.

Mu, J., Chen, B., Zhang, M., Guo, Z., Zhang, P., Zhang, Z., Sun, Y., Shao, C. and Liu, Y., (2012). Enhancement of the visible-light photocatalytic activity of In_2O_3-TiO_2 nanofiber heteroarchitectures, ACS *Applied Materials & Interfaces,* 4, 424-430.

Naik, B., Parida, K.M. and Gopinath, C.S. (2010). Facile synthesis of N- and S-incorporated nanocrystalline TiO_2 and direct solar-light-driven photocatalytic activity, *Journal of Physical Chemistry C,* 114, 19473-19482.

Nair, M.G., Nirmala, M., Rekha, K. and Anukaliani, A., (2011). Structural, optical, photo catalytic and antibacterial activity of ZnO and Co doped ZnO nanoparticles. *Materials Letters,* 65, 1797-1800.

Nakamura, R., Okamoto, A., Osawa, H., Irie, H. and K. Hashimoto, K., (2007). Design of all-inorganic molecular-based photocatalysts sensitive to visible light: Ti(IV)-O-Ce(III) Bimetallic assemblies on mesoporous silica, *Journal of the American Chemical Society,* 129 (2007), pp. 9596-9597.

Nakamura, R., Tanaka, T. and Nakato, Y., (2004). Mechanism for visible light responses in anodic photocurrents at N-doped TiO_2 film electrodes, *Journal of Physical Chemistry B,* 108, 10617 -10620.

Nakata, K. and Fujishima, A., (2012). TiO_2 photocatalysis: Design and applications, *Journal of Photochemistry and Photobiology C: Photochemistry Reviews,* 13, 169-189.

Nash, M., (2008). An investigation into the photocatalytic properties of microporous titanosilicate materials, ProQuest LLC, Umi Dissertation Publishing, 1-231.

Nasir, M., Xi, Z., Xing, M., Zhang, J., Chen, F., Tian, B. and Bagwasi, S., (2013). Study of synergistic effect of Ce- and S‑Codoping on the enhancement of visible-light photocatalytic activity of TiO_2, *Journal of Physical Chemistry C,* 117, 9520-9528. *Nature*, 488, 294-303.

Ngoh, S.K. and Njomo, D., (2012). An overview of hydrogen gas production from solar energy, *Renewable and Sustainable Energy Reviews,* 16, 6782-6792.

Ni, M., Leung, M.K.H., Leung, D.Y.C. and Sumathy, K., (2007). A review and recent developments in photocatalytic water-splitting using TiO_2 for hydrogen production, *Renewable and Sustainable Energy Reviews,* 11, 401-425.

Niu, Y., Xing, M., Tian, B. and Zhang, J., (2012). Improving the visible light photocatalytic activity of nano-sized titanium dioxide via the synergistic effects between sulfur doping and sulfation, *Applied Catalysis B: Environmental,* 115-116, 253-260.

Niyomkarn, S., Puangpetch,T. and Chavadej, S., (2014). Mesoporous-assembled In_2O_3-TiO_2 mixed oxide photocatalysts for efficient degradation of azo dye contaminant in aqueous solution, *Materials Science in Semiconductor Processing*, 25, 112-122.

Nomikos, G.N., Panagiotopoulou, P., Kondarides, D.I. and Verykios, X.E., (2014). Kinetic and mechanistic study of the photocatalytic reforming of methanol over Pt/TiO_2 catalyst, *Applied Catalysis B: Environmental*, 146, 249-257.

Nosaka, Y., Matsushita, M., Nishino, J. and Nosaka, A. Y., (2005). Nitrogen-doped titanium dioxide photocatalysts for visible response prepared by using organic compounds, *Science and Technology of Advanced Materials*, 6, 143-148.

Nowotny, J., Bak, T., Nowotny, M.K. and Sheppard, L.R., (2007). Titanium dioxide for solar-hydrogen I. Functional properties. *International Journal of Hydrogen Energy*, 32, 2609-2629.

Nowotny, J., Sorrell, C.C., Bak, T. and Sheppard, L.R., (2005). Solar-hydrogen: Unresolved problems in solid-state science, *Solar Energy*, 78,593-602.

Ohno, T., (2004a). Preparation of visible light active S-doped TiO_2 photocatalysts and their photocatalytic activities, *Water Science and Technology*, 49,159-163,

Ohno, T., Akiyoshi, M., Umebayashi,T., Asai, K., Mitsui, T. and Matsumura, M., (2004b). Preparation of S-doped TiO_2 photocatalysts and their photocatalytic activities under visible light. *Applied Catalysis A: General*, 265,115-121.

Ohno, T., Mitsui, T. and Matsumura, M., (2003). Photocatalytic activity of S-doped TiO_2 photocatalyst under visible light, *Chemistry of Letters*, 32, 364-365.

Ohtani, B., (2014). Revisiting the fundamental physical chemistry in heterogeneous photocatalysis: its thermodynamics and kinetics, *Physical Chemistry Chemical Physics*, 16, 1788-1797.

Footer Page TH-1334_08610706

Osterloh, F.E., (2008). Inorganic materials as catalysts for photochemical splitting of water, *Chemistry of Materials*, 20, 35-54.

Ou, Y., Lin, J., Fang,S., and Liao, D., (2006). MWNT-TiO_2:Ni composite catalyst: A new class of catalyst for photocatalytic H_2 evolution from water under visible light illumination, *Chemical Physics Letters*, 429, 199-203.

Pagliaro, M. and Konstandopoulos, A.G., (2012). Solar hydrogen: Fuel of the future, Dorset press, Dorchester, UK, 1-164.

Pal, U., Ghosh, S. and Chatterjee, D., (2012). Effect of sacrificial electron donors on hydrogen generation over visible light-irradiated nonmetal-doped TiO_2 photocatalysts, *Transition Metal Chemistry*, 37, 93-96.

Paleocrassas, S.N., (1974). Review article: Photocatalytic hydrogen production: A solar energy conversion alternative?, *Solar Energy*, 16, 45-51.

Panwar, N.L., Kaushik, S.C., Surendra Kothari, S., (2011). Role of renewable energy sources in environmental protection: A review. *Renewable and Sustainable Energy Reviews*, 15, 1513-1524.

Papageorgiou, P., Zervos, M. and Othonos, A., (2011). An investigation into the conversion of In_2O_3 into InN nanowires, *Nanoscale Research Letters*, 6, 311-315.

Peharz, G., Dimroth, F. and Wittstadt, U., (2007). Solar hydrogen production by water splitting with a conversion efficiency of 18%, *International Journal of Hydrogen Energy*, 32, 3248-3252.

Pelaez, M., Nolan, N. T., Pillai, S. C., Seery, M. K., Falaras, P., Kontos, A.G., Dunlop, P. S.M., Hamilton, J.W.J., Byrne, J.A., O'Shea, K., Entezari, M. H. and Dionysiou, D. D., (2012). A review on the visible light active titanium dioxide photocatalysts for environmental applications, *Applied Catalysis B Environmental*, 125, 331- 349.

Peng, X.S., Meng, G.W., Zhang, J., Wang, X.F., Wang, Y.W, Wang, C.Z. and Zhang, L.D., (2002). Synthesis and photoluminescence of single-crystalline In_2O_3 nanowires, *Journal of Materials Chemistry*, 12, 1602-1605.

Periyat, P., Pillai, S.C., McCormack, D.E., Colreavy, J. and Steven J. Hinder, S.J., (2008). Improved high-temperature stability and sun-light-driven photocatalytic

Footer Page TH-1334_08610706

activity of sulfur-doped anatase TiO_2, *Journal of Physical Chemistry C*, 112, 7644-7652.

Priyanka, K.P., Tresa, S.A., Jaseentha, O.P. and Varghese, T., (2014). Cerium doped nanotitania-extended spectral response for enhanced photocatalysis, *Materials Research Express*, 1, 015003 (11 pages)

Qin, S., Xin, F., Liu, Y., Yin, X. and Ma, W., (2011). Photocatalytic reduction of CO_2 in methanol to methyl formate over CuO-TiO_2 composite catalysts, *Journal of Colloid and Interface Science*, 356, 257-261.

Rajeshwar, K., Chenthamarakshan, C.R., Ming, Y. and Sun, W., (2002). Cathodic photoprocesses on titania films and in aqueous suspensions, *Journal of Electroanalytical Chemistry*, 538-539, 173-182.

Rajeshwar, K., McConnel, R. and Licht, S., (2009). Solar hydrogen generation: Toward renewable energy future, Springer publications, 1-338.

Reddy, B.M., Khan, A., Yamada, Y., Kobayashi, T., Loridant, S. and Volta, J.C., (2003). Structural characterization of CeO_2−TiO_2 and V_2O_5/CeO_2−TiO_2 catalysts by raman and XPS techniques, *Journal of Physical Chemistry B*, 107, 5162-5167.

Reddy, J.K., Lalitha, K., Reddy, P.V.L., Sadanandam, G., Subrahmanyam, M. and Durga Kumari, V., (2014). Fe/TiO_2: A visible light active photocatalyst for the continuous production of hydrogen from water splitting under solar irradiation, *Catalysis Letters*, 144, 340-346.

Rehman, S., Ullah, R., Butt, A.M. and Gohar, N.D.,(2009). Review: Strategies of making TiO_2 and ZnO visible light active, *Journal of Hazardous Materials*, 170, 560-569.

Rothenberger, G., Moser,J., Gratzel, M., Serpone,N. and Sharma, D.K., (1985). Charge carrier trapping and recombination dynamics in small semiconductor particles, *Journal of the American Chemical Society*, 107, 8054-8059.

Rouquerol, F., Rouquerol, J. and Sing, K.S.W., (1999). Adsorption by powders and porous solid: principle, methodology and applications. Academic Press, San Diego.

Sabio E. M., Chamousis R. L., Browning N. D. and Osterloh F. E. (2012). Photocatalytic water splitting with suspended calcium niobium oxides: why nanoscale

Footer Page TH-1334_08610706

is better than bulk- a kinetic analysis, *Journal of Physical Chemistry C,* 116, 3161-3170.

Sahu, N., Upadhyay, S.N. and Sinha, A.S.K., (2009). Kinetics of reduction of water to hydrogen by visible light on alumina supported Pt-CdS photocatalysts, *International Journal of Hydrogen Energy*, 34, 130-137.

Sakata, T. and Kawai, T., (1981). Heterogeneous photocatalytic production of hydrogen and methane from ethanol and water, *Chemical Physics Letters*, 80, 341-344.

Sakthivel, S. and Kisch, H., (2003). Daylight photocatalysis by carbon-modified titanium dioxide, *Angewandte Chemie International Edition*, 42, 4908-4911.

Saliby, I.E., Erdei, L., Shon, H.K. and Kim, J.H., (2011). Development of visible light sensitive titania photocatalysts by combined nitrogen and silver doping, *Journal of Industrial and Engineering Chemistry*, 17, 358-363.

Sasikala, R., Shirole, A., Sudarsan, V., Sakuntala, T., Sudakar, C., Naik, R. and Bharadwaj, S.R., (2009). Highly dispersed phase of SnO_2 on TiO_2 nanoparticles synthesized by polyol-mediated route: Photocatalytic activity for hydrogen generation, *International Journal of Hydrogen Energy*, 34, 3621-3630.

Sasikala, R., Shirole, A.R., Sudarsan, V., Jagannath, Sudakar, C., Naik, R., Rao, R. and Bharadwaj, S.R., (2010). Enhanced photocatalytic activity of indium and nitrogen co-doped TiO_2-Pd nanocomposites for hydrogen generation, *Applied Catalysis A: General*, 377, 47-54.

Sasikala, R., Sudarsan, V., Sudakar, C., Naik, R., Sakuntala, T. and Bharadwaj, SR., (2008). Enhanced photocatalytic hydrogen evolution over nanometer sized Sn and Eu doped titanium oxide, *International Journal of Hydrogen Energy*, 33, 4966-4973.

Sathish, M., Viswanathan, B. and Viswanath, R.P., (2007). Characterization and photocatalytic activity of N-doped TiO_2 prepared by thermal decomposition of Ti-melamine complex. *Applied Catalysis B: Environmental*, 74, 307-312.

Sathish, M., Viswanathan, B., Viswanath, R.P. and Gopinath, C,S., (2005). Synthesis, characterization, electronic structure and photocatalytic activity of N-doped TiO_2, *Chemistry of materials*, 17, 6349-6353.

Footer Page TH-1334_08610706

Sato, S. and White, J.M., (1980). Photodecomposition of water over Pt/TiO_2 catalysts, *Chemical Physics Letters*, 72, 83-86.

Sayama, K. and Arakawa, H., (1997). Effect of carbonate salt addition on the photocatalytic decomposition of liquid water over catalyst $Pt\text{-}TiO_2$, *Journal of the Chemical Society, Faraday Transactions*, 93, 1647-1654.

Scibioh, M.A. and Viswanathan. B., (2004). Hydrogen Future: Facts and Fallacies, *Bulletin of the Catalysis Society of India*, 3, 72-81.

Seeley, Z., Choi, Y.J. and Bose, S., (2009). Citrate-nitrate synthesis of nano-structured titanium dioxide ceramics for gas sensors, *Sensors and Actuators B*, 140, 98-103.

Selcuk, M.Z., Boroglu, M.S. and Boz, I., (2012). Hydrogen production by photocatalytic water-splitting using nitrogen and metal co-doped TiO_2 powder photocatalyst, *Reaction Kinetics and Catalysis Letters*, 106, 313-324.

Selvam, K., Balachandran, S., Velmurugan, R. and Swaminathan, M., (2012). Mesoporous nitrogen doped nano titania -A green photocatalyst for the effective reductive cleavage of azoxybenzenes to amines or 2-phenyl indazoles in methanol, *Applied Catalysis A*, 413-414, 213-222.

Semelsberger, T.A., Brown, L.F., Borup, R.L. and Inbody, M.A., (2004). Equilibrium products from autothermal processes for generating hydrogen-rich fuel-cell feeds, *International Journal of Hydrogen Energy*, 29, 1047-1064.

Shi, J., Chen, J., Feng, Z., Chen, T., Lian, Y., Wang, X. and Li, C., (2007). Photoluminescence characteristics of TiO_2 and their relationship to the photoassisted reaction of water/methanol mixture, *Journal of Physical Chemistry C*, 111, 693-699.

Sidheswaran, M. and Tavlarides, L.L., (2009). Characterization and visible light photocatalytic activity of cerium- and iron-doped titanium dioxide sol-gel materials, *Industrial & Engineering Chemistry Research*, 48, 10292-10306.

Silva, C.G., Juarez, R., Marino, T., Molinari, R. and Garcia,H., (2011). Influence of excitation wavelength (UV or Visible Light) on the photocatalytic activity of titania containing gold nanoparticles for the generation of hydrogen or oxygen from water, *Journal of the American Chemical Society*, 133, 595-602.

Sing, K.S.W., Everett, D.H., Haul, R.A.W., Moscou, L., Pierotti, R.A., Rouquerol, J. and Siemieniewska, T., (1985). Reporting physisorption data for gas/solid systems with special reference to the determination of surface area and porosity, *Pure and Applied Chemistry*, 57, 603-619.

Skinner, D.E., Colombo Jr. D.P., Cavaleri, J.J. and Robert M. Bowman, R.M., (1995). Femtosecond investigation of electron trapping in semiconductor nanoclusters, *Journal of Physical Chemistry*, 99, 7853-7856.

Slamet, Nasution, H.W., Purnama, E., Kosela, S. and Gunlazuardi, J., (2005). Photocatalytic reduction of CO_2 on copper-doped Titania catalysts prepared by improved-impregnation method**,** *Catalysis Communications,* 6, 313-319.

Sobczynski, A., Jakubowska, T. and Zielinski, S., (1989). Hydrogen photoevolution from water-methanol on Ru/TiO_2, *Monatshefte fur Chemie,* 120, 101-109.

Sreethawong, T. and Yoshikawa, S., (2005). Comparative investigation on photocatalytic hydrogen evolution over Cu-, Pd- and Au-loaded mesoporous TiO_2 photocatalysts, *Catalysis Communications,* 6 (2005) 661-668.

Sreethawong, T., Laehsalee, S. and Chavadej, S., (2008). Comparative investigation of mesoporous- and non-mesoporous-assembled TiO_2 nanocrystals for photocatalytic H_2 production over N-doped TiO_2 under visible light irradiation, *International Journal of Hydrogen Energy*, 33 (2008) 5947-5957

Sreethawong, T., Laehsalee, S. and Chavadej, S., (2009). Use of Pt/N-doped mesoporous-assembled nanocrystalline TiO_2 for photocatalytic H_2 production under visible light irradiation, *Catalysis Communications,* 10, 538-543.

Sreethawong, T., Puangpetch, T., Chavadej, S. and Yoshikawa, S., (2007). Quantifying influence of operational parameters on photocatalytic H_2 evolution over Pt-loaded nanocrystalline mesoporous TiO_2 prepared by single-step sol–gel process with surfactant template, *Journal of Power Sources*, 165, 861-869.

Sreethawong, T., Suzuki, Y. and Yoshikawa, S., (2006). Platinum-loaded mesoporous titania by single-step sol-gel process with surfactant template: photocatalytic activity for hydrogen evolution, *Comptes Rendus Chimie,* 9, 307-314.

Footer Page TH-1334_08610706

Stathatos, E., Tsiourvas, D. and Lianos, P., (1999). Titanium dioxide films made from reverse micelles and their use for the photocatalytic degradation of adsorbed dyes, *Colloids and Surfaces A: Physicochemical and Engineering Aspects*, 149, 49-56.

Strataki, N., Antoniadou, M., Dracopoulos, V. and Lianos, P., (2010). Visible-light photocatalytic hydrogen production from ethanol-water mixtures using a Pt-CdS-TiO_2 photocatalyst, *Catalysis Today*, 151, 53-57.

Sun, L. and Bolton, J.R., (1996). Determination of the quantum yield for the photochemical generation of hydroxyl radicals in TiO_2 suspensions, *Journal of Physical Chemistry* 100, 4127-4134.

Sun, X., Liu, H., Dong, J., Wei, J. and Zhang, Y., (2010). Preparation and characterization of Ce/N-Codoped TiO_2 particles for production of H_2 by photocatalytic splitting water under visible light, *Catalysis Letters*, 135, 219-225.

Tabata, S., Nishida, H., Masaki, Y. and Tabata, K., (1995). Stoichiometric photocatalytic decomposition of pure water in Pt/TiO_2 aqueous suspension system, *Catalysis Letters*, 34, 245-249.

Tan, L.L., Ong, W.J., Chai, S.P. and Mohamed, A.R., (2013). Reduced graphene oxide-TiO_2 nanocomposite as a promising visible-light-active photocatalyst for the conversion of carbon dioxide, *Nanoscale Research Letters*, 8, 465-473.

Teh, C.M. and Mohamed, A.R., (2011). Roles of titanium dioxide and ion-doped titanium dioxide on photocatalytic degradation of organic pollutants (phenolic compounds and dyes) in aqueous solutions: A review, *Journal of Alloys and Compounds*, 509, 1648-1660.

Teoh, W.Y., Scott, J.A. and Amal, R., (2012). Progress in heterogeneous photocatalysis: from classical radical chemistry to engineering nanomaterials and solar reactors, *Journal of Physical Chemistry Letters*, 3, 629-639.

Tian, F., Liu, C., Zhao, W., Wang, X., Wang, Z. and Yu, J.C., (2011). Cationic S-doped anatase TiO_2: a DFT study, *Journal of Computational Science and Engineering*, 1, 33-41.

Tiwari, A. and Pandey, A., (2012). Cyanobacterial hydrogen production-A step towards clean environment, *International Journal of Hydrogen Energy*, 37, 139-150.

Footer Page TH-1334_08610706

Tong, H., Ouyang, S., Bi, Y., Umezawa, N., Oshikiri, M. and Ye, J., (2012). Nano-photocatalytic materials: possibilities and challenges, *Advanced Materials*, 24, 229-251.

Turchi, C.S., and Ollis, D.F., (1989). Mixed reactant photocatalysis: Intermediates and mutual rate inhibition, *Journal of Catalysis*, 119, 483-496.

Turchi, C.S., and Ollis, D.F., (1990). Photocatalytic degradation of organic water contaminants: Mechanisms involving hydroxyl radical attack, *Journal of Catalysis*, 122, 178-192.

Turner, J.A., (2004). Sustainable hydrogen production, *Science*, 305, 972-974.

Umebayashi, T., Yamaki, T., Itoh, H. and Asai, K., (2002). Band gap narrowing of titanium dioxide by sulfur doping, *Applied Physics Letters*, 81, 454-456.

Umebayashi, T., Yamaki, T., Tanaka, S. and Asai**,** K., (2003a). Visible light-induced degradation of methylene blue on S-doped TiO_2, *Chemistry Letters*, 32, 330-331.

Umebayashi, T., Yamaki, T., Yamamoto, S., Miyashita, A., Tanaka, S., Sumita, T., Asai, K., (2003b). Sulfur-doping of rutile-titanium dioxide by ion implantation: Photocurrent spectroscopy and first-principles band calculation studies, *Journal of Applied Physics*, 93, 5156-5160.

Valentin, C.D. and Pacchioni, G., (2013). Trends in non-metal doping of anatase TiO_2: B, C, N and F, *Catalysis Today*, 206, 12-18.

Valentin, C.D., Pacchioni, G. and Selloni, A., (2005). Theory of carbon doping of titanium dioxide, *Chemistry of Materials*, 17, 6656-6665.

Viswanathan, B., (2003). Photocatalytic processes-Selection criteria for the choice of materials, *Bulletin of the Catalysis Society of India*, 2, 71-74.

Vogel, I.A., (1961), A text book of inorganic analysis, 3rd edition, Longmans, Green and Co Ltd, London, 593-594.

Wang, C., Hu, Q., Huang, J., Wu, L., Deng, Z., Liu, Z., Liu, Y. and Yongge Cao, Y., (2013). Efficient hydrogen production by photocatalytic water splitting using N-doped TiO_2 film, *Applied Surface Science*, 283, 188-192.

Footer Page TH-1334_08610706

Wang, D., Zou, Z. and Ye, J., (2005). Photocatalytic water splitting with the Cr-doped $Ba_2In_2O_5/In_2O_3$ composite oxide semiconductors, *Chemistry of Materials*, 17, 3255-3261.

Wang, E., He, T., Zhao, L., Chen, Y. and Cao, Y., (2011). Improved visible light photocatalytic activity of titania doped with tin and nitrogen, *Journal of Material Chemistry*, 21, 144-150.

Wang, E., Yang, W. and Cao, Y., (2009). Unique surface chemical species on Indium doped TiO_2 and their effect on the visible light photocatalytic activity, *Journal of Physical Chemistry C*, 113, 20912-20917.

Wang, Y., Chin, Y.H., Rozmiarek, R.T., Johnson, B.R., Gao, Y., Watson, J., Tonkovich, A.Y.L. and Wiel, D.A.P., (2004). Highly active and stable Rh/MgO-Al_2O_3 catalysts for methane steam reforming, *Catalysis Today*, 98, 575-581.

Wang, Y.F., Hsieh, M.C., Lee, J.F. and Yang, C.M., (2013) Nonaqueous synthesis of CoO_x/TiO_2 nanocomposites showing high photocatalytic activity of hydrogen generation, *Applied Catalysis B: Environmental*, 142-143, 626-632.

Wang, Z., Roberts, R.R., Naterer, G.F. and Gabriel, K.S., (2012). Comparison of thermochemical, electrolytic, photoelectrolytic and photochemical solar-to-hydrogen production technologies, *International Journal of Hydrogen Energy*, 37, 16287-16301.

Wieckowski, A., Savinova, E.R. and Vayenas, C.G., (2003). Catalysis and electrocatalysis at nanoparticle surfaces, CRC Press, 1-70.

Wu, N.L., and Lee, M.S., (2004). Enhanced TiO_2 photocatalysis by Cu in hydrogen production from aqueous methanol solution, *International Journal of Hydrogen Energy*, 29, 1601-1605.

Wu, P., Li, Q., Zou, X., Cheng, W., Zhang, D., Zhao, C., Chi, L. and Xiao, T., (2009). Correlation between photoluminescence and oxygen vacancies in In_2O_3, SnO_2 and ZnO metal oxide nanostructures, *Journal of Physics: Conference Series*, 188, 012054.

Wu, Y., Xing, M., Tian, B., Zhang, J. and Chen, F., (2010). Preparation of nitrogen and fluorine co-doped mesoporous TiO_2 microsphere and photodegradation of acid orange 7 under visible light, *Chemical Engineering Journal*, 162, 710-717.

Footer Page TH-1334_08610706

Xiang, Q., Yu, J. and Jaroniec, M., (2011). Nitrogen and sulfur co-doped TiO_2 nanosheets with exposed {001} facets: synthesis, characterization and visible-light photocatalytic activity, Physical Chemistry Chemical Physics, 13, 4853-4861.

Xu, C., Killmeyer, R., Gray, M.L. and Khan, S.U.M., (2006). Photocatalytic effect of carbon-modified n-TiO_2 nanoparticles under visible light illumination, *Applied Catalysis B: Environmental*, 64, 312-317.

Xu, L., Guan, J., Gao, L. and Sun, Z., (2011). Preparation of heterostructured mesoporous In_2O_3/Ta_2O_5 nanocomposites with enhanced photocatalytic activity for hydrogen evolution *Catalysis Communications*, 12, 548-552.

Xu, Y. and Langford, C.H., (2000). Variation of Langmuir adsorption constant determined for TiO_2-photocatalyzed degradation of acetophenone under different light intensity, *Journal of Photochemistry and Photobiology A: Chemistry*, 133, 67-71.

Yamamoto, T., Yamashita, F., Tanaka, I., Matsubara, E. and Muramatsu, A., (2004). Electronic states of sulfur doped TiO_2 by first principles calculations, *Materials Transactions*, 45, 1987-1990.

Yan, C., Wang, Y.J., Zhou, K.G. and Bi, Z., (2010). Morphology control of ultrafine cuprous oxide powder and its growth mechanism, *Transactions of Nonferrous Metals Society of China*, 20, s216-s220.

Yang, G., Yan, Z., Xiao, T., (2012). Low-temperature solvothermal synthesis of visible-light-responsive S-doped TiO_2 nanocrystal, *Applied Surface Science*, 258, 4016-4022.

Yang, H., Yan, J., Lu, Z., Cheng, X. and Tang, Y., (2009). Photocatalytic activity evaluation of tetragonal $CuFe_2O_4$ nanoparticles for the H_2 evolution under visible light irradiation, *Journal of Alloys and Compounds*, 476, 715-719.

Yang, M., Hume, C., Lee, S., Son, Y.H. and Lee, J.K., (2010) Correlation between photocatalytic efficacy and electronic band structure in hydrothermally grown TiO_2 nanoparticles, *Journal of Physical Chemistry C*, 114,15292-15297.

Yang, Y.Z., Chang, C.H.and Idriss, H., (2006). Photo-catalytic production of hydrogen form ethanol over M/TiO_2 catalysts (M = Pd, Pt or Rh), *Applied Catalysis B: Environmental*, 67, 217-222.

Yin, J. and Cao, H., (2012). Synthesis and photocatalytic activity of single-crystalline hollow rh-In_2O_3 nanocrystals, *Inorganic Chemistry*, 51, 6529-6536.

Yoong, L.S., Chong, F.K. and Dutta, B.K., (2009). Development of copper-doped TiO_2 photocatalyst for hydrogen production under visible light, *Energy*, 34, 1652-1661.

Yu, C. and Yu, J.C., (2009). A simple way to prepare C-N-Codoped TiO_2 photocatalyst with visible-light activity, *Catalysis Letters*, 129, 462-470.

Yu, J., Hai, Y. and Jaroniec, M., (2011). Photocatalytic hydrogen production over CuO-modified titania, *Journal of Colloid and Interface Science*, 357, 223-228.

Yu, J.C., Ho, W., Yu, J., Yip, H., Wong, P.K. and Zhao, J., (2005). Efficient visible-light-induced photocatalytic disinfection on sulfur-doped nanocrystalline titania, *Environmental Science & Technology*, 39, 1175-1179.

Yu, T., Tan, X., Zhao, L., Yin, Y., Chen, P. and Wei, J., (2010). Characterization, activity and kinetics of a visible light driven photocatalyst: Cerium and nitrogen co-doped TiO_2 nanoparticles, *Chemical Engineering Journal*, 157, 86-92.

Yu, Y., Zhang, L., Wang, J., Yang, Z., Long, M., Hu, N. and Zhang, Y., (2012). Preparation of hollow porous Cu_2O microspheres and photocatalytic activity under visible light irradiation, *Nanoscale Research Letters*, 7, 347-352.

Yuan, J., Chen, M., Shi, J. and Shangguan, W., (2006). Preparations and photocatalytic hydrogen evolution of N-doped TiO_2 from urea and titanium tetrachloride, *International Journal of Hydrogen Energy*, 31, 1326 -1331.

Zeng, J., Li, J., Zhong, J., Huang, S., Shi, W. and He,J.,(2013). Synthesis, characterization and solar photocatalytic performance of In_2O_3-decorated Bi_2O_3, *Materials Science in Semiconductor Processing*, 16, 1808-1812.

Zhang, D., (2013). Synergetic effects of Cu_2O photocatalyst with titania and enhanced photoactivity under visible irradiation, *Acta Chimica Slovaca*, 6, 141-149.

Zhang, X., and Liu, Q., (2008). Visible-light-induced degradation of formaldehyde over titania photocatalyst co-doped with nitrogen and nickel, *Applied Surface Science*, 254, 4780-4785.

Zhang, Y.X., Li, G.H., Jin, Y.X., Zhang, Y., Zhang, J. and Zhang, L.D., (2002). Hydrothermal synthesis and photoluminescence of TiO_2 nanowires, *Chemical Physics Letters*, 365, 300-304.

Zhao, W., Ma, W., Chen, C., Zhao, J. and Shuai, Z., (2004). Efficient Degradation of toxic organic pollutants with $Ni_2O_3/TiO_{2-x}B_x$ under visible irradiation, *Journal of the American Chemical Society*, 126, 4782 -4783.

Zhao, W., Wang, Y., Yang, Y., Tang, J. and Yang, Y., (2012). Carbon spheres supported visible-light-driven CuO-$BiVO_4$ heterojunction: Preparation, characterization, and photocatalytic properties, *Applied Catalysis B: Environmental*, 115-116, 90-99.

Zhong, J., Li, J., Zeng, J., He, X., Huang, S., Jiang, W. and Li, M., (2014). Enhanced photocatalytic activity of In_2O_3-decorated TiO_2, *Applied Physics A: Materials science and Processing*, 115, 1231-1238.

Zhou, H., Qu, Y., Zeid, T. and Duan, X., (2012).Towards highly efficient photocatalysts using semiconductor nanoarchitectures, *Energy & Environmental Science*, 5, 6732-6743.

Zhu, J. and Zach, M., (2009). Nanostructured materials for photocatalytic hydrogen production, *Current Opinion in Colloid and Interface Science*, 14**,** 260-269.

Footer Page TH-1334_08610706

Appendices

Appendix A: Preparation steps for various catalysts

1. Preparation procedure of cerium and nonmetal codoped TiO_2

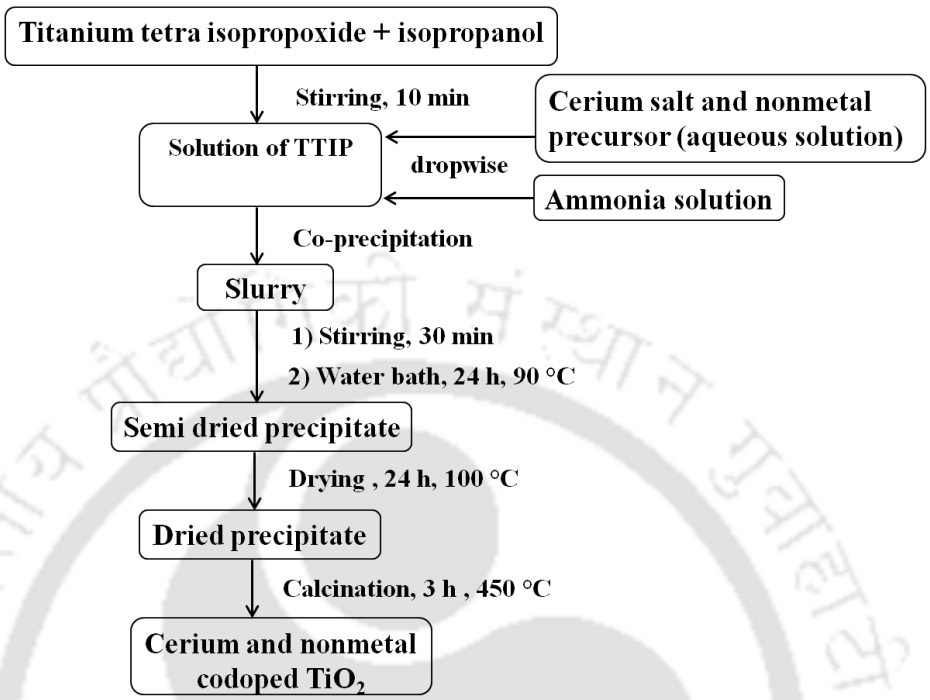

Fig.A.1. Steps for preparation of cerium and nonmetal codoped TiO_2

2. Preparation procedure of transition metal and nonmetal codoped TiO_2

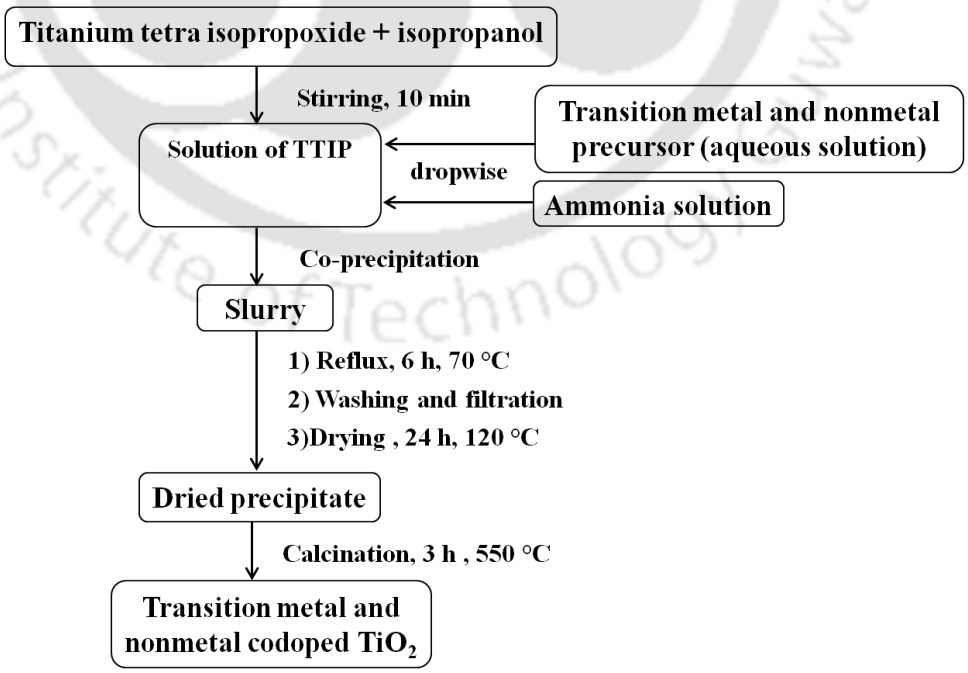

Fig.A.2. Steps for preparation of transition metal and nonmetal codoped TiO_2

Footer Page TH-1334_08610706

3. Preparation procedure of copper doped indium-titanium coupled oxide

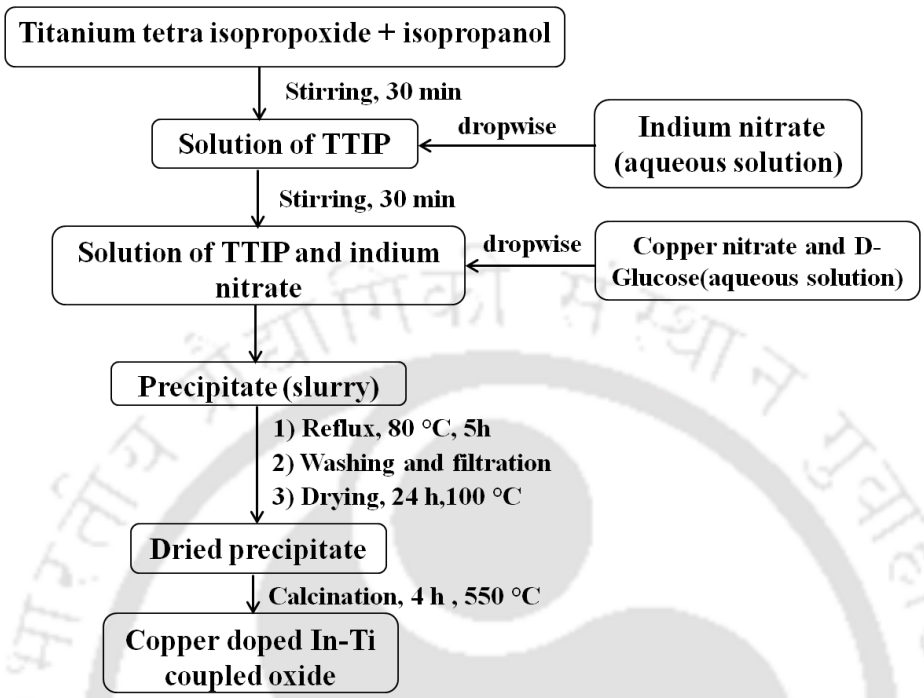

Fig.A.3. Steps for preparation of copper doped indium-titanium coupled oxide

Footer Page TH-1334_08610706

Appendix B: Calibration plots

1. Calibration plot for Hydrogen (GC)

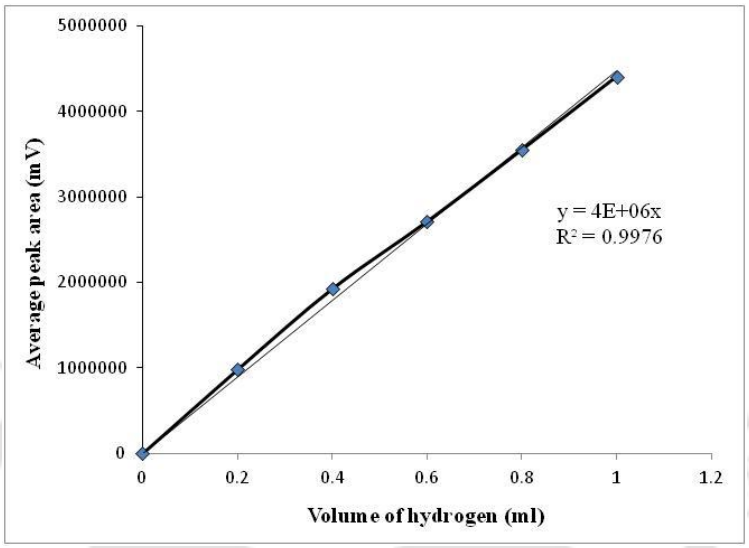

Fig.A.4. Calibration plot for hydrogen (GC)

2. Calibration plot for methanol (GC)

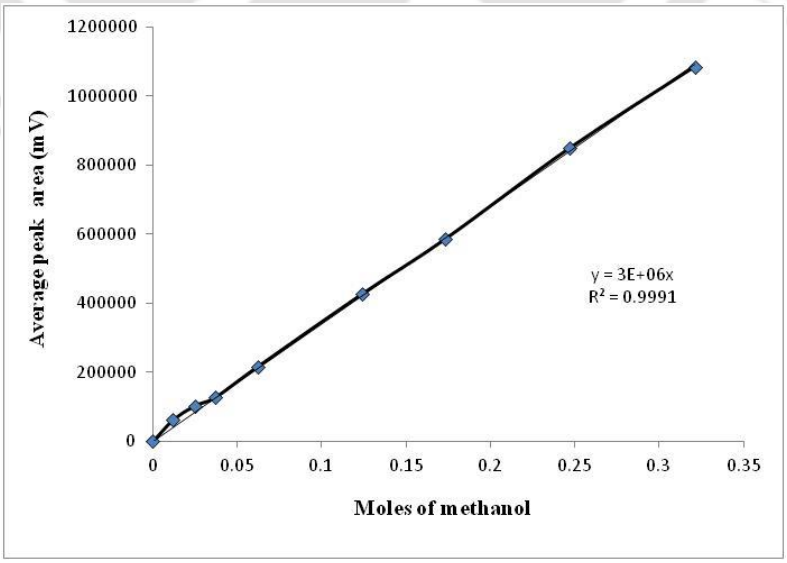

Fig.A.5. Calibration plot for methanol (GC)

Footer Page TH-1334_08610706

3. Calibration plot for formaldehyde (HPLC)

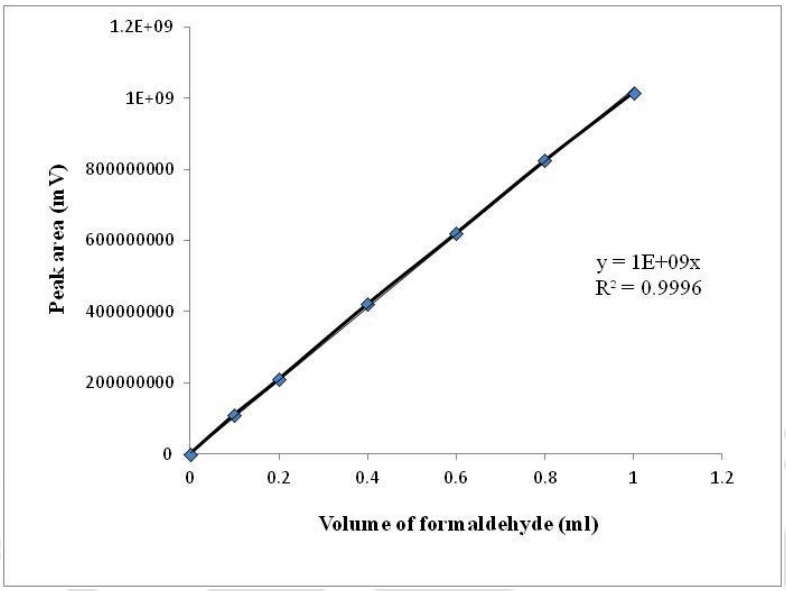

Fig.A.6. Calibration plot for formaldehyde (HPLC)

Footer Page TH-1334_08610706

Appendix C: Calculation of lattice parameters, d-spacing and lattice distortion

Sample calculation for Ce-TiO_2:

Reference planes 101 (2θ =25.6°) and 004 (2θ =38 °)

1. d-spacing values can be obtained from the Bragg's equation

$$d = \frac{n\lambda}{2 \sin\theta} \qquad (1)$$

λ = 1.5406 Å for X-ray source Cu K-alpha), θ = diffraction angle

For 004 (2θ =38°), d_{004} = 2.3648 Å and d_{101} = 3.4822 Å

2. Lattice parameters

For tetragonal system, a = b ≠ c

$$\frac{1}{d^2} = \frac{h^2}{a^2} + \frac{k^2}{b^2} + \frac{l^2}{c^2} \qquad (2)$$

Substituting the d_{004} value in the equation 2 the value of "c" can be obtained as

$$\frac{1}{d^2} = \frac{0^2 + 0k^2}{a^2} + \frac{4^2}{c^2}$$

or c = 9.4599 Å

Substituting the value of d_{101} and 'c' value in the equation 2

$$\frac{1}{d^2} = \frac{1^2 + 0^2}{a^2} + \frac{1^2}{c^2}$$

or a = 3.7451 Å

Lattice parameters for Ce-TiO_2 are: a = b= 3.7451 Å; c = 9.4599 Å

3. Lattice distortion

The lattice distortion of the prepared catalysts were calculated by using the Stokes and Wilson's formula; ε = β/ (4 tan θ), where β is the full width at half maximum of diffracted peak and θ is the Bragg angle of the [*h k l*] planes (Llordés et al., 2012).

Using 2θ =25.6°, ε = β/ (4 tan θ) = 0.2431/ (4 x tan 12.8) = 0.268

Footer Page TH-1334_08610706

Appendix D: Calculation of band gap energy

Using Kubelka-Munk equation

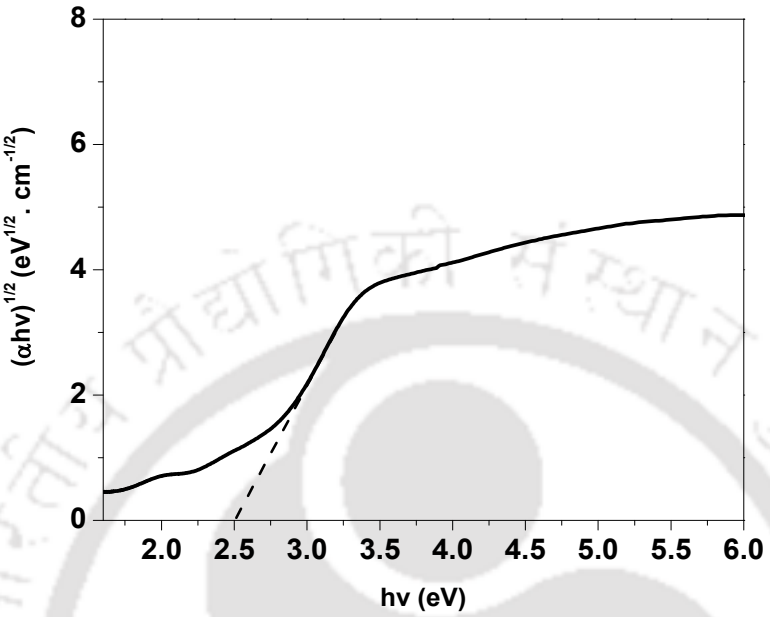

Fig.A.7. Kubelka-Munk plot of 5%In-Ti

The equation is given as $\alpha h\nu = A(h\nu - E_g)^n$ (1)

A, α, E_g, and ν are the proportional constant, absorption coefficient, bandgap, and light frequency respectively.

The band gap can be calculated by using the "n" value of direct allowed transition

(n= 2)

$\alpha h\nu = A(h\nu - E_g)^2$

Sample calculation:

For 5% In-Ti , the absorbance was 0.2109 at wavelength λ = 440 nm

The absorption coefficient was obtained from Lambert Beer law as α = 0.92 cm^{-1} for 0.1 cm cuvette

λ = 440 nm = 0.000044 cm;

The hν was calculated from hν (eV) = h(c/ λ)

Footer Page TH-1334_08610706

For λ = 440 nm = 0.000044 cm; using c = 3×10^{10} cm/s; h = 4.135 667 516 x 10^{-15} eVs

$h\nu$ = 2.82 eV

$\alpha h\nu = 0.92\times2.82 = 2.58$ eV cm^{-1}

$(\alpha h\nu)^{1/2} = 1.60708$ $eV^{1/2}$ $cm^{-1/2}$

The $(\alpha h\nu)^{1/2}$ was plotted against $h\nu$ and the linear region of the plot was extrapolated to intersect the photon energy axis. A line tangent to the slope in the linear region of the absorption onset is drawn. The line can be extrapolated to meet the photon energy axis, which corresponds to the best estimate of the band gap energy. For 5% In-Ti, the band gap calculated by Kubelka-Munk equation was **2.5 eV**.

Footer Page TH-1334_08610706

Appendix E: Calculation of apparent quantum efficiency

(Calculation is based on the method followed by Sasikala et al. 2008)

The reaction volume was about 25 ml. It was assumed that surface area of equivalent sphere was exposed to light. The equivalent diameter can be obtained as

$4/3\ \pi\ r^3 = 25\ cm^3$ or $r = 1.8142\ cm = 0.0184\ m$

The surface area of equivalent sphere= $4 \times \pi \times (0.0184)^2 = 0.00425\ m^2$

Total incident light intensity = 25600 lx

Surface area of the sphere = $0.00425\ m^2$

Total luminous for equivalent sphere = 25600 × 0.00425 = 108.8 lumen

Total power = 108.8 (lumen) x (1/20) (conversion factor) = 5.44 Watt

Total energy for 1 h = 5.44 (Watt) x 3600 (s) = 19584 Joule

Average energy of single photon (E_a) can be calculated as $E_a = \sum_{\lambda_i=450}^{550} E_i(\lambda_i)$

Where $E_i(\lambda_i) = \frac{I_{\lambda_i}}{I_{total}} \times \frac{hc}{\lambda_i}$; h is Planck's constant (6.626×10^{-34} J s); c is the speed of light (3×10^8 m/s); λ is the wavelength (m)

Sample calculation for $\lambda_i = 450.3$ nm

$I_{(450.26)} = 965.956$ (a.u) and I_{total} (450-550 nm) = 1468743.44 (a.u)

Ei (λ_i) = [965.956/1468743.44] × [(6.626×10^{-34}) (J.s) × (3×10^8) (m/s)) / (4.5026 $\times 10^{-7}$) (m)]

= 2.9034×10^{-22} Joule

$E_a = \sum_{\lambda_i=450}^{550} E_i(\lambda_i) = 3.8692 \times 10^{-19}$ Joule

Then E_m, the total incident light in 1h in the range of 450-550 nm is given as

Footer Page TH-1334_08610706

$$E_m = \frac{\text{Total incident light intensity} \times \text{Area under the curve for wavelength in the range of 450-550 nm}}{\text{Area under the curve for the entire emission profile}}$$

$E_m = [(19584\ J \times 392594\ m^2) / 3299756\ m^2]$

$E_m = 2330$ Joule

Total number of incident photons (N) in 1 h in the range of 450-550 nm

$N = E_m/E_a = 2330/ (3.8692 \times 10^{-19}) = 6.022 \times 10^{21}$

Apparent quantum efficiency (AQE) can be calculated as

$$\text{AQE (\%)} = \frac{2 \times \text{number of moles of hydrogen evolved in 1 h} \times (6.023 \times 10^{23})}{\text{Total number of incident photons in 1 h}} \times 100$$

For 1 g of 5% In-Ti amount of hydrogen evolved= 0.001546 moles

Apparent Quantum Efficiency = $[(2 \times 0.001546 \times 6.023 \times 10^{23}) / 6.022 \times 10^{21})] \times 100$

AQE = **30.9 %**

Footer Page TH-1334_08610706

Appendix F: Derivation of rate expression

The rate of methanol oxidation is derived from the elementary steps based on the Langmuir-Hinshelwood model.

[1] $\text{photocatalyst} + \text{h}\nu \rightarrow e_{cb}^{-} + h_{vb}^{-}$

[2] $H_2O_{(l)} + C_v \rightleftharpoons H2O_{ads}$

[3] $CH_3OH_{(l)} + C_v \rightleftharpoons CH_3OH_{ads}$

[4] $H_2O_{ads} + h_{vb}^{+} \xrightarrow{k'_{H_2O}} {}^{\bullet}OH_{ads} + H_{ads}^{+}$

[5a] $CH_3OH_{ads} + h_{vb}^{+} \xrightarrow{k_{CH_3OH}^{h^+}} HCHO_{ads} + H_{ads}^{+}$

[5b] $CH_3OH_{ads} + {}^{\bullet}OH_{ads} \xrightarrow{k_{CH_3OH}^{OH}} HCHO_{ads} + H_2O$

[6] $HCHO_{ads} \xrightarrow{k_{des,HCHO}} HCHO_{(l)}$

[7] $2H^{+} + 2e_{cb}^{-} \xrightarrow{k_{red}} H_{2ads}$

[8] $H_{2ads} \xrightarrow{k_{des,H_2}} H_2\ (g)$

[9] $e_{cb}^{-} + h_{vb}^{+} \xrightarrow{k_{recombination}} Q$

The rate for methanol oxidation from step 5 for both hole and hydroxyl mediated path can be written as:

$$r = \frac{-dC_{CH_3OH}}{dt} = k_{CH_3OH}^{OH}\ C_{OH}\ C_{CH_3OH_{ads}} + k_{CH_3OH}^{h^+}\ C_{h_{vb}^+}\ C_{CH_3OH_{ads}} \qquad (1)$$

$k_{CH_3OH}^{OH}$ - rate constant for methanol oxidation reaction according to hydroxyl radical mediated path

$k_{CH_3OH}^{h^+}$ - rate constant for methanol oxidation reaction according to hole-mediated path

At steady state, concentration of intermediate species is assumed to be constant. From steps (4) and (5),

$$\frac{d[C_{OH_{ads}}]}{dt} = k'_{H_2O}\ C_{h_{vb}^+}\ C_{H_2O_{ads}} - k_{CH_3OH}^{OH}\ C_{OH_{ads}} C_{CH_3OH_{ads}} = 0$$

Footer Page TH-1334_08610706

$$C_{OH_{ads}} = \frac{k'_{H_2O}\ C_{h^+_{vb}}\ C_{H_2O_{ads}}}{k^{OH}_{CH_3OH}\ C_{CH_3OH_{ads}}} \qquad (2)$$

From step (2) and step (3)

$$C_{H_2O_{ads}} = K_{H_2O}\ C_{H_2O_{(l)}}\ C_v \qquad (3)$$

$$C_{CH_3OH_{ads}} = K_{CH_3OH}\ C_{CH_3OH_{(l)}}\ C_v \qquad (4)$$

Substituting $C_{H_2O_{ads}}$ and $C_{CH_3OH_{ads}}$ from equation 3 and 4 in equation 2

$$C_{OH_{ads}} = \frac{k'_{H_2O}\ C_{h^+_{vb}}\ K_{H_2O}\ C_{H_2O(l)}}{k^{OH}_{CH_3OH}\ K_{CH_3OH}\ C_{CH_3OH}} \qquad (5)$$

Using steps (1, 4, 5 and 9);

$$\frac{d[C_{h^+}]}{dt} = I_a\Phi\ - k_{H_2O}C_{H_2O_{ads}}C_{h^+} - k^{h^+}_{CH_3OH}C_{CH_3OH_{ads}}C_{h^+} - k_{recombination}\ [h^+][e^-] = 0 \qquad (6)$$

Where , $I_a\Phi$ **:** rate of absorption of photon ; I_a : Amount of photons absorbed per unit time ; Φ **:** Quantum efficiency

Under steady state, concentration of electrons is equals to that of holes and

$[h^+_{vb}] \approx [e^-_{cb}]$

Substituting in equation 6

$$\frac{d[C_{h^+}]}{dt} = I_a\Phi\ - C_{h^+}\left(k'_{H_2O}C_{H_2O_{ads}} + k^{h^+}_{CH_3OH}C_{CH_3OH_{ads}}\right) - k_{recombination}\ (C_{h^+})^2 = 0 \qquad (7)$$

Since charge recombination in semiconductors is much faster than any electron transfer, it is assumed that $k_{recombination} >> k_{H_2O}, k^{h^+}_{CH_3OH}$

Then from equation (7) , $I_a\Phi - k_{recombination}\ (C_{h^+})^2 = 0$

$$C_{h^+} = \left(\frac{I_a\Phi}{k_{recombination}}\right)^{1/2} \qquad (8)$$

Footer Page TH-1334_08610706

Substituting the value of C_{OH} from equation 5 in equation 1

$$r = C_{CH_3OH_{ads}}\ C_{h_{vb}^+}\left(\frac{k'_{H_2O}\ K_{H_2O}\ C_{H_2O_{(l)}}}{K_{CH_3OH}\ C_{CH_3OH}} + k_{CH_3OH}^{h^+}\right) \qquad (9)$$

Substituting the values of $C_{CH_3OH_{ads}}$ from equation 4, rate can be written as

$$r = \left(K_{CH_3OH}\ C_{CH_3OH_{(l)}}\ C_v\right) C_{h_{vb}^+}\left(\frac{k'_{H_2O}\ K_{H_2O}\ C_{H_2O_{(l)}}}{K_{CH_3OH}\ C_{CH_3OH}} + k_{CH_3OH}^{h^+}\right) \qquad (10)$$

Assuming desorption of products being very fast,

$$C_O = C_{CH_3OH_{ads}} + C_{H_2O_{ads}} + C_v \qquad (11)$$

Where C_O is the total adsorption sites and constant for given catalyst.

Substituting the values of $C_{CH_3OH_{ads}}$ and $C_{H_2O_{ads}}$ from equations 3 and 4 in equation 11 and solving

$$C_v = \frac{C_O}{1 + K_{CH_3OH}\ C_{CH_3OH_{(l)}} + K_{H_2O}\ C_{H_2O_{(l)}}}$$

Substituting the value of C_V in equation 10

$$r = \left(\frac{K_{CH_3OH}\ C_{CH_3OH_{(l)}} C_O C_{h_{vb}^+}}{1 + K_{CH_3OH}\ C_{CH_3OH_{(l)}} + K_{H_2O}\ C_{H_2O_{(l)}}}\right)\left(\frac{k'_{H_2O}\ K_{H_2O}\ C_{H_2O_{(l)}}}{K_{CH_3OH}\ C_{CH_3OH}} + k_{CH_3OH}^{h^+}\right)$$

$$r = \left(\frac{K_{CH_3OH}\ C_{CH_3OH_{(l)}} C_O\ C_{h_{vb}^+}}{1 + K_{CH_3OH}\ C_{CH_3OH_{(l)}} + K_{H_2O}\ C_{H_2O_{(l)}}}\right)\left(\frac{k_{H_2O}\ K_{H_2O}\ C_{H_2O_{(l)}} + k_{CH_3OH}^{h^+} K_{CH_3OH}\ C_{CH_3OH}}{K_{CH_3OH}\ C_{CH_3OH}}\right)$$

$$r = \left(\frac{k_{H_2O}\ K_{H_2O} + k_{CH_3OH}\ K_{CH_3OH}\ C_{CH_3OH}}{1 + K_{CH_3OH}\ C_{CH_3OH_{(l)}} + K_{H_2O}\ C_{H_2O_{(l)}}}\right)$$

$k_{H_2O} = k'_{H_2O} C_o\ C_{H_2O}\ C_{h_{vb}^+}$ and $k_{CH_3OH} = k_{CH_3OH}^{h^+}\ C_o\ C_{h_{vb}^+}$

Footer Page TH-1334_08610706

K_{H_2O} and K_{CH_3OH} are the adsorption equilibrium constants of methanol and water. Since the reaction was carried out in presence of excess water, concentration of water was taken as constant. Since light intensity was high and constant during experiments, the rate of photo absorption was assumed to be constant. For a given catalyst rate of recombination can be assumed to be constant. Hence from equation 8 concentration of hole in the catalyst surface can be assumed to be constant. The two rate constants k_{H_2O} and k_{CH_3OH} and two adsorption equilibrium constants K_{H_2O} and K_{CH_3OH} were estimated.

Footer Page TH-1334_08610706